UNIVERSITY OF
Southampton

# A COMPUTATIONAL STUDY OF SUPPORTED RHODIUM CATALYSTS

by
Otello Maria Roscioni

A thesis submitted in partial fulfillment for the degree of Doctor of Philosophy

in the
Faculty of Engineering, Science and Mathematics
School of Chemistry

December 2009

*There are only two kinds of people in this world: Those who appreciate the full variety and complexity and splendor of the human condition, and those who believe that there are only two kinds of people in this world.*
Daniel F. Styer

*You don't have to be disabled to be different, because everybody's different.*
Fran Peek

# DECLARATION OF AUTHORSHIP

I, Otello Maria Roscioni, declare that this thesis titled "A computational study of supported rhodium catalysts" and the work presented in it are my own. I confirm that:

- This work was done wholly or mainly while in candidature for a research degree at this University.
- Where any part of this thesis has previously been submitted for a degree or any other qualification at this University or any other institution, this has been clearly stated.
- Where I have consulted the published work of others, this is always clearly attributed.
- Where I have quoted from the work of others, the source is always given. With the exception of such quotations, this thesis is entirely my own work.
- I have acknowledged all main sources of help.
- Where the thesis is based on work done by myself jointly with others, I have made clear exactly what was done by others and what I have contributed myself.

Signed:_____

Date:_____

UNIVERSITY OF SOUTHAMPTON

# *Abstract*

Faculty of Engineering, Science and Mathematics
School of Chemistry

*Doctor of Philosophy*

## A computational study of supported rhodium catalysts

by Otello Maria Roscioni

In this work, density functional theory (DFT) was used to obtain microscopic structures of heterogeneous catalysts based on rhodium supported on a metal oxide ($\gamma$-$Al_2O_3$). Two different methodologies were used. The first methodology uses a periodic model and a plane-wave basis set to solve the Schrödinger equation in the framework of Bloch's theorem. The optimised structures of $Rh^{I}(CO)_2/\gamma$-$Al_2O_3$ species obtained at this level of theory have bond lengths in agreement with experimental EXAFS determinations. The weighted linear combination of Rh K-edge XANES spectra computed using the three most dominant structures reproduces well the phase and shape of the oscillations of the experimental XANES spectrum, providing support for the computed structures.

The second methodology is based on hybrid quantum mechanical (QM)/molecular mechanical (MM) calculations. Within this scheme the support is described at the MM level of theory while the region of interest, the absorption site where the surface $Rh^{I}(CO)_2$ complex lies, is described with a suitable QM approach. These hybrid calculations performed at the PBE/ECP/cc-pVDZ level of theory were used to obtain minimum-energy structures and harmonic stretching frequencies of $Rh^{I}(CO)_2/\gamma$-$Al_2O_3$ species. The computed bond lengths and harmonic stretching frequencies were in good agreement with the experimental evidence and with the results obtained using periodic models.

# ACKNOWLEDGEMENTS

This thesis would not have been possible without the help of several people. Firstly I would like to acknowledge my supervisor Prof. John Evans for his kindness and for having given me the opportunity to do a PhD in Southampton. I have no idea what you thought after the conversation we and Moniek had in Grenoble, in 2005. I reckon I must have been convincing. Despite the experimental environment that gave birth to this project, it turned out to be intriguing theoretical work thank to the help of my other great supervisor, Prof. John Dyke. John, you are a good friend and I really enjoyed working with you. You taught me how to be a professional scientist, and I will never forget it. I sincerely thank Dr. Ed Lee for guiding me in the fascinating field of quantum-chemistry, and for having designed the high-quality basis sets used in this work. Ed, you are the kind of person I always dreamed to be as a child. I would like to thank Dr. Peter Sushko and Prof. Alex Shluger for their help with the program *Guess*. Working with you has been a challenging and positive experience, and I hope that the results we obtained are a fair return for all the time that you (Peter in particular) have spent with me. I kindly thank Sarah Wilsey and Helen Tsui for getting me started with the computational facilities of the NSCCS, which have been fundamental to carry out this thesis work. Many thanks to Prof. Steve Parker for guiding my first steps in the field of molecular mechanics, and to Prof. Claudio Zannoni and Dr. Roberto *"Bebo"* Berardi for their support at the very end of the thesis work.

I gratefully thank the EU Early Stage Research Training Network (SEARCHERS) for financial support which enabled me to do this work.

Once again, I must thank my family for their love and support throughout all these years. You are simply great. A special mention goes to my fiancée Fabiola: we shared the best years of our lives as friends, colleagues and lovers, and I am delighted that

you have always been with me. Finally I want to thank all my friends without whom I would have not survived the lonely, long rainy days. You have been a family, and there are no words to say how much I owe to everyone of you, so I will simply say *grazie*! But I must also say diolch, thenk ye, merci, danken, gracias, obrigado, dzieki, spasibo, arigato and cheers in all the spoken tongues of the word, because friendship and culture are truly universal activities, probably the loftiest of all human activities.

# INDEX

**Declaration of Authorship** i

**Abstract** ii

**Acknowledgements** iii

**1 Introduction** 1

1.1 Aims of the Thesis . . . 1

1.2 Catalysis . . . 2

1.2.1 Heterogeneous Catalysis . . . 2

1.2.2 Catalyst structure . . . 9

1.3 The Chemistry of Alumina . . . 10

1.3.1 The Bulk Structure . . . 11

1.3.2 Surface Properties . . . 13

1.4 Supported Rhodium Catalysts . . . 14

1.4.1 Industrial Use and Applications . . . 14

1.4.2 Surface Species . . . 15

1.4.3 Preparation . . . 16

1.4.4 Characterisation . . . 17

1.5 Theoretical Studies . . . 18

1.5.1 Methodologies . . . 19

1.6 Outline of the thesis . . . 21

**2 Theoretical Methods** 22

2.1 Approximate Solutions of the Schrödinger equation . . . 22

2.1.1 Born-Oppenheimer Approximation . . . 23

2.1.2 Spin Orbitals and Space Orbitals . . . . . 23
2.1.3 Slater Determinants . . . . . 24
2.1.4 Hartree-Fock Theory . . . . . 26
2.1.5 Hartree-Fock-Roothaan equations . . . . . 32
2.1.6 Basis Sets . . . . . 34
2.2 Electron Correlation . . . . . 37
2.2.1 Perturbation Theory . . . . . 40
2.2.2 Coupled-Cluster Methods . . . . . 41
2.2.3 The Density Functional Theory . . . . . 42
2.3 Systems with Periodic Boundary Conditions . . . . . 45
2.3.1 Bloch's Theorem . . . . . 45
2.3.2 Pseudopotential Approximation . . . . . 46
2.4 Molecular Mechanics . . . . . 48
2.4.1 Atomistic Model . . . . . 48
2.4.2 Force Fields . . . . . 49
2.4.3 Shell-Model Method . . . . . 50
2.5 Combined QM/MM Calculations . . . . . 51
2.5.1 The Guess approach . . . . . 52
2.5.2 Computational procedure . . . . . 53
2.6 Computational Details . . . . . 54
2.7 Conclusions . . . . . 55

**3 Simulation of Hydroxylated $\gamma$-Alumina Surfaces 56**
3.1 Plane-wave DFT Simulations . . . . . 58
3.1.1 Simulation Parameters . . . . . 58
3.1.2 Computed Structures . . . . . 62
3.2 Molecular Mechanics Simulations . . . . . 71
3.2.1 Simulation Parameters . . . . . 71
3.2.2 Computed Structures . . . . . 76
3.3 Conclusions . . . . . 80

**4 Calculations on Rhodium Compounds** **82**
4.1 Basis Set Design . . . 84
4.2 DFT and MP2 Calculations . . . 86
4.2.1 Rhodium Mono-carbonyl Complexes . . . 86
4.2.2 Rhodium Di-carbonyl Complexes . . . 91
4.2.3 Rhodium Carbonyl Chloride Complexes . . . 95
4.2.4 Enthalpy of a Splitting Reaction . . . 101
4.2.5 Basis Set Effect . . . 104
4.3 Periodic DFT Calculations . . . 106
4.3.1 Simulation Parameters . . . 106
4.3.2 Computed Structures . . . 107
4.4 Conclusions . . . 108

**5 Simulation of Supported Catalysts** **110**
5.1 Periodic Simulations . . . 111
5.1.1 Computed Structures . . . 112
5.1.2 Theoretical XANES Spectra . . . 118
5.2 Embedded Molecular Cluster Calculations . . . 120
5.2.1 Preliminary Operations . . . 122
5.2.2 $\gamma$-Alumina Surfaces . . . 125
5.2.3 Surface Rhodium Species . . . 134
5.3 Conclusions . . . 143

**6 Conclusions** **146**
6.1 Future work . . . 149

**A Support Information** **151**
A.1 Castep Input Files . . . 151
A.1.1 Building a Slab Model of Surfaces with Gdis . . . 153
A.2 Gulp Input Files . . . 154

A.3 Lanl2 ECP Basis Sets for Rhodium . . . . . 158
A.4 Software . . . . . 161
A.5 Guess Tutorial . . . . . 169

**Bibliography** **174**

CHAPTER 1

# INTRODUCTION

## 1.1 Aims of the Thesis

This project aims to provide a theoretical description of the chemical properties and activity of a particular class of heterogeneous catalysts based on a transition metal supported on a metal oxide surface.

The study of catalysis dates back to early in the nineteenth century [1]. Since the discovery that some chemical reactions occured faster when they were carried out in the presence of a particular material –then called a *catalyst*–, catalysis has had a tremendous impact on the development of the industrial world: it is estimated that about 90% of all modern chemical products involve the use of a catalyst in at least one stage in their manufacture [2, 3]. Huge efforts have been made to understand the mechanisms with which catalysts work and to improve the efficiency of catalytic reactions.

Often, a solid catalyst is a substance characterised by the presence of structural defects and different crystalline structures. This makes the correlation between structural properties and catalytic behaviour very difficult to determine. In this case, theory can be very valuable to gain a better understanding of the way a catalyst works by investigating its electronic structure.

The catalyst under investigation in this project is rhodium supported on $\gamma$-$Al_2O_3$ ($\gamma$-*alumina*). The main objective was to compute the electronic structure of different rhodium gem-dicarbonyl ($Rh^{I}(CO)_2$) surface species, whose presence has been well characterised experimentally [4–7]. In this thesis, an original theoretical approach has

been developed and tested on some simple complexes containing rhodium, before being applied to the study of catalyst surface species.

## 1.2 Catalysis

A rigorous definition of a *catalyst* is "a substance that increases the rate of a reaction without modifying the overall standard Gibbs energy change in the reaction" [2]. This means that the catalyst chemically interacts with the reactants and lowers the energy barrier necessary for the formation of the products. Catalysts are usually divided into two main categories called *homogeneous* and *heterogeneous*.

In homogeneous catalysis the reactants and the catalyst are in the same phase, be it liquid or gas. The advantage of having the catalyst and the reactants in the same phase is that they can easily interact with one another and as consequence the catalyst has a high activity. Fine control of the structure of the catalyst active site allows the achievement of a high degree of selectivity, allowing the catalyst to make a specific reaction pathway more favourable when multiple pathways are possible.

In heterogeneous catalysis the reactants and the catalyst are in different phases, typically the catalyst is a solid. In such catalysts only the surface is exposed to the reactants and promotes the reaction. The surface active species generally exhibits a number of different structures, and this can result in a reduced selectivity. The separation and the re-use of a heterogeneous catalyst is nonetheless far more easy compared to re-use of homogeneous catalysts: this leads to a reduced use of solvents and generally a smaller production of waste, which makes this approach appealing for the perspective of environmentally sustainable chemistry.

### 1.2.1 Heterogeneous Catalysis

The surface area-to-volume ratio of a physical object increases as the size of the object decreases, *i.e.* small objects have a relatively large surface area-to-volume ratio compared to large objects. In heterogeneous catalysis only the surface of the catalyst is

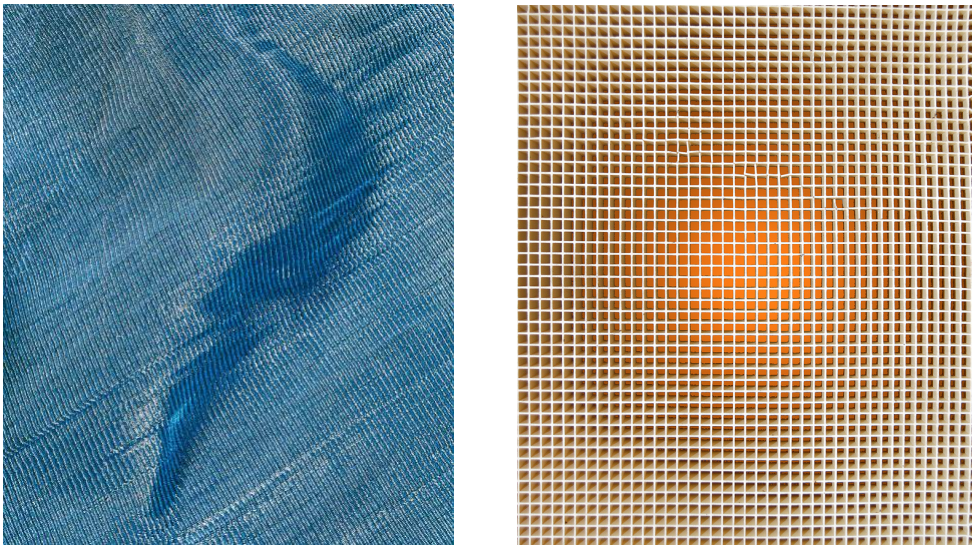

*(a)* *(b)*

**Figure 1.1:** Different types of heterogeneous catalysts. *(a)* Platinum gauze used for the catalytic oxidation of ammonia in the production of nitric acid [9]. *(b)* A ceramic honeycomb support used for the removal of nitrogen oxides from diesel exhaust.

accessible to the reactants and becomes engaged in a chemical reaction: it is therefore of fundamental importance to maximise the surface area-to-volume ratio in order to increase the catalyst activity.

Transition metals are used as catalysts due to their unique ability to coordinate several kinds of chemical species. They are normally used finely divided or dispersed on a high-area porous support [8], although pure metals can be used for particular applications (see Figure 1.1).

Examples of metallic heterogeneous catalysts include Raney nickel, a porous solid used in the hydrogenation and desulfurisation of organic molecules. It is prepared by treating an aluminium-nickel alloy with concentrated sodium hydroxide. This dissolves most of the aluminium in the alloy and leaves a finely-divided highly-porous nickel powder [10]. In the industrial production of nitric acid, a gauze composed of small platinum wires is used to catalytically oxidise ammonia to nitric oxide [11]. More often however the metal is dispersed on a high-area porous support that prevents the

metal particles from sintering together, and provides the mechanical strength that a commercial catalyst must have in order to be used in practical applications, whose operating conditions often involve high pressure and temperature. Furthermore, the interaction between the metal and the support can alter significantly the properties of the catalystab: a recently developed approach for the synthesis of catalysts focuses on precise control of the active site architecture using macroporous and mesoporous zeolites. The high degree of selectivity is reached by anchoring the catalyst to well-defined, monodispersed and easily accessible molecular units on the support's surface. The resulting single-site catalyst thus has the selectivity of a homogeneous catalyst and the strength of a heterogeneous catalyst [12, 13]. Achieving all these features is not easy and requires a precise understanding of the catalysed reaction pathway, as well as a careful synthesis ot the catalyst.

The reaction mechanism in heterogeneous catalysis is characterised by a sequence of events that can be summarised as follows [2]:

1. Diffusion of the reactants through the gas or liquid phase to the catalyst surface.

2. Adsorption of the reactants on the catalyst surface. *Chemisorption* occurs when new chemical bonds are formed. In contrast, *physisorption* occurs when only weak electrostatic interactions are present between the adsorbate and the substrate.

3. Surface diffusion of the adsorbed species. The mobility of the reactants on the catalyst's surface is of fundamental importance for the reaction to take place.

4. Reaction between the adsorbed reactants. The activation energy of the catalysed reaction is lower than the analogous uncatalysed reaction, resulting in a more rapid reaction.

5. Desorption of the products and their subsequent diffusion into a different phase.

The activity of a catalyst is the extent to which it influences the rate of a reaction, which depends on the surface absorption mechanism and on the thermodynamic variables pressure, volume, molar fraction and temperatue. The absorption mechanism of

a gas over a surface involves two steps:

$$\mathrm{A_{(g)}} \xrightarrow{k_{1a}} \mathrm{A_{(a)}} \tag{1.1}$$

$$\mathrm{A_{(a)}} \xrightarrow{k_{1d}} \mathrm{A_{(g)}} \tag{1.2}$$

The rate of adsorption of the species $\mathrm{A_{(g)}}$ in step (1.1) is given by:

$$-\frac{d[\mathrm{A_{(g)}}]}{dt} = k_{1a}(1-\theta_A)P_A \tag{1.3}$$

where $P_A$ is the pressure of gas and $\theta_A$ is the fractional blocking of the surface by the adsorbate. When the surface is completely filled by the adsorbate the absorption rate is zero and consequently $\theta_A = 1$. The rate of desorption of the species $\mathrm{A_{(a)}}$ due to reaction (1.2) is given by:

$$-\frac{d[\mathrm{A_{(a)}}]}{dt} = k_{1d}\theta_A \tag{1.4}$$

which depends only on the fractional coverage of the surface $\theta_A$. At equilibrium the absorption and desorption rates are equivalent, therefore it follows that

$$k_{1a}(1-\theta_A)P_A = k_{1d}\theta_A \tag{1.5}$$

This gives

$$\theta_A = \frac{k_1 P_A}{1 + k_1 P_A} \tag{1.6}$$

where $k_1 = k_{1a}/k_{1d}$ is the adsorption equilibrium constant. This expression is known as the *Langmuir isotherm*.

In heterogeneous catalysis there are two main reaction mechanisms, depending on whether one or more reactants are adsorbed on the catalyst surface. In the first mechanism, called the Eley-Rideal mechanism [14], the reaction occurs between an adsorbate and a gas (see Figure 1.2). This process can be described as a species *A* being adsorbed on the catalyst surface, and then reacting directly with a species *B* in the gas phase to give *C*, that is adsorbed on the surface and subsequently desorbed. The overall mech-

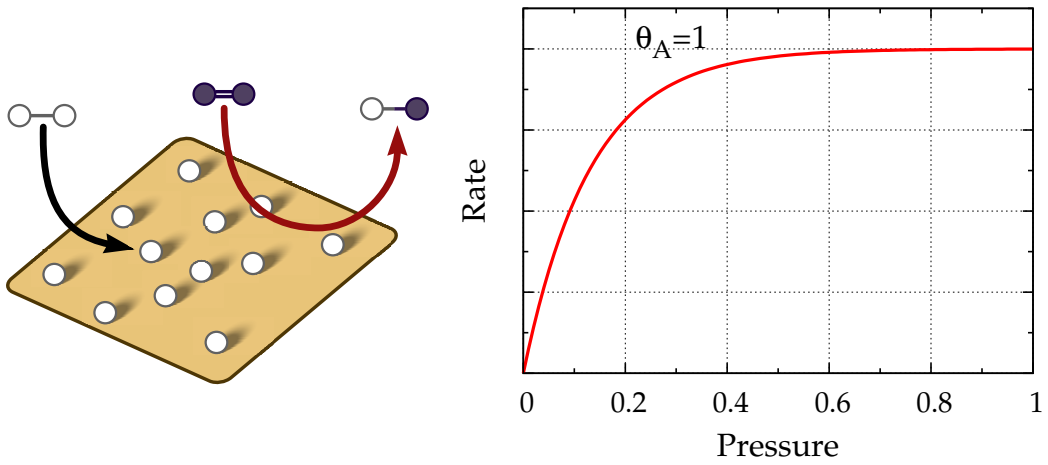


**Figure 1.2:** Eley-Rideal Mechanism: the reaction occurs between an adsorbate $A$ (white atoms) and a gas $B$ (blue atoms). The reaction rate (at $P_B$ = constant.) depends on the adsorbate coverage $\theta_A$ only.

anism of this reaction can be written as:

$$A_{(g)} \underset{k_{1d}}{\overset{k_{1a}}{\rightleftharpoons}} A_{(a)} \tag{1.7}$$

$$A_{(a)} + B_{(g)} \xrightarrow{k_2} C_{(a)} \tag{1.8}$$

$$C_{(a)} \xrightarrow{k_3} C_{(g)} \tag{1.9}$$

Assuming that step (1.8) is rate-limiting the overall process, it follows that the rate of the reaction is given by:

$$\frac{d[C_{(a)}]}{dt} = k_2 \theta_A P_B \tag{1.10}$$

(the surface coverage of $C_{(a)}$ can be neglected since it desorbs rapidly). At equilibrium the surface coverage is in a steady state:

$$\frac{d\theta_A}{dt} = k_{1a}(1-\theta_A)P_A - k_{1d}\theta_A - k_2\theta_A P_B = 0 \tag{1.11}$$

It follows that,

$$\theta_A = \frac{k_{1a}P_A}{k_{1a}P_A + k_{1d} + k_2 P_B} \tag{1.12}$$

Substitution of equation (1.12) into equation (1.10) yields:

$$\frac{d[\mathrm{C_{(a)}}]}{dt} = \frac{k_{1a}k_2P_AP_B}{k_{1a}P_A + k_{1d} + k_2P_B} \tag{1.13}$$

At $P_B =$ constant, this equation can be rewritten as:

$$\frac{d[\mathrm{C_{(a)}}]}{dt} = \frac{k'k_2P_AP_B}{1 + k'P_A} \tag{1.14}$$

where $k' = \dfrac{k_{1a}}{k_{1d} + k_2P_B}$ is a complex rate constant. This is known as the *Eley-Rideal equation*. The rate changes from first order in $[\mathrm{A}]$ at low pressure of A, to zero order in $[\mathrm{A}]$ at high pressure, as shown in the right panel of Figure 1.2.

The second mechanism is called the Langmuir-Hinshelwood mechanism [14] and involves both reactants being adsorbed on the catalyst surface before reaction occurs (see Figure 1.3). The process can be described as follows.
Consider the reaction $\mathrm{A_{(a)}} + \mathrm{B_{(a)}} \longrightarrow \mathrm{C_{(g)}}$ where both reactants are adsorbed on the catalyst surface. The full mechanism of the reaction is then:

$$\mathrm{A_{(g)}} \underset{k_{1d}}{\overset{k_{1a}}{\rightleftharpoons}} \mathrm{A_{(a)}} \tag{1.15}$$

$$\mathrm{B_{(g)}} \underset{k_{2d}}{\overset{k_{2a}}{\rightleftharpoons}} \mathrm{B_{(a)}} \tag{1.16}$$

$$\mathrm{A_{(a)}} + \mathrm{B_{(a)}} \xrightarrow{k_3} \mathrm{C_{(a)}} \tag{1.17}$$

$$\mathrm{C_{(a)}} \underset{}{\overset{k_4}{\rightleftharpoons}} \mathrm{C_{(g)}} \tag{1.18}$$

The surface coverage $\theta_A$ and $\theta_B$ depends now on the pressure of both species. At equilibrium, the rate of change of the surface coverage is:

$$\frac{d\theta_A}{dt} = k_{1a}(1 - \theta_A - \theta_B)P_A - k_{1d}\theta_A - k_3\theta_A\theta_B = 0 \tag{1.19a}$$

$$\frac{d\theta_B}{dt} = k_{2a}(1 - \theta_A - \theta_B)P_B - k_{2d}\theta_B - k_3\theta_A\theta_B = 0 \tag{1.19b}$$

Assuming the loss of the adsorbed reactants due to the formation of $\mathrm{C_{(a)}}$ can be ne-

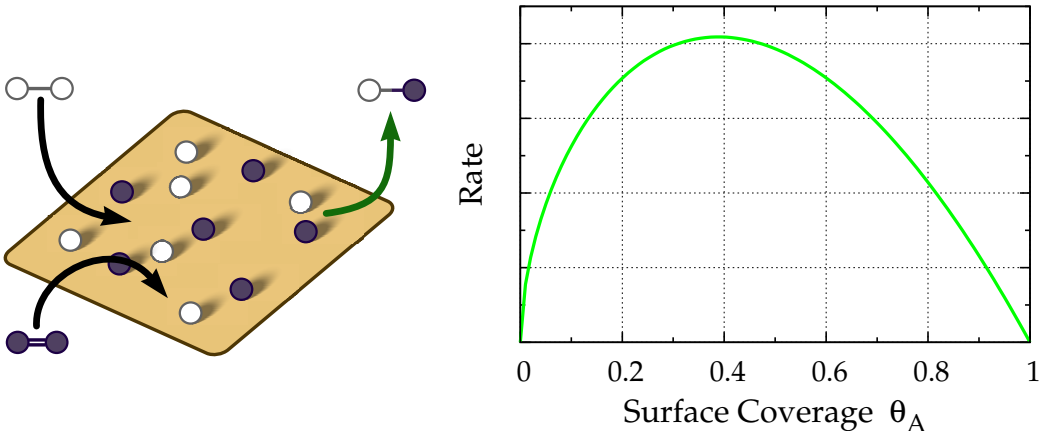


**Figure 1.3:** Langmuir-Hinshelwood Mechanism: the reaction occurs between two adsorbates $A$ (white atoms) and $B$ (blue atoms). The reaction rate depends on the the adsorbate coverage of both species.

glected, *i.e.* :

$$k_3\theta_A\theta_B \ll k_{1a}(1-\theta_A-\theta_B)P_A - k_{1d}\theta_A \tag{1.20a}$$

$$k_3\theta_A\theta_B \ll k_{2a}(1-\theta_A-\theta_B)P_B - k_{2d}\theta_B \tag{1.20b}$$

Then, as a consequence, the term $k_3\theta_A\theta_B = 0$ and the Langmuir isotherms for the reactants are obtained by reordening the equations 1.19a and 1.19b:

$$\theta_A = \frac{k_1 P_A}{1 + k_1 P_A + k_2 P_B} \tag{1.21a}$$

$$\theta_B = \frac{k_2 P_B}{1 + k_1 P_A + k_2 P_B} \tag{1.21b}$$

were $k_1 = \dfrac{k_{1a}}{k_{1d}}$ and $k_2 = \dfrac{k_{2a}}{k_{2d}}$ are the adsorption equilibrium constants. Assuming that the rate-limiting step is again the (1.17), the rate equation has the following form and is known as the *Langmuir-Hinshelwood equation*.

$$\frac{d[\mathrm{C_{(a)}}]}{dt} = k_3\theta_A\theta_B = \frac{k_1 k_2 k_3 P_A P_B}{(1 + k_1 P_A + k_2 P_B)^2} \tag{1.22}$$

At low pressures the rate is of the first order in [A], as shown in the right panel of


**Figure 1.4:** Schematic representation of different surface structures.

Figure 1.3. The highest rate of conversion is reached when the ratio of the surface compositions are similar to the stoichiometry of the reaction.

The equations presented in this section provide a quantitative way of assessing the activity of a catalyst. These simple mechanisms are useful because the macroscopic behaviour of a catalyst is correlated to its microscopic structure. In principle, the absorption energies of reactants and reaction intermediates can be computed using theoretical methods, and then used to determine the rate constants as a function of the catalyst surface composition and morphology.

### 1.2.2 Catalyst structure

In this thesis the structure-activity relationship of supported rhodium catalysts is investigated with theoretical methods. Particular attention is given to the role played by the support, in terms of the geometrical constraints it provides and the electronic interaction between the metal active centre and the support atoms.

Figure 1.4 shows a schematic representation of the principal structures involved in heterogeneous catalysis. The most common structure is a flat surface exposing a specific crystallographic face. Surface atoms have a coordination number smaller than bulk atoms, and experience an anisotropic field that modifies greatly their chemical properties, making them more able to coordinate other species. Defects on surfaces can occur, and they too contribute to the final properties of the catalysts. A vacancy is a single atom missing from a crystal surface and an adatom is a single atom adsorbed on a crystal surface. These kinds of defects are involved in surface growth and often promote the adsorption of reactants. The dislocation between bulk atoms causes a

mismatch between crystal planes and the formation of steps and kinks. The atoms in steps and kinks have a very low coordination number, a high free energy and as a consequence a high reactivity and a strong binding energy for an adsorbate.

Such a rich surface topography makes a supported metal catalyst extremely difficult to characterise. Preparation of a metal single crystal followed by cleavage exposing a particular crystal plane is a technique widely used in surface science. It can be used as a model for the fundamental understanding of the interactions between the adsorbates and the metal, but it does not account for the effect of the support. Deposition of a thin film of metal on a low-area planar support (such as $TiO_2$) provides a structurally simple model that accounts for the support interaction. Although the well-defined and measurable properties of these surfaces make them appealing as catalyst models, the deposited metal particles show a non-uniform distribution of size and shape that limit the correlation of measured average properties with catalytic properties.

Another class of support for heterogeneous catalysis includes high surface area ceramic materials such as $\gamma$-alumina. This material has a typical surface area of 100 $m^2/g$ [15] and a bulk structure characterised by an octahedral aluminum sub-lattice with a percentage of tetrahedral aluminum sites of about 25-31% [16]. The statistical character of the $\gamma$-alumina structure makes the structure-activity relationship very difficult to detemine experimentally, and this will be discussed in more detail in the next section.

## 1.3 The Chemistry of Alumina

One of the most used supports in heterogeneous catalysis is undoubtly $\gamma$-alumina. There are many reasons for this choice: primarily its mechanical strength and thermal stability, its stability under oxidising conditions, and finally its high surface area-to-volume ratio. Alumina surfaces have also remarkable chemical properties: surface OH groups act as weak Brønsted acids, where unsaturated $Al^{3+}$ atoms act as Lewis acid sites and $O^{2-}$ atoms act as Lewis base sites. Due to the rigidity of the surface, these groups coexist without reacting with one another. Although alumina is a cat-

alyst used on its own for many commercially important reactions (for example, it is used as a desulphurising agent in the Claus process), it is more commonly used as a support for transition metals. For some supported metal catalysts there is no dependence on surface structure, while for others the catalytic behaviour of the metal changes significantly in response of its interaction with the surface atoms. For supported Rh/$Al_2O_3$catalysts, it has been shown that surface $OH^-$ groups are involved in the disruption of small rhodium particles under a CO atmosphere, leading to the formation of monodispersed rhodium *gem*-dicarbonyl species and molecular hydrogen [6]. The nature of the support also determines the size and distribution of the metal particles, and hence the nature of the surface species produced under operating conditions.

### 1.3.1 The Bulk Structure

The structure of $\gamma$-alumina is usually characterised[1] by techniques such as IR spectroscopy, NMR spectroscopy, X-ray diffraction (XRD), transmission electron microscopy and a variety of computational methods ranging from atomistic simulations [18–22] to plain-wave/pseudopotential density functional calculations [16, 23–25].

Although a large scientific effort has been devoted to the characterisation of $\gamma$-alumina, its structure still remains a matter of investigation. The transformation sequence that leads aluminium hydroxides such as AlOOH (bohemite) to be converted into $\alpha$-alumina (corundum)[2], gives rise to a series of metastable phases, known as *transition aluminas* [24]:

$$\mathrm{AlOOH} \xrightarrow{450\ ^\circ\mathrm{C}} \gamma\text{-}\mathrm{Al_2O_3} \xrightarrow{750\ ^\circ\mathrm{C}} \delta\text{-}\mathrm{Al_2O_3} \xrightarrow{1000\ ^\circ\mathrm{C}} \theta\text{-}\mathrm{Al_2O_3} \xrightarrow{1200\ ^\circ\mathrm{C}} \alpha\text{-}\mathrm{Al_2O_3}$$

The transition aluminas can be produced in the laboratory: depending on the synthetic

[1] See the comprehensive review of the fundamental aspects of $\gamma$-alumina by M. Trueba and S. P. Trasatti and the references therein [17].

[2] The most thermodynamically stable phase of aluminium oxides with stoichiometry $Al_2O_3$

| | | | | | |
|---|---|---|---|---|---|
| **1** | *Acta Cryst.* **B47**, 617 (1991) [26] | | | | |
| | *a* | 7.911 | $\alpha$ | 90. | space group: $Fd\overline{3}m$ |
| | *b* | 7.911 | $\beta$ | 90. | unit cell: *cubic* |
| | *c* | 7.911 | $\gamma$ | 90. | |
| **2** | *Phys. Rev. B* **65**, 012101 (2001) [23] | | | | |
| | *a* | 7.887 | $\alpha$ | 90. | space group: $Fd\overline{3}m$ |
| | *b* | 7.887 | $\beta$ | 90. | unit cell: *cubic* |
| | *c* | 7.887 | $\gamma$ | 90. | |
| **3** | *J. Phys. Chem. B* **105**, 5121 (2001) [16, 27] | | | | |
| | *a* | 5.587 | $\alpha$ | 90. | space group: $P2_1/m$ |
| | *b* | 8.413 | $\beta$ | 90.59 | unit cell: *monoclinic* |
| | *c* | 8.068 | $\gamma$ | 90. | |
| **4** | *Phys. Rev. B* **68**, 144110 (2003) [28] | | | | |
| | *a* | 5.652 | $\alpha$ | 90. | space group: $I4_1/amd$ |
| | *b* | 5.652 | $\beta$ | 90. | unit cell: *tetragonal* |
| | *c* | 7.871 | $\gamma$ | 90. | |

**Table 1.1:** Overview of four recently proposed models of the $\gamma-$alumina bulk structure.

method used, a mixture of different polymorphs is obtained, with a variable degree of amorphous structure. All transition aluminas share some common structural properties: they have a well-defined oxygen sublattice that forms interstices filled by aluminum atoms occupying octahedral and tetrahedral sites. Traditionally the structure of $\gamma-$alumina is regarded as a defect cubic spinel type, where the magnesium atoms in the ideal spinel $\mathrm{MgAl_2O_4}$ are replaced with aluminum atoms. To satisfy the $\mathrm{Al_2O_3}$ stoichiometry, some sites remain empty and form defects whose exact position is difficult to determine. The controversy regarding the alumina structure arises from the fact that the position of defects determines the space group of a given polymorph: $\gamma-$aluminas prepared from different precursors have been reported to have a cubic structure with tetragonal distortion, while other studies report only a tetragonal structure [17].

In Table 1.1, four recently proposed structures have been considered as possible candidates for the simulation of $\gamma-$alumina as a support for heterogeneous catalysts. The model no. **3**, shown in Figure 1.5, was chosen in this present work because it accounts

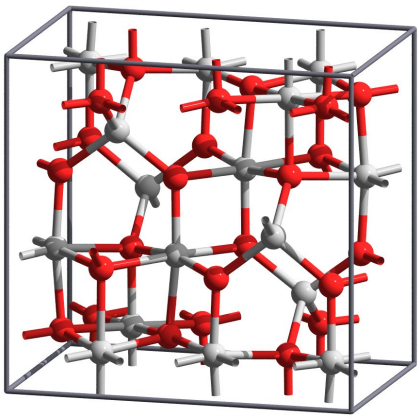

**Figure 1.5:** The structural model of $\gamma$-$Al_2O_3$ proposed by Digne *et al.* [27] has a monoclinic cell containing eight $Al_2O_3$ units. Red atoms are oxygen, grey atoms are aluminium.

for the surface hydroxylation/dehydroxylation process induced by temperature effects [16, 27, 29]. In the original work [29], this model has been optimised with the use of calculations performed at the plane-wave/DFT level of theory with periodic boundary conditions. The bulk structure obtained is consistent with XRD, IR and NMR determinations, and in particular gives a realistic representation of the alumina surfaces by taking into account the presence of different types of surface hydroxy groups, correlating their properties with the chemical environment, morphology and composition of the exposed crystal planes.

### 1.3.2 Surface Properties

The acid-base properties of $\gamma-$alumina surfaces determine the dispersion of the supported active species and ultimately the characteristics of the final catalyst. The reactivity and the acidity of surface hydroxyl groups is determined by their local chemical environmentab: up to seven different bands have been identified in the IR spectrum of hydroxylated alumina surfaces. These bands are generally assigned to OH groups in different environments depending on the number of aluminum atoms coordinated to the oxygen, and to their coordination number [30]. Although this simple model is the most widely used, it suffers of serious limitations due to the crude representation

of alumina surfaces. The bulk model of $\gamma-$alumina proposed by Digne *et al.* contains 8 $Al_2O_3$ units and offers the best compromise in terms of computational cost and structural accuracy. In reference [29], the computed surface density and vibrational properties of the surface hydroxyl groups are in agreement with the experimental data, and have been shown to be dependant on the morphology of $\gamma-$alumina surfaces. Therefore, this model appears to be the most suitable candidate for the representation of $\gamma-$alumina supported heterogeneous catalysts.

## 1.4 Supported Rhodium Catalysts

### 1.4.1 Industrial Use and Applications

Supported rhodium catalysts are very important in industry since the metal centre can easily coordinate different ligands and, for example, activate the C-H bond in alkanes [31–33] and the H-H bond in hydrogen [34]. The primary use of rhodium however is in the automotive industry for the production of three-way catalytic converters. These devices are practical examples of heterogeneous catalysts: they consist in a monolithic ceramic support coated with a high area material such as $\gamma-$alumina that acts as a support for the active catalyst, a mixture of the precious metals platinum, palladium and rhodium. Three-way catalytic converters promote the removal of pollutants such as nitrogen oxides, carbon monoxide and unburnt hydrocarbons from exhaust emissions, as shown in Figure 1.6. Rhodium is an efficient catalyst for $NO_x$ reduction, whereas palladium and platinum metals are used in CO and hydrocarbon oxidation reactions, in particular during 'cold start'. The simultaneous conversion of all pollutants is achieved when the fuel is burned in stoichiometric conditions. When the engine does not operate under these conditions, the exhaust stream contains more reducing reactants (CO and $C_xH_y$) or more oxidising reactants ($O_2$ and $NO_x$) and the conversion efficiency of the catalyst decreases. To overcome this problem, reversible metal oxides such as ceria ($CeO_2$) and zirconia ($ZrO_2$) are added to the catalyst. In this way the catalyst is able to store some oxygen that can be reversibly released when the exhaust does not contain


**Figure 1.6:** The automobile three-way catalytic converter is a practical example of heterogeneous catalysis. The device catalyses the oxidation of CO and hydrocarbons, and the reduction of nitrogen oxides.

enough oxygen.

The interactions between oxygen and precious metals are complicated and the interaction mechanism is not fully understood. A practical problem is the ageing of the catalyst due to thermal treatments and oxidation/reduction cycles: it has been shown that the loss of activity is related to the reduction of surface area, the sintering of rhodium particles and the encapsulation of rhodium particles into the porous support [35].

### 1.4.2 Surface Species

Due to the complex structure of supported metal catalysts, a wide range of parameters can be expected to affect catalytic selectivity and activity such as type of metal used, the type and porosity of the support, the introduction of promoters to the catalyst composition, and the size and shape of the agglomerated Rh particles. Moreover, some changes in catalytic activity are ascribed to a modification of the electronic properties of the metal particles induced by a metal-support interaction *e.g.* the hydroxyl groups of the alumina support are effective in particle degradation and subsequent formation of oxidised metal centres such as $Rh^+$ [6]. The strong interaction between Rh metal and the $\gamma$-alumina support may lead to a decreased catalytic activity at high temperature, *e.g.* rhodium forms an oxide phase and is encapsulated into the support, thus lowering the total amount of active catalyst [35].

In 1957 a pioneering IR study on the chemisorption of CO on rhodium supported on high area alumina reported the presence of several types of rhodium carbonyl species,

including a single CO molecule bound to a rhodium atom, a bridged CO molecule connecting two rhodium atoms and two CO molecules bound to a rhodium atom [4]. In 1985 Van't Blik *et al.* [5] investigated the behaviour of highly dispersed metallic rhodium particles supported on $\gamma$-alumina. The oxidative adsorption of CO at room temperature led to the disruption of the Rh crystallites and formation of monodispersed geminal dicarbonyl species in which rhodium has an oxidation state of +1 and is surrounded by two carbon monoxide molecules and three oxygen atoms. Later studies confirmed the presence of isolated gem-dicarbonyl rhodium species [36–41], suggesting a square planar coordination for the rhodium centre [42, 43] while other work confirmed the interaction with three basal oxygen atoms [44].

Other studies investigated the influence of chlorine on the lability of rhodium particles, some concluding that chlorine stabilises the gem-dicarbonyl species (thus promoting the disruption of rhodium particles) [45], while other workers claimed that chlorine-free monodispersed gem-dicarbonyl species were observed in a catalyst prepared from chlorinated precursors [44].

Even though a number of experimental techniques have been employed to investigate the nature of supported rhodium catalysts, open questions still remain. In particular the morphology of monodispersed rhodium species on $\gamma-$alumina surfaces is not fully established.

### 1.4.3 Preparation

The samples of Rh/$\gamma$-$Al_2O_3$ studied in the laboratory by experimental research groups are in general synthesized according to a standard protocol, in order to make the measurements reproducible. There are two methods to prepare supported Rh/$Al_2O_3$ catalysts.

In the first method, the samples are prepared by metallo-organic chemical vapour deposition (MOCVD) of a stable complex such as $[Rh(CO)_2Cl]_2$ onto hydroxylated $\gamma$-$Al_2O_3$. In this case the $Al_2O_3$ is first dried in a He flow at about 500 K for 6 hours. Under these conditions the alumina is dried but not extensively dehydroxylated. The

$[Rh(CO)_2Cl]_2$ is then sublimed onto the $\gamma$-$Al_2O_3$ to produce a yellow powder. The catalyst so produced is finally stored under an inert He atmosphere and kept refrigerated until use [42].

In the second method the samples are prepared by a wet incipient impregnation of the $\gamma$-$Al_2O_3$ with an aqueous solution of a Rh salt, usually $RhCl_3 \cdot 3H_2O$, with an adequate amount of the Rh precursor for particular surface loading. To prepare chlorine-free catalysts, $Rh(NO_3)_3$ is used. The sample is then dried in air to remove the solvent and calcined for 6 hours at 673 K in 5% $O_2$/He. It is then reduced for 5 hours under flowing 5% $H_2$/He at 573 K [42].

### 1.4.4 Characterisation

The morphological characterisation and the quantitative assessment of catalyst efficiency involves the use of surface science techniques carried out under operating conditions, *i.e. in-situ*. The study of heterogeneous catalysts can be reliably achieved by using a combination of complementary techniques such as Energy Dispersive Extended X-ray Absorption Fine Structure (EDE), Mass Spectrometry (MS) and Diffuse Reflectance Infrared Fourier Transform Spectroscopy (DRIFTS) carried out simultaneously, under well-defined conditions [7, 42, 46, 47].

X-ray absorption spectroscopy is a powerful technique used to study the evolution of the electronic and the local structure of matter. Its sensitivity to short range order and its chemical selectivity make it complementary to X-ray diffraction. The recording of X-ray absorption spectra in a dispersive mode takes advantage of the absence of any mechanical movement of the spectrometer, thus allowing the acquisition of a complete spectrum in a timescale of $\sim$ 300 ms [46].

In EDE, a quasi-parallel and polychromatic beam, supplied by a synchrotron radiation source, is dispersed and focused by an elliptically curved crystal. Because the incident X-ray strikes the crystal at slightly different angles along its length, the bent crystal acts as a polychromator, diffracting a different energy at each point. This energy-dispersed beam converges to a focal point at the sample position, it is trans-

mitted through the sample and then it diverges toward a detector. The position of the beam on the detector can be directly correlated to energy. The X-ray absorption spectrum is obtained by taking the logarithm of the ratio of $I_0$ and $I_1$ data, where $I_0$ and $I_1$ are spatial X-ray intensity distributions with and without the sample, respectively [48].

Infrared spectroscopy is a technique that is widely used to characterise molecules in solution and in the gas phase. This technique is limited to the analysis of samples transparent to IR radiation, that can be formed into the shape of a self-supported pellet. DRIFTS is a powerful technique for non-transparent materials and for *in-situ* measurements under varying environmental and reaction conditions. This kind of spectroscopy offers a number of advantages including minimal or no sample preparation, a very high sensitivity to surface species, the ability to study most non-reflective materials and finally the ability to investigate irregular surfaces or coating [49–51].

Mass spectrometry is an analytical tool used for measuring the molecular mass of a gaseous sample, and its breakdown pattern on electron impact. In a mass spectrometer, the gas molecules are converted into charged particles, typically positive ions, by electron bombardment generated from a hot wire filament. These ions are extracted into the analyser region of the mass spectrometer where they are separated according to their mass-to-charge ratios (m/z). The separated ions are detected and the signals sent to a data system where the m/z ratios are stored together with their relative abundance for presentation in the format of a m/z spectrum. In *in-situ* experiments the m/z spectrum gives informations about the nature of species produced during a chemical reaction.

## 1.5 Theoretical Studies

Quantum chemical methods, especially when used in combination with accurate experimental investigations, are powerful tools in exploring the molecular basis of catalysis. In particular, they are used to model accurately the structure of active sites and ultimately to explain the mechanism of catalytic reactions [52].

The main pieces of information that can be obtained from a quantum mechanical calculation is the energy $E$ and the wavefunction $\Psi$ of a system. This follows directly from the Schrödinger equation:

$$\hat{H}\Psi = E\Psi \tag{1.23}$$

where for each set of coordinates of a system, a Hamiltonian $\hat{H}$ can be set up that can give the energy $E$ of this structure. The minima of the energy with respect to structural coordinates define the structure of reactants, intermediates and products. The accuracy of a quantum mechanical calculation depends on the theoretical method used: this can pose serious limitations to the size of the system investigated. For this reason, different theoretical methodologies are employed to study systems of different type.

### 1.5.1 Methodologies

Very accurate solutions of the Schrödinger equation (1.23) are obtained with theoretical methods that use very large basis sets and account for effects such as electron correlation or multi configurational character of an electronic state. These methods are called *ab-initio*, meaning from first principles, because they are based entirely on theory (although some approximations are made). Methods based on the density functional theory (DFT) cannot be defined *ab-initio* because the functional form of the electron density, on which the theory is based, is unknown and is determined empirically.

Accurate theoretical methods are time-demanding and can be applied to systems containing a limited number of atoms. One of the aims of contemporary catalytic science is to deal with environmental effects, and for heterogeneous catalysts this means taking into account the interactions between the support and the active catalyst, *i.e.* the metal centre. There is, therefore, a strong interest to use methods that allow the study of large systems. In this section three different theoretical approaches are described, each one employing different levels of approximation to describe the effect of the extended environment [52].

**The molecular cluster approach** In this approach, the active site is represented as a

molecular cluster. Due to the intrinsic simplicity of such a model, this approach allows the use of sophisticated electronic structure-based methods. Here the main source of error is the cutting of chemical bonds at the cluster boundary, which is partially corrected for by saturating the resulting dangling bonds with appropriate atoms or chemical residues. This approach ignores the effect of the sourrounding atoms and is generally used to investigate the fundamental interactions between the metal and some ligands (see, for example, the work of Russo *et al.* [53, 54]). This method has been successfully used by Andrews and co-workers to compute harmonic frequencies for small rhodium carbonyl complexes, and the results compared with infrared measurements performed in a solid neon matrix [55, 56].

**The embedded molecular cluster approach** This approach is more sophisticated compared the molecular cluster approach. Electrostatic, steric and possibly elastic constraints on the cluster imposed by its environment are included by embedding the cluster in some way. Within this approximation, just a small portion of the system is studied at the quantum mechanical (QM) level of theory, while the interaction between this small region and the rest of the system is accounted for with a suitable embedding scheme. This approach is motivated by the fact that the active region of a catalyst typically includes a few atoms. Such hybrid methods are popular in the literature because they combine the high accuracy provided by an *ab-initio* method with the efficiency of a molecular mechanics (MM) approach (see for instance the *Oniom* method [57] and the program *Guess* [58, 59]).

**The periodic approach** The periodic nature of condensed matter is often better represented using the theoretical framework derived from Bloch's theorem. The wavefunction of a periodic system is then computed using plane waves, whose wavevectors are linear combinations of the reciprocal lattice vectors of the system. This approach has been used to study catalysis over metal, metal oxide surfaces and

metal/metal oxides interfaces [16, 60–66], where the delocalised electronic states are of fundamental importance. For a supported catalyst, a possible source of error is the size of the repeated unit cell, composed by the active site and the support. Too small a unit cell results in a unphysical repetition of defects (if present) and a high density of active sites. A large unit cell correctly represents a monodispersed and non-interacting active site, but the computational cost of such a calculation would be very expensive.

The work presented in this thesis will take advantage of all three theoretical approaches described in this section.

## 1.6 Outline of the thesis

This thesis is organised as follows. The Chapter 2 gives an extensive description of all the theoretical methods used in this thesis work. In Chapter 3 the properties of $\gamma$-alumina, the structure of the bulk and the structure of the most important crystal surfaces are computed at the plane-wave DFT level of theory. It is also presented a comparison with the same structures computed at the Molecular Mechanics level of theory. Chapter 4 focuses on benchmarking different theoretical methods applied to the study of small molecules containing one or more rhodium atoms, and Chapter 5 gives the results of periodic and hybrid calculations on supported rhodium catalysts. Finally in Chapter 6, conclusions and suggestions for a further extension of this work are presented.

CHAPTER 2

# THEORETICAL METHODS

In quantum mechanics all the relevant information of a molecular system can be obtained from first principles by solving the time independent Schrödinger equation (1.23). However, exact solutions of this equation can be calculated only for a few special cases [67], *e.g.* hydrogen-like atoms: H, $He^{+}$, $Li^{2+}$. Solving the Schrödinger equation exacly for a multi-electron molecular system is not possible and only approximate solutions can be obtained. The choice of approximations can take advantage of the chemical knowledge of the system: a remarkable example is the Hückel method [68] for determining the energies of molecular orbitals of $\pi$ electrons in conjugated hydrocarbon systems. Despite its simplicity, the results are often in agreement with experimental observations and this method is still used for didactic purposes.

In order to obtain quantitative predictions, accurate theoretical methods have been developed that correct the errors introduced by the approximations needed to solve the Schrödinger equation. In this Chapter these approximations will be discussed, along with the limits and applicability of different theoretical approaches, with particular emphasis on the theoretical methods used in this thesis.

## 2.1 Approximate Solutions of the Schrödinger equation

This section focuses on the approximations that are the foundations of Hartree-Fock theory [69–71], a powerful method to compute approximate solutions of the time-independent Schrödinger equation. In this method all the terms of the exact Hamil-

tonian (2.7) are rewritten as a sum of one-electron operators, thus making the determination of the energy and wavefunction of equation (1.23) a solvable task.

### 2.1.1 Born-Oppenheimer Approximation

The Born-Oppenheimer (BO) Approximation [72] states that the electronic coordinates can be separated from the nuclear coordinates in a molecule. In mathematical terms, this means the total wavefunction is written as the product of nuclear and electronic components:

$$\Psi_T(\mathbf{R}, \mathbf{r}) = \Psi_N(\mathbf{R})\Psi_e(\mathbf{r}) \tag{2.1}$$

This approximation is based on the big difference in mass between electrons and nuclei (a factor of $10^3$–$10^5$) and assumes that the electrons move in a fixed potential generated by the nuclei.

In the rest of this Chapter, the all-electron wavefunction $\Psi_e$ will be noted as $\Psi$ to simplify the notation.

### 2.1.2 Spin Orbitals and Space Orbitals

A common way of solving the time-independent Schrödinger equation for a many-electron system is to assume that each electron in the system can be considered separately. This approximation is known as the *one-electron* approximation [73, 74]. The total wavefunction for the system is then written as a product of one-electron wavefunctions, the *molecular orbitals* (MO) [75]

$$\Psi(\mathbf{r}_1, \mathbf{r}_2, \ldots, \mathbf{r}_n) = \phi_1(\mathbf{r}_1)\phi_2(\mathbf{r}_2)\ldots\phi_n(\mathbf{r}_n) \tag{2.2}$$

In equation (2.2), the functions $\phi_i$ are called *spatial orbitals* and they are functions of the position vector $\mathbf{r} = \{x, y, z\}$ that describes the spatial coordinates of an electron.

Spatial molecular orbitals are assumed to be orthonormal:

$$\int \phi_i^*(k)\phi_j(k)d\mathbf{r}_k = \langle \phi_i | \phi_j \rangle = \delta_{ij} \tag{2.3}$$

In (2.3), the $(k)$ following each MO wavefunction is a shorthand indicating the coordinates of the electron $k$.

To completely describe an electron, it is necessary to specify its spin coordinate. This is done by introducing two orthonormal functions $|\alpha\rangle$ and $|\beta\rangle$, *i.e.* spin up ($\uparrow$) and spin down ($\downarrow$). The wavefunction for an electron that describes both its spatial distribution and its spin is called a *spin orbital*, $\psi$, and is defined as:

$$\psi(i) = \begin{cases} \phi(\mathbf{r}_i)|\alpha\rangle \\ \phi(\mathbf{r}_i)|\beta\rangle \end{cases} \tag{2.4}$$

Since two electrons can occupy the same space orbital, provided that they have a different spin[1], the spin orbitals can be constrained to have the same spatial function for any $|\alpha\rangle$ and $|\beta\rangle$ couple. It follows that given a set of $K$ spatial orbitals $\{\phi_1, \ldots, \phi_K\}$, one can thus form a set of $2K$ *restricted* spin orbitals [76]. In contrast, *unrestricted* spin orbitals have different spatial functions for $|\alpha\rangle$ and $|\beta\rangle$ spins.

### 2.1.3 Slater Determinants

As electrons are fermions, the all-electron wavefunction must satisfy the Pauli exclusion principle [77]:

> "A many-electron wavefunction must be anti-symmetric with respect to interchange of the coordinates of any two electrons."

This means that the total wavefunction must change sign when any two electrons in the system are interchanged. A way to ensure the antisymmetry of a wavefunction of

[1] This follows from the Pauli exclusion principle. A rigorous definition is given in the next Section.

a molecular system with $n$ electrons, is by using Slater determinants [73]:

$$\Psi = \frac{1}{\sqrt{n!}} \begin{vmatrix} \psi_1(1) & \psi_2(1) & \cdots & \psi_n(1) \\ \psi_1(2) & \psi_2(2) & \cdots & \psi_n(2) \\ \vdots & \vdots & \ddots & \vdots \\ \psi_1(n) & \psi_2(n) & \cdots & \psi_n(n) \end{vmatrix} \tag{2.5}$$

This Slater determinant has $n$ electrons occupying $n$ spin orbitals. It is easy to demonstrate that the resulting wavefunction –a linear combination of MOs– is antysymmetric with respect to the exchange of two electrons. For $n = 2$ equation (2.5) becomes:

$$\begin{aligned} \Psi(1,2) &= \frac{1}{\sqrt{2}} \begin{vmatrix} \psi_1(1) & \psi_2(1) \\ \psi_1(2) & \psi_2(2) \end{vmatrix} \\ &= \frac{1}{\sqrt{2}} \big[\psi_1(1)\psi_2(2) - \psi_1(2)\psi_2(1)\big] \end{aligned}$$

Permutation of electron 1 and electron 2 gives:

$$\begin{aligned} \Psi(2,1) &= \frac{1}{\sqrt{2}} \big[\psi_1(2)\psi_2(1) - \psi_1(1)\psi_2(2)\big] \\ &= -\Psi(1,2) \end{aligned}$$

The exchange of two electrons is equal to the exchange of two rows in the determinant, which results in a change of sign.

The normalised single Slater determinant wavefunction (2.5) will now be re-written using the short-hand *bra-ket* notation:

$$\big|\Psi\big\rangle = \big|\psi_1\psi_2 \ldots \psi_n\big\rangle \tag{2.6}$$

### 2.1.4 Hartree-Fock Theory

The electronic Hamiltonian operator for a many-electron system is (in atomic units) [75]:

$$\hat{H} = \sum_i \hat{h}_i + \sum_{i<j} \hat{g}_{ij} + \hat{h}_0 \tag{2.7}$$

In the equation (2.7), $\hat{h}_i$ is the one-electron Hamiltonian consisting of the electron kinetic energy and nuclear attraction terms,

$$\hat{h}_i = -\frac{1}{2}\nabla_i^2 - \sum_\mu \frac{Z_\mu}{r_{i\mu}} \tag{2.8}$$

where $r_{i\mu} = |\mathbf{r}_i - \mathbf{R}_\mu|$, $Z_\mu$ is the nuclear charge and $\nabla_i^2$ is the gradient operator for the $i^{th}$ electron

$$\nabla_i^2 = \frac{\partial^2}{\partial x_i^2} + \frac{\partial^2}{\partial y_i^2} + \frac{\partial^2}{\partial z_i^2} \tag{2.9}$$

$\hat{g}_{ij}$ is the two-electron operator that describes the interaction between two electrons

$$\hat{g}_{ij} = \frac{1}{r_{ij}} \tag{2.10}$$

and $\hat{h}_0$ is the repulsion between the nuclei in the system

$$\hat{h}_0 = \sum_{\mu<\nu} \frac{Z_\mu Z_\nu}{R_{\mu\nu}} \tag{2.11}$$

In the equations (2.10) and (2.11), $r_{ij} = |\mathbf{r}_i - \mathbf{r}_j|$ and $R_{\mu\nu} = |\mathbf{R}_\mu - \mathbf{R}_\nu|$. Within the BO approximation, the term (2.11) is an additive constant and it will be omitted in the following derivation. It should be noted however that the electronic wavefunction $\big|\Psi\big\rangle$ still retains a parametric dependence on the nuclear coordinates $\{\mathbf{R}\}$ through the nuclear attraction term in the operator (2.8).

Using the Slater-Condon rules [73, 78] to express the one- and two-electron operators over a Slater determinant wavefunction, it is possible to evaluate the energy as an

expectation value of the Hamiltonian [79]:

$$\begin{aligned}\bar{E}[\Psi] &= \langle \Psi | \hat{H} | \Psi \rangle \\ &= \sum_i \langle \psi_i | \hat{h}_i | \psi_i \rangle + \frac{1}{2} \sum_{i,j} \left[ \langle \psi_i \psi_j | \hat{g} | \psi_i \psi_j \rangle - \langle \psi_i \psi_j | \hat{g} | \psi_j \psi_i \rangle \right] \qquad (2.12) \\ &= \sum_i \langle \psi_i | \hat{h}_i | \psi_i \rangle + \frac{1}{2} \sum_{i,j} \langle \psi_i | \hat{J}_j - \hat{K}_j | \psi_i \rangle \\ &= \sum_i \langle \psi_i | \hat{h}_i | \psi_i \rangle + \frac{1}{2} \sum_i \langle \psi_i | \hat{J} - \hat{K} | \psi_i \rangle \qquad (2.13)\end{aligned}$$

where $\langle \psi_a \psi_b | \hat{g} | \psi_c \psi_d \rangle$ denotes the integral

$$\langle \psi_a \psi_b | \hat{g} | \psi_c \psi_d \rangle = \int \psi_a^*(1) \psi_b^*(2) \frac{1}{r_{12}} \psi_c(1) \psi_d(2) d\mathbf{r}_1 d\mathbf{r}_2 \qquad (2.14)$$

In the equation (2.13), $\hat{J}_j$ and $\hat{K}_j$ are called *Coulomb* and *exchange* operators. They are defined through their action on an arbitrary function $\psi_i$ such that

$$\hat{J}_j(1)\psi_i(1) = \left[ \int \frac{\psi_j^*(2)\psi_j(2)}{r_{12}} d\mathbf{r}_2 \right] \psi_i(1) \qquad (2.15)$$

$$\hat{K}_j(1)\psi_i(1) = \left[ \int \frac{\psi_j^*(2)\psi_i(2)}{r_{12}} d\mathbf{r}_2 \right] \psi_j(1) \qquad (2.16)$$

The total Coulomb and exchange operators are defined as:

$$\hat{J}(1) = \sum_i \hat{J}_i(1) \qquad (2.17)$$

$$\hat{K}(1) = \sum_i \hat{K}_i(1) \qquad (2.18)$$

In order to determine the spin orbitals that define the Slater determinant wavefunction $|\Psi\rangle$, the variation principle is applied to the energy expression (2.13). In doing so, the implicit assumption is that the orbitals leading to the lowest total energy are the *best*. The minimum of the energy is found when the energy change with respect to a small

(infinitesimal) change in the spin orbital

$$\psi_i \leftarrow (\psi_i + \delta\psi_i) \tag{2.19}$$

is equal to zero. The substitution (2.19) leads to a change in the total wavefunction $\big|\Psi\big\rangle \leftarrow \big|\Psi + \delta\Psi\big\rangle$ and in the energy expression (2.12)

$$\begin{aligned}
\bar{E}[\Psi + \delta\Psi] &= \big\langle \Psi + \delta\Psi \big| \hat{H} \big| \Psi + \delta\Psi \big\rangle \\
&= \bar{E}[\Psi] + \{\big\langle \delta\Psi \big| \hat{H} \big| \Psi \big\rangle + \big\langle \Psi \big| \hat{H} \big| \delta\Psi \big\rangle\} + \dots \\
&= \bar{E}[\Psi] + \delta\bar{E} + \dots
\end{aligned} \tag{2.20}$$

The first order variation $\delta\bar{E}$ can now be expressed by collecting the terms linear in $\delta\psi$

$$\begin{aligned}
\delta\bar{E} &= \sum_i \big\langle \delta\psi_i \big| \hat{h}_i \big| \psi_i \big\rangle + \sum_{i,j} \left[ \big\langle \delta\psi_i\psi_j \big| \hat{g} \big| \psi_i\psi_j \big\rangle - \big\langle \delta\psi_i\psi_j \big| \hat{g} \big| \psi_j\psi_i \big\rangle \right] \\
&+ \sum_i \big\langle \psi_i \big| \hat{h}_i \big| \delta\psi_i \big\rangle + \sum_{i,j} \left[ \big\langle \psi_i\psi_j \big| \hat{g} \big| \delta\psi_i\psi_j \big\rangle - \big\langle \psi_i\psi_j \big| \hat{g} \big| \psi_j\delta\psi_i \big\rangle \right] + \dots \\
&= \sum_i \big\langle \delta\psi_i \big| \hat{h}_i \big| \psi_i \big\rangle + \sum_i \big\langle \delta\psi_i \big| \hat{J} - \hat{K} \big| \psi_i \big\rangle + \dots \\
&= \sum_i \big\langle \delta\psi_i \big| \hat{f} \big| \psi_i \big\rangle + \dots
\end{aligned} \tag{2.21}$$

In (2.21), $\hat{f}$ is the one-electron Fock operator

$$\hat{f}(1) = \hat{h}_1 + \hat{J}(1) - \hat{K}(1) \tag{2.22}$$

The minimum of the energy is found when the variation $\delta\bar{E}$ vanishes, which according to (2.21) implies

$$\big\langle \delta\psi_i \big| \hat{f} \big| \psi_i \big\rangle = 0 \tag{2.23}$$

The $\delta\psi_i$ term in (2.23) can be re-written in terms of occupied $\psi_j$ and unoccupied (vir-

tual) $\psi_a$ molecular orbitals

$$\delta\psi_i = \sum_j \delta_{ij}\psi_j + \sum_a \delta_{ia}\psi_a \tag{2.24}$$

where $\delta_{ij}$ denotes infinitesimal quantities. The first term in (2.24) vanishes since it describes an (infinitesimal) transformation of occupied molecular orbitals which leave $\big|\Psi\big\rangle$ invariant[2] [79]. From the second term of (2.24), the equation (2.23) can be used to derive

$$\big\langle\psi_a\big|\hat{f}\big|\psi_i\big\rangle = 0 \tag{2.25}$$

This expression is known as the *general Hartree-Fock equation*. The left-hand side of equation (2.25) is equivalent to

$$\hat{f}\psi_i = \sum_k \lambda_{ki}\psi_k \tag{2.26}$$

where $k$ runs over occupied molecular orbitals. Since $\hat{f}$ is hermitian, the matrix $\boldsymbol{\lambda}$ can be expressed in a diagonal form $\delta_{kj}\epsilon_k$. Using this property of $\boldsymbol{\lambda}$, equation (2.26) can be re-written as

$$\hat{f}\tilde{\psi}_i = \epsilon_i\tilde{\psi}_i \tag{2.27}$$

where $\tilde{\psi}_i$ are new molecular orbitals obtained from the linear transformation

$$\tilde{\psi}_i = \sum_k \psi_k V_{ki} \tag{2.28}$$

where $\mathbf{V}$ denotes the matrix which diagonalizes $\boldsymbol{\lambda}$ ($\boldsymbol{\lambda}\mathbf{V} = \mathbf{V}\boldsymbol{\epsilon}$, $\boldsymbol{\epsilon}$ diagonal).

The equations (2.27) are referred to as the *canonical Hartree-Fock equations* [75]. The corresponding orbitals are the Hartree-Fock (HF) molecular orbitals, and the eigenvalues $\epsilon_i$ are the *orbital energies*. The physical meaning of the orbital energies is explained

[2]This is a consequence of the Brillouin theorem [76, 80]:

> Singly excited determinants $\big|\Psi'_a\big\rangle$ will not interact directly with a reference Hartree-Fock determinant $\big|\Psi_0\big\rangle$, *i.e.* $\big\langle\Psi_0\big|\hat{H}\big|\Psi'_a\big\rangle = 0$.

in Koopmans' theorem [81], which states:

> The negative of the orbital energy of occupied orbitals from a Hartree-Fock calculation gives the best zero$^{th}$ order approximation of the vertical ionization energy, and the orbital energy of virtual orbitals gives the best zero$^{th}$ order approximation of the electron affinity.

Finally, it is easy to demonstrate that the total energy $\bar{E} \neq \sum_i \epsilon_i$. From the (2.13) it follows that

$$\bar{E} = \sum_i \epsilon_i - \frac{1}{2} \sum_i \langle \tilde{\psi}_i | \hat{J} - \hat{K} | \tilde{\psi}_i \rangle \tag{2.29}$$

In this derivation the spin coordinates have not been explicitly considered, since the antisymmetry of the wavefunction has been assured with the use of Slater determinants. Spin coordinates can be introduced in the Hartree-Fock equations using the substitutions (2.4) and the rules for spin integration

$$\langle \alpha | \alpha \rangle = \langle \beta | \beta \rangle = 1 \tag{2.30a}$$

$$\langle \alpha | \beta \rangle = 0 \tag{2.30b}$$

With these conditions, an energy expression which involves only spatial orbitals can be obtained, *i.e.* equation (2.12) becomes

$$\begin{aligned} \bar{E} = \sum_i \langle \phi_i | \hat{h}_i | \phi_i \rangle + \frac{1}{2} \sum_{i^{(\alpha)} j^{(\alpha)}} \left[ \langle \phi_i \phi_j | \hat{g} | \phi_i \phi_j \rangle - \langle \phi_i \phi_j | \hat{g} | \phi_j \phi_i \rangle \right] \\ + \frac{1}{2} \sum_{i^{(\beta)} j^{(\beta)}} \left[ \langle \phi_i \phi_j | \hat{g} | \phi_i \phi_j \rangle - \langle \phi_i \phi_j | \hat{g} | \phi_j \phi_i \rangle \right] + \sum_{i^{(\alpha)} j^{(\beta)}} \langle \phi_i \phi_j | \hat{g} | \phi_i \phi_j \rangle \end{aligned} \tag{2.31}$$

From this expression it can be seen that the Coulomb operator term always remains unchanged on integration over spin, whereas the exchange operator term is non-zero only between electrons having the same spin. As a consequece, the Fock operator (2.22)

will be now different depending if it operates on $\alpha$ or $\beta$ electrons

$$\hat{f}^{(\alpha)}(1) = \hat{h}_1 + \hat{J}(1) - \hat{K}^{(\alpha)}(1) \tag{2.32a}$$

$$\hat{f}^{(\beta)}(1) = \hat{h}_1 + \hat{J}(1) - \hat{K}^{(\beta)}(1) \tag{2.32b}$$

In these expressions, the new exchange operators $\hat{K}^{(\alpha)}$ and $\hat{K}^{(\beta)}$ are defined by:

$$\hat{K}^{(\alpha)} = \sum_{i^{(\alpha)}} \hat{K}_i \tag{2.33a}$$

$$\hat{K}^{(\beta)} = \sum_{i^{(\beta)}} \hat{K}_i \tag{2.33b}$$

This is known as the *Unrestricted Hartree-Fock* (UHF) method [82] and it is used for open-shell systems. However, it should be noted that UHF wavefunctions are not generally eigenfunctions of the spin operators $\hat{S}^2$ and $\hat{S}_z$.

For a closed-shell system of $n$ electrons, the space orbitals for electrons occupying the same MO can be constrained to be the same. Therefore the energy in equation (2.31) becomes [83]

$$\bar{E} = 2\sum_{i=1}^{\frac{n}{2}} \langle \phi_i | \hat{h}_i | \phi_i \rangle + \sum_{i,j=1}^{\frac{n}{2}} \left[ 2\langle \phi_i \phi_j | \hat{g} | \phi_i \phi_j \rangle - \langle \phi_i \phi_j | \hat{g} | \phi_j \phi_i \rangle \right] \tag{2.34}$$

where the summations in (2.34) are over $n/2$ doubly occupied orbitals. Since the $\alpha$ and $\beta$ orbitals have identical spatial parts, the Fock operators (2.32a) and (2.32b) must be the same, and can be rewritten as:

$$\hat{F}(1) = \hat{h}_1 + \sum_{i=1}^{\frac{n}{2}} 2\hat{J}_i(1) - \hat{K}_i(1) \tag{2.35}$$

This is known as the *Restricted Hartree-Fock* (RHF) method and it is the most commonly used since the work and memory requirements are reduced by about 50% compared to other Hartree-Fock methodologies [79].

To summarise, the essence of HF theory is to approximate the complex many-electron

problem by a one-electron problem in which the instantaneous interaction between an electron $i$ and all the other electrons is replaced with a mean field potential due to the remaining electrons.

### 2.1.5 Hartree-Fock-Roothaan equations

Although the theoretical framework offered by the HF theory represents an immense simplification of the original Schrödinger equation, the determination of the unknown molecular orbital functions remains a complicated problem to be solved [75]. Expanding an arbitrary function as a series of known orthogonal functions is a common way of addressing this kind of problem. In quantum chemistry it is common practice to expand the (spatial) molecular orbitals $\phi_i(\mathbf{r})$ as a Linear Combination of Atomic Orbitals $\chi_p(\mathbf{r})$ (the LCAO method):

$$\phi_i(\mathbf{r}) = \sum_{p=1}^{K} C_{pi}\chi_p(\mathbf{r}) \tag{2.36}$$

In (2.36), $C_{pi}$ are numerical coefficients and the $\chi_p(\mathbf{r})$ are a set of $K$ basis functions. In practice a finite number of basis functions is used to express the molecular orbitals, thus introducing a *truncation* error that decreases as the number of basis functions increases.

For closed-shell singlet systems the HF eigenvalue equations (2.27) can be re-written in terms of restricted space orbitals:

$$\hat{F}(1)\phi_i(1) = \epsilon_i\phi_i(1) \tag{2.37}$$

Substitution of equation (2.36) into (2.37) gives

$$\hat{F}\sum_q C_{iq}\chi_q = \epsilon_i \sum_q C_{iq}\chi_q \tag{2.38}$$

Multiplying from the left by $\chi_p^*$ and integrating over the space coordinates gives the so

called Roothaan-Hall equations [75]:

$$\int \chi_p^* \hat{F} \sum_q C_{iq} \chi_q d\mathbf{r} = \epsilon_i \int \chi_p^* \sum_q C_{iq} \chi_q d\mathbf{r} \tag{2.39}$$

$$\sum_q C_{iq} \int \chi_p^* \hat{F} \chi_q d\mathbf{r} = \epsilon_i \sum_q C_{iq} \int \chi_p^* \chi_q d\mathbf{r} \tag{2.40}$$

$$\sum_q C_{iq} F_{pq} = \epsilon_i \sum_q C_{iq} S_{pq} \tag{2.41}$$

where $F_{pq}$ are elements of the Fock matrix

$$F_{pq} = \int \chi_p^*(\mathbf{r}) \hat{F} \chi_q(\mathbf{r}) d\mathbf{r} = \left\langle \chi_p \middle| \hat{F} \middle| \chi_q \right\rangle \tag{2.42}$$

and $S_{pq}$ is the overlap matrix

$$S_{pq} = \int \chi_p^*(\mathbf{r}) \chi_q(\mathbf{r}) d\mathbf{r} = \left\langle \chi_p \middle| \chi_q \right\rangle \tag{2.43}$$

Both matrices $F_{pq}$ and $S_{pq}$ are hermitian and $K \times K$ in size. equations (2.41) can be written as a single equation between matrices

$$\mathbf{FC} = \mathbf{SC}\boldsymbol{\epsilon} \tag{2.44}$$

where C is the coefficient matrix and $\boldsymbol{\epsilon}$ is the diagonal matrix of orbital energies. As the Fock matrix depends on its own solutions (through the Coulomb and exchange operators), the solutions of (2.44) must be obtained in an iterative way until self-consistency is achieved. For this reason, the LCAO-HF theory is also called self-consistent field (SCF) theory.

In the SCF procedure, an initial estimate of the electronic wavefunction is feeded into an algorithm that solves the equations (2.44) via the following steps:

1. Use an initial estimate of the LCAO coefficients $C_{iq}$.

2. Evaluate the matrix $S_{pq}$.

3. Evaluate the matrix $F_{pq}$.

4. Solve the set of linear equations

$$|\mathbf{F} - \mathbf{S}\boldsymbol{\epsilon}| = 0 \tag{2.45}$$

   *i.e.* requirements for non-trivial solution of equations (2.44).

5. For each $\boldsymbol{\epsilon}$, determine the new coefficients $C_{iq}$ from equations (2.44).

6. Go back to (3.) and use the new coefficients to evaluate new matrix elements $F_{pq}$. Repeat until some pre-determined tolerance (usually the overall energy) is reached.

The energy computed with this SCF procedure is an upper limit of the $E^{HF}$ energy, whose exact value can be computed only with a LCAO expansion that uses a complete (*i.e.* infinite) basis set.

### 2.1.6 Basis Sets

The evaluation of the electron energy using the LCAO expansion is done variationally, by optimizing the molecular orbital coefficients in the basis set expansion (2.36). The most obvious choice of basis functions are atomic orbitals (AO), as obtained from the exact solutions of the Schrödinger equation for the hydrogen atom. These functions are *local* (*i.e.* centered on each atom) and are of the form [84]:

$$\psi(\mathbf{r}) = R(r)Y_{lm}(\theta, \phi) \tag{2.46}$$

where $Y_{lm}(\theta, \phi)$ is an angular function and $R(r)$ is a radial function. The AO wave-function has a cusp at the nucleus, and it decays exponentially when the electron is far from the atomic nucleus. Such a behaviour is assured by using Slater-type AOs, which

have the functional form [74]:

$$\chi^{STO}(\mathbf{r}) = P(r)e^{-\zeta r}Y_{lm}(\theta,\phi) \tag{2.47}$$

where $P(r)$ in (2.47) is a polynomial in the radial coordinate. Although STOs have a correct physical behaviour, the evaluation of two-electron integrals cannot be achieved analytically but only numerically, with great computational effort. A more successfull approach uses gaussian-type functions, with which two-electron integrals can be evaluated analytically. The gaussian-type atomic orbitals (GTO) expressed in cartesian coordinates are [85, 86]:

$$\chi^{GTO}(\mathbf{r}) = (x-A_x)^k(y-A_y)^l(z-A_z)^m e^{-\alpha(\mathbf{r}-\mathbf{A})^2} \tag{2.48}$$

Each function is completely specified by the postition of the centre $\mathbf{A}$, the gaussian exponent $\alpha$ and the powers $k$, $l$ and $m$. Compared to STOs, GTOs represent atomic orbitals less well, particularly at short and long distances as shown in Figure (2.1). However, this problem can be easily corrected by using a linear combination of several GTOs to represent an atomic orbital. Such functions are known as *contracted* gaussian-type atomic orbitals (CGTO) [87]:

$$\chi_i^{CGTO} = \sum_a c_{ai}\chi_a^{GTO} \tag{2.49}$$

The use of CGTOs reduces the number of basis functions used to compute SCF energies, and leads to a better representation of the MOs.

Gaussian basis sets generally contain contracted and uncontracted (*i.e.* single) functions. In addition to functions of these types, additional functions are added to account for different effects. When an atom forms a chemical bond, the shape of its orbitals can change significantly and in particular its electron density may be displaced from a nucleus-centred position towards the bond direction. This change is accounted for with the use of *polarization* functions, *i.e.* gaussian functions with the same orbital ex-

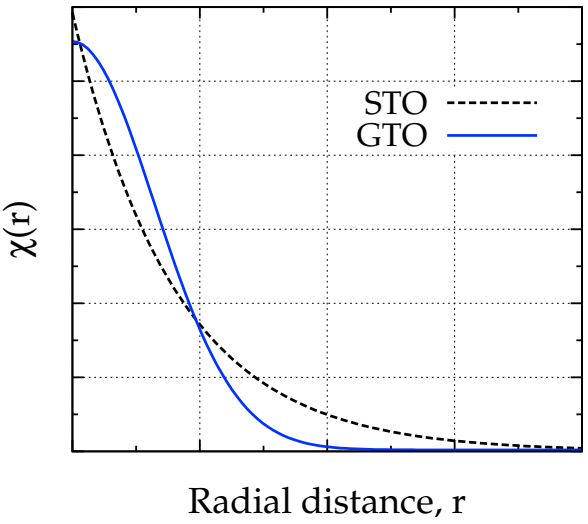


**Figure 2.1:** Comparison between a Slater-type atomic orbital (STO) and a gaussian-type atomic orbital (GTO). The GTO does not have a cusp at $r = 0$, and its radial distribution decays more rapidly than the STO, that is less physically realistic. To correct these problems, contracted GTOs are used instead of single GTOs.

ponents but with an angular momentum quantum number larger than the angular momentum quantum number of the valence electrons.

Negatively charged ions experience a relaxation of their atomic orbitals, because they carry more electrons compared to a neutral state. In this case, *diffuse* functions, *i.e.* gaussian functions with very small orbital coefficients, are added to the basis set to allow the AOs to have a greater spatial extention.

A basis set that uses a single basis function for each formally occupied AO is said to be a *minimal* basis set. If two basis functions are used for each formally occupied AO, then the basis set is said to be of *double zeta* (DZ) quality. Analogously, basis sets of triple zeta, quadruple zeta,... quality can be constructed.

The split-valence basis sets, first introduced by Pople and coworkers [88, 89], are designed to achieve a compromise between economy and flexibility in a molecular orbital calculations. In these basis sets, a minimal set of basis functions are used to describe the core electrons, and a basis set of a higher quality is used to describe valence

electrons. In the same spirit, effective core potentials (ECP) [90–92] are used to describe the core electrons in heavy atoms.

A completely different kind of basis set is composed of plane waves (PW) and is generally used in calculations involving systems with periodic boundary conditions, such atoms in a crystal. Plane wave functions are of the form [93]:

$$\chi^{PW}(\mathbf{r}) = C_{\mathbf{G}} e^{\mathrm{i}\mathbf{G}\cdot\mathbf{r}} \tag{2.50}$$

where $C_{\mathbf{G}}$ is the wave amplitude and $\mathbf{G}$ is the reciprocal lattice vector defined by $\mathbf{G}\cdot\mathbf{l} = 2\pi m$, with $\mathbf{l}$ a lattice vector and $m$ an integer. The plane waves described in equation (2.50) have a kinetic energy that increases as the vector $\mathbf{G}$ increases. In particular, plane waves with a small kinetic energy have a more important role compared with those with a large kinetic energy [94]. The introduction of an energy cut-off therefore reduces the basis set to a finite size.

Plane wave functions are non local, *i.e.* independent of atomic positions, and are mutually orthogonal. On the other hand, a large number of plane waves is required to accurately describe a molecular system. Plane wave basis sets are often used in combination with atomic *pseudopotentials* that replace the Coulomb potential for the electron-nuclear interaction with an effective potential that accounts for the presence of core electrons, as well as relativistic effects.

## 2.2 Electron Correlation

A wavefunction $\left|\Psi\right\rangle$ does not have a physical meaning on its own. However, the integral

$$\int_{r_0}^{r_1} \Psi^* \Psi d\mathbf{r}_i \tag{2.51}$$

gives the probability of finding the electron $i$ in the interval $\left|r_1 - r_0\right|$ [95]. Such a probability is (or, *should be*) influenced by the presence of other electrons. In HF theory this is not exactly the case: each electron does not interact instantaneously with all the

other electrons, but only with a mean potential through the Coulomb and exchange terms in the Fock operator. The uncorrelated motion of the electrons in HF theory is the origin of the *electron correlation* error, defined as the difference between the "true" energy of a system and the HF energy computed at the complete basis set limit [96], *i.e.*

$$E_{\text{corr}} = E_{\text{exact}} - E_{\text{HF}} \tag{2.52}$$

However, electronic motion is not completely uncorrelated in HF theory. The single determinant wavefunction prevents two electrons from occupying the same position in space: in this case the coordinates of two electrons would be identical and as a consequence the Slater determinant (2.5) vanishes. This correlation is only due to the antysimmetry of the wavefunction and is often referred as Fermi correlation [97]. The exchange term in the Fock operator also accounts for some electron correlation, since it describes the interaction between electrons with the same spin.

The electron correlation, which is neglected in HF theory, can be divided into two categories. The first kind is called *nondynamic* electron correlation and arises from the inadequacy of a single Slater determinant wavefunction to describe an electronic state influenced by other electronic configurations that contribute to lower its electronic energy [98]. This effect is observed in phenomena involving long-range effects such as molecular dissociation, and is usually dealt with multiconfigurational SCF (MCSCF) techniques, in which the wavefunction is expressed as a linear combination of single determinant wavefunctions $\Psi_i$ obtained from the ground-state HF wavefunction

$$\Psi_{MCSCF} = \sum_i C_i \Psi_i \tag{2.53}$$

In this expansion, the MCSCF coefficients $C_i$ are optimised variationally. One of the most widely used MCSCF techniques is the complete active space SCF (CASSCF) method [99, 100], in which a set of *active orbitals* (composed of occupied and unoccupied MOs) is used to generate the excited determinants $\Psi_i$ appearing in equation (2.53). All possible Slater determinants arising from the excitation of the electrons in the active

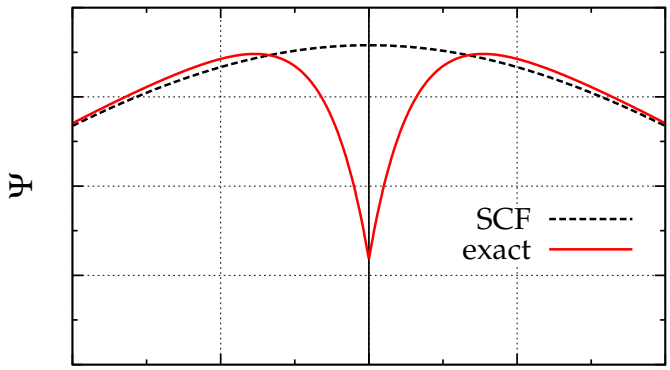


**Figure 2.2:** The interelectronic cusp. The wavefunction is plotted against the distance between two electrons.

space are considered in the CASSCF wavefunction.

The second kinf of electron correlation energy is referred to as *dynamic* and arises from overstimation of short-range electron interaction in Hartree-Fock wavefunctions [98, 101]. This error originates from the $r_{ij}^{-1}$ term in the Hamiltonian operator, which is singular as $r_{ij} \to 0$. To remove this singularity, the exact wavefunction must satisfy the so-called cusp condition [102, 103]:

$$\left(\frac{\partial \Psi}{\partial r}\right)_{r=0} = \frac{1}{2}\Psi(r=0) \tag{2.54}$$

This equation shows that the wavefunction has a linear trend in the region close to $r = 0$, as shown in Figure 2.2. Hence dealing with dynamical electron correlation means describing this cusp behaviour. Among the methods that account for dynamical electron correlation, one of the most complete is the configuration interaction (CI) method. The CI wavefunction consists of a linear combination of excited Slater determinants obtained from the ground-state HF wavefunction $\Psi_0$ [104]:

$$\Psi_{CI} = c_0\Psi_0 + \sum_i \sum_a c_i^a \Psi_i^a + \sum_{i>j} \sum_{a>b} c_{ij}^{ab} \Psi_{ij}^{ab} + \dots \tag{2.55}$$

In equation (2.55) $\Psi_i^a$, $\Psi_{ij}^{ab}$, ... are excited determinants, $i, j, \dots$ are the index of occupied

MO in $\Psi_0$, $a, b, \ldots$ are the index of unoccupied MO in $\Psi_0$, and $\Psi_{ij}^{ab}$ denotes a configuration obtained by exciting two electrons in MOs $i$ and $j$ to MOs $a$ and $b$. All the excited configurations appearing in equation (2.55) have the same total angular and spin momentum as the reference wavefunction $\Psi_0$. A full CI wavefunction is obtained when all excitations are considered and it is (at the complete basis set limit) a complete expansion of the exact wavefunction. However in practical cases only a few levels of excitations are considered, typically a CI with single and double excitations (CISD). A limit of truncated CI models is that they are not size consistent, *i.e.* the energy of two molecular systems placed at very long distance is not twice the energy of the single system.

The CI approach can be easily extended to handle non-dynamical effects: in this case other electronic states are included in the CI expansion: this gives the multi-reference CI (MRCI) approach.

In the next paragraphs, three different approaches to account for the dynamical electron correlation are discussed.

### 2.2.1 Perturbation Theory

Perturbation theory (derived by Rayleigh and Schrödinger, [105]) is a mathematical procedure to solve the Schrödinger equation when the exact solution is not known. The simple assumption behind this theory is that the Hamiltonian describing a physical problem can be separated into a part whose solution is known, and a part which has no analytic solution. The latter is treated as a small perturbation of the original, unperturbed system.

In the Møller-Plesset formulation [106], the correlation energy is assumed to be a perturbation added to the HF Hamiltonian:

$$\hat{H} = \hat{f} + \lambda \hat{V} \tag{2.56}$$

where $\hat{f}$ is the Fock operator (2.22) and $\hat{V}$ is defined as the difference between the

instantaneous and the average electron-electron interaction included in the HF theory:

$$\hat{V} = \sum_{i<j} \hat{g}_{ij} - \sum_{i} \hat{J}(i) - \hat{K}(i) \tag{2.57}$$

It is straightforward to verify that substution of equation (2.57) into (2.56) gives the exact Hamiltonian operator (2.7). The parameter $\lambda$ in equation (2.56) is a real number with a value between 0 and 1. When $\lambda = 0$, the Schrödinger equation using the Hamiltonian in equation (2.56) is soluble and the solutions are the HF wavefunctions and the HF MO energies. As the perturbation is added to the problem, the solutions of the Schrödinger equation can be written as an expansion in powers of $\lambda$:

$$E_i = E_i^{(0)} + \lambda E_i^{(1)} + \lambda^2 E_i^{(2)} + \lambda^3 E_i^{(3)} + \dots \tag{2.58}$$

$$\psi_i = \psi_i^{(0)} + \lambda \psi_i^{(1)} + \lambda^2 \psi_i^{(2)} + \lambda^3 \psi_i^{(3)} + \dots \tag{2.59}$$

where $E_i$, $E_i^{(0)}$, ...are total energies. The $n$th-order treatment is denoted as MP$n$. The sum of zero-*th* and first order energies corresponds to the HF energy, therefore the first MP level to go beyond the HF level includes the second order correction term and is denoted as MP2. However, to recover a sufficient amount of correlation energy, higher order of perturabative terms should be used.

### 2.2.2 Coupled-Cluster Methods

In coupled-cluster (CC) theory, the CI wavefunction is formed with an excitation operator given in exponential form. The ansatz is therefore [107, 108]:

$$\Psi_{CC} = e^{\hat{T}} \Psi_0 \tag{2.60}$$

were $\hat{T}$ is the excitation operator. The CC wavefunction can be expanded as

$$\Psi_{CC} = (1 + T_1 + T_2 + T_1^2 + T_1 T_2 + T_2^2 + T_3 + \dots)\Psi_0 \tag{2.61}$$

The excitation operators in (2.61), $T_1, T_2, T_3, \ldots$, correspond to different levels of excitation. A wavefunction computed at the CC level of theory that employs all levels of excitation would be the *exact* solution of the Schrödinger equation within a given basis set. However, this method is extremely expensive and can be applied only to small systems. In practical cases, the expansion (2.61) is truncated to a finite order because the importance of excitations decreases at higher levels of excitation.

The CC method with single and double excitations is denoted as CCSD, and the corresponding excitation operator is therefore

$$\hat{T} = \hat{T}_1 + \hat{T}_2 \tag{2.62}$$

Substitution of (2.62) into (2.60) gives the following CC wavefunction:

$$\Psi_{CCSD} = (1 + T_1 + T_2 + T_1^2 + T_1 T_2 + T_2^2)\Psi_0 \tag{2.63}$$

With a large enough basis set, the CCSD method recovers about 95% of the correlation energy for a molecule at the equilibrium geometry [109]. Additional excitations are denoted with letters such as triple (T), quadruples (Q) and so on. An interesting compromise between accuracy and computational cost is represented by the CCSD(T) method, in which the single and double excitations are accounted for using the CC theory, and the triple excitations are included with perturbation theory.

### 2.2.3 The Density Functional Theory

The Density Functional Theory (DFT) uses a completely different approach to recover the electron correlation energy. The key point is to replace the complicated many-body problem of $N$ electrons ($3N$ coordinates) with the electron density $\rho(\mathbf{r})$, which depends only on 3 spatial coordinates. The formulation of DFT is based on the work of Hohenberg and Kohn [110, 111], who proved that the total energy of a system is a

unique functional of the ground state density:

$$E_0 = E\left[\rho(\mathbf{r})\right] \tag{2.64}$$

In 1965, Kohn and Sham suggested the following expression for the total energy functional [112]:

$$E\left[\rho(\mathbf{r})\right] = \int \rho(\mathbf{r}) V_{\text{ion}}(\mathbf{r}) d\mathbf{r} + \frac{1}{2} \iint \frac{\rho(\mathbf{r})\rho(\mathbf{r}')}{\left|\mathbf{r} - \mathbf{r}'\right|} d\mathbf{r} d\mathbf{r}' + G\left[\rho(\mathbf{r})\right] \tag{2.65}$$

In equation (2.65), the first term is the Coulomb interaction between electrons and nuclei, the second term is the Coulomb interaction between the electrons, and the last term is an universal functional of the electron density. This functional can be approximated in the following way:

$$G\left[\rho(\mathbf{r})\right] \equiv T_{\text{s}}\left[\rho(\mathbf{r})\right] + E_{\text{xc}}\left[\rho(\mathbf{r})\right] \tag{2.66}$$

where $T_{\text{s}}\left[\rho(\mathbf{r})\right]$ is the kinetic energy of a system of non-interacting electrons with density $\rho$ and $E_{\text{xc}}\left[\rho(\mathbf{r})\right]$ is the exchange and correlation energy of an interacting system of electrons with density $\rho$.

If the electron density is sufficiently slowly varying (and this is the case for the electronic ground state density), the exchange and correlation energy can be written as

$$E_{\text{xc}}\left[\rho(\mathbf{r})\right] = \int \rho(\mathbf{r}) \epsilon_{\text{xc}}\left[\rho(\mathbf{r})\right] d\mathbf{r} \tag{2.67}$$

where $\epsilon_{\text{xc}}\left[\rho(\mathbf{r})\right]$ is the exchange and correlation energy of a homogeneous electron gas of density $\rho$. This expression for the exchange and correlation energy is known as the local spin-density approximation (LDA).

The electronic ground-state density is found by solving the Kohn-Sham (KS) one-

particle Schrödinger equation [112]:

$$\left[-\frac{1}{2}\nabla^2 + V_{\text{ion}}(\mathbf{r}) + \frac{1}{2}\int \frac{\rho(\mathbf{r}')}{\left|\mathbf{r}-\mathbf{r}'\right|}d\mathbf{r}' + \mu_{\text{xc}}(\mathbf{r})\right]\psi_i(\mathbf{r}) = \varepsilon_i\psi_i(\mathbf{r}) \tag{2.68}$$

where

$$\mu_{\text{xc}}(\mathbf{r}) = \frac{d\left(\rho(\mathbf{r})\epsilon_{\text{xc}}\left[\rho(\mathbf{r})\right]\right)}{d\rho(\mathbf{r})} \tag{2.69}$$

is the exchange and correlation contribution to the chemical potential of a uniform gas of electrons with density $\rho(\mathbf{r})$. The single-particle wavefunctions $\psi_i(\mathbf{r})$ in equation (2.68) are known as the KS orbitals and are related to the electron density as follows:

$$\rho(\mathbf{r}) = \sum_{i=1}^{N}\left|\psi_i(\mathbf{r})\right|^2 \tag{2.70}$$

where $N$ is the number of electrons. This formulation leads to a self-consistent procedure analogous to that in HF theory, where an initial estimate of the electron density $\rho(\mathbf{r})$ is used to solve the equations (2.68) and the new set of KS orbitals is used to generate the new density $\tilde{\rho}(\mathbf{r})$ from (2.70), until self-consistency is achieved.

The inhomogeneity of the electron density usually present in a molecular system can be accounted for by including gradient corrections [113]. This is done by making the correlation energy a functional of the density and its gradient, and therefore this approach is known as the generalised-gradient approximation (GGA). The correlation energy (2.67) is thus re-written as:

$$E_{\text{xc}}^{GGA}\left[\rho(\mathbf{r})\right] = \int \rho(\mathbf{r})\epsilon_{\text{xc}}\left[\rho(\mathbf{r})\right]d\mathbf{r} + \int F_{\text{xc}}\left[\rho(\mathbf{r}), \nabla\rho(\mathbf{r})\right]d\mathbf{r} \tag{2.71}$$

Unfortunately, the exact expression of the functional $F_{\text{xc}}$ is unknown and as a result a multitude of different functionals have been proposed in the literature. Commonly used functionals include the Perdew-Burke-Ernzerhof (PBE) and Becke (B) gradient-corrected exchange functionals [114, 115], the Lee-Yang-Parr (LYP) gradient-corrected correlation functional [116] and the hydrid functional B3LYP [117], which uses a com-

bination of exchange energy from Hartree-Fock theory with exchange and correlation energy from Becke and Lee-Yang-Parr functionals.

## 2.3 Systems with Periodic Boundary Conditions

The atoms in a crystal are disposed in such a way to form a regular periodic array $\mathbf{R}$, called a Bravais lattice, and to generate a potential $U(\mathbf{r})$ which has the same periodicity of the underlying lattice, *i.e.*

$$U(\mathbf{r}+\mathbf{R}) = U(\mathbf{r}) \tag{2.72}$$

The periodicity of the potential $U(\mathbf{r})$ has major consequences for the solutions of the Schrödinger equation for electrons in a periodic system. It is convenient to define here a set of wave vectors $\mathbf{K}$ that yield plane waves with the same periodicity of a given Bravais lattice. The lattice defined by the vectors $\mathbf{K}$ is known as a *reciprocal* lattice [118], and the corresponding plane waves have the following properties:

$$e^{i\mathbf{K}\cdot(\mathbf{r}+\mathbf{R})} = e^{i\mathbf{K}\cdot\mathbf{r}} \tag{2.73a}$$

$$e^{i\mathbf{K}\cdot\mathbf{R}} = 1 \tag{2.73b}$$

### 2.3.1 Bloch's Theorem

Bloch's theorem [119] states that the wavefunction of an electron within a periodic potential can be written as the product of a wave-like part and a cell-periodic part

$$\psi_{i,\mathbf{k}}(\mathbf{r}) = e^{i\mathbf{k}\cdot\mathbf{r}} u_{i,\mathbf{k}}(\mathbf{r}) \tag{2.74}$$

where $\mathbf{k}$ is a wavevector that is confined to the first Brillouin zone[3]. The cell-periodic part can be expressed as a sum of the plane-wave basis functions (2.50). With this

[3] *i.e.* the smallest unit cell in the reciprocal space.

substitution, equation (2.74) can be re-written as

$$\psi_{i,\mathbf{k}}(\mathbf{r}) = \sum_{\mathbf{G}} C_{i,\mathbf{k}+\mathbf{G}}\, e^{\mathrm{i}(\mathbf{k}+\mathbf{G})\cdot\mathbf{r}} \tag{2.75}$$

This expression for the electronic wavefunctions leads to a reciprocal-space representation of the Kohn-Sham equations. Substitution of (2.75) into (2.68) and integration over $\mathbf{r}$ gives the secular equation [94]

$$\sum_{\mathbf{G}'} \left[\frac{1}{2}|\mathbf{k}+\mathbf{G}|^2\delta_{\mathbf{G}\mathbf{G}'} + V_{\text{ion}}(\mathbf{G}-\mathbf{G}') + V_{\text{Coul}}(\mathbf{G}-\mathbf{G}') + \mu_{\text{xc}}(\mathbf{G}-\mathbf{G}')\right] C_{i,\mathbf{k}+\mathbf{G}'} = \varepsilon_i C_{i,\mathbf{k}+\mathbf{G}'} \tag{2.76}$$

where the first term is the kinetic energy, the second is the ion-electron interaction, the third is the Coulomb interaction between electrons and the fourth term is the exchange potential. In can be shown that the kinetic energy in (2.76) is diagonal and the other potential terms are described in terms of their Fourier transform [94].

As the wave-vector $\mathbf{k}$ varies, the eigenvalues of equation (2.76) –the energy levels $\varepsilon_i$– vary continuously, *i.e.*

$$\varepsilon_i = \varepsilon_i(\mathbf{k}) \tag{2.77}$$

This gives rise to a description of the energy levels of an electron in a periodic potential in terms of an infinite family of solutions characterised by the *band index* $i$, each with the periodicity of the reciprocal cell. The information contained in these functions is referred to as the *band structure* of the solid.

### 2.3.2 Pseudopotential Approximation

The solutions of equation (2.76) proceed by diagonalisation of a Hamiltonian given by the terms in brackets in equation (2.76), with matrix elements $H_{\mathbf{k}+\mathbf{G},\mathbf{k}+\mathbf{G}'}$. The size of this matrix is determined by the basis set cut-off energy and by the number of electrons in the system. For a large system containing core and valence electrons this problem becomes quickly intractable; in particular, a large number of plane waves would be

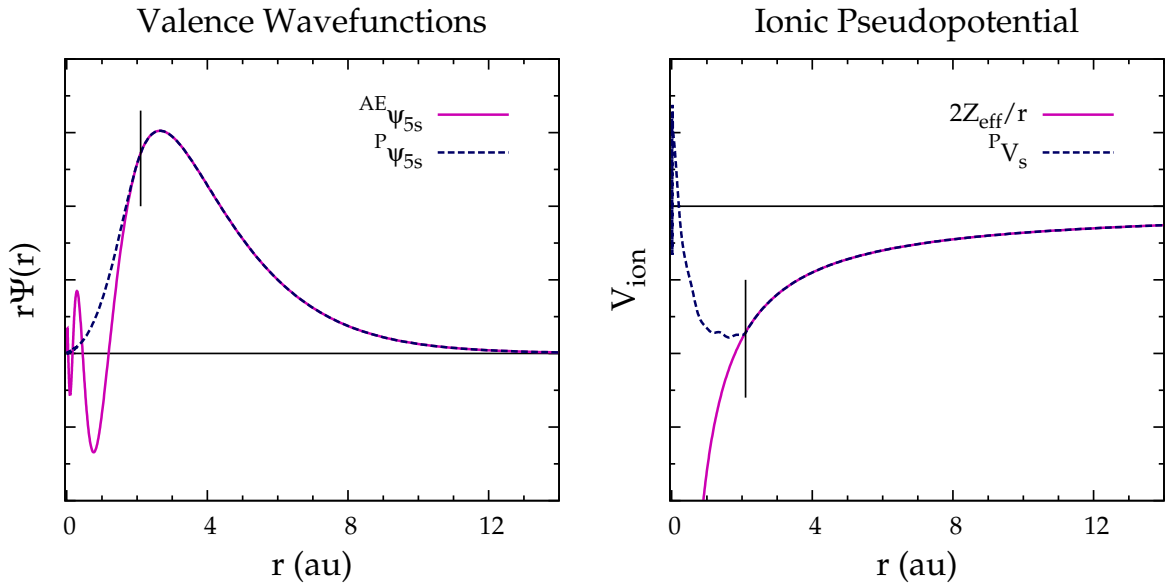


**Figure 2.3:** Comparison between the all-electron wavefunction for rhodium (solid line) and the pseudopotential-wavefunction (dashed line). The second panel shows the corresponding pseudopotential (dashed line) and, as reference, the classic Coulomb potential (solid line). The vertical line represents the pseudopotential cut-off radius, $r_c = 2.10$ a.u. Calculations were performed with the program *Opium* [123, 124].

required to satisfactorily describe the tightly bound core electrons.

Based on the assumption that the chemical and physical properties of solid matter depend mainly on valence electrons, the pseudopotential approximation [120–122] reduces the number of plane-wave basis functions required to expand the wavefunction by removing the core electrons and replacing the strong ionic potential with a smooth pseudopotential [94]. A comparison between an all-electron wavefunction and a pseudopotential-wavefunction, along with the corresponding ionic potential and pseudopotential, is shown in Figure 2.3. The pseudopotential-wavefunction has the same scattering properties (*i.e.* phase shift) of the all-electron wavefunction, but no nodes in the core region. Outside the core region, the pseudopotential becomes identical to the Coulomb potential and as a consequence in this region the pseudopotential-wavefunction and the all-electron wavefunction are indistinguishable. The most general form for a pseudopotential is obtained by projecting the all-electron wavefunction

into a specific spherical harmonic function $\langle lm|$, and by multiplying each component for a specific pseudo-potential, *i.e.*

$$^{P}V_{\mathrm{NL}} = \sum_{lm} |lm\rangle V_l \langle lm| \tag{2.78}$$

where the subscript NL stands for *non-local*. A pseudopotential that uses the same potential for all the angular components of the wavefunction is referred to as *local* and is a function only of the distance from the nucleus [94]. A *norm-conserving* pseudopotential [125] is constructed to ensure that the pseudopotential- and all-electron wavefunctions give identical electron density inside the core region. If the norm conservation is not required, the pseudopotentials can have a very smooth behaviour in the core region, resulting in a smaller basis set required to describe the valence electrons. Such a pseudopotential is referred to as *ultrasoft* [126].

## 2.4 Molecular Mechanics

In molecular mechanics the Newtonian laws of motions are used to model molecular systems. Within this approximation, the atoms are considered as classical spheres with a given charge and mass, and the bonds between atoms are represented with appropriate interaction potentials. Other types of potential are used to model bond angles, dihedral angles, etc. This approach can be used to study very large systems composed of thousands of atoms since it is computationally much less expensive than quantum mechanics. On the other hand, this approach cannot be used to study chemical reactions involving bond making and breaking.

### 2.4.1 Atomistic Model

In molecular mechanics the energy of a system is a function of the atom positions only, *i.e.* the motion of electrons is completely neglected and their effect may be accounted for by effective atoms. The energy of a system can thus be decomposed into an expan-

sion in terms of interactions between atoms:

$$U = \sum_{i=1}^{N} U_i + \sum_{i=1}^{N}\sum_{j=1}^{N} U_{ij} + \sum_{i=1}^{N}\sum_{j=1}^{N}\sum_{k=1}^{N} U_{ijk} + \dots \tag{2.79}$$

where the first term represents the self energies of the atoms, the second the pairwise interaction, etc. This decomposition is exact if performed to a high enough order [127]. However, the contribution of high-order terms becomes progressively smaller and as a consequence a finite number of terms is usually sufficient to describe a given system. The functional form of the interaction terms is chosen according to the physical properties of the system, and the parametrisation of each potential term is done using experimental and theoretical methods. The ensemble of potentials used to calculate the energy of a system is referred to as a *force field*.

### 2.4.2 Force Fields

In a typical force field the atoms are represented as point particles connected by two- three- and four-body interaction terms, as shown in equation (2.79). The potential energy of the ionic interaction between two particles is described by a combination of repulsive and attractive terms, given in a radial or exponential form. Potentials of this type are the Lennard-Jones-type potential [128]

$$U_{ij}^{\mathrm{LJ}} = \frac{C_m}{r_{ij}^m} - \frac{C_n}{r_{ij}^n} \tag{2.80}$$

and the Buckingham potential [129]

$$U_{ij}^{\mathrm{B}} = Ae^{-\frac{r_{ij}}{\rho}} - \frac{C_6}{r_{ij}^6} \tag{2.81}$$

Both potentials have a long-range attractive term due to dispersion interactions, and a short range repulsive term that accounts for the repulsion between overlapping electron densities experienced at short distances.

The vibrational structure of covalently bound atoms is better described by the Morse potential [130], that also accounts for the anharmonicity of real bonds:

$$U_{ij}^{\mathrm{M}} = D_e \left[1 - e^{-a(r_{ij} - r_0)}\right]^2 \tag{2.82}$$

In this expression, the parameter $D_e$ is the electronic dissociation energy and the parameter $a = \sqrt{k_e/2D_e}$ is proportional to the square root of force constant of the bond, $k_e$. The three-body potential term is defined as

$$U_{ijk}^{\mathrm{T}} = \frac{1}{2}k_2(\theta_{ijk} - \theta_0)^2 + \frac{1}{6}k_3(\theta_{ijk} - \theta_0)^3 + \frac{1}{24}k_4(\theta_{ijk} - \theta_0)^4 \tag{2.83}$$

Here $\theta_{ijk}$ is the angle formed between the atoms $i$, $j$ and $k$. However, additional potential terms are added for particular purposes, *e.g.* describing the torsional angle between two groups or the inversion of a flexible group.

In molecular mechanics force fields, the Coulomb interaction, and usually also the dispersion term, is subtracted from interactions between neighbouring atoms. This is done so that the parameters in the two- and three-body potentials can be directly equated with experimentally observable quantities, such as force constants from spectroscopy [127]. The quality of a force field strongly depends on the determination of a large number of parameters from experimental reference data: this ensures the reliability and accuracy of a given MM approach, but also restricts its application to the classes of molecules for which it has been designed [131].

### 2.4.3 Shell-Model Method

In the core-shell model [132] an ion is divided into a core, which represents the nucleus and the inner electrons, and a mass-less shell, which mimics the valence electrons. The core and shell are linked by an harmonic constant, as illustrated in Figure 2.4. This approach reproduces a dipolar polarisability by coupling the core and shell charges with a harmonic spring of force constant $k_{cs}$ . If the shell charge is $q_s$ , then the polarisability

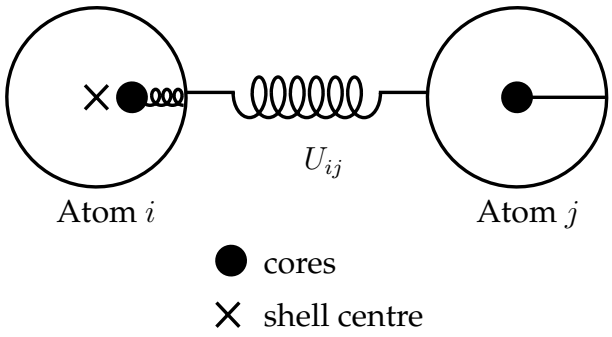


**Figure 2.4:** Schematic representation of the core-shell model, composed of a positively charged core and a negatively charged shell with no mass and spherical charge distribution. Atom $i$ is polarised and atom $j$ is unpolarised. The electrostatic interaction occurs between all cores and shells except for the core and shell of the same atom.

of the ion in vacuo is given by [127]:

$$\alpha = \frac{q_s^2}{k_{cs}} \tag{2.84}$$

By convention, the short-range forces are specified to act on the shell, while the long-range Coulomb potential acts on both core and shell. As a consequence, the short-range forces actively modify the polarisability by modifying the spring constant, and thus the polarisability is environment dependent.

The core-shell model is particularly effective in the description of solids with covalent character such as silica polymorphs because the polarisability of an ion is phenomenologically equivalent to a charge tranfer between two atoms.

## 2.5 Combined QM/MM Calculations

The idea behind the quantum and molecular mechanics (QM/MM) approach is to divide a large molecular system into two regions and to compute the properties of each at two different levels of theory. This approach is particularly well suited to study point defect in crystals [58, 133–136], active sites in enzymes [137–141] and catalysts [142–148] because it enables the reactive chemical site to be studied with the precision

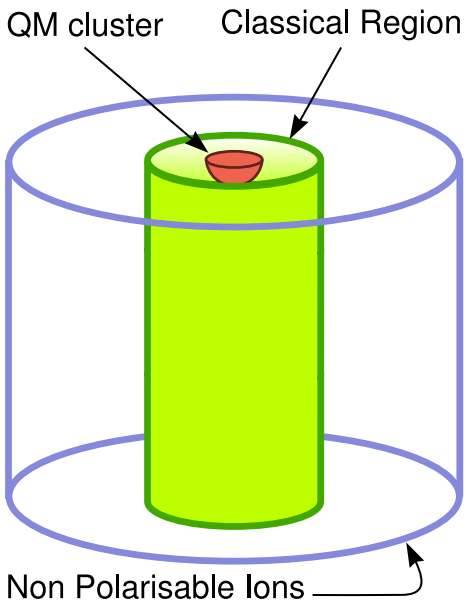


**Figure 2.5:** The division of space in an hybrid QM/MM calculation: the quantum cluster is surrounded by a region where the atom positions are optimised at the molecular mechanics level of theory. The system is finally embedded in a lattice of fixed ions.

of QM, whereas the structural and electrostatic constraints due to the rest of the system are treated with a suitable MM scheme [149]. Several hybrid QM/MM models have been proposed in the literature [57, 58, 131, 150–154], combining semiempirical, density functional or *ab-initio* methodologies with different kinds of force field.

### 2.5.1 The Guess approach

The *Guess* code for hybrid QM/MM calculations has been successfully applied to study bulk defects and surface vacancies in various metal oxides [58, 59, 135], and will be used in this thesis to study supported rhodium catalysts.

The *Guess* program is a hybrid QM/MM code that uses the program *Gaussian* [155] for the computation of the QM part and the program *Gulp* [127] for the MM part. A schematic representation of the embedding scheme implemented in *Guess* is showed in Figure 2.5. A quantum cluster (of up to several tens of ions) is embedded in a finite array of point charges located at the lattice sites. The part of the ions closest to the

quantum cluster is treated by the core-shell model, and these ions interact with themselves and with the quantum cluster atoms via a force field. The interface between the quantum cluster and classical ions is constituted of positive ions represented using ECPs and a minimal basis set with tight functions for the valence electrons. The atoms in the interface region interact quantum mechanically with atoms of the quantum cluster and classically with the rest of ions in the system. In this way the interface region prevents an artificial spreading of electronic states outside the quantum cluster. The positions of the cores and shells in the classical region are optimised in response to the changes in the charge density distribution within the quantum cluster to minimise the total energy of the whole system. The rest of the point ions form a region of fixed non-polarisable ions, which provide the correct electrostatic potential distribution in the quantum cluster and in MM region [58].

### 2.5.2 Computational procedure

The scheme of embedding that interfaces the QM treatment of a QM cluster with the classical representation of the lattice polarisation is described in references [156, 157]. The total energy of the system can be written as [58]:

$$E = \left\langle \Psi \middle| \hat{H}_0 + V_{\text{env}} \middle| \Psi \right\rangle + \frac{1}{2} \sum_{\text{env}} \frac{q_i q_j}{R_{ij}} + \frac{1}{2} \sum_{\text{env}} W_{ij} + \frac{1}{2} \sum_{\text{env}} k_i \rho_i^2 + \sum_{i \in \text{QM}} \sum_{j \in \text{env}} W_{ij} \qquad (2.85)$$

where $\hat{H}_0$ is the Hamiltonian of a free cluster, and

$$V_{\text{env}} = \sum_{i \in \text{QM}} \sum_{j \in \text{env}} \frac{q_j}{|r_i - R_j|} + \sum_{i \in \text{QM}} \sum_{j \in \text{env}} \frac{Z_i q_j}{|R_i - R_j|} \qquad (2.86)$$

is the electrostatic potential due to point charges $q_i$ of cores and shells representing the polarisable environment of the QM cluster. The first term in equation (2.85) is the QM energy of electrons in the potential of the nuclei of the QM cluster and the external monopoles and dipoles representing ions of the polarisable environment [equation (2.86)]. The second and third terms are respectively the Coulomb interaction, between

the point charges of cores and shells in the environment and the short-range interaction $W_{ij}$ , between the shells. The fourth term in equation (2.85) represents the elastic interaction between cores and shells that are connected by a spring with the spring constant $k_i$ and are separated by the distance $r_i$ . The last term in equation (2.85) is due to the short-range interaction of the ions of the QM cluster and those of the environment. It is calculated using the short-range part of interatomic potentials, $W_{ij}$, and is included in order to describe better the Pauli repulsion and the dispersion interaction across the QM cluster border. The total forces acting on each centre, *i.e.* the QM ions and the classical cores and shells, are calculated by differentiating the total energy with respect to the coordinates of corresponding species.

In this scheme total forces are calculated on both QM and classical ions. In such a way the total energy of the system is simultaneously minimised with respect to the electronic coordinates and the positions of QM ions and classical ions.

## 2.6 Computational Details

The calculations presented in this thesis work are based on the theoretical methods described in this Chapter, and have been carried out on the Columbus and Magellan clusters at the National Service for Computational Chemistry Software[4]. The Columbus cluster is based on servers with two 2.4GHz Opteron processors and 8 GB of memory for each node (250 CPUs in total). The Magellan cluster is a Silicon Graphics Altix 4700 server with 224-core, 1.6GHz, Montecito Itanium2 processors, 896 GB of memory and 15 TB of disk space. SUSE Linux Enterprise with SGI ProPack 4 is installed on Magellan and RedHat Enterprise Linux is installed on Columbus.

A small number of calculations have been carried out on the Iridis2 cluster mantained by the University of Southampton. Iridis2 is a Beowulf cluster[5] based on AMD

[4]Website: *http://www.nsccs.ac.uk*

[5]A Beowulf cluster is a scalable performance cluster based on commodity hardware, on a private system network, with open source software (Linux) infrastructure (*http://www.beowulf.org*).

Opteron processors, running RedHat Enterprise Linux. It has over 1000 processor-cores (of which approximately 600 are single-core CPUs and approximately 480 are dual-core CPUs), 900 GB of memory and over 30 TB of local disk storage.

## 2.7 Conclusions

An overview of the theoretical methods employed in this thesis work has been presented in this chapter. The plane-wave/DFT methodology, as implemented in the program *Castep* [158], is used in Chapters 3, 4 and 5 to study the $\gamma$-$Al_2O_3$ support, several molecular rhodium species and finally the supported catalyst. The results of these calculations are compared with *ab-initio* and DFT calculations performed with the programs *Gaussian* [155] and *Molpro* [159].

*Ab-initio* molecular orbital calculations have been used to compute the geometries and reaction enthalpies for some selected rhodium complexes. The results are presented and compared with experimental results in Chapter 4.

Molecular mechanics, as implemented in the program *Gulp* [127], is used to simulate the structure of hydroxylated $\gamma$-$Al_2O_3$ surfaces through different force fields, and comparison is made with results of periodic DFT calculations. The results are reported in Chapter 3.

The QM and MM methodologies are then used to study supported rhodium catalysts using the hybrid QM/MM scheme, as implemented in the program *Guess* [58]. The results of these calculations are presented in Chapter 5 and compared with the calculations performed at the periodic-DFT level of theory.

CHAPTER 3

# SIMULATION OF HYDROXYLATED $\gamma$-ALUMINA SURFACES

The aim of the work described in this Chapter is to simulate hydroxylated $\gamma$-$Al_2O_3$ surfaces using theoretical methods. As stated in the Introduction (Chapter 1), the bulk structure of $\gamma$-alumina was taken from the work of Digne *et al.* [16, 27, 29] because this model has been proved to reproduce the physical and chemical properties of hydroxylated $\gamma$-alumina surfaces, with particular emphasis on hydroxylation/dehydroxylation processes induced by temperature [29].

In the work of Digne *et al.*, the simulations were performed at the plane-wave/DFT level of theory, with periodic boundary conditions applied to the systems investigated. In this thesis work, the plane-wave/DFT approach was used as implemented in the program *Castep* [158]. The crystal model of $\gamma$-$Al_2O_3$ was optimised and used to generate the principal crystallographic surfaces *via* a periodic model composed of a slab of appropriate thickness coupled with a vacuum gap large enough to avoid unphysical interactions between the top and bottom surfaces of the slab. At this stage, the program *Gdis* [160] was used to cleave the bulk structure along the desired crystallographic plane and to build slab models of surfaces.

An important point in solid state calculations is to check computed quantities such as energies and forces with respect to the simulation parameters in order to have meaningful results. Once a set of simulation parameters has been chosen that gives the best compromise in terms of computational demand and accuracy, the same approach can

be used to compute minimum-energy structures of supported rhodium species that are found to be present on the catalyst surface (see Chapter 5).

The simulations performed in this thesis work were tested on $\gamma$-$Al_2O_3$ and the results compared with those published by Digne *et al.* [16, 27, 29]. Additional tests were performed on $\alpha$-$Al_2O_3$ (*corundum*), whose structure is well known experimentally [161–169]. The bulk modulus is an important physical parameter that it is correlated to the character of chemical bonds and is used as an indicator for the strength and hardness of crystals [170]. The bulk modulus of $\alpha$ and $\gamma$ alumina have been computed in this thesis work by optimising the crystal bulk structure in the presence of an external pressure. The equilibrium unit cell volumes, obtained for a range of pressures from 0 to 250 GPa, were used to obtain a pressure-to-volume (PV) dataset that was fitted using the third-order Birch-Murnagham equation of state [171, 172]:

$$P(V) = \frac{2}{3}K_0 \left[ \left(\frac{V_0}{V}\right)^{\frac{7}{3}} - \left(\frac{V_0}{V}\right)^{\frac{5}{3}} \right] \left\{ 1 + \frac{3}{4}(K_0' - 4) \left[ \left(\frac{V_0}{V}\right)^{\frac{2}{3}} - 1 \right] \right\} \tag{3.1}$$

where $K_0$ is the bulk modulus, $V_0$ the equilibrium unit-cell volume at zero pressure and $K_0' = \frac{dK_0}{dV}$ (the value of $K_0'$ is actually fitted). The fit was performed with the program *Gnuplot* [173] by minimising the least-square residues between the binding curve and the data points.

In the second part of this chapter, molecular mechanics (MM) is used to investigate the structure of bulk and hydroxylated surfaces of $\gamma$-$Al_2O_3$. The aim was to find a force field capable of reproducing the mechanical and electrostatic properties of hydroxylated $\gamma$-$Al_2O_3$ surfaces and to use it for hybrid QM/MM calculations, described in Chapter 5. Several force fields were used to study the crystal structure of $\alpha$-$Al_2O_3$, $\gamma$-$Al_2O_3$, and *diaspore* (AlOOH), an aluminium hydroxide. Among the force fields which give the best agreement with the *reference* structures optimised at the plane-wave/DFT level of theory, one was modified in order to account for the presence of surface hydoxyl groups. The structures calculated at the MM level of theory were found to be in good agreement with the reference structures.

## 3.1 Plane-wave DFT Simulations

The calculations presented in this section were performed at the plane-wave/DFT level of theory, following the methodology described in the work of Digne and co-workers, from which the model of $\gamma$-$Al_2O_3$ was taken. In the original work [27, 29], the PW91 functional was used in the calculations. In this thesis work, the PBE functional has been used because it gives essentially the same results as the PW91 functional, although it has a simplier form [114] and this makes the calculations easier to carry out. The other simulation parameters were chosen according to convergence of quantities such as total electron energy and forces with respect to parameters such as the basis-set energy cut-off, the k-point grid and the fast Fourier Transform (FFT) numerical grid.

The ($h\ k\ l$) surface was simulated by slicing the bulk structure in the ($h\ k\ l$) crystallographic direction and coupling the resulting slab with a vacuum gap. The stability of the results and the quality of the simulations were checked by studying the variation of the surface free energy ($E_{\text{surf}}$) with respect to the slab thickness and the vacuum gap until convergence of the value $E_{\text{surf}}$ is obtained. The surface energy is defined as:

$$E_{\text{surf}} = \frac{E_{\text{slab}} - E_{\text{bulk}}}{A} \tag{3.2}$$

where $A$ is the total area of the surface in the slab model, $E_{\text{slab}}$ is the computed energy of the slab and $E_{\text{bulk}}$ is the energy of an equivalent amount of bulk atoms.

### 3.1.1 Simulation Parameters

The calculations presented in this thesis work are based on the plane-wave/DFT approach, as implemented in the program *Castep* [158]. The gradient-corrected exchange correlation functional PBE [114] was used to solve the Kohn-Sham (KS) equations, with periodic boundary conditions applied to the systems under investigation. Vanderbilt ultrasoft pseudopotentials [126] were used to describe the ion-electron interaction and the core electrons. The KS orbitals were expanded in a plane-wave basis set, with a

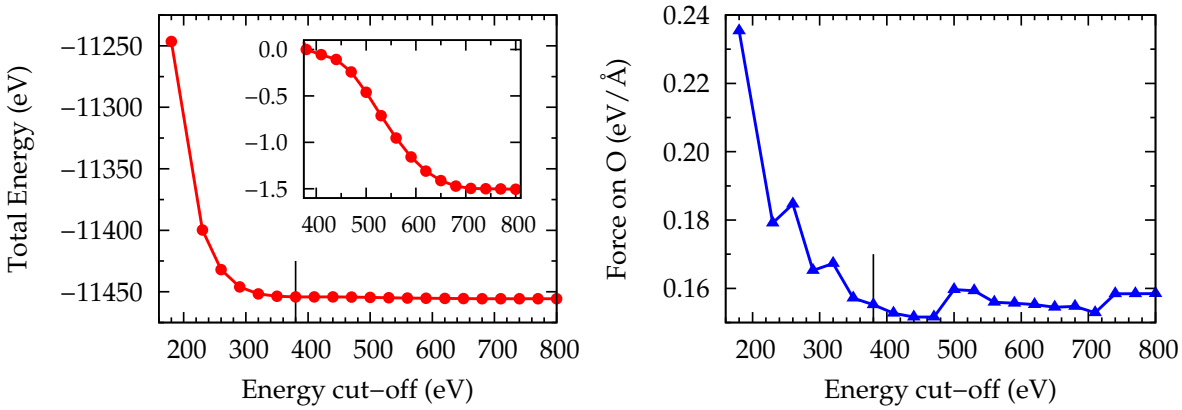


**Figure 3.1:** Convergence of the total electronic energy and the force acting on the first oxygen atom (see the output file of a Castep calculation, on Support Information A.1) with respect to the basis set energy cut-off. A cut-off energy $E_{\text{cut}} = 380$ eV was chosen for the calculations presented in this thesis work. The inset in the left-hand side of this Figure shows the relative energy difference (in eV) in the region from $E_{\text{cut}} = 380$ eV to $E_{\text{cut}} = 800$ eV.

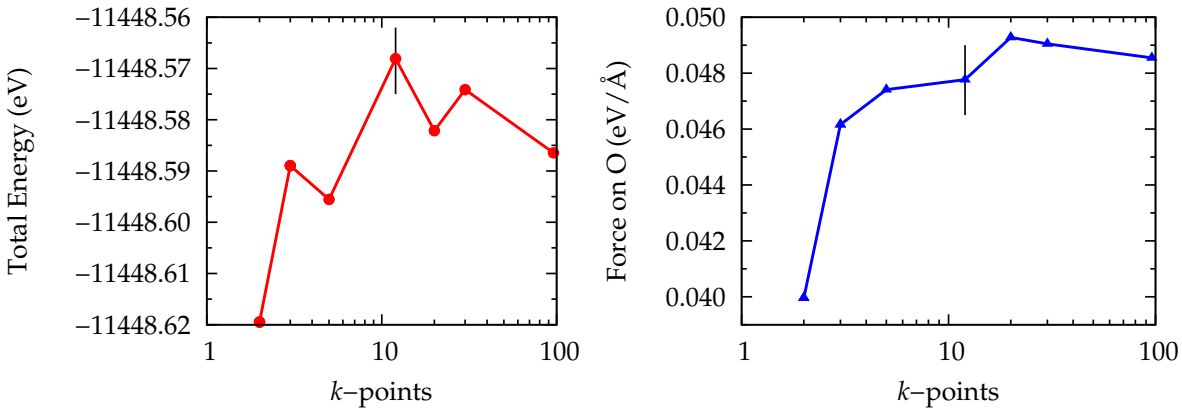


**Figure 3.2:** Convergence of the total electronic energy and forces with respect to the number of $k$-points. A grid of 12 points, obtained with a $k$-point spacing of 0.05 $\text{Å}^{-1}$, was chosen for the calculations presented in this thesis work. Specifying the grid spacing instead of the total number of $k$-points yields a constant density of points regardless of the size of the unit cell.

cut-off energy of 380 eV. The basis-set cut-off energy was determined on the basis of single-point calculations performed on the bulk structure of $\gamma$-$Al_2O_3$. The total electronic energy and the atomic forces computed as a function of the basis-set energy cut-off are shown in Figure 3.1. Both the total electronic energy and the forces acting

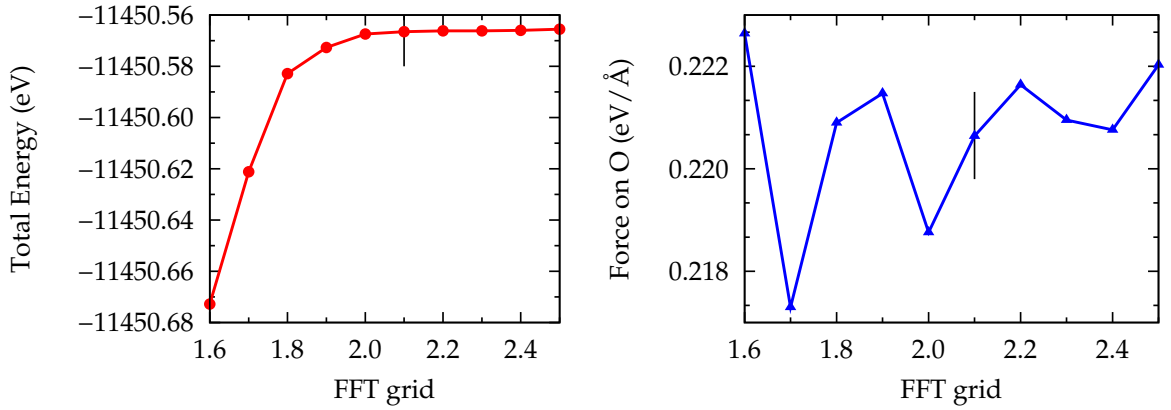


**Figure 3.3:** Convergence of the total electronic energy and forces with respect to the fast Fourier transform (FFT) grid. A value of 2.1 was chosen for the calculations presented in this thesis work. The computed forces shown in the right-hand side do not show a clear dependance on this parameter.

on atoms smoothly converge to stationary values. The difference between the energy computed at $E_{\text{cut}} = 380$ eV and the value computed at higher cut-off energies is shown in the small inset of Figure 3.1. As can be seen, the error due to a finite basis set is really small (about 0.04 eV/atom).

The first Brillouin zone is defined as the Wigner-Seitz primitive cell of the reciprocal lattice (*i.e.* the $k$-space). The bigger the unit cell, the smaller the first Brillouin zone will be. Therefore a relatively large number of $k$-points is required for an accurate $k$-sampling of small unit cells such as those of $\alpha$ and $\gamma$ alumina, whereas a few points are required for large unit cells. For very large unitary cells such as the one of an isolated molecule, just the point at $\mathbf{k} = 0$ (known as the $\Gamma$ point) is used for calculations in the reciprocal space. Figure 3.2 shows the convergence of the total electronic energy and forces of bulk $\gamma$-$Al_2O_3$ with respect to the number of $k$-points. The number of $k$-points increases as the distance between $k$-points decreases. In practice, satisfactory energies and forces were computed with a $k$-point spacing of 0.05 $\text{Å}^{-1}$. The advantage of specifying the $k$-point spacing instead of a fixed grid is to assure a constant sampling in the $k$ space independently of the unit cell size.

Fast Fourier transformation (FFT) is used to transform between real and reciprocal

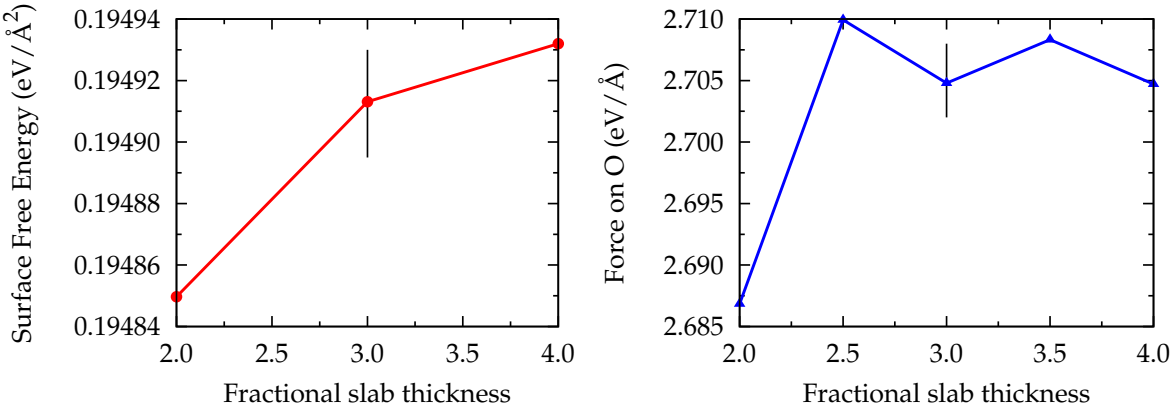


**Figure 3.4:** Convergence of the surface energy and forces computed for the (100) surface of $\gamma$-$Al_2O_3$. The calculations are carried out varying the thickness of the slab. A fractional thickness of three units was chosen as a compromise between computational cost and accuracy.

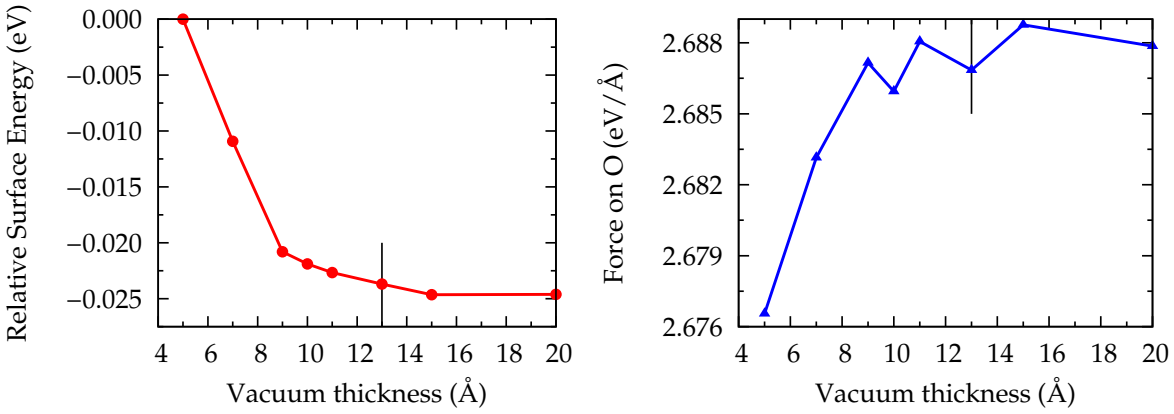


**Figure 3.5:** Convergence of the relative total electronic energy and forces computed for the (100) surface of $\gamma$-$Al_2O_3$. The calculations are carried out varying the vacuum gap. A vacuum gap of 13 Å was chosen for the calculations presented in this thesis work.

space. The fineness of the grid for numerical integration in real space is given as a multiple of the diameter of the plane-wave sphere[1] in the $k$-space. A value of 2.1 was used to yield accurate energy calculations, as shown in Figure 3.3. The computed forces do not show a clear dependance on this parameter.

[1] *i.e.* the sphere that contains the wave-vectors, that satisfies the condition $\frac{(\mathbf{G}+\mathbf{k})^2}{2} \leq E_{\text{cut}}$.

| Parameter | *Castep* keyword | Value |
|---|---|---|
| XC functional | `xc_functional` | PBE |
| Energy cut-off | `cut_off_energy` | 380 eV |
| FFT grid | `grid_scale` | 2.1 |
| $k$-point grid finess | `kpoints_mp_spacing` | 0.05 $\text{Å}^{-1}$ |
| Pseudopotentials | `species_pot` | Ultrasoft |

**Table 3.1:** Summary of the parameters used for the simulations performed with the program *Castep*.

The surfaces are modelled as slabs cleaved from the bulk structure of the crystal. Periodic boundary conditions are applied in all directions and a vacuum gap added in the direction perpendicular to the surface in order to avoid unphysical interactions between the periodic images of the system. The top and bottom surfaces in the slab are identical, and the cell volume is kept fixed in all the geometrical optimisations. The convergence of the surface energy $E_{\text{surf}}$ was studied as a function of the slab thickness and the vacuum gap. A slab thickness of 3.0 fractional units has been chosen as the best compromise between accuracy and computational cost. Figure 3.4 shows a rapid convergence of the computed forces to stationary values, and a slow convergence of $E_{\text{surf}}$ with respect to the fractional thickness of the slab. A vacuum gap of 13 Å is found to give accurate energy and forces, as shown in Figure 3.5. For this test, the relative variation of the surface energy is shown. It should be noted that because of their non-locality, a large number of plane waves is required to simulate the vacuum gap, thus increasing significantly the computational cost of the calculations. A summary of the parameters used for the plane-wave/DFT simulations carried out in this thesis work is presented in Table 3.1.

### 3.1.2 Computed Structures

The structure of corundum ($\alpha$-$Al_2O_3$) is rhombohedral with two $Al_2O_3$ units in each primitive cell, and its space group is $R\bar{3}c$. The three primitive lattice vectors have equal lengths and are separated by equal angles. The lattice can also be viewed as a hexago-

nal lattice containing six formula units per cell with lattice parameters $a$ and $c$, where the $c$-axis is the threefold axis of the primitive rhombohedral cell and $c$ is the length of the primitive cell along that axis [174]. A comparison of the two representations is shown in Figure 3.6.

The rhombohedral representation was used in the present calculations because, being smaller than the hexagonal representation, it also has a smaller computational cost. The computed equilibrium structure at $P = 0$ GPa has lattice vectors $a = 5.181632$ Å and angles $\alpha = 55.290794$ deg. The resulting cell is slightly bigger than the experimental cell, and the corresponding density lower (see Table 3.2). However, this is a known effect since the GGA approximation is known to give longer bond lengths and smaller bond force constants compared to the LDA approximation [175]. A summary of the computed and experimental properties of corundum is reported in Table 3.2.

The calculated bulk modulus of $\alpha$-$Al_2O_3$ is $227.5 \pm 0.2$ GPa, and the fit of the theoretical $PV$ data-set is shown in Figure 3.7. As expected, the calculated bulk modulus is smaller than the experimental value of about $250$ GPa. Theoretical values of the

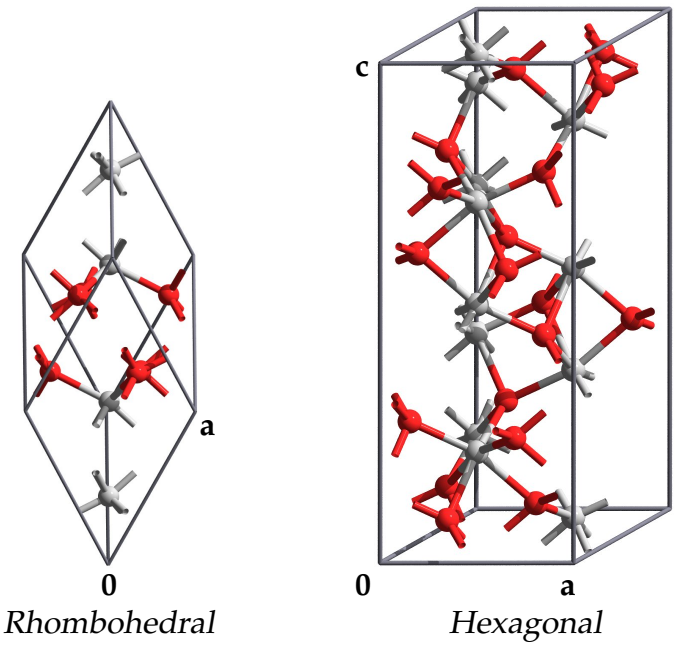


**Figure 3.6:** Rhombohedral and hexagonal representation of the corundum unit cell. Red atoms are oxygen, grey atoms are aluminium.

| *Source* | $a$ | $c$ | $c/a$ | $V_0$ | $K_0$ | density |
|---|---|---|---|---|---|---|
| Exp. [164] | 4.7657 (9) | 13.010 (14) | 2.730 (8) | 85.298 | 254.4 | 3.9699 |
| Exp. [167, 176] | 4.7540 (5) | 12.9820 (6) | 2.7308 (4) | 84.697 | 255 | 3.9980 |
| Exp. [168, 177] | 4.7602 (4) | 12.993 (2) | 2.7295 (5) | 84.990 | 252 | 3.9843 |
| Theo.[a][174] | 4.7665 | 12.969 | 2.7209 | 85.059 | 248.7 | 3.9810 |
| This work[b] | 4.8085 | 13.125 | 2.7296 | 87.609 | 227.5 (2) | 3.8647 |

[a] Total-energy calculations performed with the all-electron, full-potential linear combinations of Gaussian type orbitals-fitting function technique.
[b] Calculations performed at the plane-wave/PBE level of theory with periodic boundary conditions.

**Table 3.2:** Comparison of theoretical and experimental properties of corundum: the hexagonal cell lattice constants $a$ and $c$ (Å), $c/a$ ratio, zero-pressure volume of the rhombohedral cell $V_0$ (Å$^3$), bulk modulus $K_0$ (GPa) and density (g/cm$^3$).

bulk modulus calculated by other research groups show a better agreement with the experimental value (see below):

| | | | | | |
|---|---|---|---|---|---|
| *Bulk modulus* (GPa) | 248.7 | 248 | 253.5 | 246.9 | 243.7 |
| *XC functional* | LDA | LDA | LDA | LDA | GGA |
| *Reference* | [174] | [178] | [179] | [180] | [181] |

In the cited works, the bulk modulus has been computed by ($i$) fitting the modified "universal" equation of state [182, 183], ($ii$) from theoretical elastic constants [184], and ($iii$) using the Cohen's empirical formula [185].

The discrepancy with the value computed in this thesis work can be attributed either to the GGA approximation, or to the different methodology used to compute the bulk modulus. In this thesis work, the bulk modulus was computed with the Birch-Murnagham equation of state (3.1) because it describes the phenomenological response of a crystal to compression. The advantage of such an approach is that it can be used to fit PV data-sets obtained from MM calculations, and the results compared with those obtained at the plane-wave/DFT level of theory.

The electronic density of states (DOS) computed for bulk corundum at the plane-wave/DFT level of theory is shown in Figure 3.8. The computed electronic band gap is 5.94 eV, a value typical for highly insulating metal oxides, is nevertheless lower

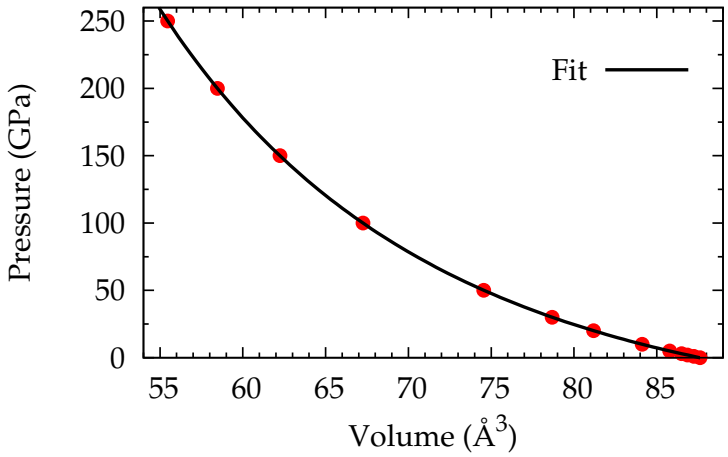


**Figure 3.7:** Cell volume of $\alpha$-$Al_2O_3$ (in the rhombohedral representation) calculated at the plane-wave PBE level of theory, at different pressures. The dataset is fitted with the Birch-Murnagham equation of state (3.1) to yield the bulk modulus.

than the experimental value of 8.8 eV [186]. Calculations performed by other research groups show similar results (see below):

| | | | | | | | |
|---|---|---|---|---|---|---|---|
| *Band gap* (eV) | 6.14 | 6.6 | 6.33 | 6.23 | 6.29 | 6.72 | 8.0 |
| *XC functional* | LDA | LDA | LDA | GGA | LDA | LDA | – |
| *Reference* | [174] | [179] | [180] | [181] | [187] | [188] | [189] |

The band gap computed in reference [189] has the best agreement with the experimental value: in this article the electronic structure of corundum was computed using the first principles extended tight-binding method, tuning the exchange parameter to reproduce the experimental band gap [189]. For the other calculations, the computed band gap is lower than the experimental value. This discrepancy is associated with the fact that DFT systematically underestimates the band gap width in solids.

The structure of $\gamma$-alumina used in this thesis work is monoclinic with eight $Al_2O_3$ units in each primitive cell, and its space group is $P21/m$. Compared to the traditional defective spinel-like structure, this model does not impose constraints on the type and number of interstices occupied by aluminum atoms, and it gives significantly lower electronic energies [27]. The present model has 25% of aluminium atoms in tetrahedral

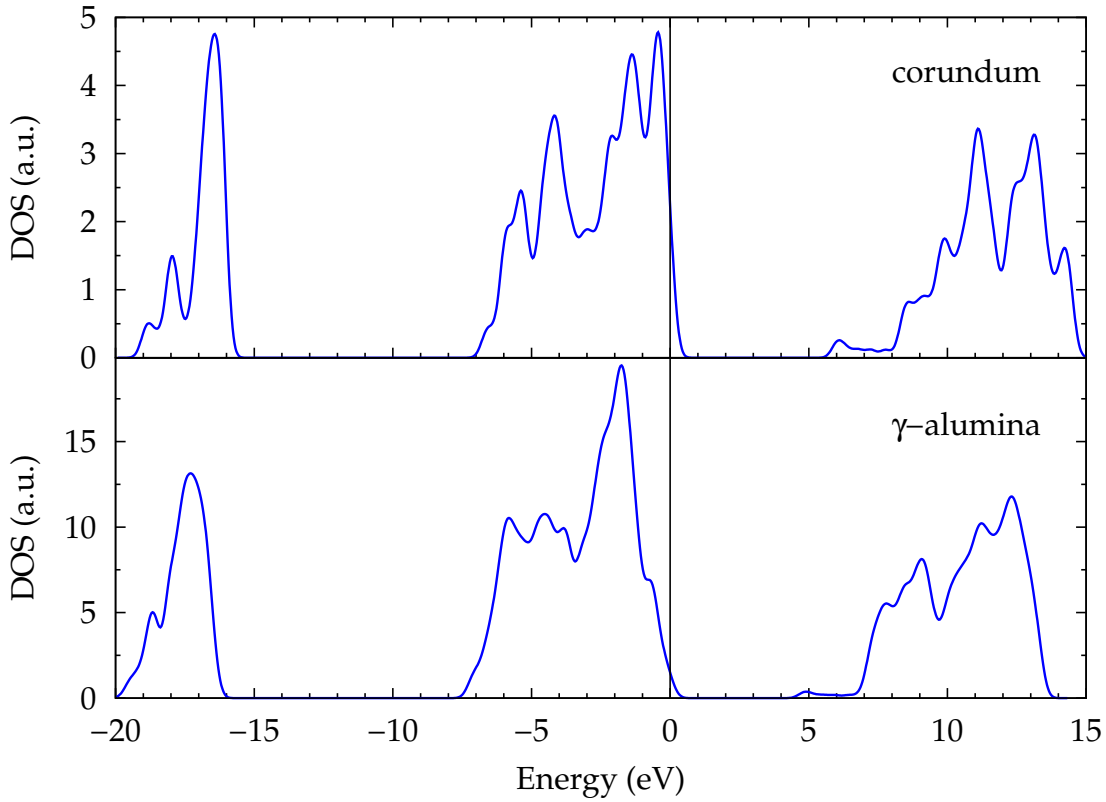


**Figure 3.8:** Comparison between the total density of states (DOS) for the corundum and $\gamma$-alumina bulk models at zero pressure computed at the plane-wave PBE level of theory. The two phases show a remarkably similar electronic structure. The band gap of corundum is bigger than the band gap of $\gamma$-alumina, in agreement with the experimental determinations.

sites and the rest in octahedral sites. The unit cell is shown in Figure 3.9

The computed equilibrium structure at $P = 0$ GPa has a cell volume/$Al_2O_3$ unit equal to $47.38$ Å$^3$, in very good agreement with the experimental mean value of $46.39$ Å$^3$ [190]. The bulk modulus was computed using the same approach described for corundum, and similar considerations apply. The PV data-set from which the bulk modulus has been computed is shown in Figure 3.10. The computed value of $175.7 \pm 0.4$ GPa is in good agreement with the theoretical value of $171$ GPa, calculated on the same bulk structure [27]. This value matches the experimental value of $162 \pm 14$ GPa [191] better than values computed at the DFT level with spinel-like models, that lead to larger values (Table 3.3).

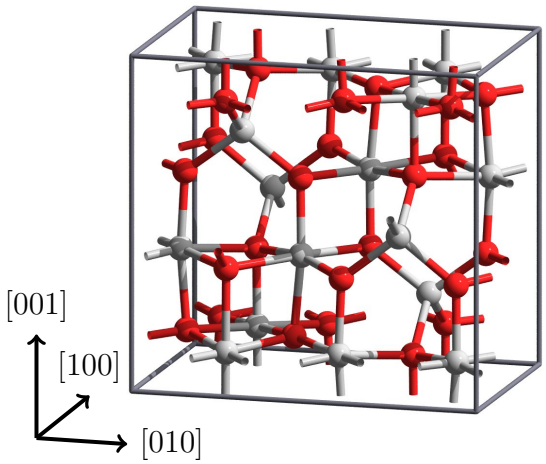


**Figure 3.9:** Unit cell of the $\gamma$-$Al_2O_3$ bulk, according to Digne *et al.* [27]. The cell is monoclinic with space group $P2_1/m$ and contains eight $Al_2O_3$ units. Red atoms are oxygen, grey atoms are aluminium.

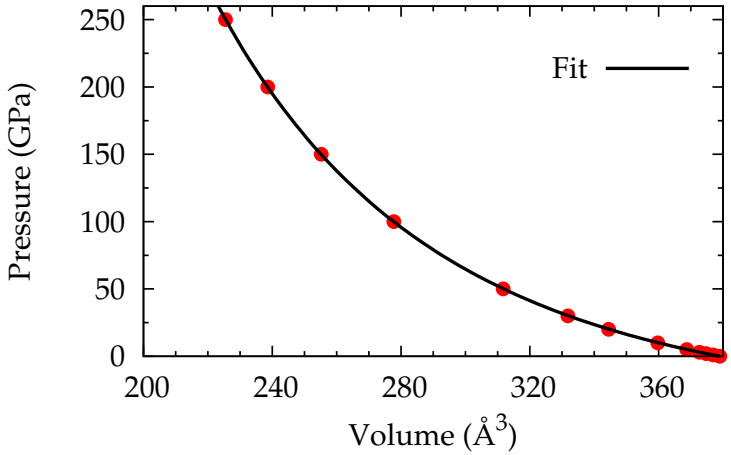


**Figure 3.10:** Cell volume of $\gamma$-$Al_2O_3$ calculated at the plane-wave PBE level of theory, at different pressures. The dataset is fitted with the Birch-Murnagham equation of state (3.1) to yield the bulk modulus.

The computed electronic density of states of bulk $\gamma$-alumina is shown in Figure 3.8. The computed band gap is $4.70$ eV which is lower than typical experimental values, which range from $7.0$ eV [191] to $8.7$ eV [192]. Despite the fact that the band gap is understimated with DFT, the DOS vs Energy plots of $\alpha$ and $\gamma$ alumina are similar. This result is in agreement with the fact that the experimental band gap for these two

| *Reference* | *XC functional* | $K_0$ | *Band gap* |
|---|---|---|---|
| [23] | LDA | 219 | 4.0 |
| [179] | LDA | 232 | 3.9 |
| [180] | LDA | 204.0 | 4.22 |
| This work | GGA (PBE) | 175.7 (4) | 4.70 |

**Table 3.3:** Comparison between the bulk modulus $K_0$ (GPa) and band gap (eV) of $\gamma$-alumina computed using different XC functionals.

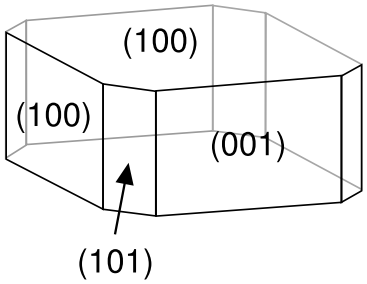


**Figure 3.11:** Morphology of a typical $\gamma$-$Al_2O_3$ nanoparticle, according to reference [27]. The indeces of the crystallographic planes (001), (100) and (101) correspond to the indeces (100), (110) and (111) in the spinel representation.

insulators is very similar, suggesting that their electronic structures are also similar.

Hydroxylated surfaces of $\gamma$-alumina were generated by cleaving the bulk structure along the plane defined by the ($h$ $k$ $l$) Miller indices. The topology of $\gamma$-alumina surfaces depends mainly on the fcc oxygen atom sublattice. In the spinel-type indexation, the (100) surface has a square oxygen atom sublattice, the (110) surface has a rectangular oxygen atom sublattice and the (111) surface has a hexagonal one. In the work of Digne and co-workers [27], the $\gamma$-alumina surfaces are indexed in this way. In this thesis work, these surfaces are indexed according to the Miller indexes of the monoclinic bulk structure. Therefore the correspondence is:

| | | | |
|---|---|---|---|
| *Original notation [27]:* | (100) | (110) | (111) |
| *This work:* | (001) | (100) | (101) |

A pictorial view of a typical $\gamma$-$Al_2O_3$ nanoparticle, adapted from reference [27], is shown in Figure 3.11. According to the morphology of a typical $\gamma$-alumina nanoparticle proposed by Digne *et al.* [27], the (100) surface accounts for 74% of the total exposed

surfaces, the (001) for 16% and the (101) surface accounts for 10% of the total exposed surfaces [27].

The slab model of these surfaces were obtained following the convergence criteria described in the previous section. The (001) and (100) surfaces were generated with a slab cut along the ($h\ k\ l$) direction and coupled with 13 Å of a vacuum gap added in the direction normal to the resulting plane. Each slab contains 24 $Al_2O_3$ units, corresponding to 12 atomic planes. The resulting periodic cells are orthorhombic with the following lattice parameters (in Å): the (001) surface has cell axes $a = 5.584061$, $b = 8.405571$ and $c = 40.200000$; the (100) surface has cell axes $a = 8.410048$, $b = 8.068898$ and $c = 33.400000$. Only the (100) and (001) surfaces have been considered in this thesis work because of the high computational cost of the simulations.

A stoichiometric number of water molecules was added to both sides of each slab in order to reproduce the degree of hydroxylation of the alumina surfaces under experimental conditions. As stated in the paragraph 1.4.3, the samples of supported rhodium catalysts are synthetised by wet impregnation of $\gamma$-alumina followed by thermal treatment at temperature $T = 500$ K. Under these conditions the alumina is dried but not extensively dehydroxylated [42]. Thus the number of water molecules used to cap the surface atoms has been chosen according to the most thermodynamically stable surface coverage of water at 500K, as determined in reference [29]:

| | (001) | (100) | (101) |
|---|---|---|---|
| $\theta$ | 8.8 | 11.8 | 14.7 |

where $\theta$ is the surface coverage index in [OH nm$^{-2}$].

The simulation parameters used to optimise the position of surface atoms and water molecules are the same as employed for the optimisation of the bulk structure. During the optimisation of the hydroxylated $\gamma$-$Al_2O_3$ surfaces, the water molecules undergo into dissociation, leading to formation of different kinds of hydroxyl groups and reorganisation of surface atom positions. The morphology of such surfaces has been described extensively in references [27, 29] and will not be further discussed here. From the point of view of catalysis, the aim of this work was to obtain realistic models of

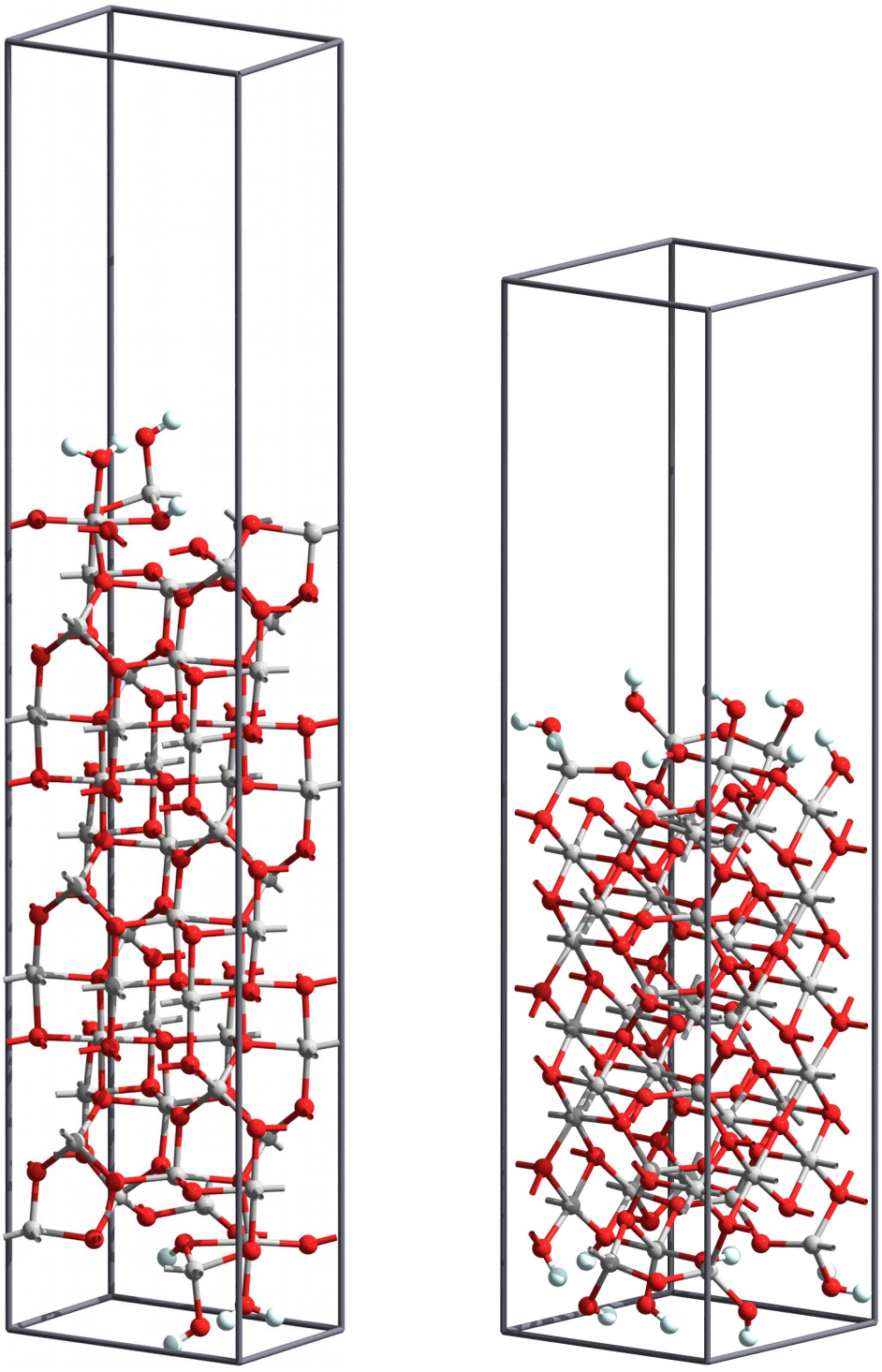

(001) (100)

**Figure 3.12:** Pictorial view of the (001) and (100) hydroxylated $\gamma$-$Al_2O_3$ surfaces after the geometrical optimisation performed at the plane-wave PBE level of theory. The (001) surface model contains 132 atoms, and the (100) surface model contains 144 atoms.

hydroxylated alumina surfaces to be used to study the metal-support interaction. A pictorial view of the minimum-energy structures obtained for the (001) and (100) $\gamma$-alumina surfaces is given in Figure 3.12.

## 3.2 Molecular Mechanics (MM) Simulations

The calculations presented in this section were performed at the MM level of theory, using the core-shell approximation, as implemented in the program *Gulp* [127]. In this method, interatomic potentials are used to model the interactions between ions in the molecular system considered. This method has been applied to study a great variety of materials, ranging from biological systems and organic molecules, to metal oxides and defective crystals. The family of transition aluminas in particular has been the subject of a huge number of studies in the past 40 years, resulting in several published potential libraries which are available for use. The results presented in Tables 3.4 and 3.5 show the capability of these force fields to reproduce the structural properties of both $\alpha$ and $\gamma$ alumina.

### 3.2.1 Simulation Parameters

Several force fields published in the literature were used to optimise the bulk structure of different aluminium oxides and hydroxides. The aim was to select a force field able of reproducing the structural and electrostatic features of hydroxylated $\gamma$-alumina surfaces to be used for hybrid QM/MM calculations. The collection of force fields that comes with the program *Gulp*, as well as others taken from the database of published interatomic potential parameters[2], were used to optimise the bulk structure of corundum and $\gamma$-alumina.

For corundum, very good agreement between the experimental and computed structure was found using the potentials proposed by Grimes (1999), Streitz and Mintmire

[2]Website: *http://www.dfrl.ucl.ac.uk/Potentials/*

| *Potential library*[1] | $a$ (Å) | $c$ (Å) | $V_0$ (Å$^3$) |
|---|---|---|---|
| Grimes (1999) | 4.81305 | 12.72738 | 255.335 |
| Catlow (1992) | 4.78796 | 12.49673 | 248.100 |
| Bush (1994) | 4.82006 | 13.01165 | 261.798 |
| Bush-modified[2] | 4.83065 | 12.93743 | 261.451 |
| Streitz and Mintmire (1994) | 4.74550 | 13.00733 | 253.678 |
| Gale (2005)[3] | 5.10027 | 13.43181 | 302.588 |
| Baram (1996) | 4.77925 | 12.56377 | 248.525 |
| Sauer (1997) | 4.79651 | 12.69413 | 252.921 |
| Binks (1994) | 4.81306 | 12.72797 | 255.348 |
| Maglia (2008)[4] | 4.97137 | 13.11363 | 280.676 |
| Sun (2006)[5] | 4.77268 | 12.99000 | 256.250 |
| De Leeuw and Parker (1999)[6] | 4.81765 | 12.68044 | 254.879 |
| *Experimental* [167] | 4.7540(5) | 12.9820(6) | 254.09(6) |
| *Reference*[7] | 4.80853 | 13.12546 | 262.827 |

[1] Potential libraries taken from the Database of Published Interatomic Potential Parameters website *http://www.dfrl.ucl.ac.uk/Potentials/*, unless otherwise specified.
[2] Three-body potential taken from Catlow's library.
[3] From "Handbook of Materials Modelling" [193].
[4] From reference [22].
[5] From reference [177].
[6] From reference [194].
[7] Reference structure of $\alpha$-$Al_2O_3$ optimised in this thesis work at the plane-wave/DFT level of theory.

**Table 3.4:** Computed cell parameters for the $\alpha$-$Al_2O_3$ unit cell in the hexagonal representation.

(1994), Sauer (1997) and Binks (1994) and De Leeuw and Parker (1999) [194–196]. For $\gamma$-alumina, good agreement (in terms of calculated lattice parameters) was also found using these potentials. However, the lattice vectors computed with these potentials are in general bigger compared to the lattice vectors of the reference structure. This effect is compensated with an expansion of the lattice angle $\beta$. For this reason, a more realistic structure is the one obtained using the Bush potential modified by adding the three-body potential taken from the Catlow force field.

The simulation of $\gamma$-$Al_2O_3$ surfaces using a shell-model presents more difficulties

| *Potential library* | $a$ (Å) | $b$ (Å) | $c$ (Å) | $\beta$ (deg.) | $V_0$ (Å$^3$) |
|---|---|---|---|---|---|
| Grimes (1999) | 5.5481 | 8.4205 | 8.1182 | 92.66 | 378.85 |
| Catlow (1992) | 5.5328 | 8.3757 | 7.9667 | 92.40 | 368.86 |
| Bush (1994) | 7.6610 | 9.4875 | 7.3123 | 81.30 | 525.38 |
| Bush-modified | 5.6917 | 8.5493 | 7.9796 | 90.27 | 388.29 |
| Streitz and Mintmire (1994) | 5.5684 | 8.4266 | 8.0186 | 91.99 | 376.03 |
| Gale (2005) | 5.8930 | 8.9430 | 8.5834 | 93.21 | 451.64 |
| Baram (1996) | 5.5058 | 8.3672 | 8.0309 | 92.57 | 369.60 |
| Sauer (1997) | 5.5386 | 8.4568 | 8.1098 | 92.43 | 379.51 |
| Binks (1994) | 5.5483 | 8.4208 | 8.1182 | 92.66 | 378.88 |
| Maglia (2008) | 5.7311 | 8.6701 | 8.0240 | 92.01 | 398.46 |
| Sun (2006) | 7.6734 | 9.2158 | 7.7187 | 88.37 | 545.61 |
| De Leeuw and Parker (1999) | 5.5385 | 8.4434 | 8.0567 | 92.66 | 376.35 |
| *Reference*[1] | 5.5853 | 8.4100 | 8.0689 | 90.59 | 379.20 |

[1] Reference structure of $\gamma$-$Al_2O_3$ optimised in this thesis work at the plane-wave/DFT level of theory.

**Table 3.5:** Computed cell parameters for the $\gamma$-$Al_2O_3$ unit cell obtained using different force fields.

compared with those of the bulk structures, because additional potential terms are needed to account for the interaction of water molecules adsorbed on metal oxide surfaces. Also, surface atoms experience a different potential compared to bulk atoms. The force field proposed by De Leeuw and Parker (DLP) [194] was designed to study the chemisorption and physisorption of water molecules on $\alpha$-alumina surfaces, and appeared to be the most obvious choice for the study of hydroxylated $\gamma$-alumina surfaces. Figure 3.13 shows the different atom types present in (001) and (100) $\gamma$-alumina surfaces. Oxygen atoms belonging to the bulk structure are designed as *O1*, oxygen atoms from hydroxyl groups are designed as *O2* and oxygen atoms from water molecules are designed as *O3*. Tetrahedrally coordinated aluminium atoms on the (100) surface are designed as *Al2*.

The original DLP force field was modified [197] in order to be used with the program *Gulp*, and used to optimise the structure of an aluminium oxide hydroxide ($AlO(OH)$, or diaspore) in order to test the Al–OH and O–OH interactions, as performed in the

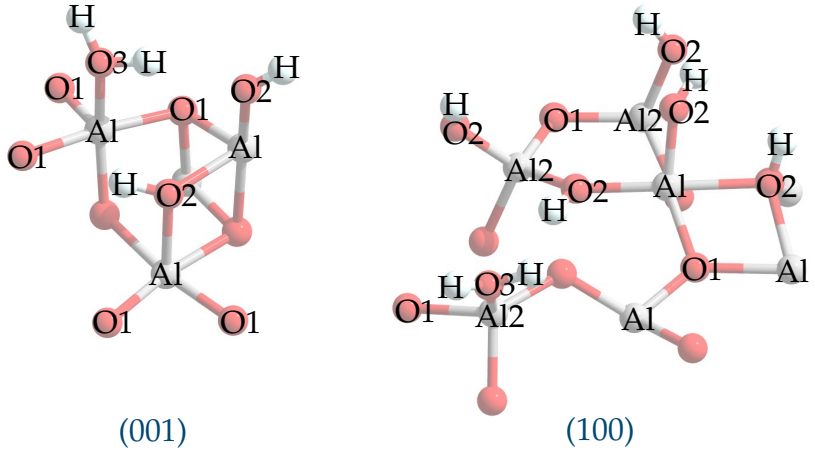


**Figure 3.13:** Definition of atom types in the *modified* DLP force field.

original paper from which the force field has been taken [194]. Two additional terms were added to the Buckingham potential in order to account for the long-range repulsion between the hydrogen atoms and the bulk oxygen atoms, and between hydrogen atoms. The potential parameters were fitted with the program *Gulp* on the experimental structure of diaspore. The resulting potential parameters used in this work are listed in Table 3.6.

The slab models for the (001) and (100) planes were built using the program *Gdis* [160], following the same methodology described for the simulation of surfaces at the plane-wave/DFT level of theory. The positions of adsorbed water molecules and hydroxyl groups in the initial configurations were chosen according to the DFT structures. The optimisation of the hydroxylated surfaces was achieved in about 1000 steps, and convergence problems were experienced for the (100) surface. In this case, the analysis of the computed trajectory revealed a mispositioning of the surface hydroxyl groups coordinated to tetrahedral aluminium atoms. To solve this problem, a three-body potential whose parameters were fitted to reproduce the structures obtained at the plane-wave/DFT level of theory was used for tetrahedrally coordinated surface aluminium atoms (Table 3.7). With this included, the geometrical optimisation of the hydroxylated (100) surface was achieved.

| Ion or ion pair | Parameters and values | | | | |
|---|---|---|---|---|---|
| | | *Core-shell model* | | | |
| | core | shell | $K_2$ (eVÅ$^{-2}$) | | |
| Al | 3.00 | – | – | | |
| H | 0.40 | – | – | | |
| O1 (*oxide*) | 1.00 | -3.00 | 60.78 | | |
| O2 (*hydroxide*) | 0.90 | -2.30 | 74.92 | | |
| O3 (*water*) | 1.25 | -2.05 | 209.449602 | | |
| | | *Buckingham potential* | | | |
| | A (eV) | $\rho$ (Å) | C (eVÅ$^6$) | $r_{min}$ | $r_{max}$ |
| $Al_{core}$-$O1_{shell}$ | 1474.40 | 0.30060 | 0.00 | 0.0 | 16.0 |
| $Al_{core}$-$O2_{shell}$ | 1032.08 | 0.30060 | 0.00 | 0.0 | 16.0 |
| $Al_{core}$-$O3_{shell}$ | 590.04 | 0.30060 | 0.00 | 0.0 | 16.0 |
| $O1_{shell}$-$O1_{shell}$ | 22764.00 | 0.14900 | 27.88 | 0.0 | 16.0 |
| $O1_{shell}$-$O2_{shell}$ | 22764.00 | 0.14900 | 13.94 | 0.0 | 16.0 |
| $O1_{shell}$-$O3_{shell}$ | 22764.00 | 0.14900 | 28.92 | 0.0 | 16.0 |
| $O2_{shell}$-$O2_{shell}$ | 22764.00 | 0.14900 | 6.97 | 0.0 | 16.0 |
| $O2_{shell}$-$O3_{shell}$ | 22764.00 | 0.14900 | 8.12 | 0.0 | 16.0 |
| $H_{core}$-$O1_{shell}$ | 353.73 | 0.24700 | 0.49 | 0.0 | 20.0 |
| $H_{core}$-$O2_{shell}$ | 311.97 | 0.25000 | 0.00 | 1.2 | 20.0 |
| $H_{core}$-$O3_{shell}$ | 396.27 | 0.25000 | 10.00 | 1.2 | 20.0 |
| $H_{core}$-$H_{core}$ | 1126.07 | 0.25200 | 32.86 | 1.7 | 20.0 |
| | | *Lennard-Jones potential* | | | |
| | A (eVÅ$^{12}$) | B (eVÅ$^6$) | $r_{min}$ | $r_{max}$ | |
| $O3_{shell}$-$O3_{shell}$ | 39344.98 | 42.15 | 0.0 | 20.0 | |
| | | *Morse potential* | | | |
| | $D_e$ (eV) | $\alpha$ (Å$^{-1}$) | $r_0$ (Å) | $r_{min}$ | $r_{max}$ |
| $H_{core}$-$O2_{shell}$ | 7.052500 | 3.17490 | 0.94285 | 0.0 | 1.2 |
| $H_{core}$-$O3_{shell}$ | 6.203713 | 2.22003 | 0.92376 | 0.0 | 1.2 |
| | | *Coulomb subtraction* | | | |
| | Scale | $r_{min}$ | $r_{max}$ | | |
| $H_{core}$-$O2_{shell}$ | 0.5 | 0.0 | 1.2 | | |
| $H_{core}$-$O3_{shell}$ | 0.5 | 0.0 | 1.2 | | |
| $H_{core}$-$H_{core}$ | 0.5 | 0.0 | 1.7 | | |
| | | *Three-body potential* | | | |
| | K (eV$rad^{-2}$) | $\Theta_0$ ($deg$) | $r_{max}^{(1-2)}$ | $r_{max}^{(1-3)}$ | $r_{max}^{(2-3)}$ |
| $O3_{shell}$-$H_{core}$-$H_{core}$ | 4.19978 | 108.69 | 1.2 | 1.2 | 1.7 |

**Table 3.6:** Interatomic potential parameters used in this work, adapted from De Leeuw and Parker [194]. Cut-off radii are given in Å. The core-shell model is defined in Section 2.4.3, and the atom types are defined in Figure 3.13.

| Ion pair | | Parameters and values | | | |
|---|---|---|---|---|---|
| | | *Core-shell model* | | | |
| | core | shell | $K_2$ (eVÅ$^{-2}$) | | |
| Al2 | 3.00 | – | – | | |
| | | *Buckingham potential* | | | |
| | A (eV) | $\rho$ (Å) | C (eVÅ$^6$) | $r_{min}$ | $r_{max}$ |
| Al2$_{core}$-O1$_{shell}$ | 1474.40 | 0.30060 | 0.00 | 0.0 | 16.0 |
| Al2$_{core}$-O2$_{shell}$ | 1032.08 | 0.30060 | 0.00 | 0.0 | 16.0 |
| Al2$_{core}$-O3$_{shell}$ | 590.04 | 0.30060 | 0.00 | 0.0 | 16.0 |
| | | *Three-body potential* | | | |
| | K (eV$rad^{-2}$) | $\Theta_0$ ($deg$) | $r_{max}^{(1-2)}$ | $r_{max}^{(1-3)}$ | $r_{max}^{(2-3)}$ |
| Al2$_{core}$-O1$_{shell}$-O1$_{shell}$ | 6.24339 | 119.658 | 2.1 | 2.1 | 4.5 |
| Al2$_{core}$-O1$_{shell}$-O2$_{shell}$ | 6.24339 | 119.658 | 2.1 | 2.1 | 4.5 |
| Al2$_{core}$-O1$_{shell}$-O3$_{shell}$ | 6.24339 | 119.658 | 2.1 | 2.1 | 4.5 |

**Table 3.7:** Additional potential terms used to assure a tetrahedral coordination for surface aluminium atoms coordinated to hydroxyl groups on the (100) surface. The potential parameters of the Buckingham potential are identical to those of bulk aluminium atoms, where the parameters of the three-body potential have been fitted on the reference structure of $\gamma$-alumina.

### 3.2.2 Computed Structures

The modified DLP force field was employed to optimise the bulk structure of diaspore, corundum and $\gamma$-alumina, giving in all cases good agreement with experimental unit cells and the results of analogous optimisations performed at the plane-wave/DFT level of theory.

The structure of diaspore is orthorhombic, it belongs to the space group $Pbnm$ and has the following experimental lattice constants: $a = 4.4010$ Å, $b = 9.4210$ Å, $c = 2.8450$ Å, and $\alpha = \beta = \gamma = 90\,^{\circ}$[198]. The zero-pressure unit cell optimised using the modified DLP force field is in good agreement with the experimental structure, as shown in Table 3.8. A pictorial view of the optimised unit cell is shown in Figure 3.14.

The calculated primitive cell volumes of corundum and $\gamma$-alumina also are in agreement with the reference structures optimised at the plane-wave/DFT level of theory. The rhombohedral unit cell of corundum has a volume of $84.960$ Å$^3$ (cell volume of the

| | Molecular Mechanics | | | | Reference | | | |
|---|---|---|---|---|---|---|---|---|
| | $a$ | $b$ | $c$ | $V_0$ | $a$ | $b$ | $c$ | $V_0$ |
| *Diaspore* | 4.4440 | 9.1141 | 2.9510 | 119.52 | 4.4010 | 9.4210 | 2.8450 | 117.96 |
| *Corundum* | 5.0599 | 5.0599 | 5.0599 | 84.960 | 5.1816 | 5.1816 | 5.1816 | 87.609 |
| *$\gamma$-Alumina* | 5.5386 | 8.4435 | 8.0569 | 376.37 | 5.5853 | 8.4100 | 8.0689 | 379.20 |

**Table 3.8:** Lattice parameters (in Å) and zero-pressure unit cell volumes (in Å$^3$) computed at the MM level of theory using the DLP force field. Reference structures from plane-wave/DFT calculations were obtained in this thesis work, except for diaspore (experimental structure taken from ref. [198]).

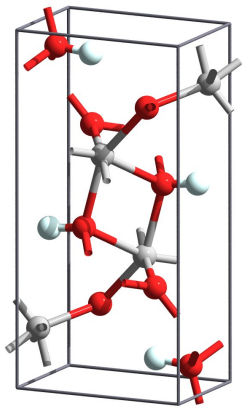

**Figure 3.14:** Structure of diaspore optimised using the force field from De Leew and Parker.

reference structure is $87.609$ Å$^3$) and the unit cell of $\gamma$-alumina has a volume of $376.355$ Å$^3$ (cell volume of the reference structure is $379.20$ Å$^3$). These results prove that structural properties computed with the DLP force field are in good agreement both with the experimental data and with DFT results. A summary of the lattice parameters computed for bulk structures is given in Table 3.8.

The bulk modulus of corundum and $\gamma$-alumina was determined by fitting the Birch-Murnagham equation of state (3.1) to a $PV$ data-set obtained by optimising the unit cell structure in a range of pressures from 0 to $250$ GPa. The data-sets and the fitted curves for the two systems are shown in Figures 3.15 and 3.16. The calculated bulk modulus of $\alpha$-$Al_2O_3$ is $333.9 \pm 0.7$ GPa, and the bulk modulus of $\gamma$-$Al_2O_3$ is $182 \pm 8$ GPa. These values are higher than the corresponding values computed at the DFT level of theory,

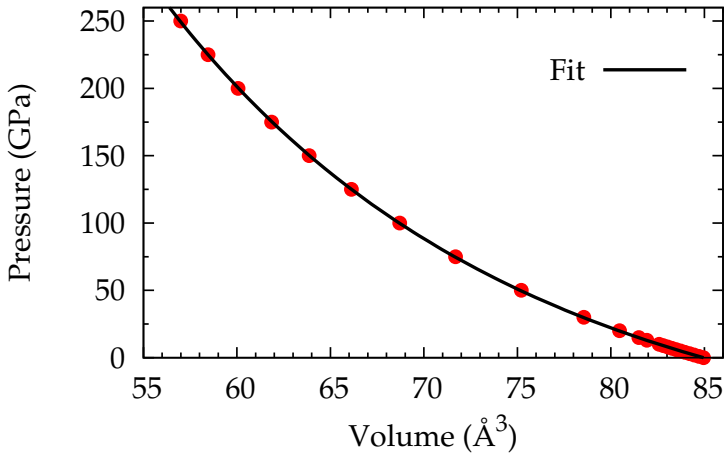


**Figure 3.15:** Calculated cell volume at different pressures and fitted Birch-Murnagham equation of state for $\alpha$-$Al_2O_3$ (corundum).

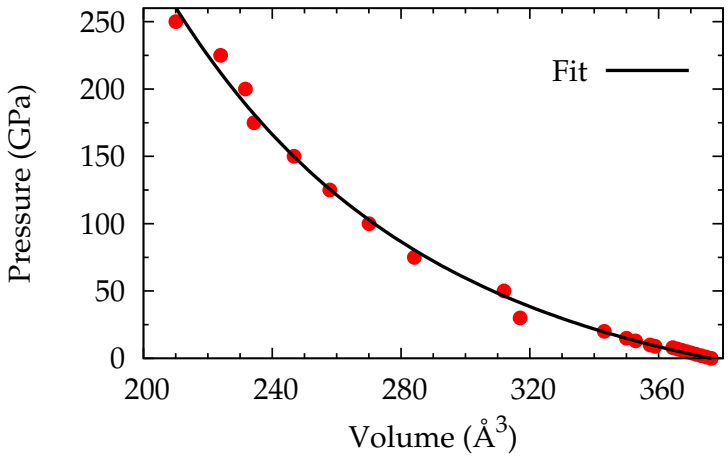


**Figure 3.16:** Calculated cell volume at different pressures and fitted Birch-Murnagham equation of state for $\gamma$-$Al_2O_3$.

but nevertheless they are in agreement with the experimental values.

The structures of hydroxylated (001) and (100) $\gamma$-$Al_2O_3$ surfaces were successfully optimised using the DLP force field. As stated in the previous section, tetrahedally coordinated aluminium atoms on the (100) surface had to be considered with an additional three-body potential (Table 3.7) in order to maintain their coordination geometry. Using these settings the position of surface atoms was relaxed until convergence of the

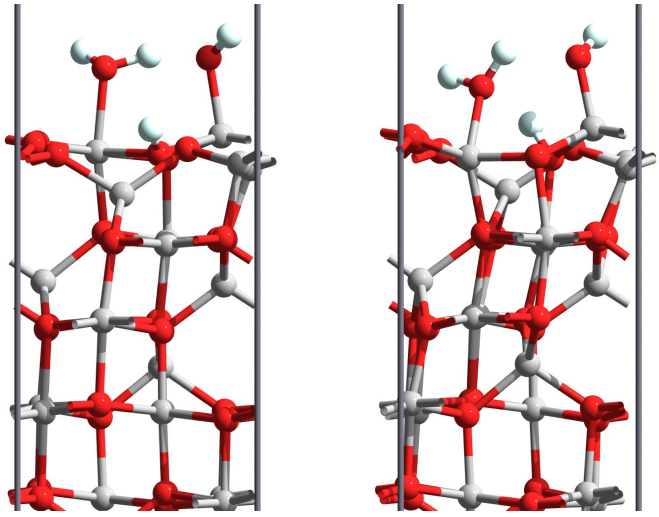

(a) (b)

**Figure 3.17:** Comparison between the structures of the hydroxylated (001) $\gamma$-*alumina* plane computed at the plane-wave/DFT level of theory (a) and at the molecular mechanics level of theory (b).

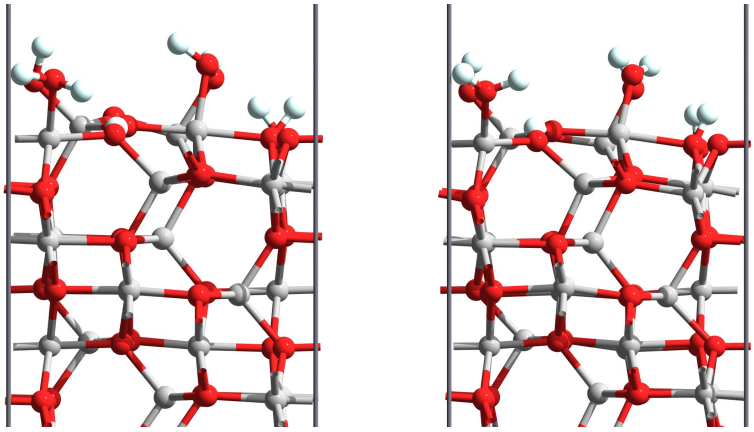

(a) (b)

**Figure 3.18:** Comparison between the structures of the hydroxylated (100) $\gamma$-*alumina* plane computed at the plane-wave/DFT level of theory (a) and at the molecular mechanics level of theory (b).

total energy was reached. Both surfaces retained their bulk coordination while the surface atoms experienced a re-organisation of their positions.

The overall structure of hydroxylated surfaces is well reproduced using interatomic potentials. A graphical comparison between the morphology of (001) and (100) sur-

faces optimised at the DFT and MM level of theory is presented in Figures 3.17 and 3.18. Small differences in the position of bulk atoms are due to the difference between the cell angle $\beta$ of the primitive unit cell in the reference structure and in the MM structure. Also, surface hydroxyl groups are oriented in a different way in the MM structures. However, compared to DFT simulations, the MM approximation has a major advantage in terms of computational cost. As an example the geometrical optimisation of the (001) surface, performed at the plane-wave/DFT level of theory on a cluster of *Silicon Graphics Altix 4700* servers with 1.6GHz Montecito Itanium2 processors (24 cores used), took about 10000 CPU hours of computing time. The geometrical optimisation of the same surface computed at the MM level of theory took about 1 hour of computing time on a desktop workstation. Thus this method appears to be an attractive alternative for a cheap estimation of the structural properties of complex systems such as hydroxylated $\gamma$-$Al_2O_3$ surfaces.

## 3.3 Conclusions

The structure of the hydroxylated (001) and (100) surfaces of $\gamma$-alumina were simulated at the plane-wave/DFT and MM levels of theory. The two theoretical methods were first applied to compute the structural properties (zero-pressure lattice parameters and bulk modulii) of corundum, $\gamma$-alumina and diaspore. The results obtained at the plane-wave/DFT level of theory are in good agreement with the experimental evidence and results of similar published calculations. The results obtained at the MM level of theory are consistent with DFT calculations and have the major advantage of being computationally inexpensive.

For high-quality DFT calculations, the simulation parameters were determined to assure complete convergence of the computed results, and to give the best compromise between accuracy and computational cost. The determination of such parameters was performed for the bulk corundum and $\gamma$-alumina systems. The set of simulation parameters that gives the best compromise in terms of quality of calculations and com-

putational cost was used in all the simulations presented in this thesis work.

The structures of hydroxylated $\gamma$-alumina surfaces computed in this thesis work are in agreement with the theoretical results of Digne and co-workers [27, 29]. This model of surfaces has been shown to reproduce the experimental chemical and physical properties of hydroxylated $\gamma$-alumina surfaces at 500K, and is therefore reliable for the simulation of supported rhodium catalysts under operating conditions.

For MM calculations, a force field taken from the published literature [194–196] was used to study hydroxylated $\gamma$-alumina surfaces. This force field was first validated by determining the lattice parameters and structural properties of corundum, $\gamma$-alumina and diaspore, and then applied for the geometrical optimisation of hydroxylated $\gamma$-alumina surfaces. The resulting models of surfaces were found to have a morphology similar to the ones obtained using electronic structure methods.

The structural models of hydroxylated $\gamma$-alumina surfaces will be used in Chapter 5 to study the chemisorption of supported $\mathrm{Rh^{I}(CO)_2}$ species at the plane-wave/DFT level of theory and at the QM/MM level of theory using the modified DLP force field described in this Chapter.

CHAPTER 4

# CALCULATIONS ON RHODIUM COMPOUNDS

In this chapter electronic structure methods have been applied to study small rhodium complexes, whose structures and properties have been previously characterized either experimentally or theoretically. The aim was to test different theoretical methods and to select a method that gives the best agreement with the results published in literature, at an affordable computational cost.

As soon as computational resources made it possible for research groups to carry out accurate *ab-initio* calculations, the use of theoretical methods quickly became a essential tool to interpret the results of experimental determinations and to make predictions. In 1988, McKee and Worley studied isolated Rh-carbonyl species at the HF level of theory in order to gain information on CO surface species adsorbed on supported rhodium catalysts [199]. Two years later, Barnes and co-workers presented a systematic theoretical study of the first- and second-row transition-metal mono- and dicarbonyl positive ions performed with the size-consistent modified coupled pair functional [200], and in 1994 Dai and Balasubramanian used a multi-configurational approach to compute potential energy surfaces for Rh-CO and Rh-OC interactions [201]. The role of the rhodium basis set was first investigated by Couty and co-workers in 1996 by calculating the exothermicity of the oxidative addition of methane to (cyclopentadienyl)rhodium carbonyl at the MP3, MP4 and QCISD levels of theory, using different basis sets with an increasing number of basis functions [202]. Following these studies,

in 1997 McKee and Worley presented a new study of the interaction of rhodium with dinitrogen and carbon monoxide performed at the B3LYP level of theory, where a split-valence triple-$\zeta$ (TZ) quality basis was used for all the atoms and a ECP [6s5p3d] basis set was used for rhodium [203]. Similar computations were performed for rhodium mono-carbonyl species and the computed results were compared with evidence from infrared spectra of $\mathrm{RhCO^+}$, $\mathrm{RhCO}$, and $\mathrm{RhCO^-}$ in solid neon [56]. In 1999 a comparison between experimental and computed quantities were made for the optical absorption spectrum of the octahedral $\mathrm{RhCl_6^{3-}}$ complex, investigated at the CASSCF level, followed by a second-order perturbation correlation treatment CASPT2 [204]. In 2001 the vibrational spectrum and structure of *cis*-$\mathrm{Rh(NH_3)(CO)_2Cl}$ were investigated at the BLYP/6-311G** level of theory, using an ECP [6s5p3d] basis set for rhodium [205], and in 2003 the ionisation and fragmentation of $\mathrm{[RhCl(PF_3)_2]_2}$ was investigated at the DFT/VTZ level of theory [206].

In the recent literature, the combination of DFT and ECP basis sets has been successfully applied to compute 0°K structures and vibrational spectra of many rhodium complexes [207–209]. In particular, Stevens and co-workers showed that DFT is a viable method to describe the rhodium-ligand bond when the system under investigation can be represented as a single electronic configuration but it fails to produce quantitative agreement with the experimental evidence when the molecule has a strong multi-configurational character [209]. A great variety of density functionals has been developed to reproduce specific thermodynamic properties and to give accurate molecular geometries. Truhlar and co-workers have presented a systematic assessment of density functional methods applied to transition-metal chemistry, giving guidelines as to which functional is best suited to study a specific problem [210, 211].

From this literature survey, it was decided to test a selection of density functionals and post-HF methods on small rhodium complexes in this work. The results of these calculations are presented in the first part of this chapter. Plane-wave/DFT calculations, with periodic boundary conditions applied, have been used to study the same rhodium complexes and the results compared with reference theoretical determina-

tions; this is described in section 4.3 of this chapter.

## 4.1 Basis Set Design

to The choice of basis set is of fundamental importance to high-quality calculations. Wavefunction based theoretical methods such as MP$n$, CI and CC are very sensitive to the quality and size of the basis set because a good representation of the atomic wavefunction requires an adequate number of basis functions of different types. Basis sets which use effective core potentials (ECP) to describe the core electons are based on the assumption that the chemical properties of an element depend mainly on the valence electrons; therefore the exclusion of the core electrons and their representation via a pseudopotential does not alter significantly the behavior of the valence electrons. This approximation leads to a reduction of the total number of basis functions needed to describe a many-electron atom, but maintains an adequate representation of the valence electrons. Furthermore, relativistic effects can be included in effective potentials.

At the beginning of this thesis work, a survey of a database containing published gaussian basis sets (the *EMSL Basis Set Exchange* website, https://bse.pnl.gov/bse) revealed that only a few rhodium ECP basis sets were available for use. From these, the Los Alamos ECP basis set [212–214] was used to design new basis sets for the valence electrons of rhodium. The Lanl2DZ basis set is a standard published basis set with double-$\zeta$ (DZ) quality, that uses the Los Alamos ECP (denoted as Lanl2) to describe the 28 core electrons $1s^2 2s^2 2p^6\ 3s^2 3p^6\ 3d^{10}$, and 22 contracted functions for the valence $4s^2 4p^6 4d^8 5s^1$ electrons.

ROHF calculations were performed on the Rh $^4F$ state, with a $4d^8 5s^1$ electronic configuration, using an increasing number of uncontracted basis functions. The MO coefficients computed at this level of theory were then used as contraction coefficients to give a new basis set.

The basis sets obtained with such a procedure were employed to compute ionization energies (IE) and electron affinities (EA) at the unrestricted CCSD(T) level of theory

| Basis Set | Contractions (s/p/d/f) | Basis | IE | EA |
|---|---|---|---|---|
| Lanl2DZ | (3,4,1/3,2,1/3,1) | 22 | 6.7173 | 0.3867 |
| Lanl2DZ+1d1f | (3,4,1/3,2,1/3,1,1/1) | 34 | 7.0173 | 0.6285 |
| Lanl2DZ+2s2p2d2f | (3,4,3x1/3,2,3x1/3,3x1/1,1) | 54 | 7.2972 | 1.0399 |
| Lanl2-[5s4p4d2f] | (11,12,3x1/9,3x1/10,3x1/1,1) | 51 | 7.3275 | 1.0669 |
| Lanl2-[6s4p4d2f] | (11,12,4x1/9,3x1/10,3x1/1,1) | 52 | 7.3376 | 1.0724 |
| Lanl2-[10s8p7d3f2g] | (16,16,8x1/13,7x1/13,6x1/3x1/1,1) | 108 | 7.4671 | 1.1218 |
| *Experimental* | | | 7.4589 | 1.1370 |
| | | | | 1.1429 |

**Table 4.1:** Different ECP basis sets for rhodium. The Rh ionisation enery (IE) and electron affinity (EA), in eV, have been computed at the UCCSD(T) level of theory with Gaussian G03 rev. C.02, neglecting spin-orbit coupling. The experimental IE is from laser spectroscopy [215], and the experimental EAs is from laser photoelectron spectroscopy [216] and laser spectroscopy [217].

with the program *Gaussian* G03 Rev. C.02 [155]. No allowance was made for spin-orbit coupling. The result of these calculations is shown in Table 4.1.

The calculations performed on Rh, $Rh^+$ and $Rh^-$ with the Lanl2DZ basis set gave poor agrement both in terms of IE and EA (see Table 4.1). In particular, the very large error in the EA indicates that diffuse functions are required to describe the expanded orbitals of the $Rh^-$ ion. When two augmented functions (1d 1f) are added to this basis set the relative error decreases from 11% to 6% for the IE and from 195% to 81% for the EA. Further incorporation of diffuse and polarisation functions reduces these figures. The best agreement with the experimental values is obtained using the largest basis set. The errors obtained at the UCCSD(T)/Lanl2-[10s8p7d3f2g] level of theory are of 0.1% for IE and 7.4% for EA (see Table 4.1). In the calculations presented in this work, the Lanl2DZ+1d1f basis set is used for a routine estimations of molecular properties, and the Lanl2-[6s4p4d2f] basis set, composed of 52 basis functions, is used as an augmented-polarised TZ basis set for high-quality calculations.

The basis sets presented in this section, printed in the Gaussian94 format, are shown on Table A.1, section A.3 of the Appendix.

## 4.2 DFT and MP2 Calculations

The Lanl2-[6s4p4d2f] basis set was used to compute minimum energy structures, harmonic vibrational frequencies and relative energies of rhodium mono- and di-carbonyl species at different levels of theory. For all the molecules in this study, different electronic configurations were considererd in order to determine the correct ground state.

### 4.2.1 Rhodium Mono-carbonyl Complexes

Coordinatively unsaturated metal carbonyls have been suggested as active catalyst sites in several processes, particularly for rhodium supported on alumina [55]. Neutral and ionic $\mathrm{RhCO}$ species have been studied theoretically at the DFT level and experimentally by infrared matrix-isolation spectroscopy [55, 56, 218], providing a method to correlate the carbonyl stretching frequency with the oxidation state of the metal centre.

In this thesis work, rhodium mono carbonyl species in different electronic states have been studied at the unrestricted MP2 and B3LYP levels of theory. The Lanl2-[6s4p4d2f] basis set was used for rhodium, and the cc-pVTZ basis set was used for carbon and oxygen.

For $\mathrm{RhCO^-}$ the ground state is found to be a $^1\Sigma^+$ state at both the MP2 and B3LYP levels of theory. For $\mathrm{RhCO}$, the ground state is a $^2\Delta$ state and for $\mathrm{RhCO^+}$ the ground state is found to be a $^3\Delta$ state. These results are in agreement with previous calculations [55, 203]. The relative energies for all the rhodium monocarbonyl species are also consistent with that given in references [55] and [203]. In Table 4.2 the relative energies, $S^2$ values, and geometrical parameters are reported for different electronic states computed at the MP2 and B3LYP level of theory. Not all the states computed at the MP2 level have been obtained at the B3LYP level. The reason is that the use of a DFT method often leads the calculation converging to a more stable state.

For a linear triatomic molecule (Figure 4.1) 4 real frequencies are expected, and 3 real frequencies are expected for a bent structure. When all the computed harmonic vibrational frequencies are real, the electronic state is a minimum in energy. If one or

| Molecule | State | | Relative Energy | Binding Energy | $S^2$ | Geometry (Å, deg) Rh–C | C–O | RhCO | $\nu$(CO)[a] |
|---|---|---|---|---|---|---|---|---|---|
| | | | | MP2 | | | | | |
| $RhCO^+$ | $C_{\infty v}$ | $^1\Sigma^+$ | 11.16977 | 0.63379 | 0.0000 | 1.807 | 1.141 | 180° | 2084.2 |
| $RhCO^+$ | $C_{\infty v}$ | $^3\Delta$ | 10.24426 | -0.29171 | 2.0081 | 1.965 | 1.135 | 180° | 2166.4 |
| RhCO | $C_{\infty v}$ | $^2\Sigma^+$ | 2.29191 | -0.94697 | 0.7555 | 1.774 | 1.168 | 180° | 1955.4 |
| RhCO | $C_{\infty v}$ | $^2\Delta$ | 2.13391 | -1.10498 | 0.7795 | 1.810 | 1.161 | 180° | 2046.3 |
| RhCO | $C_{\infty v}$ | $^2\Pi$ | 3.35138 | 0.11250 | 0.8016 | 1.919 | 1.151 | 180° | 2106.0 |
| $RhCO^-$ | $C_{\infty v}$ | $^1\Sigma^+$ | 0.00000 | -2.50104 | 0.0000 | 1.731 | 1.225 | 180° | 2067.7 |
| $RhCO^-$ | $C_{\infty v}$ | $^3\Sigma^+$ | 1.71062 | -0.79042 | 2.0196 | 1.774 | 1.195 | 180° | 1915.1 |
| $RhCO^-$ | $C_{\infty v}$ | $^3\Pi$ | 2.83240 | 0.33136 | 2.0264 | 1.759 | 1.185 | 180° | 1852.0 |
| | | | | B3LYP | | | | | |
| $RhCO^+$ | $C_{\infty v}$ | $^1\Sigma^+$ | 10.10390 | -0.78694 | 0.0000 | 1.837 | 1.128 | 180° | 2207.1 |
| $RhCO^+$ | $C_{\infty v}$ | $^3\Delta$ | 9.35718 | -1.53367 | 2.0037 | 1.972 | 1.122 | 180° | 2252.6 |
| RhCO | $C_{\infty v}$ | $^2\Sigma^+$ | 1.40982 | -1.76948 | 0.7514 | 1.817 | 1.153 | 180° | 2044.7 |
| RhCO | $C_{\infty v}$ | $^2\Delta$ | 1.35411 | -1.82518 | 0.7557 | 1.841 | 1.148 | 180° | 2085.3 |
| RhCO | $C_s$ | $^4A'$ | 2.82867 | -0.35063 | 3.7585 | 2.033 | 1.146 | 148° | 2026.0 |
| RhCO | $C_{\infty v}$ | $^4\Delta$ | 2.92025 | -0.25905 | 3.7612 | 2.031 | 1.137 | 180° | 2120.3[b] |
| $RhCO^-$ | $C_{\infty v}$ | $^1\Sigma^+$ | 0.00000 | -2.01503 | 0.0000 | 1.746 | 1.181 | 180° | 1887.6 |
| $RhCO^-$ | $C_{\infty v}$ | $^3\Sigma^+$ | 0.77861 | -1.23641 | 2.0043 | 1.833 | 1.171 | 180° | 1914.1 |
| | | | | *Experimental*[c] $\nu$*(CO) (cm*$^{-1}$*)* | | | | | |
| $RhCO^+$ 2174.1 | | | | RhCO 2022.5 | | | | $RhCO^-$ 1828.6 | |

[a] For a minimum energy structure, 4 real frequencies are expected for $C_{\infty v}$ symmetry, and 3 real frequencies are expected for $C_s$ symmetry.
[b] Transition state.
[c] From reference [55].

**Table 4.2:** Electronic states, relative energies (eV), binding energies (eV), expectation value of $S^2$ of the wavefunction, bond lengths, angles and harmonic frequencies ($cm^{-1}$) computed at the MP2 and B3LYP levels of theory.

more vibrational frequencies are imaginary, the electronic state is a transition state.

As shown in Table 4.2, at the B3LYP level the $^4\Delta$ state of RhCO is a transition state, and two doubly degenerate imaginary frequencies are present. The computed geometrical parameters for this state are in agreement with the findings of Mineva et al. [53] who computed the structure at the B3LYP level with the Lanl2DZ basis set for rhodium and 6-311+G* basis sets for carbon and oxygen.

In conclusion, the calculations presented in this thesis work agree well with previ-

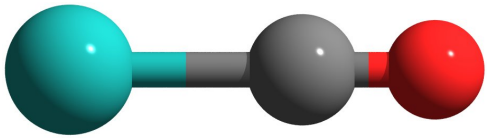

**Figure 4.1:** Computed structure of linear $\mathrm{RhCO}$. The red atom is oxygen, the dark grey atom is carbon and the aquamarine atom is rhodium.

| Molecule | Symm. | State | Relative Energy | $S^2$ | Geometry (Å, deg) Rh–C | C–O | ∠Rh,C,O |
|---|---|---|---|---|---|---|---|
| | | | *McKee and Worley* [203] | | | | |
| $\mathrm{RhCO^+}$ | $C_{\infty v}$ | $^3\Delta$ | 9.34085 | 2.00 | 1.959 | 1.123 | 180° |
| $\mathrm{RhCO}$ | $C_{\infty v}$ | $^2\Sigma$ | 1.42125 | 0.75 | | | 180° |
| $\mathrm{RhCO}$ | $C_{\infty v}$ | $^2\Pi$ | 2.45746 | 0.77 | | | 180° |
| $\mathrm{RhCO}$ | $C_{\infty v}$ | $^2\Delta$ | 1.32356 | 0.76 | 1.832 | 1.148 | 180° |
| $\mathrm{RhCO^-}$ | $C_{\infty v}$ | $^3\Sigma$ | 0.78450 | 2.00 | | | 180° |
| $\mathrm{RhCO^-}$ | $C_{\infty v}$ | $^1\Sigma$ | 0.00000 | 0.00 | 1.740 | 1.181 | 180° |
| | | | *Zhou and Andrews* [55] | | | | |
| $\mathrm{RhCO^+}$ | $C_{\infty v}$ | $^3\Delta$ | 10.021 | - | 1.913 | 1.147 | 180° |
| $\mathrm{RhCO}$ | $C_{\infty v}$ | $^2\Delta$ | 1.613 | - | 1.824 | 1.173 | 180° |
| $\mathrm{RhCO}$ | $C_{\infty v}$ | $^2\Sigma^+$ | 1.583 | - | 1.791 | 1.180 | 180° |
| $\mathrm{RhCO^-}$ | $C_{\infty v}$ | $^1\Sigma^+$ | 0.000 | - | 1.736 | 1.209 | 180° |

**Table 4.3:** Electronic states, relative energies (eV), expectation value of $S^2$ of the wavefunction, bond lengths and angles computed at the B3LYP/ECP level of theory by McKee and Worley [203] (upper panel) and at the BP86/ECP level of theory by Zhou and Andrews [55] (bottom panel).

ous theoretical and experimental determinations published in the literature for these systems. For comparison, a summary of the results presented in the cited works is shown on Table 4.3.

From the literature cited in this chapter and from the calculations performed on rhodium monocarbonyls, DFT calculations with an ECP basis set appeared to be a viable approach to reproduce the chemical properties of rhodium metal complexes. A selection of the density functionals cited in the literature reported in this chapter was used to compare the computed harmonic stretching frequency of CO with the computed Mulliken charge on the metal centre in rhodium monocarbonyl neutral, cation

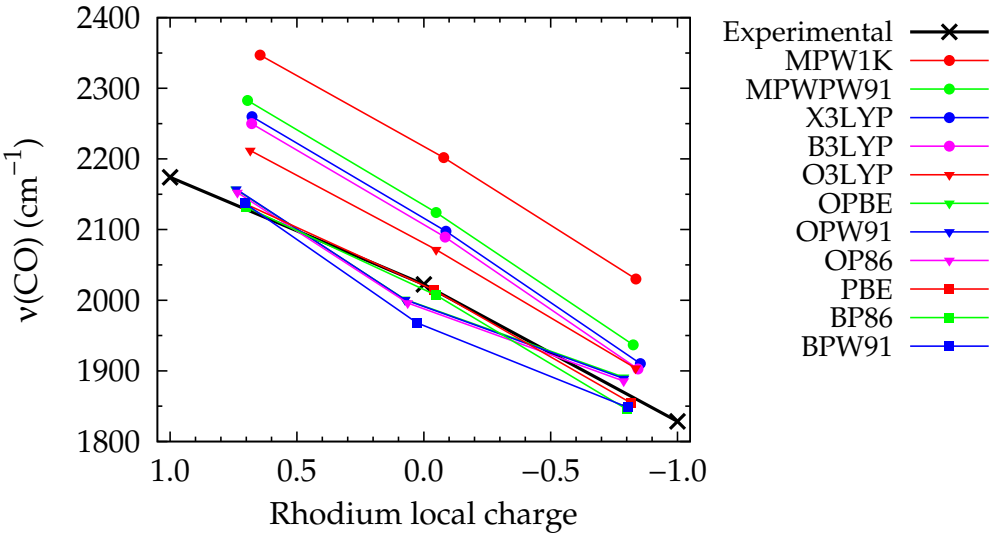


**Figure 4.2:** Plot of experimental $RhCO^+$, $RhCO$ and $RhCO^-$ carbonyl stretching frequencies *vs* net local charge on Rh for each species (black line), assumed to be +1, 0 and -1 [56]. For comparison, Rh Mulliken charges *vs* harmonic frequencies computed at different DFT levels of theory are also plotted. The results obtained with the OPBE, OPW91 and OP86 density functionals are very similar.

and anion. In Figure 4.2 the carbonyl stretching frequencies vs the net local charge on rhodium in $RhCO$ species are reported. The experimental trend shows a clear correlation between the CO stretching frequency and the net charge of the molecular species. As the negative charge increases on the molecule, the $\pi$ back donation from rhodium to carbon monoxide strengthens and the bond order of the ligand decreases. As a consequence, the CO stretching frequency diminishes. This effect is well reproduced for calculations performed at the DFT level of theory, for which the computed carbonyl stretching frequency is plotted as a function of the rhodium atomic Mulliken charge. The functionals that give the best agreement with experimental IR frequencies are the BPW91, BP86, PBE, OPW91, OP86 and OPBE functionals. The results obtained for isolated rhodium monocarbonyl species suggest that the carbonyl stretching frequency can be used to estimate the local charge on $Rh(CO)$ sites in supported catalysts [56]. The implicit assumption is that most of the electronic charge of the molecule is carried by the rhodium atom; therefore a change in the rhodium oxidation state affects

the strength of the metal-carbon bond. In order to support this idea, the electronic densities computed at the B3LYP level were used to display the electrostatic potential around each molecule of $\mathrm{RhCO^+}$, $\mathrm{RhCO}$ and $\mathrm{RhCO^-}$.

The electrostatic potential describes the potential energy associated with a charge distribution at a given position in space. It is defined as the electrostatic energy of a test particle divided by the charge of the particle itself. The unit of the electrostatic potential in molecular orbital calculations is the electronvolt (eV). The electrostatic potential generated by the charge distribution around the $\mathrm{RhCO^+}$, $\mathrm{RhCO}$ and $\mathrm{RhCO^-}$ molecules has been computed with the program *Molekel* [219] and it is displayed in Figure 4.3 as color-coded isosurfaces. To provide a reference, the computed electrostatic potential of carbon monoxide is also shown. The ground state of CO computed at the B3LYP/cc-pVTZ level of theory is a $^1\Sigma^+$ state. The computed Mulliken charges are 0.02707 for oxygen and -0.02707 for carbon; the relative sign of the charges is in agreement with that expected from high-level *ab-initio* calculations [220, 221]. However, calculations performed at the B3LYP/6-311+G* level of theory found the same electronic ground state but a dipole moment with opposite direction.

As shown in Figure 4.3, the rhodium centre carries most of the net electronic charge of the molecule, confirming the relationship between the oxidation state of rhodium and the CO stretching frequency. In $\mathrm{RhCO^+}$, the positive charge is centred mainly on rhodium (blue region) while the negative charge is centred on oxygen. In $\mathrm{RhCO}$, the metal centre shows a neutral charge while the oxygen carries some negative charge. Again, back donation from the metal to CO causes the electron density between carbon and rhodium atoms to increase, and the one between carbon and oxygen atoms to decrease. In $\mathrm{RhCO^-}$, most of the negative charge (red region) is carried by the rhodium atom, whose $d$ orbitals are the main component of the highest occupied MOs.

From this analysis it can be concluded that the variation in the harmonic CO stretching frequency in neutral, cation and anion $\mathrm{RhCO}$ species is indeed correlated to a change in the rhodium oxidation state.

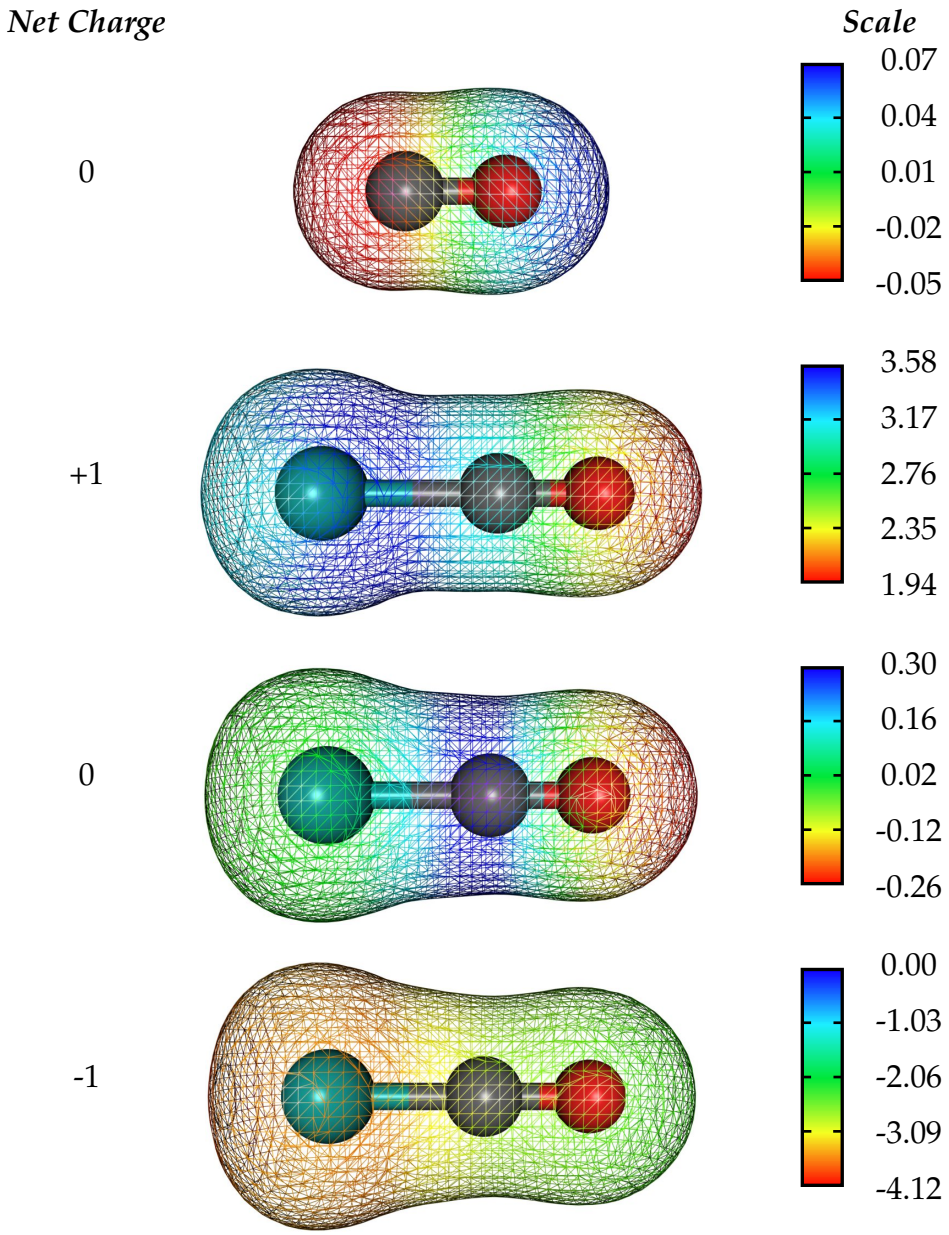


**Figure 4.3:** Colour-coded electrostatic potential isosurfaces of RhCO species computed at the B3LYP/cc-pVTZ level of theory. The electron density on rhodium increases as the net charge of the molecule increases. The program Molekel was used to display the isosurfaces, using a contour value of 0.02 au.

### 4.2.2 Rhodium Di-carbonyl Complexes

Rhodium dicarbonyl species have been investigated previously by several research groups using electronic structure calculations [53, 55, 56, 200, 201, 203].

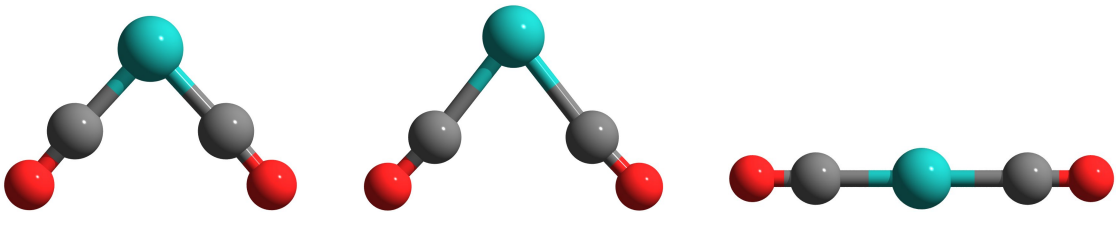


**Figure 4.4:** Computed structures for rhodium dicarbonyl species.

In this thesis work, the ground state of rhodium dicarbonyl neutral, cation and anion have been computed at the MP2 and B3LYP levels of theory using the same basis sets described in the previous section, and the results compared with the results in the literature.

The ground state for $\mathrm{Rh(CO)_2^-}$ is found to be a $^1A_1$ electronic state at both the MP2 and B3LYP levels of theory. The optimised geometry at the B3LYP level for that state is bent with a C-Rh-C angle of 128.8°and a Rh-C-O angle of 163.2°. The optimised geometry at the MP2 level is similar. This result is in agreement with previous DFT calculations [55, 203].

For $\mathrm{Rh(CO)_2}$ the computed ground state at the B3LYP level is a $^2\Delta_g$ state, but it is a $^2B_2$ state at the MP2 level. This result is not in agreement with the calculations of Zhou and Andrews [55] who found the ground state to be a $^2B_2$ state, and the $^2\Delta_g$ state 0.24 eV higher in energy at the BP86 level. Furthermore, the computed geometrical parameters for the $^2B_2$ state computed at the MP2 level differ from those obtained by Zhou and Andrews at the BP86 level for the same state [55]. However, the computed geometrical parameters for the $^2B_2$ state obtained in this present work at the MP2 level are in good agreement with the DFT calculations of McKee and Worley [203] and Mineva et al. [53] for this state.

In this present work, the $^2B_2$ and $^2\Delta_g$ states are found to be very close in energy at both the B3LYP and MP2 levels. At the MP2 level, the $^2B_2$ state has an energy 0.02 eV lower than the $^2\Delta_g$ state. However, the computed wavefunction for the $^2B_2$ state has an high degree of spin contamination which makes the computed energy not reliable.

| Molecule | | State | Relative Energy | Binding Energy | $S^2$ | Geometry (Å, deg.) Rh–C | C–O | CRhC | RhCO | $\nu$(CO)[a] | | Shape [b] |
|---|---|---|---|---|---|---|---|---|---|---|---|---|
| $Rh(CO)_2^+$ | $C_{2v}$ | $^1A_1$ | 11.21580 | -0.63296 | 0.0000 | 1.798 | 1.144 | 83.2 | 178.5 | 2061.4 | 2113.0 | 1 |
| $Rh(CO)_2^+$ | $D_{\infty h}$ | $^1\Sigma_g^+$ | 12.04570 | 0.19693 | 0.0000 | 1.977 | 1.135 | *linear* | | 2125.1 | – | 3 |
| $Rh(CO)_2^+$ | $C_{2v}$ | $^3A_2(b_1^1, b_2^1)$ | 12.23956 | 0.39079 | 2.0153 | 2.058 | 1.134 | 117.1 | 178.9 | 2161.2 | 2187.3 | 1 |
| $Rh(CO)_2^+$ | $C_{2v}$ | $^3B_2(a_1^1, b_2^1)$ | 11.64466 | -0.20410 | 2.0166 | 2.005 | 1.136 | 105.7 | 176.4 | 2137.3 | 2155.5 | 1 |
| $Rh(CO)_2^+$ | $D_{\infty h}$ | $^3\Delta_g(\delta_g^1, \sigma_g^1)$ | 11.22874 | -0.62002 | 2.0088 | 2.021 | 1.134 | *linear* | | 2151.7 | – | 3 |
| $Rh(CO)_2$ | $C_{2v}$ | $^2A_1$ | 4.96266 | 0.41099 | 0.7619 | 1.768 | 1.164 | 75.7 | 172.5 | 1949.2 | 2067.4 | 2 |
| $Rh(CO)_2$ | $C_{2v}$ | $^2A_2$ | 8.17105 | 3.61938 | 0.8813 | 1.864 | 1.178 | 85.3 | 177.8 | 1944.8 | 2351.9[c,d] | 1 |
| $Rh(CO)_2$ | $C_{2v}$ | $^2B_1$ | 5.90332 | 1.35165 | 0.7919 | 1.773 | 1.169 | 82.1 | 178.4 | 2009.3 | 8266.4[c] | 2 |
| $Rh(CO)_2$ | $C_{2v}$ | $^2B_2$ | 3.09063 | -1.46104 | 0.7844 | 1.839 | 1.159 | 97.8 | 170.9 | 1972.4 | 2021.6 | 1 |
| $Rh(CO)_2$ | $D_{\infty h}$ | $^2\Sigma_g^+$ | 3.33964 | -1.21204 | 0.7545 | 1.924 | 1.151 | *linear* | | 1966.7 | – | 3 |
| $Rh(CO)_2$ | $D_{\infty h}$ | $^2\Delta_g$ | 3.10674 | -1.44493 | 0.7674 | 1.933 | 1.149 | *linear* | | 1996.9 | – | 3 |
| $Rh(CO)_2^-$ | $C_{2v}$ | $^1A_1$ | 0.00000 | -3.81383 | 0.0000 | 1.855 | 1.184 | 126.8 | 164.4 | 1870.3 | 1900.1 | 1 |
| $Rh(CO)_2^-$ | $D_{\infty h}$ | $^1\Sigma_g^+$ | 0.55075 | -3.26307 | 0.0000 | 1.897 | 1.175 | *linear* | | 1777.7 | – [d] | 3 |
| $Rh(CO)_2^-$ | $C_{2v}$ | $^3B_2(b_2^1, a_1^1)$ | 2.14012 | -1.67371 | 2.0616 | 1.812 | 1.178 | 94.1 | 174.2 | 1931.3 | 1958.5 | 1 |
| $Rh(CO)_2^-$ | $D_{\infty h}$ | $^3\Sigma_g^+(\sigma_g^1, \sigma_g^1)$ | 3.74106 | -0.07277 | 2.0044 | 1.923 | 1.152 | *linear* | | 1934.7 | – [d] | 3 |

*Experimental*[e] *$\nu$(CO) (cm$^{-1}$)*

$Rh(CO)_2^+$ 2184.7 $Rh(CO)_2$ 2033.2 $Rh(CO)_2^-$ 1902.7, 1813.2

[a] For this molecule, 9 real frequencies are expected for $C_{2v}$ symmetry, and 10 real frequencies are expected for $D_{\infty h}$ symmetry.

[b] The shape of molecule refers to Figure 4.4.

[c] The computed wavefunction has an high spin contamination; the computed frequencies are not reliable.

[d] Transition state.

[e] From reference [55].

**Table 4.4:** Electronic states, relative energies (eV), binding energies (eV), expectation value of $S^2$ of the wavefunction, bond lengths, angles, harmonic frequencies (cm$^{-1}$) and molecule shapes computed at the MP2 level of theory.

| Molecule | | State | Relative Energy | Binding Energy | $S^2$ | Geometry (Å, deg.) Rh–C | C–O | CRhC | RhCO | $\nu$(CO)[a] | | Shape [b] |
|---|---|---|---|---|---|---|---|---|---|---|---|---|
| $Rh(CO)_2^+$ | $C_{2v}$ | $^1A_1$ | 10.29394 | -2.69332 | 0.0000 | 1.861 | 1.127 | 87.3 | 178.1 | 2191.2 | 2241.5 | 1 |
| $Rh(CO)_2^+$ | $D_{\infty h}$ | $^1\Sigma_g^+$ | 10.74153 | -2.24572 | 0.0000 | 1.999 | 1.122 | *linear* | | 2225.8 | – | 3 |
| $Rh(CO)_2^+$ | $C_{2v}$ | $^3B_2(a_1^1, b_2^1)$ | 10.43115 | -2.55610 | 2.0061 | 2.035 | 1.123 | 105.8 | 175.3 | 2225.6 | 2252.7 | 1 |
| $Rh(CO)_2^+$ | $D_{\infty h}$ | $^3\Delta_g(\delta_g^1, \sigma_g^1)$ | 10.13296 | -2.85429 | 2.0044 | 2.056 | 1.120 | *linear* | | 2248.7 | – | 3 |
| $Rh(CO)_2$ | $C_{2v}$ | $^2A_1(a_1^1, b_2^2, b_1^2)$ | 2.19541 | -3.08029 | 0.7548 | 1.944 | 1.142 | 150.4 | 171.7 | 2066.0 | 2107.7 | 1 |
| $Rh(CO)_2$ | $C_{2v}$ | $^2A_1(b_1^2, a_2^2, a_1^1)$ | 3.95759 | -1.31811 | 0.7524 | 1.841 | 1.149 | 82.1 | 170.3 | 2032.5 | 2079.6 | 2 |
| $Rh(CO)_2$ | $C_{2v}$ | $^2B_2$ | 2.24965 | -3.02605 | 0.7565 | 1.888 | 1.146 | 101.5 | 170.3 | 2036.6 | 2094.1 | 1 |
| $Rh(CO)_2$ | $D_{\infty h}$ | $^2\Sigma_g^+$ | 2.21295 | -3.06278 | 0.7516 | 1.954 | 1.139 | *linear* | | 2068.2 | [c] | 3 |
| $Rh(CO)_2$ | $D_{\infty h}$ | $^2\Delta_g$ | 2.16181 | -3.11390 | 0.7553 | 1.964 | 1.137 | *linear* | | 2095.5 | – | 3 |
| $Rh(CO)_2^-$ | $C_{2v}$ | $^1A_1$ | 0.00000 | -4.11143 | 0.0000 | 1.858 | 1.172 | 128.8 | 163.2 | 1872.7 | 1949.3 | 1 |
| $Rh(CO)_2^-$ | $D_{\infty h}$ | $^1\Sigma_g^+$ | 0.38720 | -3.72423 | 0.0000 | 1.905 | 1.160 | *linear* | | 1915.7 | – [c] | 3 |
| $Rh(CO)_2^-$ | $C_{2v}$ | $^3B_2(b_2^1, a_1^1)$ | 1.46295 | -2.64849 | 2.0080 | 1.874 | 1.164 | 100.4 | 176.0 | 1916.2 | 1950.4 | 1 |

*Experimental*[d] *$\nu$(CO) (cm$^{-1}$)*

$Rh(CO)_2^+$ 2184.7 $Rh(CO)_2$ 2033.2 $Rh(CO)_2^-$ 1902.7, 1813.2

[a] For this molecule, 9 real frequencies are expected for $C_{2v}$ symmetry, and 10 real frequencies are expected for $D_{\infty h}$ symmetry.

[b] The shape of molecule refers to Figure 4.4.

[c] Transition state.

[d] From reference [55].

**Table 4.5:** Electronic states, relative energies (eV), binding energies (eV), expectation value of $S^2$ of the wavefunction, bond lengths, angles, harmonic frequencies (cm$^{-1}$) and molecule shapes computed at the B3LYP level of theory.

The same problem has been found for the $^2B_1$ electronic state computed at the MP2 level.

The ground state for $\mathrm{Rh(CO)_2^+}$ is a $^3\Delta_g$ state at the B3LYP level. This result is in agreement with previous DFT calculations[1] [55, 203]. The computed ground state at the MP2 level is a $^1A_1$ state. Nevertheless the $^3\Delta_g$ state computed at this level is just 0.013 eV higher in energy. For $Rh(CO)_2$ and $Rh(CO)_2^+$, the presence of electronic states close in energy suggests that multireference calculations are required to describe accurately the true ground state, and obtain reliable relative energies between states.

The calculation of harmonic vibrational frequencies reveal which states are transition states. For $\mathrm{Rh(CO)_2}$, 9 real frequencies are expected for $C_{2v}$ symmetry and 10 real frequencies are expected for $D_{\infty h}$ symmetry. For a transition state, one or more frequencies will be imaginary. A summary of the results obtained from calculations at the MP2 and B3LYP levels respectively is shown in Tables 4.4 and 4.5.

To conclude, the results of electronic structure calculations carried out on rhodium mono- and di-carbonyl species indicate that a combination of DFT and a TZ quality basis sets such as Lanl2-[6s4p4d2f] produce high-quality results. A detailed analysis of all the possible electronic states for each rhodium species has been carried out, and a good agreement with the published results has been obtained. Comparison with the different results in the literature (*e.g.* the geometrical parameters for the $^2B_2$ state of $\mathrm{Rh(CO)_2^+}$ computed by Zhou and Andrews [55], McKee and Worley [203], and Mineva et al. [53]), shows that the results obtained in this work are closer to the results of calculations performed at the highest level of theory.

### 4.2.3 Rhodium Carbonyl Chloride Complexes

The *cis*-$\mathrm{[Rh(CO)_2Cl_2]^-}$ and $\mathrm{[Rh(CO)_2Cl]_2}$ molecules have been widely studied in the literature as they are precursors of catalytic systems and ideal prototypes for supported $\mathrm{Rh^I(CO)_2Cl}$ species [7, 42, 207, 222, 223]. These molecules are closed shell with a $C_{2v}$

[1] In the cited papers only the $^1A_1$, $^3B_2$ and $^3\Delta_g$ states have been considered.

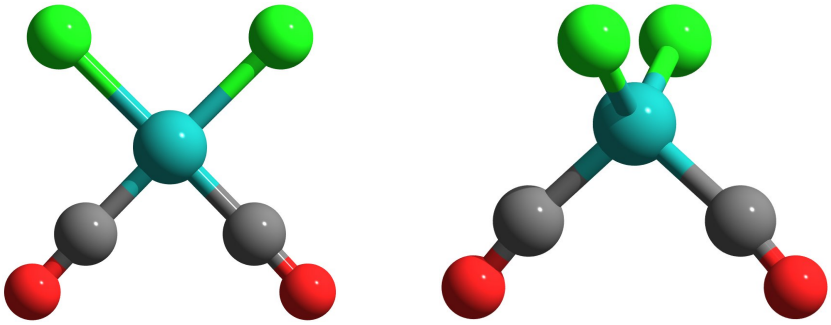

1 2

**Figure 4.5:** Computed structures for the *cis*-$[Rh(CO)_2Cl_2]^-$ anion with $C_{2v}$ symmetry: (1) square-planar, (2) tetrahedral. Red atoms are oxygen, dark grey atoms are carbon, aquamarine atoms are rhodium and green atoms are chlorine.

symmetry for the ground state structures. Calculations were carried out using the computational procedures described in the previous sections, with the only difference being the aug-cc-pVTZ basis set was used for chlorine atoms.

For *cis*-$[Rh(CO)_2Cl_2]^-$, the computed ground state is a $^1A_1$ state at both the MP2 and B3LYP levels of theory, with the rhodium coordinating the ligands in a square planar geometry in the optimised structure. The optimised geometry of the excited $^3B_2$ state is found to be tetrahedral ($T_d$-type) at both levels of theory. A pictorial view of the two different molecular geometries is given in Figure 4.5. These results are in agreement with previous calculations performed at the B3LYP and CCSD(T) levels of theory [222]. A summary of the results is given in Table 4.6. The computed Mulliken charges reveal a significant change in the electronic distribution on the molecule for different geometries and electronic states.

For $[Rh(CO)_2Cl]_2$ (IUPAC name: *di-$\mu$-chloro-bis[dicarbonyl-rhodium(I)]*), the computed ground state is a $C_{2v}$ $^1A_1$ state at both the MP2 and B3LYP levels of theory, in agreement with previous theoretical determinations [207, 223]. The first excited state is found to be a $D_{2h}$ $^3B_{3g}$ state at both the MP2 and B3LYP levels of theory. Relative energies and Mulliken atomic charges computed for different electronic states of this molecule are shown on Table 4.7. For this molecule the calculation of frequencies at the MP2 level of theory was not performed because of their high computational

| Sym. | State | Relative Energy | $S^2$ | Mulliken atomic charges Rh | Cl | C | O | $im.$[a] | Shape[b] |
|---|---|---|---|---|---|---|---|---|---|
| | | | | MP2 | | | | | |
| $C_{2v}$ | $^1A_1$ | 0.00000 | 0.00000 | 1.764 | -1.031 | -0.063 | -0.288 | 0 | 1 |
| $C_{2v}$ | $^1A_1$ | 1.51234 | 0.00000 | 0.744 | -0.762 | 0.205 | -0.315 | 1 | 2 |
| $C_{2v}$ | $^3B_2$ | 3.39944 | 2.04981 | 1.570 | -0.969 | -0.070 | -0.246 | 4 | 1 |
| $C_{2v}$ | $^3B_2$ | 2.27352 | 2.04216 | 1.102 | -0.858 | -0.076 | -0.269 | 0 | 2 |
| | | | | B3LYP | | | | | |
| $C_{2v}$ | $^1A_1$ | 0.00000 | 0.00000 | 1.194 | -0.909 | -0.043 | -0.145 | 0 | 1 |
| $C_{2v}$ | $^1A_1$ | 1.42211 | 0.00000 | 0.248 | -0.667 | 0.232 | -0.189 | 1 | 2 |
| $C_{2v}$ | $^3B_2$ | 2.35882 | 2.01289 | 1.102 | -0.832 | -0.153 | -0.066 | 4 | 1 |
| $C_{2v}$ | $^3B_2$ | 1.35823 | 2.01093 | 0.818 | -0.771 | -0.022 | -0.116 | 0 | 2 |

[a] Number of computed imaginary frequencies. For this molecule, 15 real frequencies are expected.
[b] The shape of molecule refers to Fig. 4.5.

**Table 4.6:** Results of MP2 and B3LYP calculations for *cis*-$[\mathrm{Rh(CO)_2Cl_2}]^-$. Relative energies (eV), electronic states, Mulliken atomic charges, and computed frequencies are shown.

cost. Instead, a systematic study was carried out on the ground-state by computing minimum energy geometries and harmonic frequencies with some of the density functionals listed in Figure 4.2. Among the functionals cited in this work, the BP86 functional has been reported to give reliable bond distances, vibrational frequencies, and dipole moments for rhodium complexes [55, 209, 224]. Furthermore, functionals with Handy's optimised exchange (denoted with the prefix *O*) [225] have been reported to give accurate geometries and energies for different spin states of organometallic complexes [226–228]. The calculations presented in this section were therefore performed using the B3LYP, BPW91, BP86, O3LYP, OPW91, OP86, BB1K and PBE density functionals.

The results of calculations performed at the B3LYP, OP86 and PBE levels of theory are shown on Table 4.8. The computed ground-state structural parameters are close to the parameters determined experimentally by X-ray diffraction. Small differences in the $\theta$ (Rh,Cl,Cl,Rh) dihedral angle and consequently the distance between rhodium atoms is due to the fact that the calculations are performed on the isolated molecule,

| Sym. | State | Relative Energy | $S^2$ | Mulliken atomic charges Rh | Cl | C | O | $im.$[a] |
|---|---|---|---|---|---|---|---|---|
| | | | MP2 | | | | | |
| $C_{2v}$ | $^1A_1$ | 0.00000 | 0.00000 | 1.698 | -0.850 | -0.250 | -0.174 | – |
| $D_{2h}$ | $^1A_g$ | 0.33697 | 0.00000 | 1.775 | -0.959 | -0.230 | -0.178 | – |
| $C_{2v}$ | $^3B_2$ | 3.06573 | 2.04684 | 1.370 | -0.818 | -0.132 | -0.144 | – |
| $D_{2h}$ | $^3B_{3g}$ | 1.73137 | 2.17518 | 1.743 | -0.868 | -0.254 | -0.183 | – |
| | | | B3LYP | | | | | |
| $C_{2v}$ | $^1A_1$ | 0.00000 | 0.00000 | 1.257 | -0.765 | -0.218 | -0.028 | 0 |
| $D_{2h}$ | $^1A_g$ | 0.05018 | 0.00000 | 1.332 | -0.876 | -0.189 | -0.039 | 1 |
| $C_{2v}$ | $^3B_2$ | 2.78613 | 2.00573 | 1.003 | -0.637 | -0.174 | -0.009 | 1 |
| $D_{2h}$ | $^3B_{3g}$ | 2.35621 | 2.01868 | 1.391 | -0.771 | -0.273 | -0.037 | 0 |

[a] Number of computed imaginary frequencies. For this molecule, 30 real frequencies are expected.

**Table 4.7:** Results of MP2 and B3LYP calculations for the $[\mathrm{Rh(CO)_2Cl}]_2$molecule. Relative energies (eV), electronic states, Mulliken atomic charges, and computed frequencies are shown.

while the experimental structure refers to the crystal structure. The harmonic vibrational frequencies computed at the B3LYP level are within 2.7% of the experimental values, those computed at the OP86 level are within 0.1% and finally those computed at the PBE level are within 1.1%. Similar results were obtained with the other density functionals studied.

The last molecule considered in this study was $[\mathrm{Rh(CO)_2Cl}(py)]$, where $\mathrm{py}$ stands for pyridine (IUPAC name: *cis-[chloro-dicarbonyl-pyridyl-rhodium(I)]*). For this complex, the computed ground state is a $C_1$ $^1A$ electronic state at both the MP2 and B3LYP levels of theory. The ground state geometries and harmonic vibrational frequencies for this molecule were computed using the same density functionals as used to study the $[\mathrm{Rh(CO)_2Cl}]_2$ complex. The ground state geometries computed at the DFT level of theory are similar, and all are in agreement with the X-ray crystal structure [231].ligand A summary of the results obtained at the B3LYP, OP86 and PBE levels of theory is shown in Table 4.9: the harmonic frequencies computed at the B3LYP level are within 2.8% of the experimental values [232], those computed at the OP86 level are within 0.2% of the

| Parameter | Experimental[a] | B3LYP[b] | OP86[b] | PBE[b] | PBE[c] |
|---|---|---|---|---|---|
| r(Rh–C) | 1.840, 1.853 | 1.866 | 1.824 | 1.847 | 1.885 |
| r(Rh–Cl) | 2.382, 2.386 | 2.426 | 2.384 | 2.408 | 2.409 |
| r(C–O) | 1.128, 1.129 | 1.138 | 1.153 | 1.153 | 1.164 |
| r(Rh–Rh) | 3.138 | 3.280 | 3.082 | 3.123 | 3.215 |
| $\omega$ (C,Rh,C) | 90.7 | 90.7 | 88.7 | 90.0 | 90.6 |
| $\omega$ (Cl,Rh,Cl) | 85.2 | 84.3 | 84.2 | 84.3 | 84.7 |
| $\theta$ (Cl,Rh,Rh,Cl) | 128.0 | 132.5 | 123.0 | 123.6 | 129.5 |
| $\theta$ (Rh,Cl,Cl,Rh) | 126.8 | 133.1 | 121.2 | 122.0 | 129.1 |
| $\nu$(CO), $B_1$ | 2043 | 2102.5 (1465) | 2043.0 (1205) | 2019.5 (1243) | – |
| $\nu$(CO), $B_2$ | 2095 | 2150.9 (1351) | 2096.0 (1163) | 2069.5 (1182) | – |
| $\nu$(CO), $A_1$ | 2107 | 2165.7 (154) | 2113.0 (201) | 2086.3 (192) | – |

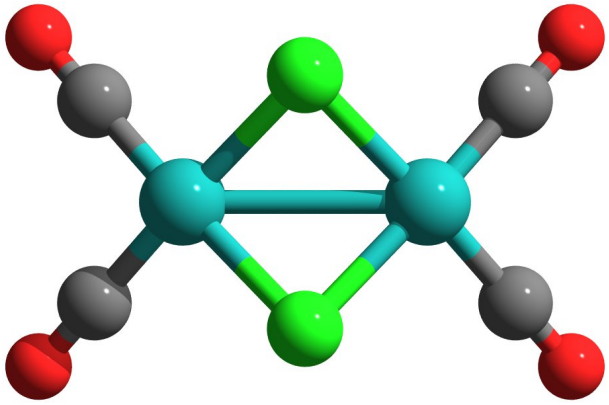

[a] Structural parameters from X-ray measurements [229], infrared frequencies from gas phase measurements [230].
[b] Computed with *Gaussian* 03 using the basis sets desctibed in the previous sections.
[c] Computed with *Castep* 4.4 at the plane-wave/PBE level of theory (section 4.3).

**Table 4.8:** Comparison between the experimental structures of the $[\mathrm{Rh(CO)_2Cl}]_2$ molecule and the minimum energy structures computed at the DFT level of theory with different programs. The calculated harmonic CO stretching frequencies ($\mathrm{cm}^{-1}$) have not been multiplied by a calibration factor; intensities (km/mol) in parentheses, bond lengths (r, Å), bond angles ($\omega$, deg), dihedral angles ($\theta$, deg).

experimental values and finally those computed at the PBE level are within 1.2% of the experimental values.

The results presented in this section show that single-reference methods such as DFT are capable of reproducing correctly the ground state properties of the rhodium complexes considered in this study. In particular, the structures and harmonic frequencies

| Parameter | Experimental[a] | B3LYP | OP86 | PBE |
|---|---|---|---|---|
| r(Rh–Cl) | 2.347(4), 2.344(3) | 2.362 | 2.323 | 2.345 |
| r(Rh–N) | 2.122(7), 2.114(7) | 2.157 | 2.143 | 2.145 |
| r(Rh–C) | 1.84(1), 1.81(1) | 1.868, 1.872 | 1.828, 1.825 | 1.850, 1.852 |
| r(C–O) | 1.12(1), 1.14(1) | 1.137, 1.144 | 1.159, 1.152 | 1.160, 1.152 |
| r(N–$C_2$) | 1.35(1), 1.34(1) | 1.341 | 1.344 | 1.350 |
| r($C_2$–$C_3$) | 1.37(1), 1.38(1) | 1.385 | 1.390 | 1.391 |
| $\omega$ (Cl,Rh,N) | 91.3(2), 90.6(2) | 88.1 | 88.3 | 88.1 |
| $\omega$ (Cl,Rh,$C_5$) | 177.5(3), 176.6(3) | 178.1 | 178.2 | 178.2 |
| $\omega$ (Cl,Rh,$C_6$) | 87.4(4), 87.2(5) | 88.0 | 88.1 | 88.5 |
| $\omega$ (N,Rh,$C_5$) | 91.2(4), 92.8(4) | 92.1 | 92.8 | 92.4 |
| $\omega$ (N,Rh,$C_6$) | 175.7(5), 177.7(5) | 176.2 | 177.4 | 176.6 |
| $\omega$ ($C_5$,Rh,$C_6$) | 90.1(5), 89.4(6) | 91.7 | 89.9 | 91.0 |
| $\theta$ ($C_2$,N,Rh,$C_5$) | 141.9, 139.2 | 129.1 | 122.3 | 131.8 |
| $\theta$ ($C_5$,Rh,$C_6$,Cl) | 179.8, 179.5 | 178.2 | 178.5 | 178.3 |
| $\nu$(CO), $A$ | 2014 | 2073.5 (807) | 2017.1 (674) | 1992.2 (683) |
| $\nu$(CO), $A$ | 2090 | 2147.8 (738) | 2093.6 (647) | 2067.4 (663) |

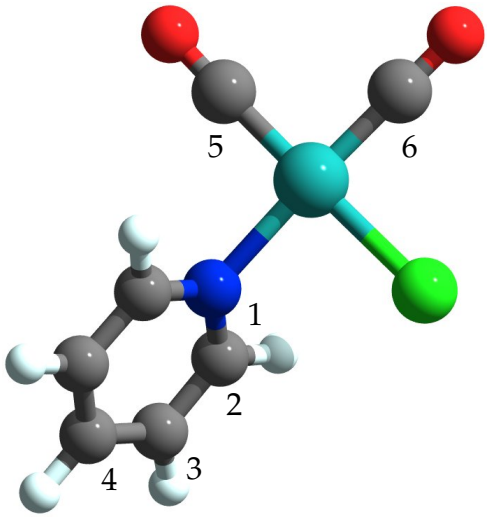


[a] Structural parameters from X-ray measurements [231], infrared frequencies from measurements in benzene [232].

**Table 4.9:** Comparison between the experimental and computed structures of the $[Rh(CO)_2Cl(py)]$. The calculated harmonic CO stretching frequencies ($cm^{-1}$) have not been multiplied by a calibration factor; intensities (km/mol) in parentheses, bond lengths (r, Å), bond angles ($\omega$, deg), dihedral angles ($\theta$, deg).

of various rhodium complexes computed at the DFT level of theory with a TZ quality basis set that includes polarisation functions for all the atoms and diffuse functions for

chlorine and rhodium, are in good agreement with the experimental values.

### 4.2.4 Enthalpy of a Splitting Reaction

In 1976, Pribula and Drago published a detailed calorimetric and spectroscopic study of the acid-base chemistry of $[\mathrm{Rh(CO)_2Cl}]_2$ in benzene [232]. This complex is known to undergo reactions of various types with Lewis bases, depending on the experimental conditions used and the specific base involved. When $[\mathrm{Rh(CO)_2Cl}]_2$ reacts with pyridyne, the observed reaction is:

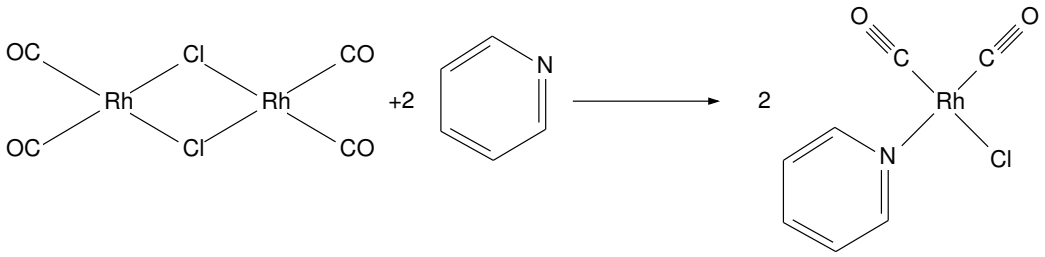


(4.1)

Among the bases considered in the experimental work of Pribula and Drago [232], pyridine is the ligand with the smallest number of atoms and for this reason reaction (4.1) is the best suited to be studied from a computational point of view.

Ground state geometries, energies and harmonic vibrational frequencies have been computed in this work for the species involved in reaction (4.1). For the $[\mathrm{Rh(CO)_2Cl}]_2$ and $[\mathrm{Rh(CO)_2Cl}(py)]$ molecules, the results of calculations have been reported and discussed in the previous section. For pyridine, the computed geometries and harmonic stretching frequencies are not reported in this thesis work. However, it was verified that the computed values are in good agreement with the experimental determinations.

Classically, the free enthalpy is defined as [233]:

$$\begin{aligned} H &= U + PV \\ &= U + nRT \end{aligned} \tag{4.2}$$

The internal energy $U$ for an isolated molecule in the gas phase is the sum of the total electronic energy and the thermal energy:

$$U = E_{\text{elec}} + E_{\text{therm}} \tag{4.3}$$

where the total electronic energy $E_{\text{elec}}$ is computed with an *ab-initio* or DFT method and the thermal energy $E_{\text{therm}}$ is the sum of the translational, rotational, and vibrational energies:

$$E_{\text{therm}} = E_{\text{trans}} + E_{\text{rot}} + E_{\text{vib}}$$

In this work the translational and rotational terms were accounted for classically as the sum of $\frac{1}{2}RT$ for each degree of freedom, and the zero-point vibrational energy was calculated from the computed vibrational frequencies. From equations (4.2) and (4.3) the enthalpy of the reaction 4.1 can be written as:

$$\Delta H = \Delta E_{\text{elec}} + \Delta E_{\text{therm}} - RT \tag{4.4}$$

where $\Delta n = -1$ and $RT = 0.592$ kcal/mol at room temperature ($T = 298$ K).

The thermal energy in equation (4.3) has been computed at the DFT level of theory using the functionals described in the previous secton, while the electronic energy has been computed at the DFT and CC levels of theory in order to have two different ways to estimate the electron correlation energy for this system. Due to the high computational cost of the CC method, only single-point energy CC calculations on ground-state DFT geometries have been carried out.

To ensure that a single-reference description of the reactants and products is adequate, a multi-configurational self-consistent field method (the CASSCF method) has been used to compute the multi-reference ground state wavefunctions. The CASSCF calculations have been performed with the *Multi* program of the *Molpro* computer suite [234] using a DZ quality basis set. The contribution of the main single configuration in the computed ground-state wavefunctions is 97.4% for $[\mathrm{Rh(CO)_2Cl}]_2$, 98.4% for

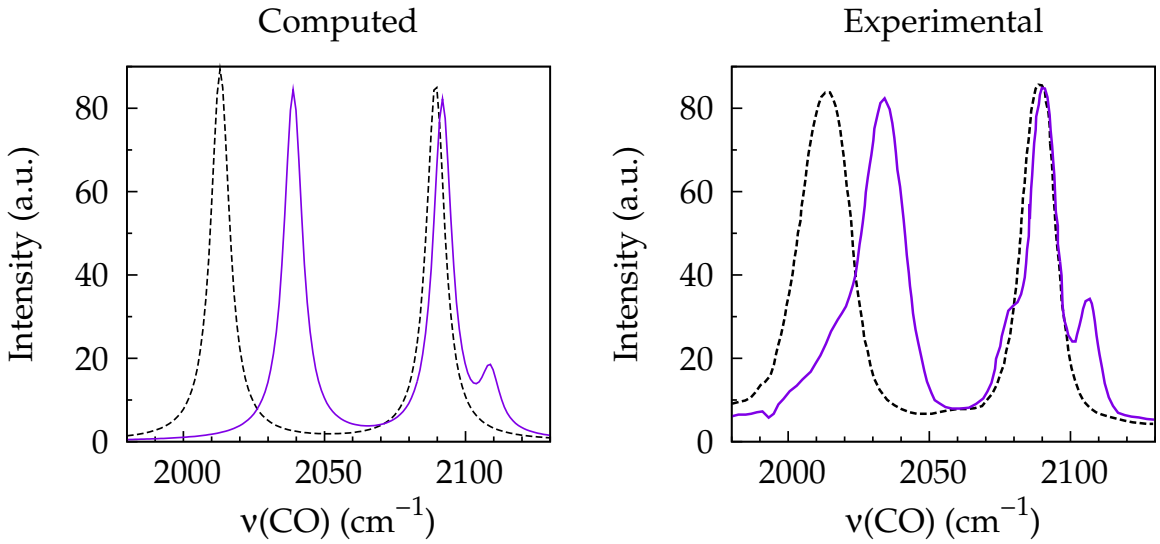


**Figure 4.6:** Infrared spectra for reaction (4.1) computed at the OP86 cc-pVTZ level of theory and measured experimentally in benzene (from reference [232]). The solid line refers to $[Rh(CO)_2Cl]_2$ and the dashed line refers to $[Rh(CO)_2Cl(py)]$. A scale factor of 0.998 has been applied to the computed frequencies, and a stoichiometric factor of 2 has been used to multiply the computed intensities of the $[Rh(CO)_2Cl(py)]$ spectrum. The infrared spectrum of pyridine does not have absorption frequencies in the region shown in this plot and it is therefore not reported.

pyridine and 95.8% for $[Rh(CO)_2Cl(py)]$. From these results it can be concluded that the electronic ground state of these molecules does not have multi-reference character.

The experimental infrared spectrum of reaction (4.1) taken before and after reaction with pyridine is shown in Figure 4.6. For comparison, the simulated infrared spectra of $[Rh(CO)_2Cl]_2$ and $[Rh(CO)_2Cl(py)]$ computed at the OP86 level of theory are shown on the left-hand side of the same Figure, where a scaling factor of 0.998 has been used for the computed frequencies. According to equation (4.1) the molar ratio of the reactants and products is 1:2, therefore the intensity of the simulated spectrum of $[Rh(CO)_2Cl(py)]$ has been multiplied by a stoichiometric factor of 2. As can be seen in Figure 4.6, the computed spectra are in very good agreement with the experimental spectra in terms of both the computed frequencies and relative intensities.

| Method | Geometry[a] | | Basis set |
|---|---|---|---|
| | B3LYP | OP86 | |
| CCSD | -17.832 | -17.873 | cc-pVDZ for H,C,N,O; aug-cc-pVDZ for Cl; |
| CCSD(T) | -20.666 | -20.165 | Stuttgart-RSC+2f for Rh. |
| CCSD | -13.991 | -14.152 | cc-pVTZ for H,C,N,O; aug-cc-pVTZ for Cl; |
| CCSD(T)[b] | -15.973 | -15.572 | Lanl2-[6s4p4d2f] for Rh. |

[a] CC single-point calculations performed on the DFT-optimised ground-state geometry, thermal contribution from the corresponding DFT calculation. DFT calculation.

[b] Extrapolated value, see the text for details.

**Table 4.10:** Computed enthalpies for the reaction 4.1 (kcal/mol). The calculations were performed at the CCSD and CCSD(T) levels of theory on minimum-energy geometries optimised at the B3LYP and OP86 level. Zero-point energies are computed at the DFT level of theory. The experimental value for this reaction is $-12.5 \pm 0.2$ kcal/mol in benzene solvent [232].

### 4.2.5 Basis Set Effect

The enthalpy for reaction (4.1) computed at the CCSD and the CCSD(T) levels of theory is shown on Table 4.10, while the enthalpy computed at the DFT level of theory is shown on Table 4.11. The experimental enthalphy for reaction (4.1), measured in benzene solvent, is $12.5 \pm 2$ kcal/mol [232]. For CC calculations, the best agreement is found for the enthalpy computed at the CCSD level of theory with a TZ quality basis set (-14.0 kcal/mol). To reduce the computational cost of high-level calculations, the total electronic energies computed at the CCSD(T)/TZ level were extrapolated as the sum of the TZ quality CCSD energy and the DZ quality triples excitation contribution. Here the assumption is that the triples excitation contribution to the total electronic energy computed with the DZ quality basis set is the same as the TZ quality basis set [235]. Although the enthalpies computed at the CCSD(T) level are less negative than those computed at the CCSD level (with the same basis set), the CCSD(T) method is expected to give better results using larger basis sets[2].

For DFT calculations, the best agreement with the experimental value of the reac-

[2]The amount of correlation energy included in CC calculations is basis set dependent [236, 237].

| | B3LYP | BPW91 | BP86 | O3LYP | OPW91 | OP86 | BB1K | PBE |
|---|---|---|---|---|---|---|---|---|
| $\Delta H^{a}$ | -15.717 | -13.682 | -16.199 | -10.395 | -6.344 | -8.581 | -11.166 | -17.492 |
| $\Delta H^{b}$ | -12.630 | -11.105 | -13.535 | -7.987 | -4.363 | -6.497 | -8.586 | -14.651 |
| $\Delta E_{\text{therm}}{}^{b}$ | 2.923 | 2.888 | 2.857 | 2.931 | 2.943 | 2.924 | 2.926 | 2.835 |
| IR error | -2.9% | 1.4% | 1.6% | -2.0% | -0.5% | -0.3% | -7.5% | 1.2% |

Basis Sets used:

[a] cc-pVDZ for H,C,N,O; aug-cc-pVDZ for Cl; Lanl2DZ+1d1f for Rh.

[b] cc-pVDZ for H; cc-pVTZ for C,N,O; aug-cc-pVTZ for Cl; Lanl2-[6s4p4d2f] for Rh.

**Table 4.11:** Enthalpies for the reaction 4.1 (kcal/mol), thermal contributions and harmonic frequency errors computed at different DFT levels of theory. The experimental value for this reaction is $-12.5 \pm 0.2$ kcal/mol in benzene solvent [232].

tion enthalpy is obtained at the B3LYP/TZ level (-12.6 kcal/mol). The calculations performed using hybrid-GGA and GGA functionals with the Becke exchange gave reaction enthalpies within 2 kcal/mol of the experimental value, while the functional with Handy's optimised exchange gave a poorer agreement in terms of reaction enthalpy, but a smaller error on the computed harmonic frequencies. From Table 4.11 it can also be seen that the use a TZ quality basis set corrects the computed reaction enthalpies by about 3 kcal/mol with respect to the calculations performed with a DZ quality basis set. A similar improvement is found for the results obtained at the CCSD and CCSD(T) levels of theory carried out with DZ and TZ quality basis sets.

To conclude, the enthalply for reaction (4.1) computed at the CCSD, CCSD(T) and DFT levels of theory is found to be in very good agreement with the experimental value. The presence of diffuse functions on chlorine and rhodium is of considerable importance to compute correctly the wavefunction for the species involved and to prevent the basis-set superposition error (BSSE) [238]. From these results it can be assumed that the most important source of error in the computation of reaction enthalpy arises from the number and type of basis functions used.

It should also be noted that the experimental work of Pribula and Drago [232] was performed in a solvent (benzene) and no account of this has been taken in the calculations that were carried out in this work.

## 4.3 Periodic DFT Calculations

Plane-wave DFT calculations can be applied to isolated molecules by using a large unit cell containing just one molecule. In such a way, the molecule does not interact with its periodic images. In this section, plane-wave/DFT calculations have been used to study the $[Rh(CO)_2Cl]_2$ complex and the results compared with the DFT calculations performed using gaussian basis sets.

The system under investigation is composed of an orthorombic unit cell with vectors $a$ = 12.5, $b$ = 15.0 and $c$ = 11.0 Å. These values have been determined by computing the total electron energy as a function of the cell vector size, until convergence is achieved.

The aim of this study was to test the capabilities of a plane-wave basis set to reproduce the structural properties of a complex containing rhodium, and to compare the results with high-quality calculations carried out with a gaussian basis set. The validation of this theoretical approach is necessary before this method can be applied to study supported rhodium catalysts.

### 4.3.1 Simulation Parameters

The calculations presented in this section were performed at the plane-wave/DFT level of theory, as implemented in the program *Castep*. The functional PBE in conjunction with Vanderbilt ultrasoft pseudopotentials was used to solve the Kohn-Sham equations, with periodic boundary conditions applied to the system. The convergence of parameters such as basis set energy cut-off, FFT grid and k-point spacing was tested for the total electronic energy of $[Rh(CO)_2Cl]_2$, as was done for tests performed on $\gamma$-$Al_2O_3$ described in Chapter 3. A basis set cut-off energy of 380 eV was found to yield reliable total energy and forces, as shown in Figure 4.7. A FFT grid of 1.2 and a k-point spacing of 0.05 $Å^{-1}$ were also found to be sufficient to give reliable energies and forces.

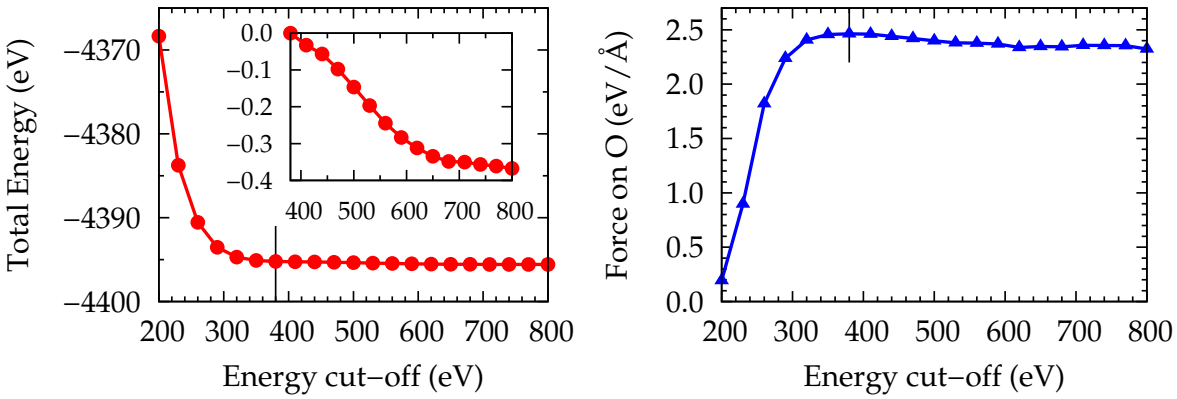


**Figure 4.7:** Convergence of the total electronic energy and forces of $[Rh(CO)_2Cl]_2$ computed with respect to the basis set energy cut-off. A cut-off energy $E_{cut} = 380$ eV was chosen for the calculations presented in this thesis work. The inset in the left-hand side of this Figure shows the relative energy difference in the region from $E_{cut} = 380$ eV to $E_{cut} = 800$ eV.

### 4.3.2 Computed Structures

The structure of $[Rh(CO)_2Cl]_2$ optimised at the plane-wave/PBE level of theory is reported in Table 4.8, section 4.2.3. The agreement of this structure with the experimental structure and those computed with conventional DFT calculations using the B3LYP, OP86 and PBE functionals is good. The computed band gap is 2.69 eV, in excellent agreement with the HOMO-LUMO energy difference (2.67 eV, computed at the PBE/ECP/cc-pVTZ level of theory with the program *Gaussian* G03). The harmonic frequencies have not been computed because this facility it is not (yet) implemented in the program *Castep*.

From this calculation it can be concluded that the structure of $[Rh(CO)_2Cl]_2$ calculated at the plane-wave/PBE level of theory is in agreement with high-quality calculations carried out at the DFT level of theory using TZ quality gaussian basis sets. The simulation parameters used in these plane-wave calculations are the same as those used to simulate the structure of hydroxylated $\gamma$-$Al_2O_3$ surfaces; therefore this method appears to be appropriate to study supported rhodium catalysts.

## 4.4 Conclusions

In this chapter DFT and *ab-initio* methods have been applied to the study of different rhodium compounds. For rhodium mono- and di-carbonyl species, a strong dependence between the carbonyl stretching frequency, molecular geometry and electronic state has been found. For rhodium monocarbonyl $\mathrm{Rh(CO)}^{-1,0,1}$, the plot of computed Mulliken rhodium charges versus the computed carbonyl stretching frequencies (Figure 4.2) shows that the functionals tested in this work reproduce well the experimental trend. In particular, the harmonic frequencies computed with the BPW91, BP86, PBE, OPW91, OP86 and OPBE functionals are within 2% of the experimental values.

Some electronic states of rhodium di-carbonyl $\mathrm{Rh(CO)}_2^{-1,0,1}$ computed at the MP2 and B3LYP levels of theory have been found to be very close in energy, and multireference methods should be applied to establish what the ground state is for these molecules. However, the results presented in this thesis work are in agreement with single-reference calculations found on the literature. Optimised geometries and harmonic frequencies of $[\mathrm{Rh(CO)_2Cl}]_2$ and $[\mathrm{Rh(CO)_2Cl}(py)]$ computed at the B3LYP levels of theory were found to be in good agreement with experimental determinations. In Figure 4.6 the experimental and computed infrared spectra are reported for these molecules. The harmonic vibrational frequencies computed at the OP86 level of theory are within 0.2% of the experimental values, and the computed intensities reproduce well the relative intensities of the most intense bands in the experimental infrared spectrum. CASSCF calculations on these species reveal that a dominant single configuration describes their ground states.

The enthalpy of the reaction 4.1 has been computed at the DFT and the CC levels of theory using different basis sets. From the results presented in this work, the functional that gives the best agreement with the experimental value is the the B3LYP functional. The values obtained at the CCSD and CCSD(T) levels of theory are within 3 kcal/mol of the experimental value. The results obtained with all the methods presented in this thesis work showed a strong dependance on basis set size. In particular, diffuse functions on chlorine and rhodium atoms are found to be essential to give accurate

electronic energies.

Finally, the structure of $[Rh(CO)_2Cl]_2$ optimised at the plane-wave/DFT level of theory was found to be in agreement with DFT calculations performed with gaussian-type TZ quality basis sets and with the experimental structure. The simulation parameters used in these plane-wave calculations were the same as those used to optimise the structure of hydroxylated $\gamma$-$Al_2O_3$ surfaces.

CHAPTER 5

# SIMULATION OF SUPPORTED CATALYSTS

In this chapter electronic structure methods are used to study supported rhodium catalysts. One approach is based on plane-wave DFT with periodic boundary conditions, as described in Chapter 3. In this method, the catalytic centre, that is, the rhodium atom(s), and the atoms of the support are studied at the same level of theory. In this way the chemical interaction between the metal centre and the metal oxide support is accounted for explicitly. However, to describe an isolated catalytic species on the support surface, the slab model of the surface must be big enough to avoid unphysical side-by-side interaction between the periodic images. This approach is the chosen reference to model materials characterised by electronic states de-localised over the entire structure, and it is limited only by the size of the system that can be investigated.

A different approach is based on the finite-cluster method, which is suited to study localised states such as those produced by point defects or isolated species monodispersed on surfaces. In this method, a finite cluster of atoms is studied at the quantum mechanical level of theory, while the effects of the environment are accounted for by an appropriate embedding scheme. The program *Guess* [58, 59, 239] combines a quantum-mechanical treatment of a subset of atoms with a molecular mechanics description of the surroundings. This program has been successfully applied to model point defects in solids [59, 135, 240] and surfaces [58, 157, 241, 242], and was employed in this work to study isolated rhodium atoms on $\gamma$ alumina surfaces.

## 5.1 Periodic Simulations

Plane-wave/DFT simulations have been widely used in the literature to investigate the absorption of molecules on well-defined metal surfaces (see for instance the studies concerning the Rh (111) surface [62–64, 243]), but only a few of them have considered the absorption of metal atoms on hydroxylated metal oxide surfaces [66, 244, 245].

In this work, plane-wave/DFT calculations were employed to obtain minimum-energy structures of isolated $\mathrm{Rh^{I}(CO)_2}$ species supported on $\gamma$-alumina surfaces. The simulations were performed employing the parameters used to study hydroxylated $\gamma$-alumina surfaces and isolated rhodium complexes, as discussed in Chapters 3 and 4.

The molecular models of supported $\mathrm{Rh^{I}(CO)_2}$ species were built with the program *Gdis* [160] starting from the optimised structures of hydroxylated (001) and (100) $\gamma$-alumina surfaces studied in Chapter 3. In order to keep the molecular systems electrically neutral and closed-shell, the models of supported $\mathrm{Rh^{I}(CO)_2}$ species must be consistent with the formation mechanism proposed by Basu and co-workers [6]:

$$\mathrm{Rh_{(s)} + 2CO_{(g)} + (Al_2O_3)_n(H_2O)_m \longrightarrow Rh^{I}(CO)_2(Al_2O_3)_n(H_2O)_{m-1}(OH) + \frac{1}{2}H_2} \quad (5.1)$$

The equation 5.1 describes the oxidative disruption of metallic rhodium nanoparticles on hydroxylated alumina surfaces [denoted as $\mathrm{(Al_2O_3)_n(H_2O)_m}$] followed by reaction with carbon monoxide yielding supported rhodium carbonyl species [denoted as $\mathrm{Rh^{I}(CO)_2(Al_2O_3)_n(H_2O)_{m-1}(OH)}$] plus molecular hydrogen.

The surface density of the supported species was chosen to match a metal loading of about 2.5 % in weight. For a commercial alumina sample with a typical surface area of 100 $m^2/g$ [15], this loading gives a surface concentration of about 1.5 $Rh/nm^2$. The slab model of the (001) $\gamma$-alumina plane has a surface area of 46.973 $Å^2$, while the slab model of the (100) plane has a surface area of 67.860 $Å^2$. In order to accommodate one rhodium atom per slab, a (1x2x1) super-cell was used for the (001) plane, while a unitary cell was used for the (100) plane.

In a typical catalytic sample, a number of different configurations is likely to be

present on the support surface. To reproduce this situation and make the models suitable to be studied computationally, single-site surface species were modelled and optimised separately. In this way, the properties of the real system can be represented as an average of the properties of the most representative structures, chosen according to their Boltzmann weighting factors.

In the initial models of supported $\mathrm{Rh^{I}(CO)_2}$ species, the rhodium atom was coordinated to one, two or three oxygen atoms of the support. Four complexes were modelled on the (001) plane and five were modelled on the (100) plane. These structures were fully optimised, and the ground-state properties were determined by performing plane-wave/DFT calculations with periodic boundary conditions applied. The Perdew-Burke-Ernzerhof (PBE) gradient-corrected functional [114] was used, and ultrasoft pseudopotentials generated with the PBE exchange and correlation functionals were used to describe the core electrons. The electronic wave-functions were expanded in a plane-wave basis set with an energy cut-off of 380 eV. These settings were determined variationally, as described in Section 3.1.1, and they are summarized in Table 3.1. The program *Castep* version 4.3 was used to perform all the calculations presented in this work.

### 5.1.1 Computed Structures

Nine structural models of surface $\mathrm{Rh^{I}(CO)_2}$ species were considered in this study. For convenience, each structure is named from *(001)-s1* to *(001)-s4* for the species supported on the hydroxylated (001) $\gamma$-$\mathrm{Al_2O_3}$ plane, and from *(100)-s1* to *(100)-s5* for the species supported on the hydroxylated (100) plane. Each model was built by removing a hydrogen atom from a hydroxylated surface of $\gamma$-alumina previously relaxed, and replacing it with a $\mathrm{Rh^{I}(CO)_2}$ group. Different starting geometries were considered, with the rhodium atom coordinated with one, two or three oxygen atoms from the surface. A pictorial view of the periodic slab models used in this work is given in Figure 5.1, while the relaxed structures of supported $\mathrm{Rh^{I}(CO)_2}$ species are shown in Figure 5.2.

Every calculation was parallelized on a 24-cores Silicon Graphics Altix 4700 server

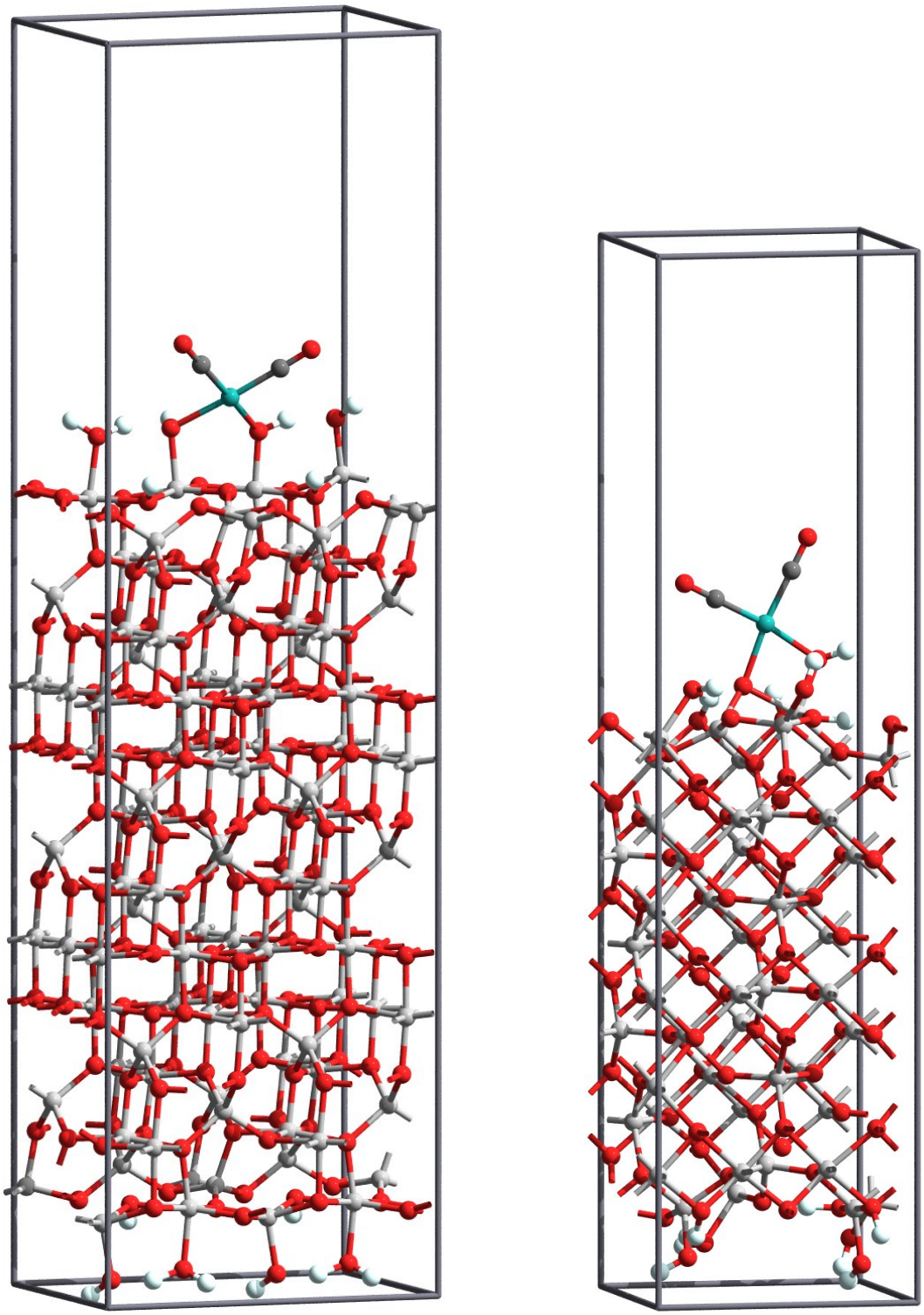

*(001)-s1* *(100)-s1*

**Figure 5.1:** Pictorial view of the (001)-s1 and (100)-s1 $Rh^{I}(CO)_2$ species supported on hydroxylated $\gamma$-$Al_2O_3$ surfaces. The optimised structures were computed at the plane-wave/PBE level of theory with periodic boundary conditions applied.

based on 1.6GHz Montecito Itanium2 processors. The typical time employed to carry out a geometrical optimisation run was of about 5000 CPU hours. The longest time employed to carry out a single run was 7127 CPU hours for the (001)-s2 complex.

In all the optimised structures the surface rhodium complexes exhibit a square-planar coordination geometry, regardless to the starting configuration used in the calculation. The formal oxidation state of rhodium in these complexes is +1, which gives the electronic configuration $4s^2 4p^6 4d^8$. It is therefore expected that this configuration, coupled with a strong ligand field, promotes the formation of a square-planar complexes as also observed for $d^8$ metal cations such as $Ir^+$, $Pt^{2+}$, $Pd^{2+}$ and $Au^{3+}$ cations [246].

The coordination geometry of supported $Rh^I(CO)_2$ species obtained in this thesis work is in agreement with *in-situ* infra-red and EXAFS spectroscopy measurements made by Evans and co-workers, who investigated supported Rh/$\gamma$-$Al_2O_3$ catalysts [7, 43, 247–250], and with quantum chemical calculations[1] performed by Vayssilov and co-workers [251]. Analogous conclusions have been reported for rhodium dicarbonyl in highly dealuminated zeolite Y investigated by EXAFS, infra-red spectroscopy and quantum mechanical calculations by Goellner and co-workers [252].

The rich morphology of hydroxylated $\gamma$-$Al_2O_3$ surfaces offers several docking sites for the formation of surface $Rh^I(CO)_2$ species. For all the complexes supported on the (001) plane and for the (100)-s4 and (100)-s5 complexes, a small reconstruction of the surface was observed during the geometrical optimisation. For these systems, the surface OH groups are arranged in a position that promotes the coordination of rhodium in a square-planar geometry. For the (100)-s1, (100)-s2 and (100)-s3 complexes, a strong reconstruction of the surface was observed. In these complexes the presence of rhodium induced a change in the position of OH groups, eventually followed by a re-arrangement of the other OH groups in order to maximise the number

[1]Molecular cluster calculations of stable $Rh^I(CO)_2$ complexes in dealuminated Y (DAY) zeolite were performed at the ECP/DFT level of theory. In the computed structures, the supported $Rh^I(CO)_2$ complexes exhibit a pseudo square planar structure with the Rh cation bonded to two oxygen centres belonging to the zeolite framework.

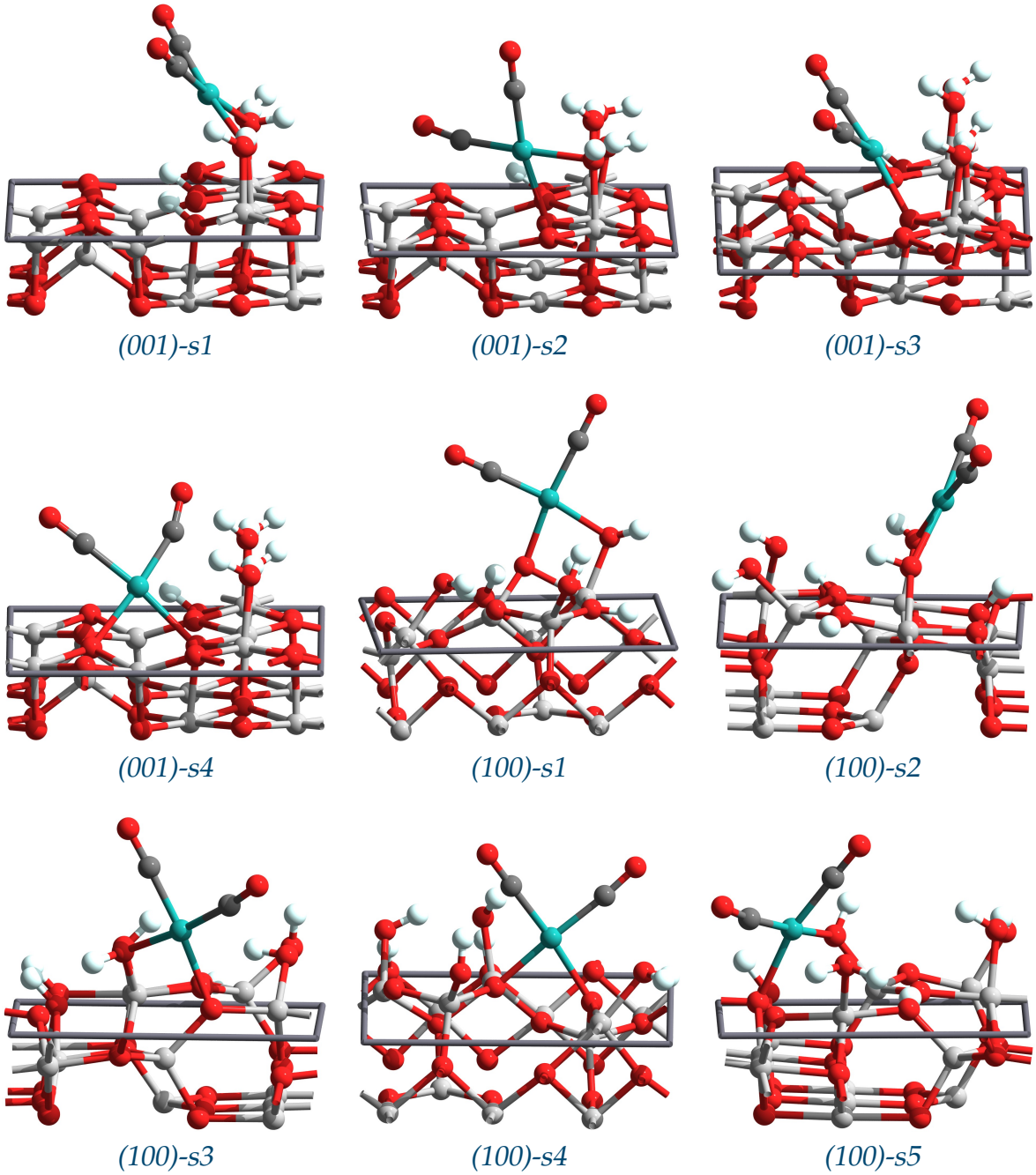


**Figure 5.2:** Models of surface $Rh^{I}(CO)_2$ complexes optimised at the plane-wave/DFT level of theory. The periodic vectors on the alumina plane are drawn as rectangles around each structure.

of hydrogen bonds on the surface.

The complex (001)-s2 (Figure 5.2) lies in the proximity of the support surface. This

| Complex | r(Rh–C) | | r(C–O) | | r(Rh–O) | |
|---|---|---|---|---|---|---|
| | | | Plane (001) | | | |
| *s1* | 1.869 | 1.881 | 1.168 | 1.168 | 2.195 | 2.100 |
| *s2* | 1.867 | 1.892 | 1.168 | 1.167 | 2.244 | 2.134 |
| *s3* | 1.862 | 1.868 | 1.170 | 1.170 | 2.202 | 2.337 |
| *s4* | 1.865 | 1.905 | 1.167 | 1.171 | 2.254 | 2.153 |
| | | | Plane (100) | | | |
| *s1* | 1.880 | 1.876 | 1.168 | 1.168 | 2.096 | 2.215 |
| *s2* | 1.872 | 1.887 | 1.165 | 1.165 | 2.101 | 2.168 |
| *s3* | 1.872 | 1.883 | 1.165 | 1.167 | 2.124 | 2.228 |
| *s4* | 1.881 | 1.898 | 1.163 | 1.169 | 2.131 | 2.118 |
| *s5* | 1.889 | 1.859 | 1.169 | 1.162 | 2.122 | 2.267 |
| | | | Experimental[a] | | | |
| | 1.814 (2) | | 1.189 (3) | | 2.038 (2) | |

[a] Structural parameters from EXAFS measurements [247].

**Table 5.1:** Bond lengths (Å) relative to surface $\mathrm{Rh^{I}(CO)_2}$ species optimised at the plane-wave/PBE level of theory.

leads to a distorted angle (RhCO) = 168.8° for one CO group. The complex (001)-s4 also has a distorted structure, which is caused by the repulsion between one CO group and neighbouring hydroxyl groups. In all the other complexes, the rhodium has a square-planar coordination geometry, with a typical RhCO angle close to 180°.

A comparison between the theoretical and experimental bond distances for surface $\mathrm{Rh^{I}(CO)_2}$ complexes is presented in Table 5.1. The agreement between the computed Rh–C, C–O and Rh–O bond lengths and the EXAFS values [247] is good. Small discrepancies in the Rh–O bond distance can be attributed to the presence in the EXAFS spectrum of signals of molecular species with different coordination geometries.

The formation energy of each surface $\mathrm{Rh^{I}(CO)_2}$ species was determined according to the equation 5.1. The electronic energies of metallic rhodium and gaseous $\mathrm{CO}$ and $\mathrm{H_2}$ species were determined at the plane-wave/DFT level of theory using the same parameter settings employed to study the surface complexes. For $\mathrm{CO}$ and $\mathrm{H_2}$, orthorhombic unit cells were used to simulate the isolated molecules. The experimental unit cell of rhodium is a face centred cubic (FCC) with space group $Fm\bar{3}m$ and lattice parame-

| Complex | Energy | Complex | Energy |
|---|---|---|---|
| Plane (001) | | Plane (100) | |
| *s1* | -18.205 | *s1* | -27.611 |
| *s2* | -12.779 | *s2* | -21.527 |
| *s3* | -12.504 | *s3* | -27.300 |
| *s4* | -14.228 | *s4* | -10.850 |
| | | *s5* | -14.693 |

**Table 5.2:** Formation energies (kcal/mol) of surface $\mathrm{Rh^{I}(CO)_2}$ species computed at the plane-wave/PBE level of theory, relative to the reagents in equation 5.1.

ter 3.803 Å, while the minimum-energy structure has a lattice parameter 3.892 Å. The energy of the support, that is, $(\mathrm{Al_2O_3})_\mathrm{n}(\mathrm{H_2O})_\mathrm{m}$, is the one of hydroxylated (001) and (100) $\gamma$-$\mathrm{Al_2O_3}$ surfaces described in Chapter 3. As supported $\mathrm{Rh^{I}(CO)_2}$ complexes on the (001) surface were modeled on a (1x2x1) super-cell (Figure 5.1), the energy of the support was twice the energy of the slab model for the hydroxylated (001) surface (Figure 3.12). For supported $\mathrm{Rh^{I}(CO)_2}$ complexes on the (100) surface, the energy of the support was that of the slab model for the hydroxylated (100) surface. A summary of the computed formation energies is shown on Table 5.2. No zero-point correction was applied to the energies listed in this table.

On the (001) plane, the most stable complex is therefore the (001)-s1 complex, which has a formation energy of -18.205 kcal/mol. The complexes (001)-s2, (001)-s3 and (001)-s4 have formation energies 5.4, 5.7 and 4.0 kcal/mol higher than the (001)-s1 complex, respectively.

On the (100) plane, the most stable complexes are the (100)-s1 complex, which has a formation energy of -27.611 kcal/mol, and the (100)-s3 complex, which has a relative formation energy just 0.311 kcal/mol higher. The complexes (100)-s2, (100)-s5 and (100)-s4 have a relative formation energy 6.084, 12.918 and 16.761 kcal/mol higher.

From this trend, one can conclude that the most stable $\mathrm{Rh^{I}(CO)_2}$ complexes are those bonded to oxygen atoms and hydroxyl groups with a high coordination number, *i.e.* in the most stable complexes, the rhodium atom is bonded to oxygen atoms belonging to the alumina surface rather than hydroxyl groups adsorbed on the surface. However,

the computed energies of supported species may be affected by artefacts due to side-by-side interaction between the periodic images.

### 5.1.2 Theoretical XANES Spectra

X-ray Absorption Near-Edge Spectroscopy (XANES) is a powerful experimental technique for studying the local structure of atoms, due to its directional short range order sensitivity and its chemical selectivity. XANES spectra of a 2% in weight Rh/$\gamma$-$Al_2O_3$ catalyst were recorded in transmission mode at the ESRF, beamline BM29 [253] (Grenoble, France). The spectra were collected at the Rh K-edge with a Si(111) double-crystal monochromator. Measurements of the catalyst sample were performed under a CO atmosphere at room temperature: under these experimental conditions the Rh clusters are disrupted and surface $Rh^{I}(CO)_2$ species are formed [36–43].

Structural models of supported rhodium catalysts obtained from plane-wave/DFT calculations were used to simulate theoretical XANES spectra in order to assess their consistency with the experimental XANES spectrum. The reason of doing such a comparison is that the XANES spectrum is sensitive to both the angular and radial distribution of atoms around the photo-absorber element [254]. The program *Feff* version 8.4 [255] was used to carry out a full multiple scattering XANES calculation for a cluster of atoms centred on the absorbing atom (*i.e.* rhodium). Atoms up to 7 Å from rhodium were included to obtain converged XANES calculations.

Since the experimental spectrum is an average over all the configurations present in the sample during the measurements, the theoretical spectrum was obtained as the average of the spectra computed from different structures, each weighted with the corresponding Boltzmann factor and the relative abundance of the alumina crystal plane[2].

[2]In a typical $\gamma$-$Al_2O_3$ nanoparticle, shown in Figure 3.11, the plane (100) accounts for 74% of the total exposed surfaces, the plane (001) for 16% and the plane (101) 10% [27]. For the calculation of the theoretical XANES spectrum, only the planes (100) and (001) were considered. The relative abundance of these planes was rounded to 80% for the (100) plane, 20% for the (001) plane and 0% for the (101) plane.

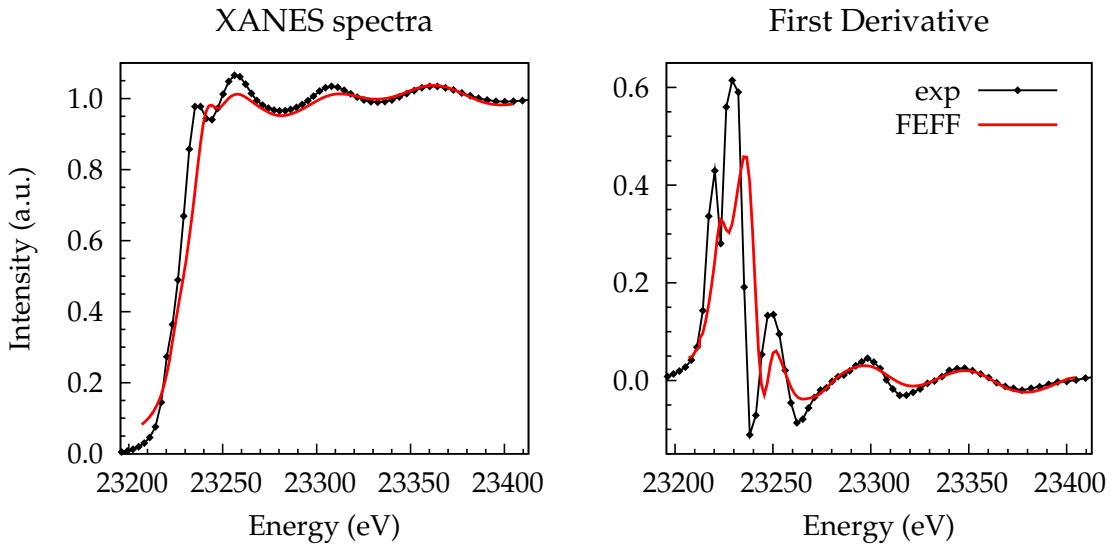


**Figure 5.3:** Comparison between experimental and theoretical XANES spectra at the Rh $K$-edge. The theoretical spectrum was calculated from the structure of complexes (001)-s1, (100)-s1 and (100)-s3. The resulting spectra were averaged using Boltzmann-weighting factors (see text).

The Boltzmann factors of systems with energy $E_i$ are given by the equation:

$$\rho(E_i, T) = \frac{N_i}{N} = \frac{e^{-E_i/k_B T}}{Z(T)} \tag{5.2}$$

where $E_i$ is the formation energy of the complex (Table 5.2), $k_B$ the Boltzmann constant, $T$ the temperature and $Z(T) = \sum_i e^{-E_i/k_B T}$ is the partition function. In Equation 5.2, all the systems were considered as non-degenerate. According to the Boltzmann factors computed at $T = 300$K, the most important surface complexes are the (100)-s1, (100)-s3 and the (001)-s1 which have relative weights of 0.41, 0.39 and 0.20 respectively.

The theoretical XANES spectrum obtained by averaging the spectra of the (001)-s1, (100)-s1 and (100)-s3 structures is shown in Figure 5.3. The theoretical spectrum reproduces well the features of the experimental spectrum, such as phase and shape of the oscillations, providing support for the structural parameters used. Amplitude discrepancies in the edge region may indicate the presence of metallic rhodium in the sample investigated [256], and therefore this feature is not reproduced with the struc-

tural models used. The first derivative of the spectra (right-hand side of Figure 5.3) shows that the obscillations of the theoretical and experimental spectra are in phase. The agreement between the experimental and theoretical spectrum is measured by the root mean square (RMS) of the difference between the absorption cross sections:

$$RMS = \frac{1}{n}\sqrt{\sum_{i=1}^{n}(\mu_i^{\text{exp}} - \mu_i^{\text{theo}})^2} \tag{5.3}$$

where $n$ is the number of data points in the experimental spectrum. The RMS computed for the theoretical XANES spectrum was found to be 0.0296 a.u.

## 5.2 Embedded Molecular Cluster Calculations

The calculations presented in this Section have been performed using the program *Guess* developed by Dr. Peter Sushko and Prof. Alexander Shluger (University College of London) [58, 59, 239], which implements a theoretical scheme to perform finite cluster calculations using a hybrid QM/MM approach. Within this scheme, the region of interest is studied with a quantum-mechanical methodology such as DFT. The quantum-mechanical (QM) cluster is embedded in a finite region of polarizable ions (referred to as region I) described with the shell model (Section 2.4.3), which provides a convenient way of describing the electrostatic and steric constraints produced by the atomic environment of the QM cluster. Fixed non-polarizable ions placed outside region I form the so-called region II. This region provides the correct electrostatic potential in the QM cluster and in region I. A schematic view of the division of the space is illustrated in Figure 5.4.

The interface region between the quantum-mechanical cluster and the classical region is composed of positive ions represented using ECPs. The interface atoms interact quantum-mechanically with atoms of the QM cluster and classically with the classical environment. The ECP on each interface atom replaces the potential hole created by a point charge with a potential which allows the electronic wavefunction to decrease

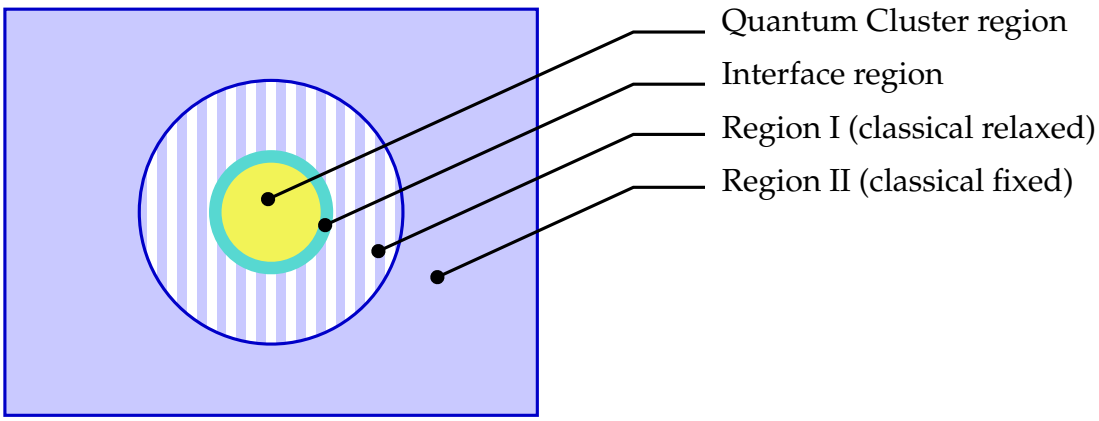


**Figure 5.4:** Division of space in an embedded molecular cluster calculation as implemented in the program *Guess*.

smoothly towards the cluster boundary.

In *Guess*, the total energy includes contributions due to the interaction of the QM region with the rest of the host lattice, the ionic and electronic polarization of the lattice by the QM region, and the reciprocal effect of the lattice polarization on the QM region itself. In this way, the electronic structure of the QM region is consistent with the perturbation which it induces on the polarizable environment and *vice-versa* [240].

The total forces acting on each centre, *i.e.* the QM ions and the classical cores and shells forming region I, are calculated by differentiating the total energy with respect to the coordinates of the corresponding species. The positions of the cores and shells for each ion are optimized in response to changes in the charge density distribution within the quantum cluster, until minimization of the total energy is achieved [239].

In this work, the DFT method as implemented in the program *Gaussian* [155] was used to calculate the quantum-mechanical contribution to the total energy. The PBE gradient-corrected exchange functional [114] was used in conjunction with a double-$\zeta$ quality basis set. The Lanl2DZ+1d1f ECP basis set was used for rhodium (see Section 4.1), and Dunning's correlation consistent cc-pVDZ basis set [257] was used for all the other atoms. The interface atoms in the QM cluster were represented using large-core Lanl2 ECPs [213] and they have a minimal basis set with high exponent (tight) $s$ and $p$ functions.

The structural units used to build the finite-cluster models of $\gamma$-$Al_2O_3$ surfaces were obtained from minimum-energy structures computed at the MM level of theory, as described in Section 3.2.2. The force field used to model region I is therefore consistent with the modified De Leeuw and Parker force field described in Tables 3.6 and 3.7.

### 5.2.1 Preliminary Operations

The finite cluster of atoms included in a hybrid QM/MM calculation is constructed from repetition of structural elements which should have a dipole moment equal to zero. In this way, the electrostatic potential provided by region II remains constant in region I and provides the correct long-range Coulomb potential. To simulate a supported rhodium catalyst, the structural unit is a slab model of a hydroxylated $\gamma$-$Al_2O_3$ surface relaxed at the MM level of theory, as described in Section 3.2.2. The top and bottom surfaces of the alumina slab are identical, and the dipole moment of the slab must be zero only in the plane parallel to the surface. Structural units with these characteristics are constructed from the periodic unit cell of $\gamma$-$Al_2O_3$ surfaces according to the procedure described in this Section. In the following derivation, the position of atoms is given in fractional coordinates, *e.g.* $x_i \in [0, 1]$.

The Cartesian components of the electrical dipole moment generated by $N$ point charges can be written as

$$D_x = \sum_{i=1}^{N} q_i x_i \tag{5.4}$$

If the position of all the charges is shifted by a constant value $x_0$, an important condition is that the dipole moment does not change:

$$D_x = \sum_{i=1}^{N} q_i (x_i - x_0) = D_x + x_0 \sum_{i=1}^{N} q_i = D_x \tag{5.5}$$

*i.e.* for a neutral system, $\sum_{i=1}^{N} q_i = 0$. If the coordinate $x$ of the $N^{\text{th}}$ point charge is

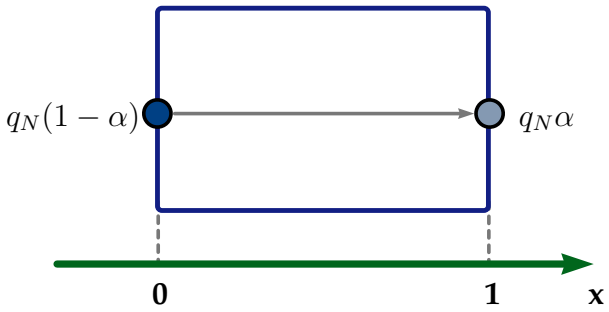


**Figure 5.5:** A schematic diagram which shows a point charge split between the fractional coordinates $x_N = 0$ and $x_N = 1$.

shifted to zero, *i.e.* $x_0 = x_N$, equation (5.5) can be re-written as

$$D_x = \sum_{i=1}^{N} q_i(x_i - x_N) = \sum_{i=1}^{N-1} q_i(x_i - x_N) = D_x \tag{5.6}$$

The dipole moment in the latter equation is equivalent to the dipole moment generated by a distribution of point charges in which the charge $q_N$ is placed at $x_N = 0$. In this particular case the point charge $q_N$ can be split between the periodic images of the unit cell, corresponding to the fractional coordinates 0 and 1, as illustrated in Figure 5.5. Equation (5.6) implies that $\alpha = 0$. For $\alpha \neq 0$, the dipole moment becomes:

$$D_x^* = \sum_{i=1}^{N-1} q_i(x_i - x_N) + \alpha q_N = D_x + \alpha q_N \tag{5.7}$$

where $x_N = 1$ has been omitted. Therefore, the condition to have $D_x^* = 0$ is that

$$\begin{aligned} D_x + \alpha q_N &= 0 \\ \alpha &= -\frac{D_x}{q_N} \end{aligned} \tag{5.8}$$

In this way, the dipole moment of the surface structural unit can easily be set to zero. Figure 5.6 shows a system in which the charge of two atoms have been split to give a structural unit which has no dipole moment along the cartesian directions $x$ and $y$.

This procedure has been implemented in a program called `cell-dipole.pl` writ-

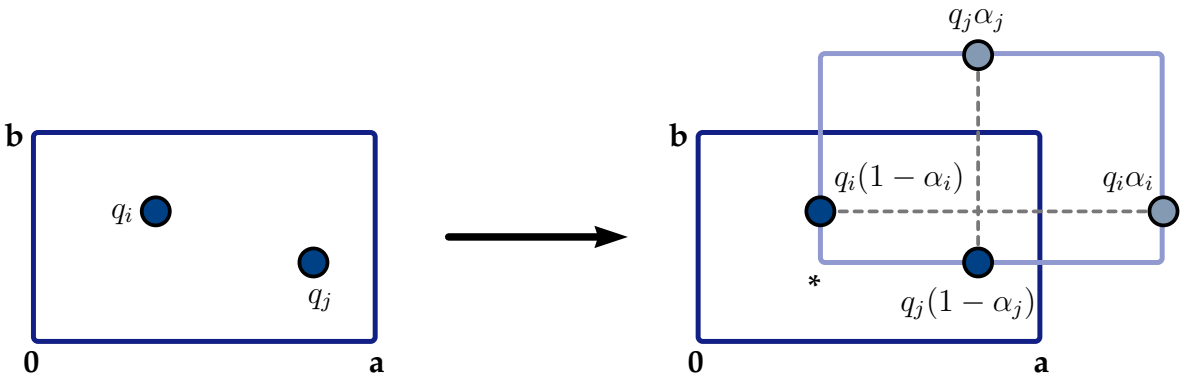


**Figure 5.6:** To make the dipole moment zero in the plane $ab$, two atoms are selected inside the unit cell and translated (right-hand side panel) to the positions $(0, b)$ and $(a, 0)$. The charge of each atom is then split between their periodic images and the coefficients $\alpha_i$ and $\alpha_j$ can be computed.

ten in the *perl* scripting language[3]. This program takes a slab model for the surface given in the CIF standard crystallographic format [258], computes the coefficients $\alpha_i$ for every atom in the unit cell and asks the user to chose two atoms to give a "building-block" structural unit. This system is saved as a Cartesian coordinate file (XYZ format), with an additional column containing the charge of every species. The program has been tested on two high-symmetry systems ($\alpha$-$Al_2O_3$ and NaCl) and it correctly computes the coefficients $\alpha$ for a finite-cluster model of the plane (001). For hydroxylated $\gamma$-alumina surfaces, the periodic slab models of the (001) and (100) planes optimised at the MM level of theory (Section 3.2.2) have been used to create the structural units used to build the finite-cluster model of supported rhodium catalysts.

After the building-block has been created, the program `xyz_slab_NxM` is used to build a finite cluster of atoms as a $N$x$M$ repetition of the structural unit. Afterwards, the program `nc_slab_to_guess` takes the finite-cluster model and the radius for region I as input data, and writes a *Guess* template file for a hybrid QM/MM calculation. These two programs have been written with the help of Dr. Peter Sushko (University College of London).

[3]This program and all the other programs mentioned in this Section are given in full in Appendix A.4. All the software presented in this Section is original work developed to help writing the input files for hybrid QM/MM calculations.

The size of region I should be large enough to accommodate the lattice distortions induced by the adsorbed species in the QM cluster. Furthermore, the Coulomb potential induced by region II should be constant inside region I or at least it must have a value with numerical noise smaller than the energy differences investigated by hybrid QM/MM calculations. The program `epotential_2D` is used to compute the electrostatic potential for atoms in a finite-cluster model. From this information, the size of region I can be determined.

The force field used in hybrid QM/MM calculations is written with the program `make_input_guess.pl`, that takes as input a force field in the *Gulp* format and the INTER section of the *Guess* input file. Finally, the *bash* scripts `missing.sh`, `divide.sh` and `charge.sh` are used to select the QM cluster inside region I. Detailed instructions on how to perform these operations are given in Section A.5.

### 5.2.2 $\gamma$-Alumina Surfaces

Finite-cluster models of the hydroxylated (001) and (100) $\gamma$-$Al_2O_3$ planes were generated and studied with the embedded molecular cluster approach. The surface (001) was represented with a 13x9 super-cell containing 10786 atoms. The surface area of this model is 54.715 nm$^2$. The surface (100) was represented with a 9x9 super-cell containing 8442 atoms, whose surface area is 55.103 nm$^2$. In both cases, the structural units were generated from the periodic slab model of the corresponding surfaces optimised at the MM level of theory, as described in the previous Section. For atoms represented with the shell model (*i.e.* the oxygen atoms), the position of the cores was used, while the charge was set as the sum of the core+shell charges.

In order to determine the size of region I, the electrostatic potential inside the whole cluster model, shown in Figure 5.4, was computed with the program `epotential_2D`. The electrostatic potential was computed for equivalent atoms, *i.e.* for atoms lying on the same plane, that is, $z = z_0$. For a system of $N_a$ atoms, the electrostatic potential

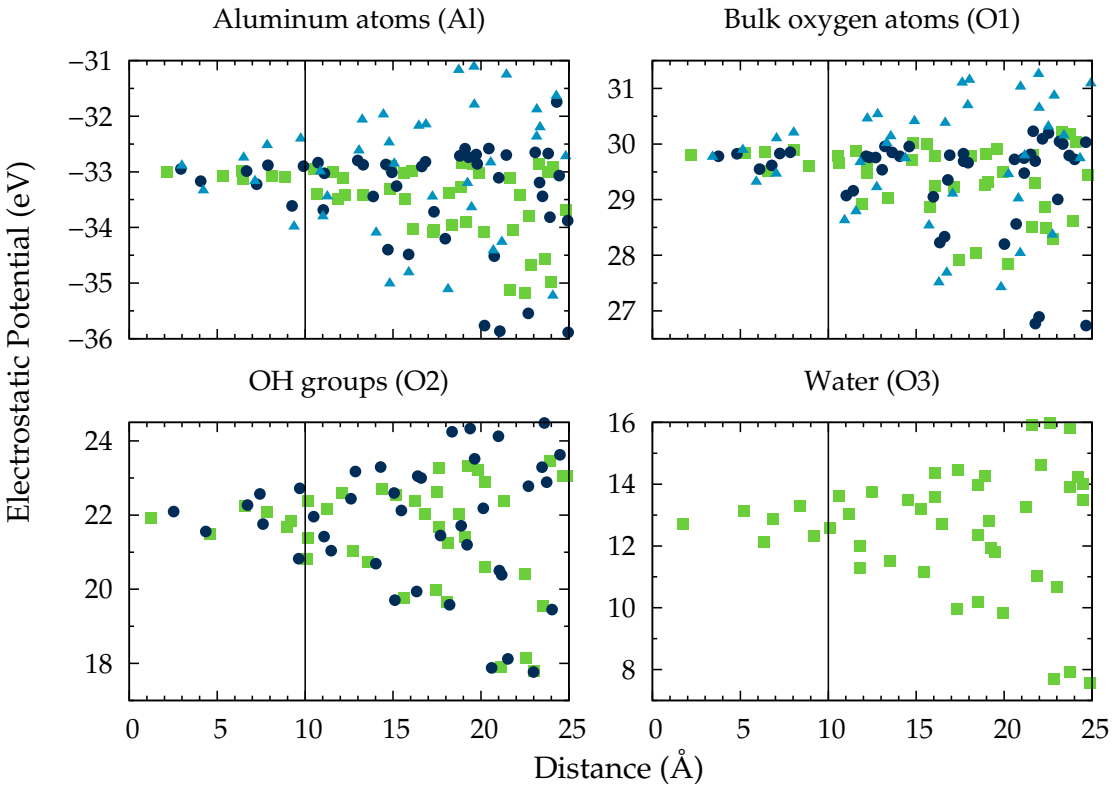


**Figure 5.7:** Electrostatic potentials of a cluster model of a hydroxylated (001) $\gamma$-$Al_2O_3$ surface composed of 13x9 structural units.

experienced by the atom $i$ is defined as

$$V_e(i) = \sum_{\substack{j=1 \\ i \neq j}}^{N_a} \frac{q_j}{r_{ij}} \tag{5.9}$$

for every $i : z_0 - \delta \leq z_i \leq z_0 + \delta$, where $\delta$ is a numerical tolerance, set to 0.01 Å. The electrostatic potential of different species on the planes (001) and (100) is shown in Figures 5.7 and 5.8.

For aluminium and bulk oxygen (*i.e.* O1) atoms, three series were computed for planes in different positions. For atoms belonging to surface groups such as hydroxyl (*i.e.* O2) and water (*i.e.* O3), the planes were chosen to intersect the position of each species. It was found that the mean Coulomb potential has a small variance at the centre of the finite-cluster model and its value increases at the borders. Furthermore,

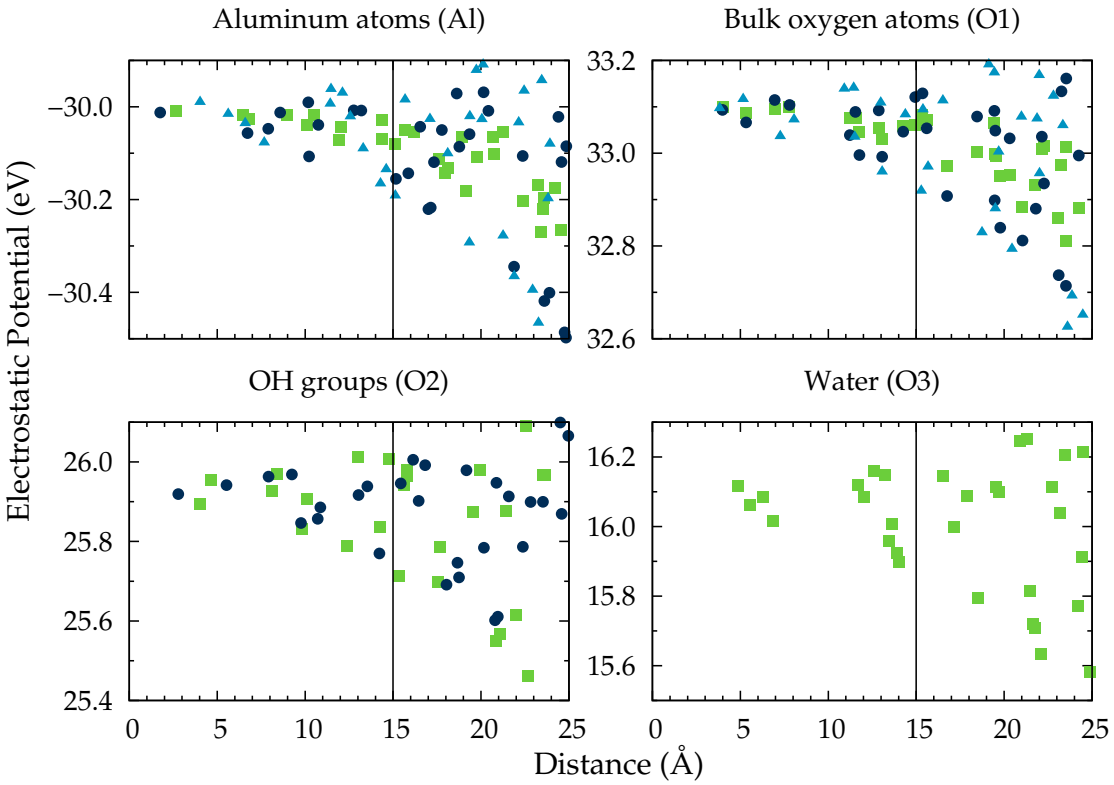


**Figure 5.8:** Electrostatic potentials of a cluster model of a hydroxylated (100) $\gamma$-$Al_2O_3$ surface composed of 9x9 structural units.

atoms on the surface experience fluctuations of the Coulomb potential larger than atoms in the bulk. For the systems considered here, a radius of 10 Å from the centre of the system was chosen to define the boundary between region I (classical relaxed ions) and region II (classical fixed ions). The standard deviation of the Coulomb potential in region I was found to range from 0.14 to 0.50 eV for atoms in the (001) plane, and from 0.0003 to 0.002 eV for atoms in the (100) plane. The differences between the standard deviations in the two planes depend on the morphology of the surfaces and on the area of the finite-cluster model. For a finite-cluster model, a smaller standard deviation is obtained using a larger super-cell. However, for the (001) plane the super-cell used (13x9 structural units) was chosen as the best compromise between accuracy and size of the system.

In order to test the embedded molecular cluster approach, the structure and elec-

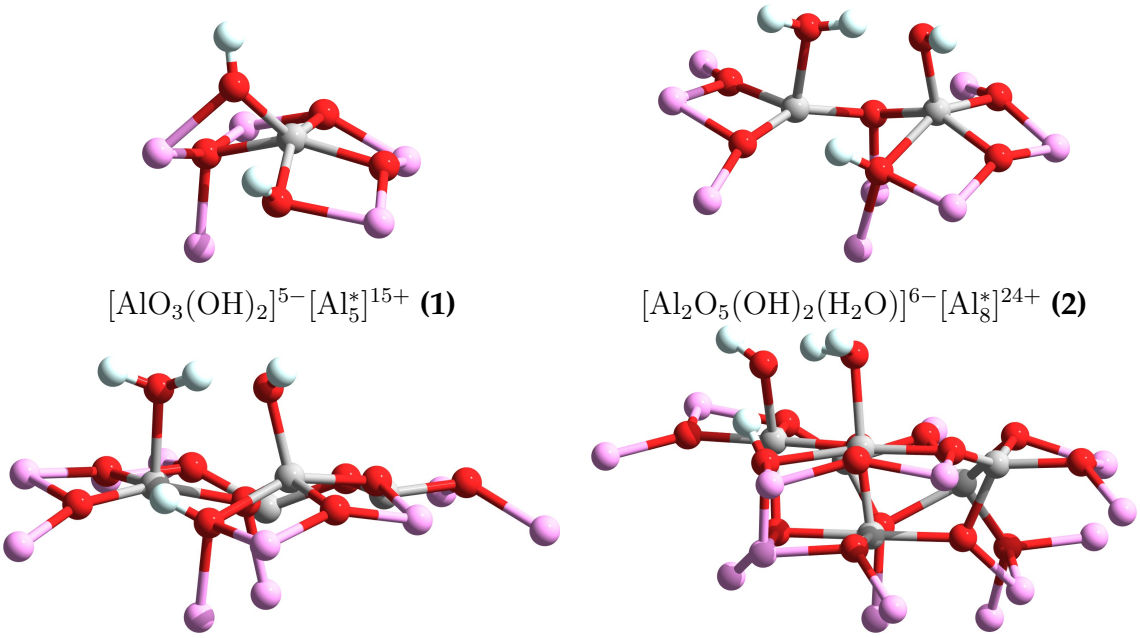

$[AlO_3(OH)_2]^{5-}[Al^*_5]^{15+}$ **(1)**

$[Al_2O_5(OH)_2(H_2O)]^{6-}[Al^*_8]^{24+}$ **(2)**

$[Al_4O_8(OH)_2(H_2O)]^{6-}[Al^*_{10}]^{30+}$ **(3)**

$[Al_6O_{13}(OH)_2(H_2O)]^{10-}[Al^*_{14}]^{42+}$ **(4)**

**Figure 5.9:** Optimised configurations of four quantum clusters used in the embedded cluster calculations of the hydroxylated (001) $\gamma$-$Al_2O_3$ surface. Red atoms are oxygen, white atoms are hydrogen, grey atoms are aluminium and violet atoms are interface aluminium.

tronic properties of hydroxylated $\gamma$-$Al_2O_3$ surfaces were computed with finite-cluster models and the results of the calculations were compared with results obtained with periodic models (Section 3.1.2). Calculations of the hydroxylated (001) $\gamma$-$Al_2O_3$ surface were performed for a sequence of clusters with increasing size. The clusters were chosen so that all the anions were fully coordinated by cations, as recommended in Ref. [58]. The largest cluster considered in this work included 20 aluminium and 16 oxygen atoms, of which two oxygen atoms were in hydroxyl groups and one oxygen atom was in a water molecule. The force field used in region I was that of De Leeuw and Parker [194]. No additional potential terms were added to correct the lattice distortions induced by interface aluminium atoms. However, it has been found that the displacement of interface atoms was small compared to the positions occupied by these atoms in a lattice entirely relaxed at the MM level of theory.

The optimised structures of the QM clusters 1 to 4 obtained for the (001) surface

| Property | QM1 | QM2 | QM3 | QM4 | PM | Structure |
|---|---|---|---|---|---|---|
| $Al^1$-$O^3$ | 2.027 | 1.984 | 2.093 | 2.033 | 1.987 | |
| $Al^1$-$O^4$ | 1.940 | 1.845 | 1.835 | 1.940 | 1.834 | |
| $Al^2$-$O^5$ | – | 1.935 | 1.943 | 1.977 | 1.960 | |
| $Al^2$-$O^6$ | 1.886 | 1.852 | 1.832 | 1.830 | 2.047 | |
| q($O^3$) | -1.21 | -0.98 | -0.97 | -0.98 | -0.97 | |
| q($O^4$) | -0.75 | -0.42 | -0.41 | -0.21 | -1.04 | |
| q($O^7$) | -1.50 | -1.03 | -0.97 | -0.57 | -1.08 | |
| q($O^8$) | – | -1.45 | -1.45 | -0.97 | -1.16 | |
| q($Al^1$) | 0.73 | 0.71 | 0.78 | 0.38 | 1.73 | |
| q($Al^2$) | – | 0.97 | 0.98 | 0.64 | 1.70 | |
| $E_{gap}$ | 6.074 | 5.738 | 5.222 | 5.178 | 4.557 | |

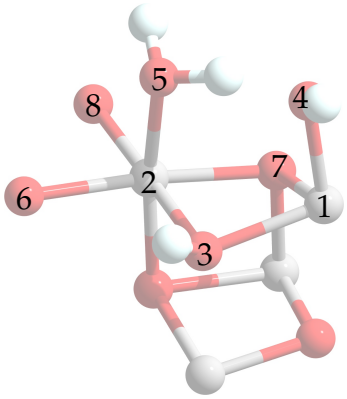


**Table 5.3:** Comparison between geometrical parameters and atomic charges (from Mulliken population analysis) computed for embedded QM clusters 1 to 4 (as in Figure 5.9) and a periodic model (PM) of the hydroxylated (001) plane. Bond lengths are given in Å, charges in $|e|$ and band gap energies in eV.

are shown in Figure 5.9. A comparative analysis of the structures obtained with this method is presented in Table 5.3. The agreement between the structures obtained with the finite model and the periodic model is good, in particular the morphology of the hydroxylated surface is well reproduced within the QM cluster. The computed Mulliken charge on oxygen atoms in hydroxyl groups and water molecules is smaller than the charge on bulk oxygen atoms. This trend is well reproduced with the finite-cluster model, although the charge on oxygen atoms coordinated with interface aluminium atoms is higher than on oxygen atoms coordinated with QM Al atoms. However, the discrepancy introduced by the interface atoms becomes less important as the size of the QM cluster increases. The embedded molecular cluster calculations produce a band-gap higher than the band-gap computed with the periodic model. Even in this case, the difference between the band-gap energy computed with finite and periodic models decreases with the size of the QM cluster.

To assess the ability of the embedded molecular cluster scheme to reproduce the electronic structure of $\gamma$-$Al_2O_3$ surfaces, the density of states (DOS) has been computed as function of the cluster size. The main features of the DOS computed with a periodic

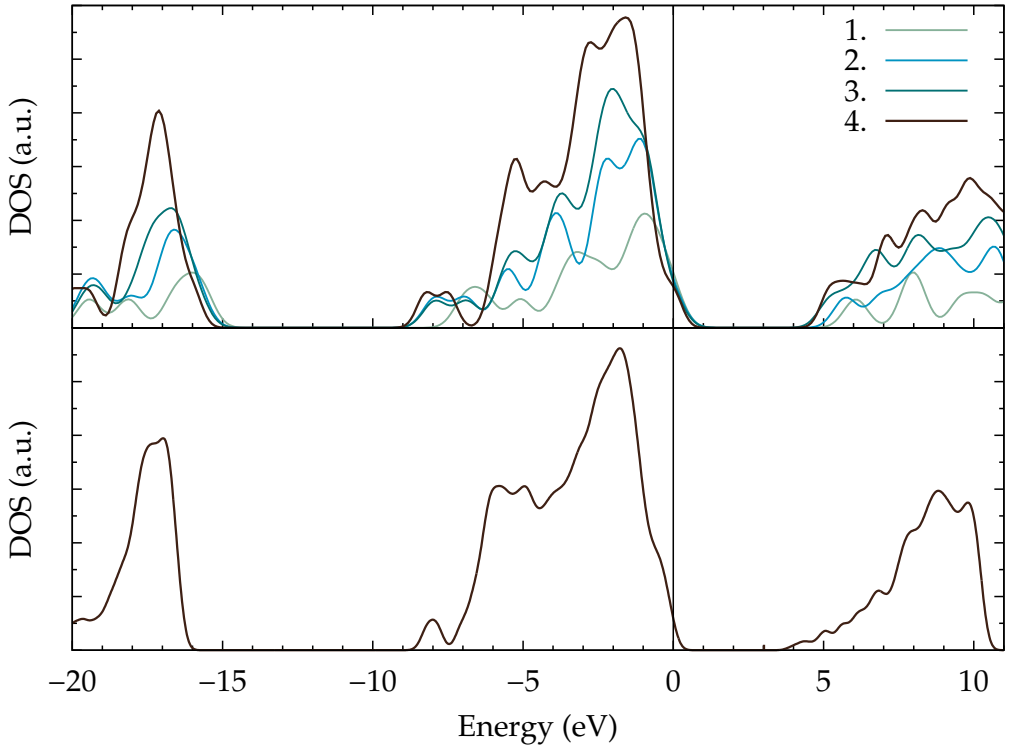


**Figure 5.10:** Density of states calculated for a hydroxylated (001) $\gamma$-alumina surface using the embedded QM clusters 1 to 4 (as shown in Figure 5.9) and a periodic model. In the top panel, embedded cluster DOS calculated at the cc-pVDZ/ECP/PBE level of theory for clusters of increasing size are shown. In the bottom panel, the DOS calculated using a periodic model and a plane-wave basis set is presented. In all cases, the top of the valence band has been shifted to zero.

model are correctly reproduced with the finite-cluster model, as shown in Figure 5.10. The position of peaks in the valence and conduction bands is similar in all the QM clusters considered in this work.

The hydroxylated (100) $\gamma$-$Al_2O_3$ surface was studied in a similar way. Four QM clusters were generated, and their structure optimised until convergence of the total energy was achieved. The optimised structures of QM clusters 5 to 8 are shown in Figure 5.11, and a comparison of the bond lengths, Mulliken charges and band-gap energies is presented in Table 5.4.

The morphology of this surface is preserved in the QM clusters, although some differences with the periodic structure are present. The position of surface hydroxyl

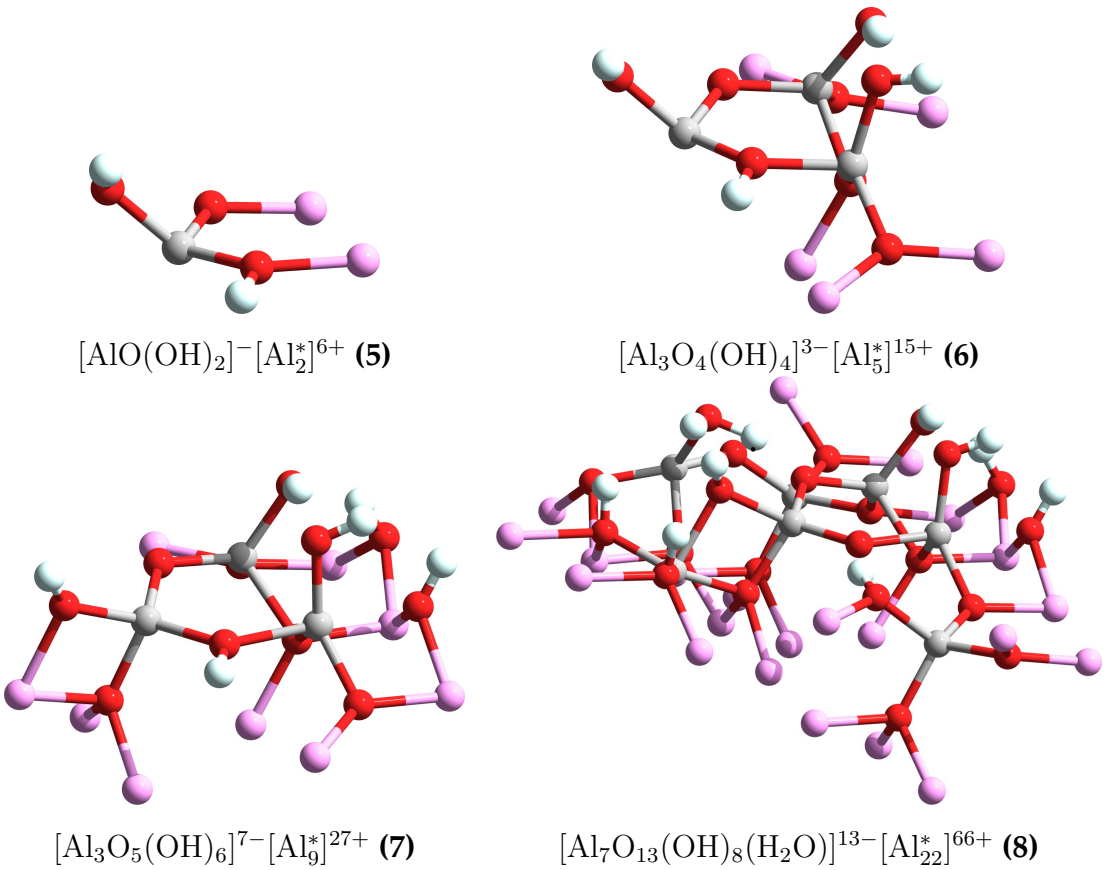

$[AlO(OH)_2]^-[Al_2^*]^{6+}$ **(5)**

$[Al_3O_4(OH)_4]^{3-}[Al_5^*]^{15+}$ **(6)**

$[Al_3O_5(OH)_6]^{7-}[Al_9^*]^{27+}$ **(7)**

$[Al_7O_{13}(OH)_8(H_2O)]^{13-}[Al_{22}^*]^{66+}$ **(8)**

**Figure 5.11:** Quantum clusters used in the embedded cluster calculations of the hydroxylated (100) $\gamma$-$Al_2O_3$ surface. Red atoms are oxygen, white atoms are hydrogen, grey atoms are aluminium and violet atoms are interface aluminium.

groups labelled 7 and 8 in Table 5.4 are well reproduced with the finite-cluster model, while the position of other atoms (*e.g.* oxygen 5 and 9) are more sensitive to the QM cluster size. However, differences between bond lengths obtained with finite and periodic models are within 0.1 Å. The choice of the QM cluster size influences also the distribution of the electronic density, as can be seen from the computed Mulliken charges. Here differences arise in the ground state of each QM cluster: in cluster number 8 for instance there is a hydrogen transfer from an hydroxyl group to a oxygen atom. This change in the morphology of the cluster is reflected in the computed DOS, as can be seen in Figure 5.12.

The band gap obtained for the finite-cluster models is higher than the band gap

| Property | QM5 | QM6 | QM7 | QM8 | PM | Structure |
|---|---|---|---|---|---|---|
| $Al^1$-$O^5$ | 1.763 | 1.762 | 1.824 | 1.869 | 1.767 | |
| $Al^2$-$O^6$ | 1.889 | 1.875 | 1.935 | 1.833 | 1.846 | |
| $Al^2$-$O^7$ | – | 1.774 | 1.790 | 1.798 | 1.773 | |
| $Al^3$-$O^8$ | – | 1.752 | 1.788 | 1.790 | 1.769 | |
| $Al^4$-$O^9$ | – | 1.867 | 1.855 | 1.806 | 1.771 | |
| q($O^5$) | -0.48 | -0.45 | -0.67 | -0.42 | -1.09 | |
| q($O^6$) | -0.88 | -0.46 | -0.43 | -0.60 | -1.07 | |
| q($O^7$) | – | -0.38 | -0.38 | -0.37 | -1.08 | |
| q($O^8$) | – | -0.42 | -0.43 | -0.42 | -1.04 | |
| q($O^9$) | – | -1.37 | -1.38 | -1.00 | -1.17 | |
| q($Al^1$) | 1.01 | 1.01 | 0.73 | 0.73 | 1.91 | |
| q($Al^2$) | – | 0.77 | 0.69 | 0.69 | 1.81 | |
| q($Al^3$) | – | 0.62 | 0.65 | 0.76 | 1.82 | |
| $E_{gap}$ | 5.363 | 4.138 | 5.218 | 4.357 | 3.997 | |

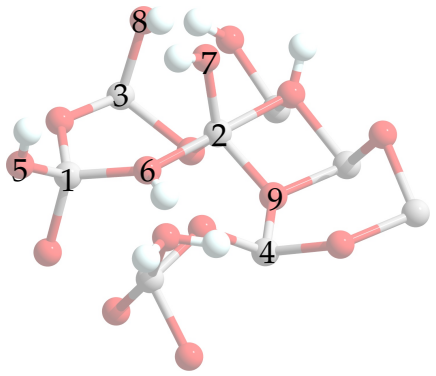


**Table 5.4:** Comparison between geometrical parameters and atomic charges (from Mulliken population analysis) computed for embedded QM clusters 5 to 8 (as in Figure 5.11) and a periodic model (PM) of the hydroxylated (100) plane. Bond lengths are given in Å, charges in $|e|$ and band gap energies in eV.

obtained with the periodic model. However, the main features of the DOS are retained although some differences between the peaks in the valence band are present. These differences are related to the ground states geometries obtained for the finite-cluster models.

In *Guess* the harmonic vibrational frequencies are calculated numerically by geometrical perturbation of the optimised structure. To establish the correct step length ($\Delta$) to be used, harmonic bond stretching frequencies of surface OH groups were computed for step lengths in the range 0.00001 to 0.63 Å. The optimal step value should be large enough to give a significant difference in the potential value (especially in the case of shallow energy potential curves) which is also small enough to avoid going beyond the harmonic region. The computed values of low- and high-frequency OH stretching vibrations on the hydroxylated (001) and (100) $\gamma$-$Al_2O_3$ planes are shown in Figure 5.13. The optimal step length was chosen as $\Delta = 0.0008$ Å, and it was used for all the stretching frequency calculations presented in this work.

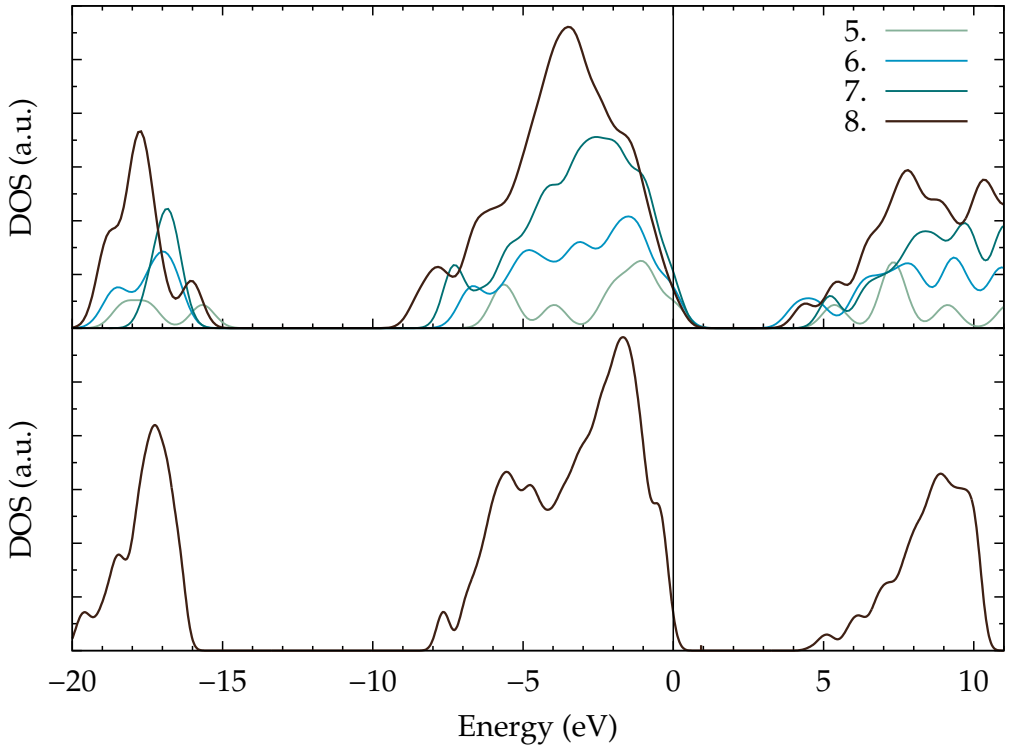


**Figure 5.12:** Density of states calculated for a hydroxylated (100) $\gamma$-alumina surface using the embedded QM clusters 5 to 8 (as shown in Figure 5.11) and a periodic model. In the top panel, embedded cluster DOS calculated at the cc-pVDZ/ECP/PBE level of theory for clusters of increasing size are shown. In the bottom panel, the DOS calculated using a periodic model and a plane-wave basis set is presented. In all cases, the top of the valence band has been shifted to zero.

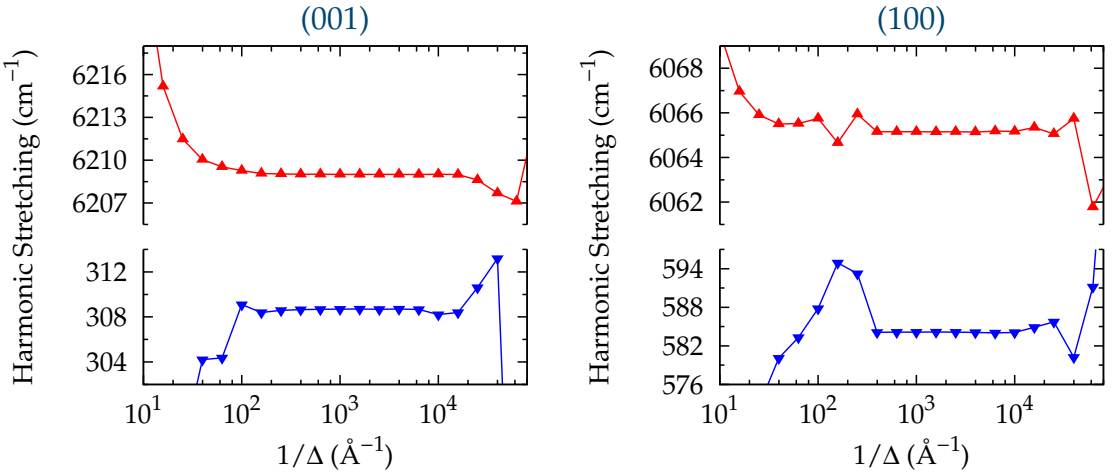


**Figure 5.13:** Convergence of the low and high vibrational modes of isolated OH groups on the (001) and (100) planes with respect to the step length parameter $\Delta$.

### 5.2.3 Surface Rhodium Species

The hydroxylated surfaces of $\gamma$-$Al_2O_3$ have a complex morphology and, as a consequence, several adsorption sites can be identified for the formation of supported $Rh^I(CO)_2$ species. Using the molecular visualisation program *Gdis* [160], six models of surface $Rh^I(CO)_2$ species were built on the hydroxylated (001) $\gamma$-$Al_2O_3$ plane, and another six models were built on the (100) plane. A pictorial view of a finite-cluster model of supported $Rh^I(CO)_2$ species is shown in Figure 5.14. The size of the finite-cluster model and that of region I were identical to those of the finite-cluster models of hydroxylated (001) and (100) $\gamma$-$Al_2O_3$ planes discussed in the previous section. The size of the QM clusters was chosen to minimise the effects of the interface region. The QM clusters of hydroxylated $\gamma$-$Al_2O_3$ surfaces presented in the previous section were used, as appropriate, as absorption sites for surface $Rh^I(CO)_2$ species.

Each model was optimized using the program *Guess*. The calculations in the QM cluster were performed at the PBE level of theory using the program *Gaussian* [155]. The Lanl2DZ(+1d1f) basis set was used for rhodium and the cc-pVDZ basis set was used for all the other atoms. The interface aluminium atoms were described with the Lanl2 ECP plus a minimal $sp$ basis set for valence electrons, as described in the previous section. All the QM clusters studied in this work were chosen to be closed-shell and in a singlet state. No classical potential was used to describe the rhodium atoms and the CO molecules, *i.e.* the adsorbed rhodium complex interacts with the support through the atoms included in the QM cluster, and with the rest of the system only electrostatically. Figures 5.15 and 5.16 show a pictorial view of the optimised structures of supported rhodium species on hydroxylated (001) and (100) $\gamma$-$Al_2O_3$ surfaces. A comparison between the labels used for the finite-cluster models and for the periodic models (section 5.1.1) is shown in Table 5.5.

As explained in Section 5.1, the formation energy of supported $Rh^I(CO)_2$ species was computed according to equation (5.1). Minimum-energy structures of the reactants and products were determined at the PBE/cc-pVDZ level of theory with the program *Gaussian* [155], while the energy of the $\gamma$-$Al_2O_3$ support and the supported

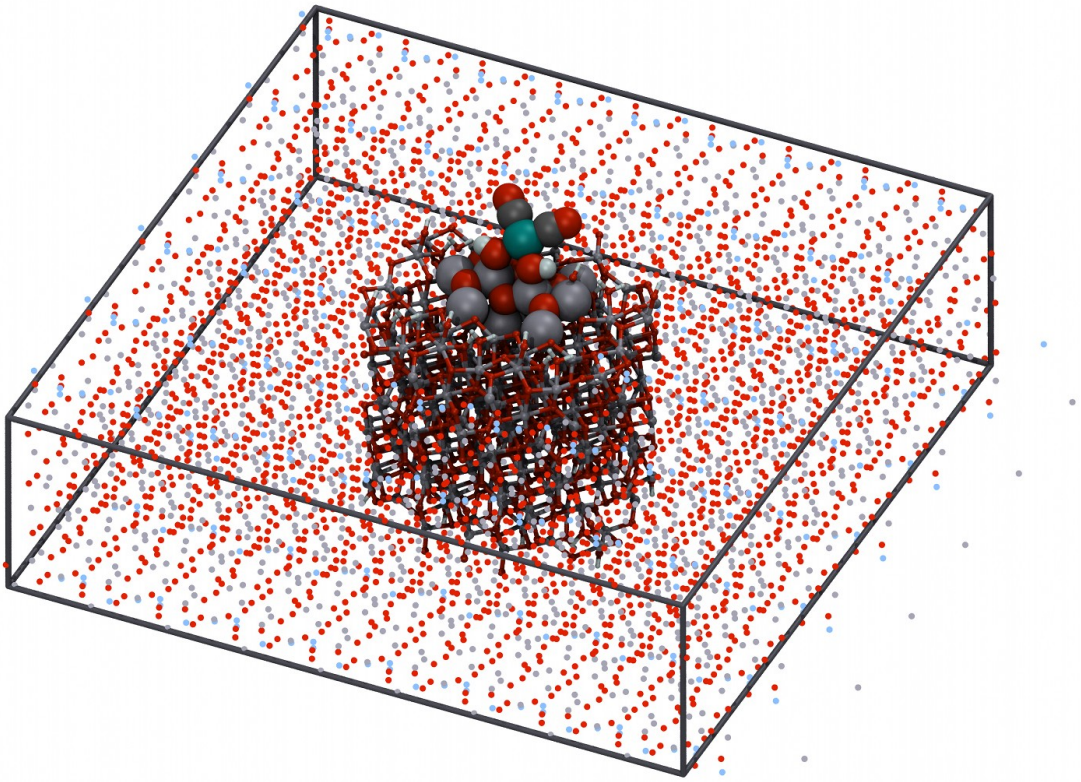

**Figure 5.14:** Pictorial view of a finite-cluster model for an embedded QM/MM calculation. The atoms in the QM cluster are represented as spheres with van der Waals radii, the atoms in region I are shown with a ball-and-stick representation, and form a cylindrical region, and the atoms in region II are represented as shadow-less points. The box around region II is drawn to mark the shape of the whole system.

rhodium carbonyl complex was computed with the program *Guess*. The stoichiometry of the embedded QM clusters was chosen to be consistent with the oxidative adsorption of a rhodium atom, *i.e.* one hydrogen atom was removed from a QM cluster representing the support, and it was replaced with a $\mathrm{Rh^{I}(CO)_2}$ complex to give a finite-cluster model of the supported rhodium species. For metallic rhodium, nanoclusters of different size were optimised in vacuum. As a reliable representation of a metallic nanocluster strongly depends on its size (as outlined in reference [259]), rhodium nanoclusters containing 2, 4, 6, 10 and 14 atoms were considered in this work. The ground state for the $\mathrm{Rh_2}$ cluster was a $^1\Sigma_g$ state, for the $\mathrm{Rh_4}$ cluster it was a $^1A_1$ state, for the $\mathrm{Rh_6}$ cluster it was a $^3A$ state, for the $\mathrm{Rh_{10}}$ cluster it was a $^3B_{2g}$ state and finally for the $\mathrm{Rh_{14}}$

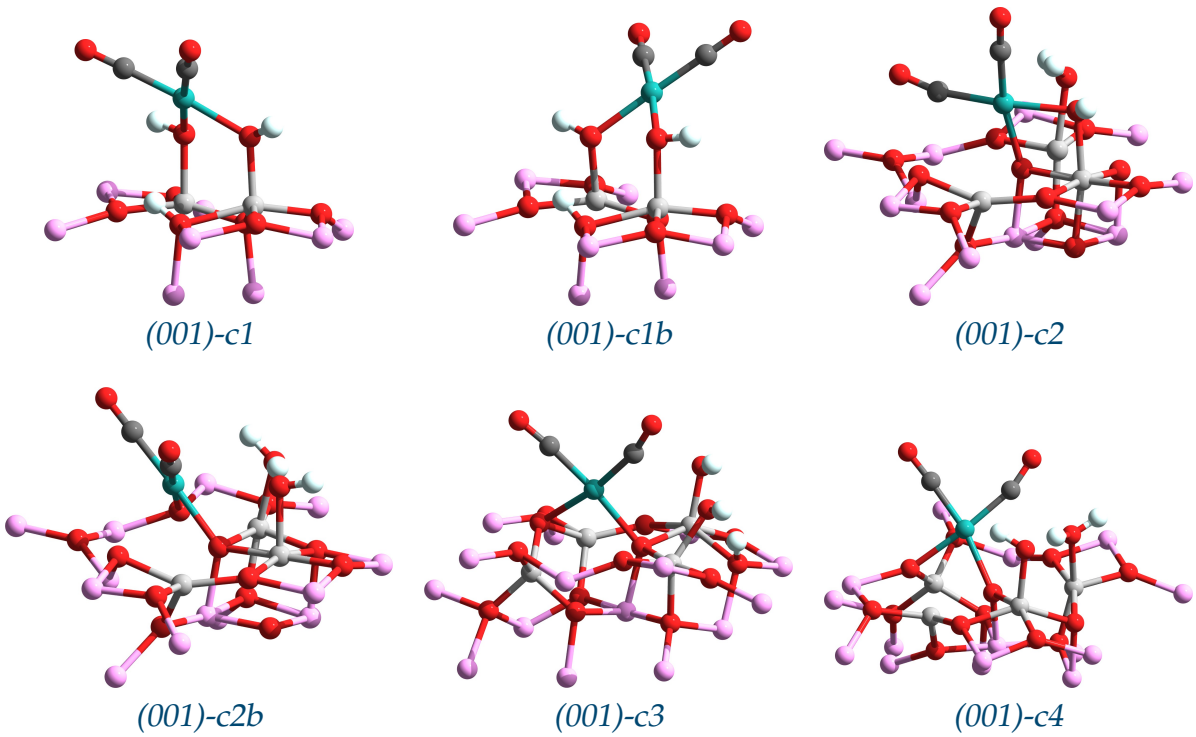


**Figure 5.15:** Models of supported $\mathrm{Rh^{I}(CO)_2}$ complexes optimised with a finite-cluster model of the hydroxylated (001) $\gamma$-$\mathrm{Al_2O_3}$ surface. Initial structures were optimised at the cc-pVDZ/ECP/PBE level of theory. Red atoms are oxygen, white atoms are hydrogen, grey atoms are aluminium, violet atoms are interface aluminium, grey atoms are carbon and aquamarine atoms are rhodium.

cluster the ground state was a ${}^3A$ state. The total energy per rhodium atom converges to a stationary value as the nanocluster increases its size, as shown in Figure 5.17. The energy of a rhodium atom was extrapolated from this trend, as suggested in reference [260].

The formation energies of supported $\mathrm{Rh^{I}(CO)_2}$ species computed in such a way are overestimated with respect to those obtained using periodic model approach (Table 5.2), as can be seen from the values reported in Table 5.6. The formation energies computed with a periodic model are expected to be more reliable than formation energies computed with a finite model since in periodic plane-wave/DFT calculations a reasonably large plane-wave basis set was used and all the reactants and products in equation 5.1 were studied in their more stable phase (*e.g.* metallic crystal rhodium). For finite-

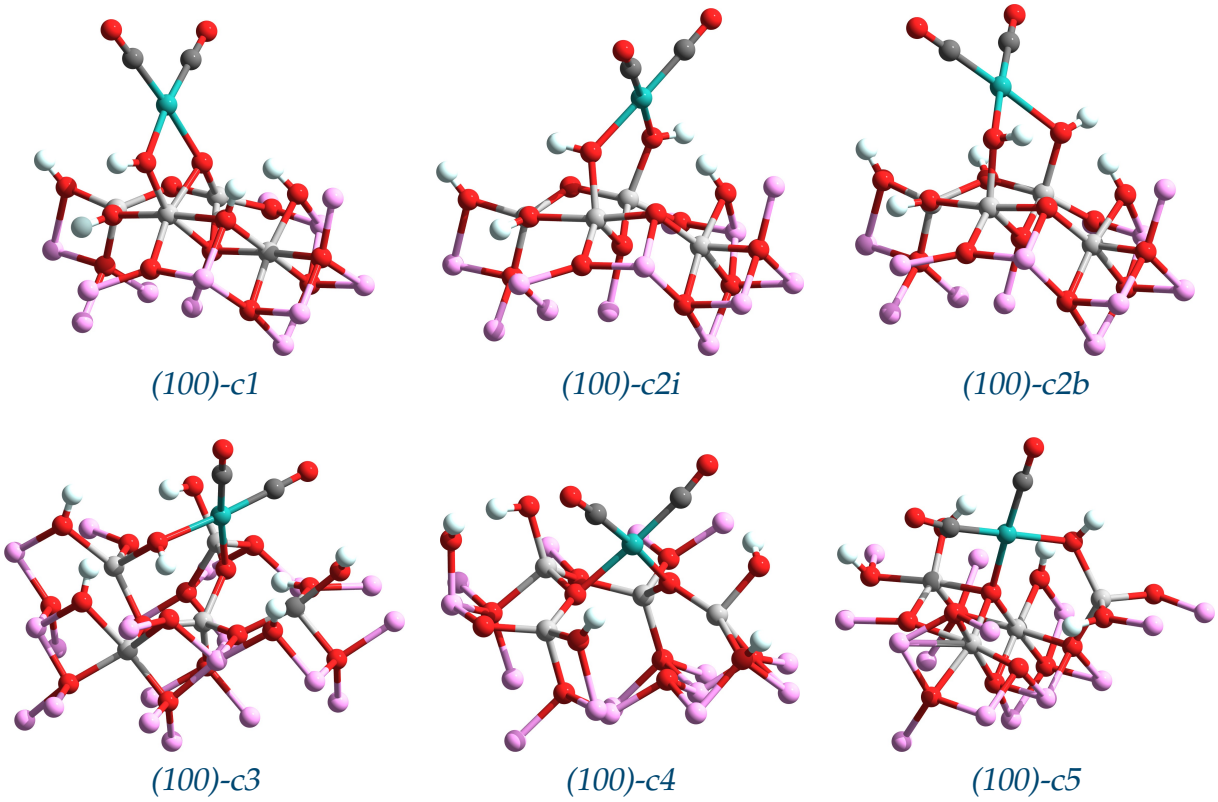


**Figure 5.16:** Models of supported $Rh^{I}(CO)_2$ complexes optimised with a finite-cluster model of the hydroxylated (100) $\gamma$-$Al_2O_3$ surface. Initial structures were optimised at the cc-pVDZ/ECP/PBE level of theory. Red atoms are oxygen, white atoms are hydrogen, grey atoms are aluminium, violet atoms are interface aluminium, grey atoms are carbon and aquamarine atoms are rhodium.

cluster calculations more realistic values are expected to be obtained using the energy of a metallic rhodium nanocluster adsorbed on $\gamma$-$Al_2O_3$ surfaces. Furthermore, it has not been verified how much the computed results change with respect to the dimension of the QM cluster and with respect to the basis set size. However, the formation energies obtained with the embedded molecular cluster approach are useful to estimate relative stability of isomers such as complexes (001)-c1 and (001)-c1b, which have the same number of atoms but different configurations.

The bond lengths of the minimum-energy structures are summarised in Table 5.7. Good agreement is found with the experimental data from EXAFS determinations [247]. For the Al–O distances, the mean value with the standard deviation is reported

| Plane (001) | | Plane (100) | |
|---|---|---|---|
| PM | FC | PM | FC |
| s1 | c1 | s1 | c1 |
| | c1b | | c2i |
| s2 | c2 | s2 | c2b |
| s3 | c2b | s3 | c3 |
| | c3 | s4 | c4 |
| s4 | c4 | s5 | c5 |

**Table 5.5:** Correspondence between the labelling used to name supported $Rh^{I}(CO)_2$ species modelled using the periodic model (PM) and the finite-cluster model (FC).

| Complex | Energy | Complex | Energy |
|---|---|---|---|
| Plane (001) | | Plane (100) | |
| *c1* | -84.772 | *c1* | -88.949 |
| *c1b* | -84.627 | *c2i* | -68.550 |
| *c2* | -73.665 | *c2b* | -69.925 |
| *c2b* | -87.118 | *c3* | -65.478 |
| *c3* | -68.017 | *c4* | -89.804 |
| *c4* | -71.571 | *c5* | -82.948 |

**Table 5.6:** Formation energies (kcal/mol) of supported $Rh^{I}(CO)_2$ species computed with the embedded molecular cluster approach. The labelling of the complexes is given in Figures 5.15 and 5.16.

for oxygen atoms coordinated to more than one aluminium atom. In all the optimised structures, rhodium complexes have a square-planar coordination geometry and a morphology consistent with the equivalent structures optimised with a periodic model (see Table 5.5 for the labels of equivalent structures).

Surface rhodium complexes adsorbed on the (001) surface induce a small reconstruction of the adsorption site. The (RhCO) angle in the complexes (001)-c2 and (001)-c4 is distorted because of the presence of the neighbouring hydroxyl groups. Complex (001)-c2 has a distorted angle (RhCO) = 168.29° and complex (001)-c4 has a distorted angle (RhCO) = 162.31°, in agreement with the equivalent structures obtained with periodic models which have distorted (RhCO) angles equal to 168.80° and 161.42° re-

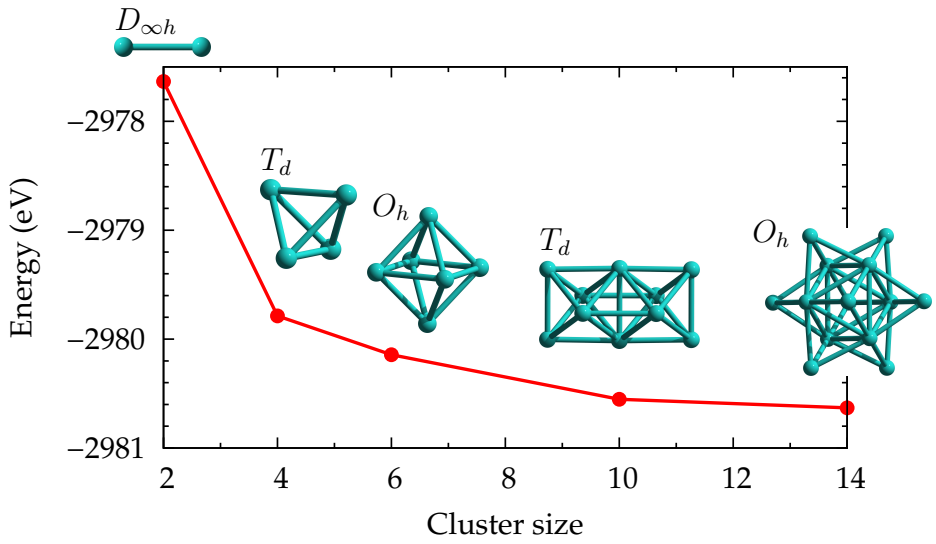


**Figure 5.17:** Electronic energy per rhodium atom in metallic rhodium nanoclusters $\mathrm{Rh_n}$, n $= 2, 3, 6, 10, 14$. Calculations were performed with respect to vacuum at the PBE/ECP level of theory. Cluster shape and point group are shown as insets.

spectively. The complex (001)-c3 is an isomer of (001)-c4 and has a distorted angle (RhCO) = 166.34°. The higher distortion gives rise to a relative formation energy 3.5 kcal/mol higher than the (001)-c4 complex.

The surface rhodium complexes adsorbed on the (100) surface induce a significant reconstruction of the adsorption site, leading to more stable structures. The complex (100)-c2i is ~1.4 kcal/mol more stable than the complex (100)-c2b, but it has a similar electronic structure, as can be seen from the computed Mulliken charges shown in Table 5.8. The geometrical optimisations of complexes (100)-c3, (100)-c4 and (100)-c5 induce a reconstruction of the surface. For the complex (100)-c4, the $\gamma$-$\mathrm{Al_2O_3}$ surface changes its morphology because of dissociation of a water molecule yielding two separate hydroxyl groups. The complex (100)-c5 has a distorted angle (RhCO) = 171.65° that is similar to that in the equivalent complex obtained with a periodic approach, which has an angle (RhCO) = 172.43°.

The harmonic frequencies computed at the QM/MM level are reported in Table 5.9. The computed symmetric and anti-symmetric stretching frequencies of the carbonyl

| Complex | r(Rh–C) | | r(C–O) | | r(Rh–O) | | r(O–Al) | |
|---|---|---|---|---|---|---|---|---|
| | | | | Plane (001) | | | | |
| *c1* | 1.839 | 1.850 | 1.161 | 1.161 | 2.053 | 2.114 | 1.896 | 1.933 |
| *c1b* | 1.837 | 1.840 | 1.161 | 1.162 | 2.085 | 2.116 | 1.894 | 1.914 |
| *c2* | 1.824 | 1.864 | 1.160 | 1.163 | 2.092 | 2.178 | 1.944 | 1.979(45) |
| *c2b* | 1.836 | 1.847 | 1.164 | 1.164 | 2.097 | 2.113 | 1.880 | 2.085 |
| *c3* | 1.821 | 1.856 | 1.159 | 1.166 | 2.191 | 2.240 | 1.909(55) | 1.971(27) |
| *c4* | 1.828 | 1.857 | 1.163 | 1.165 | 2.134 | 2.172 | 1.880 | 2.005 |
| | | | | Plane (100) | | | | |
| *c1* | 1.831 | 1.842 | 1.162 | 1.163 | 2.063 | 2.093 | 1.89(12) | 1.893 |
| *c2i* | 1.836 | 1.840 | 1.158 | 1.161 | 2.086 | 2.104 | 1.879 | 1.881 |
| *c2b* | 1.832 | 1.843 | 1.159 | 1.159 | 2.090 | 2.152 | 1.865 | 1.880 |
| *c3* | 1.829 | 1.838 | 1.159 | 1.162 | 2.178 | 2.221 | 1.880(65) | 1.897 |
| *c4* | 1.835 | 1.850 | 1.158 | 1.164 | 2.096 | 2.110 | 1.795(17) | 1.851(43) |
| *c5* | 1.827 | 1.846 | 1.160 | 1.162 | 2.137 | 2.143 | 1.864 | 1.911(38) |
| | | | | Experimental[a] | | | | |
| | 1.814 (2) | | 1.189 (3) | | 2.038 (2) | | | |

[a] Structural parameters from EXAFS measurements [247].

**Table 5.7:** Bond lengths (Å) relative to surface $\mathrm{Rh^{I}(CO)_2}$ species optimised with the embedded molecular cluster approach. QM calculations performed at the cc-pVDZ/ECP/PBE level of theory with the program *Gaussian* GO3-D02. For oxygen atoms coordinated with more than one aluminium atom, the mean value of bond length is reported, with standard deviation in parentheses. The labelling of the complexes is given in Figures 5.15 and 5.16.

groups are in good with experimental IR values. From this result, it can be concluded that the computed models of the surface $\mathrm{Rh^{I}(CO)_2}$ species give a realistic representation of the actual material.

As the computed infrared frequencies show good agreement with the experimental values and the formation energies are overestimated, it is proposed to compare the simulated XANES spectrum of each species with the experimental XANES spectrum, as a way to assess the reliability of each structure. Rh K-edge XANES spectra of supported $\mathrm{Rh^{I}(CO)_2/\gamma\text{-}Al_2O_3}$ species were computed with the program *Feff* version 8.4 [255] on the basis of full-multiple scattering theory. Atoms up to 7 Å from rhodium were included to obtain converged XANES calculations. The spectra were calculated

| Complex | q(Rh) | q(C) | q(C) | q(O) | q(O) |
|---|---|---|---|---|---|
| | | | Plane (001) | | |
| *c1* | 0.092 | -0.012 | -0.007 | -0.020 | -0.023 |
| *c1b* | 0.148 | -0.056 | -0.036 | -0.013 | -0.022 |
| *c2* | -0.203 | -0.030 | -0.004 | -0.026 | -0.016 |
| *c2b* | -0.291 | -0.031 | 0.012 | -0.035 | -0.041 |
| *c3* | 0.073 | -0.040 | -0.020 | -0.006 | -0.052 |
| *c4* | 0.055 | -0.034 | -0.034 | -0.021 | -0.013 |
| | | | Plane (100) | | |
| *c1* | 0.272 | -0.082 | -0.089 | -0.012 | -0.018 |
| *c2i* | 0.195 | -0.048 | -0.068 | 0.009 | 0.004 |
| *c2b* | 0.201 | -0.044 | -0.054 | 0.005 | 0.011 |
| *c3* | 0.088 | -0.045 | -0.029 | -0.005 | -0.016 |
| *c4* | 0.326 | -0.075 | -0.065 | -0.030 | 0.004 |
| *c5* | 0.212 | -0.048 | -0.082 | 0.020 | -0.002 |

**Table 5.8:** Computed Mulliken charges ($|e|$) of rhodium, carbon and oxygen atoms obtained from hybrid QM/MM simulations. The labelling of the complexes is given in Figures 5.15 and 5.16.

using the Hedin-Lundqvist model of the exchange potential.

Figures 5.18 and 5.19 show the spectra of complexes optimised on hydroxylated (001) and (100) $\gamma$-alumina surfaces, respectively. The agreement with the experimental spectrum is good for most of the computed spectra, as can be seen from the RMS values in Table 5.10.

The best agreement is found for the complex (100)-c4, which has a RMS = 0.0129 and which is the complex with the most negative formation energy in Table 5.6. The worst agreement is found for complexes (001)-c2 and (100)-c3, which have a RMS of 0.0213 and 0.0234, respectively. The formation energy of complexes (001)-c2 and (100)-c3 is also among the least negative, suggesting that complexes with the lowest formation energy have also unrealistic structures. However, it should be noted once again that many different structures make a contribution in the experimental spectrum, which is better described by a linear combination of the spectra of all the more energetically stable structures.

From these results it can be concluded that embedded molecular cluster calcula-

| Complex | $\nu$(CO) (cm$^{-1}$) | | Complex | $\nu$(CO) (cm$^{-1}$) | |
|---|---|---|---|---|---|
| | Plane (001) | | | Plane (100) | |
| *c1* | 2018.14 | 2079.40 | c1 | 2009.19 | 2070.05 |
| *c1b* | 2015.90 | 2078.06 | c2i | 2029.33 | 2092.11 |
| *c2* | 2010.92 | 2078.06 | c2b | 2031.83 | 2092.92 |
| *c2b* | 1993.12 | 2059.99 | c3 | 2019.45 | 2082.79 |
| *c3* | – | – | c4 | 2008.40 | 2077.10 |
| *c4* | 2001.45 | 2064.22 | c5 | 2014.72 | 2075.81 |
| | Experimental[a] | | | | |
| | 2027(2) | 2095(1) | | | |

[a] IR measurements for a 2% wt supported rhodium catalyst under CO atmosphere [4].

**Table 5.9:** Harmonic stretching frequencies of surface $\mathrm{Rh^{I}(CO)_2}$ species computed with the embedded molecular cluster approach. The QM calculations were performed at the cc-pVDZ/ECP/PBE level of theory with the program *Gaussian* GO3-D02.

| | | | | | | |
|---|---|---|---|---|---|---|
| | | | Plane (001) | | | |
| **complex** | c1 | c1b | c2 | c2b | c3 | c4 |
| **RMS** | 0.0195 | 0.0185 | 0.0213 | 0.0181 | 0.0204 | 0.0207 |
| | | | Plane (100) | | | |
| **complex** | c1 | c2i | c2b | c3 | c4 | c5 |
| **RMS** | 0.0191 | 0.0182 | 0.0192 | 0.0234 | 0.0129 | 0.0200 |

**Table 5.10:** Root mean square (RMS) values indicating the difference between the theoretical XANES spectra and the experimental XANES spectrum.

tions of supported rhodium species have produced reasonable microscopic models of the actual catalyst, being able to give very good agreement between the experimental structural and spectroscopic evidence and the corresponding computed structural and spectroscopic properties.

## 5.3 Conclusions

In this chapter periodic and finite-cluster models of supported rhodium catalysts have been produced. For periodic models, the plane-wave/DFT method was used to obtain

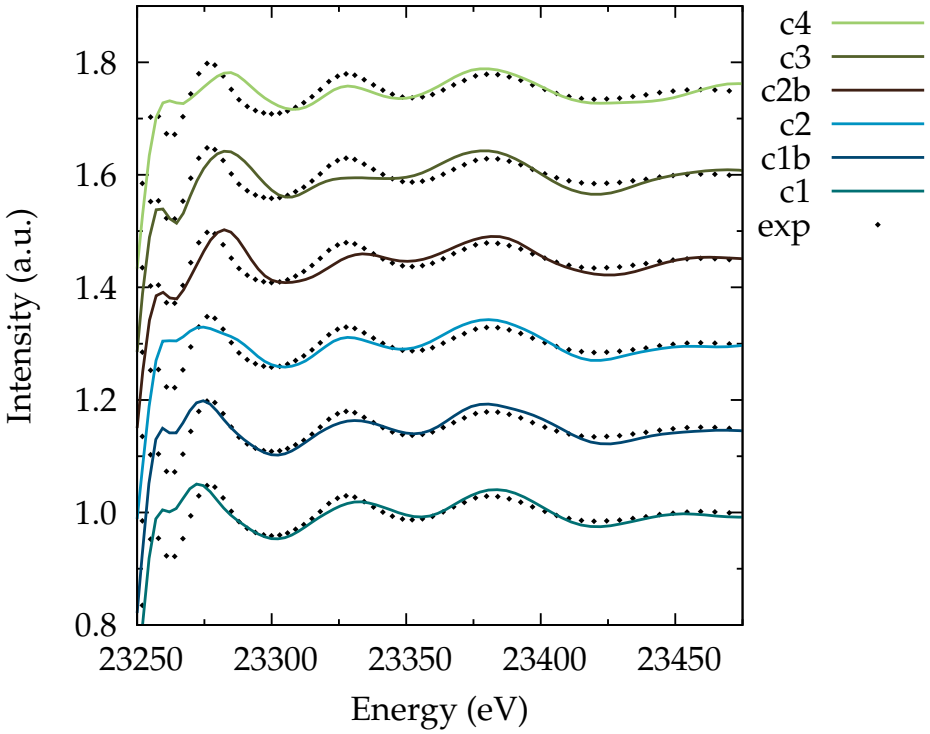


**Figure 5.18:** Comparison between experimental and theoretical XANES spectra at the Rh $K$-edge. Theoretical spectra were calculated using the structure of $\mathrm{Rh^{I}(CO)_2}$ complexes optimised on the hydroxylated (001) $\gamma$-$\mathrm{Al_2O_3}$ plane using the embedded molecular cluster approach.

minimum-energy structures and formation energies of supported $\mathrm{Rh^{I}(CO)_2}$ species.

In all the optimised structures, the surface rhodium complexes exhibit a square-planar coordination geometry, in agreement with the experimental evidence available for these species. Good agreement was found between the computed bond lengths and the bond lengths determined by EXAFS spectroscopy [247]. Furthermore, a Rh K-edge XANES spectrum was calculated on the basis of full multiple-scattering theory as an average of the spectra derived from the three most energetically stable structures. Good agreement was found between the experimental and theoretical XANES spectra. As XANES spectra are very sensitive to the spatial distribution of the atoms surrounding the photo-absorber -in terms of either bond lengths and bond angles- it can be concluded that the models obtained with this approach are highly realistic.

Finite-cluster models of supported $\mathrm{Rh^{I}(CO)_2}$ species were studied using an hybrid

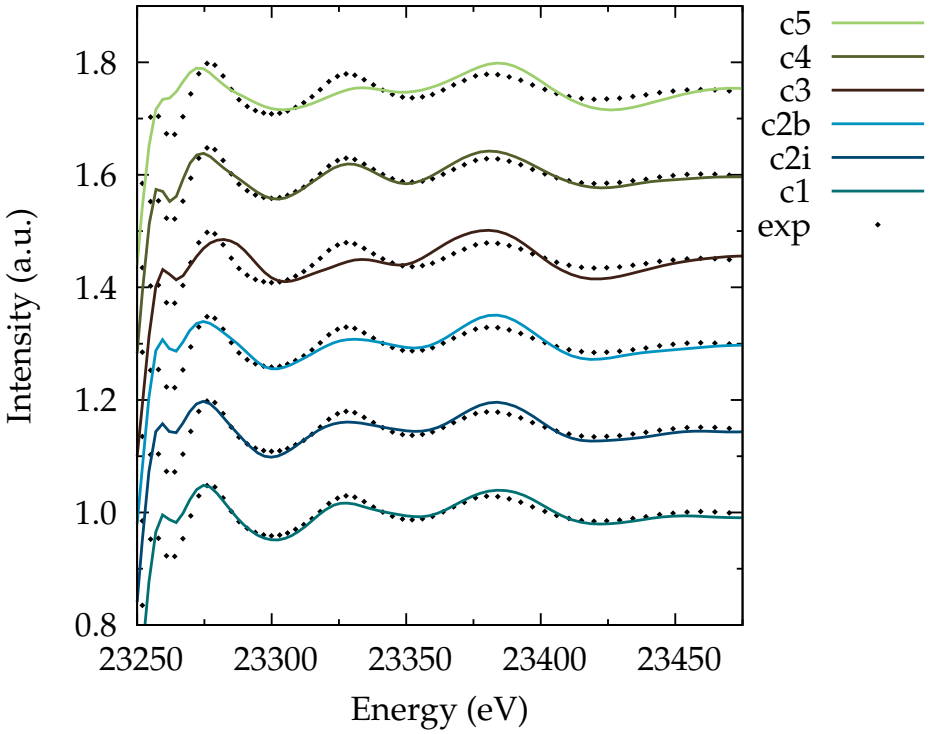


**Figure 5.19:** Comparison between experimental and theoretical XANES spectra at the Rh $K$-edge. Theoretical spectra were calculated using the structure of $\mathrm{Rh^{I}(CO)_2}$ complexes optimised on the hydroxylated (100) $\gamma$-$\mathrm{Al_2O_3}$ plane using the embedded molecular cluster approach.

QM/MM approach, as implemented in the program *Guess* [58, 59, 239]. This method was used to study hydroxylated $\gamma$-alumina surfaces; in particular properties such as bond lengths and electronic structure were investigated as a function of the dimension of the cluster studied at the QM level of theory. Supported rhodium species were studied at the PBE/ECP/cc-pVDZ level of theory: twelve structures were obtained by minimisation of the total energy and it was found that these structures had bond lengths which were within 0.02 Å of the experimental bond lengths, as determined by EXAFS spectroscopy [247]. The morphologies of the optimised complexes are consistent with that of complexes obtained using periodic models, but it was found that the formation energies computed with the finite-cluster model are overestimated with respect to those obtained with a periodic model. This result is likely due to over-estimation of the energy of the reactants, in particular the energy of rhodium is derived from QM

calculation of small rhodium nano-clusters with respect to the vacuum. In comparison, plane-wave/DFT calculations give more reliable energies since all the reactants and products in equation 5.1 were considered in their more stable phase.

To improve the results obtained using the finite-cluster approach, it is proposed to study the interaction of metallic rhodium nano-clusters with surfaces of $\gamma$-alumina, to consider the effect of a larger basis set in the calculations and to test the stability of results with respect to the size of the QM cluster.

The symmetric and anti-symmetric stretching modes of carbonyl groups of supported $\mathrm{Rh^{I}(CO)_2}$ species were computed numerically and they were found to be in very good agreement with the experimental IR determinations. Multiple-scattering calculations were carried out on the optimised structures. Theoretical Rh K-edge spectra are in very good agreement with the experimental XANES spectrum, confirming that the morphology of the $\mathrm{Rh^{I}(CO)_2}$ adsorption sites is well described with the structural model of supported rhodium catalysts presented in this work.

CHAPTER 6

# CONCLUSIONS

The main objective of this project was to provide a theoretical description of the chemical properties and reactivity of a particular class of heterogeneous catalysts based on transition metals supported on a metal oxide such as $\gamma$-alumina. The system investigated in this work was $\mathrm{Rh^{I}(CO)_2}/\gamma\text{-}\mathrm{Al_2O_3}$, a species that is formed when a catalyst composed of metallic rhodium supported on hydroxylated $\gamma\text{-}\mathrm{Al_2O_3}$ is exposed to gaseous CO at room temperature [4–7, 43]. Supported $\mathrm{Rh^{I}(CO)_2}/\gamma\text{-}\mathrm{Al_2O_3}$ species have been characterised experimentally by using a combination of complementary techniques such as energy-dispersive EXAFS (EDE), mass spectrometry (MS) and infrared spectroscopy (IR) carried out simultaneously, under well-defined conditions [7, 42, 47].

Two theoretical methods were used to compute the ground-state properties of supported $\mathrm{Rh^{I}(CO)_2}$ species. A plane-wave/DFT method with periodic boundary conditions, as implemented in the program *Castep* [158], was used to obtain realistic models of hydroxylated $\gamma\text{-}\mathrm{Al_2O_3}$ surfaces, using the bulk model of $\gamma\text{-}\mathrm{Al_2O_3}$ proposed by Digne and co-workers [16, 27, 29]. This model was chosen because it has been shown to reproduce the physical and chemical properties of hydroxylated $\gamma$-alumina surfaces, with particular emphasis on hydroxylation/dehydroxylation processes induced by temperature. Parameters of simulations presented in this work, such as basis set cut-off energy, slab thickness and vacuum thickness, were determined variationally in Chapter 3. This theoretical method was applied to compute the structural properties (zero-pressure lattice parameters and bulk modulii) of corundum, $\gamma$-alumina and diaspore, and the results obtained show good agreement with experimental data and with re-

sults of similar calculations published in the literature.

The structures of hydroxylated $\gamma$-alumina surfaces computed in this thesis work are in agreement with the results of equivalent calculations carried out at the plane-wave/DFT level of theory [27, 29]. Plane-wave/DFT calculations were also employed to optimise the complex $[\mathrm{Rh(CO)_2Cl}]_2$ in Chapter 4, obtaining bond lengths in agreement with X-ray measurements [229] and with equivalent calculations performed at the PBE/ECP/cc-pVTZ level of theory.

Nine different structures of surface $\mathrm{Rh^I(CO)_2}/\gamma\text{-}\mathrm{Al_2O_3}$ species were optimised at the plane-wave/DFT level of theory. In all the optimised structures the rhodium atom exhibits a square-planar coordination geometry, in agreement with *in-situ* infra-red and EXAFS spectroscopy measurements [7, 43, 247–250]. The formation energies for these complexes were computed using the formation mechanism proposed by Basu and co-workers [6] (equation 5.1). In all cases, a negative formation energy was found.

Formation energies were used to compute Boltzmann weighting factors at 300K. According to these factors, the three most dominant structures of surface $\mathrm{Rh^I(CO)_2}$ species were used to compute Rh K-edge XANES spectra on the basis of full-multiple scattering theory with the program *Feff* version 8.4 [255]. The weighted linear combination of the computed spectra reproduces well the features of the experimental spectrum, such as phase and shape of the oscillations, providing support for the theoretical structures used to compute the XANES spectra. From this study it can be concluded that reliable microscopic models of supported $\mathrm{Rh^I(CO)_2}/\gamma\text{-}\mathrm{Al_2O_3}$ species were obtained from calculations carried out at the plane-wave/DFT level of theory with periodic boundary conditions applied.

The other theoretical method used to study supported rhodium catalysts was the embedded molecular cluster (EMC) approach as implemented in the program *Guess* [58, 59, 239]. Within this scheme the region of interest is studied at the quantum mechanical (QM) level of theory. The QM cluster is then embedded in a region of polarizable ions described with the shell-model [132], which provides a convenient description of the electrostatic and steric constraints produced by the atomic environment of

the QM cluster. Fixed non-polarizable ions placed outside these two regions provide the correct electrostatic potential, simulating the potential produced by an infinite surface.

Basis sets based on the Los Alamos effective core potential (ECP) [212–214] were designed for the Rh atom and used to investigate the Rh ionisation energy and electron affinity at the UCCSD(T) level of theory with the program *Gaussian* [155]. The Rh ECP basis sets were also used to perform calculations at the DFT level of theory on small rhodium complexes, and very good agreement with the available experimental evidence was found (Chapter 4).

A force field proposed by De Leeuw and Parker (DLP) [194] was used to obtain structural models of hydroxylated $\gamma$-$Al_2O_3$ surfaces using the program *Gulp* [127]. This force field was modified to achieve agreement with the morphology of structures optimised at the plane-wave/DFT level of theory, as described in section 3.2.2. The modified DLP force field was also used to compute the structural properties (zero-pressure lattice parameters and bulk modulii) of corundum, $\gamma$-alumina and diaspore, and good agreement with the experimental data and with the results of plane-wave DFT calculations carried out in this thesis work was obtained.

Hybrid QM/MM calculations were carried out with the program *Guess*. Hydroxylated (001) and (100) $\gamma$-$Al_2O_3$ surfaces were studied as a function of the QM cluster size. Calculations on the QM clusters were carried out at the PBE/ECP/cc-pVDZ level of theory, while the embedding region was accounted for at the MM level of theory using the DLP force field. The computed bond lengths and electronic structures of hydroxylated $\gamma$-$Al_2O_3$ surfaces were found to be in agreement with the results of plane-wave/DFT calculations. In particular, better agreement was found for the QM clusters with the larger size.

Twelve structures of surface $Rh^{I}(CO)_2$ species were studied using the same approach used to carry out hybrid QM/MM calculations on hydroxylated $\gamma$-$Al_2O_3$ surfaces. The optimised structures of surface $Rh^{I}(CO)_2$ species have the Rh atom in a square-planar coordination geometry and morphologies of the adsorption sites con-

sistent with those obtained at the plane-wave/DFT level of theory. Good agreement was found between the computed bond lengths and the bond lengths determined by EXAFS spectroscopy [247]. The XANES spectra computed at the Rh K-edge are in good agreement with the experimental XANES spectrum, providing support for the optimised structures used to compute the XANES spectra. The computed RhC–O harmonic stretching frequencies were in good agreement with IR values [4], suggesting that the bond order for the RhC–O bond is reproduced correctly, and hence also for the Rh–CO bond. The formation energies computed with the EMC approach are over-estimated with respect of formation energies computed at the plane-wave/DFT level of theory. This effect is likely to be due to over-estimation of the energy of metallic rhodium in equation 5.1.

## 6.1 Future work

The results presented in this thesis showed that reliable microscopic structures of transition metal complexes adsorbed on hydroxylated $\gamma$-alumina surfaces can be obtained using an appropriate theoretical methodology. Plane-wave/DFT calculations provided an accurate description of the structural and electronic properties of supported rhodium species, although calculations of this kind require a significant amount of computing time.

The results of hybrid QM/MM calculations are consistent with the results of plane-wave/DFT calculations, with the significant difference of being computationally less expensive. However, the results presented in this thesis work were computed using a DZ-quality basis set. More accurate results are expected to be obtained using a larger basis set, as outlined in Chapter 4. In future work, it is proposed to improve the results of hybrid QM/MM calculations in the following way.

- To optimise the structure and to compute harmonic frequencies of supported $\mathrm{Rh^{I}(CO)_2}$ species for QM clusters of increasing size.
- To study the adsorption of small metallic rhodium nano-clusters on hydroxy-

lated alumina surfaces. The energy of metallic rhodium atoms in adsorbed nano-clusters should be lower than the energy of rhodium atoms in a nano-cluster in vacuum. In this way, more realistic formation energies can be obtained.

- To carry out hybrid QM/MM calculations at a higher level of theory, *e.g.* using a TZ-quality basis set for all the atoms in the QM cluster.

- To study other surface rhodium species adsorbed on hydroxylated $\gamma$-$Al_2O_3$ surfaces. In particular it is proposed to study chlorinated mono-dispersed rhodium species since it has not been established experimentally whether the presence of chlorine atoms influences the stability of rhodium particles.

- To study the properties of supported rhodium species in the presence of promoter and stabiliser species such as ceria ($CeO_x$) and zirconia ($ZrO_2$).

- To study the physical and chemical properties of supported rhodium catalysts in electronic states with high spin multiplicity. The properties of such electronic states have not been investigated and therefore it has not been established if these states are ground or excited states.

- To investigate the mechanism of reactions such as oxidation of CO and/or removal of $NO_x$ on supported rhodium catalysts by the mean of hybrid QM/MM calculations.

APPENDIX **A**

# SUPPORT INFORMATION

## A.1 Castep Input Files

The program *Castep* [158] requires two input files to perform an electronic structure calculation: the *cell* file describes the simulation cell and its contents, and the *param* file describes the type of run to be performed (*e.g.* geometrical optimisation, band structure calculation, etc.) and any options which may be required.

As an example, the input files for the geometrical optimisation of bulk $\gamma$-$Al_2O_3$ are shown here.

**gamma-Al2O3-JCatal_226_54.cell**

```
%block lattice_abc
 5.5853  8.4100  8.0689
90.0000 90.5200 90.0000
%endblock lattice_abc

%block positions_frac
 O    0.8888    0.4053    0.8990
 O    0.6049    0.9175    0.6136
 O    0.3565    0.4055    0.8533
 O    0.1369    0.9166    0.6369
 O    0.1112    0.9053    0.1010
 O    0.3951    0.4175    0.3864
 O    0.6435    0.9055    0.1467
 O    0.8631    0.4166    0.3631
 O    0.1112    0.5947    0.1010
 O    0.3951    0.0825    0.3864
 O    0.6435    0.5945    0.1467
 O    0.8631    0.0834    0.3631
 O    0.8888    0.0947    0.8990
 O    0.6049    0.5825    0.6136
 O    0.3565    0.0945    0.8533
 O    0.1369    0.5834    0.6369
 O    0.8814    0.7500    0.8747
 O    0.3629    0.7500    0.8899
 O    0.1186    0.2500    0.1253
 O    0.6371    0.2500    0.1101
 O    0.6138    0.2500    0.6405
 O    0.1329    0.2500    0.6264
```

```
 O    0.3862    0.7500    0.3595
 O    0.8671    0.7500    0.3736
Al    0.3670    0.0752    0.6127
Al    0.1163    0.5787    0.8621
Al    0.6330    0.5752    0.3873
Al    0.8837    0.0787    0.1379
Al    0.6330    0.9248    0.3873
Al    0.8837    0.4213    0.1379
Al    0.3670    0.4248    0.6127
Al    0.1163    0.9213    0.8621
Al    0.3779    0.7500    0.1261
Al    0.8755    0.7500    0.1253
Al    0.6151    0.7500    0.7453
Al    0.6221    0.2500    0.8739
Al    0.1245    0.2500    0.8747
Al    0.3849    0.2500    0.2547
Al    0.8681    0.2500    0.4988
Al    0.1319    0.7500    0.5012
%endblock positions_frac

kpoints_mp_spacing 0.05 1/ang
symmetry_generate

%block species_mass
       O     15.9989995956
      Al     26.9820003510
%endblock species_mass

%block species_pot
       O  ~/Pseudo/O_00PBE.usp
      Al  ~/Pseudo/Al_00PBE.usp
%endblock species_pot

%block species_lcao_states
       O         2
      Al         2
%endblock species_lcao_states
```

### gamma-Al2O3-JCatal_226_54.param

```
task                    GeometryOptimization
reuse                   gamma-Al2O3-JCatal_226_54.check
num_backup_iter         1
xc_functional           PBE
spin_polarized          false
cut_off_energy          380
grid_scale              2.1
finite_basis_corr       2
finite_basis_npoints    3
elec_energy_tol         2.00e-06
max_scf_cycles          100
fix_occupancy           true
nextra_bands            0
geom_energy_tol         1.00e-05
geom_force_tol          0.03
geom_stress_tol         0.05
geom_disp_tol           1.00e-03
geom_max_iter           200
geom_modulus_est        250 GPa
fixed_npw               false
calculate_stress        false
popn_calculate          false
calculate_densdiff      false
pdos_calculate_weights  false
num_dump_cycles         0
opt_strategy_bias       +3
data_distribution       gvector
```

The basis set cut-off energy was determined variationally using a *bash* script. With the same approach, it is possible to study any parameter on which the calculation depends.

### convergence-param.sh

```
#!/bin/bash
task=cutoff
seed=gamma-Al2O3-JCatal_226_54
numcpu=8
i=0
imax=20
# starting cut-off energy.
p=200

# Save the results into a file.
echo "# $task  Final Energy (eV) Force O1 Force Al1 (eV/A)" > $task.dat

function write_param {
cat <<EOF
task                    SinglePoint
reuse                   gamma-Al2O3-JCatal_226_54.check
xc_functional           PBE
spin_polarized          false
page_wvfns              0
cut_off_energy          $p
grid_scale              2.1
finite_basis_corr       0
elec_energy_tol         2.00e-06
max_scf_cycles          100
fix_occupancy           true
nextra_bands            0
num_dump_cycles         0
opt_strategy_bias       +3
data_distribution       gvector

EOF
}

while [ $i -lt  $imax ]; do
 number=`printf "%02d" $i`
 write_param > $seed.param
 # run the program
 mpirun -np  $numcpu /usr/local/Castep-4.3/castep $seed
 energy=`tail -n 60 $seed.castep | grep  "Final energy" - | awk '{print $4}'`
 force1=`tail -n 50 $seed.castep | grep "* O    1  " -    | awk '{printf "%9.5f",
 sqrt($4**2+ $5**2 +$6**2)}'`
 force2=`tail -n 50 $seed.castep | grep "* Al   1  " -    | awk '{printf "%9.5f",
 sqrt($4**2+ $5**2 +$6**2)}'`
 mv $seed.castep  $seed.$task.$number.castep
 echo $p $energy $force1 $force2    >> $task.dat
 p=$((p  + 30))
 i=$((i+1))
done
```

## A.1.1 Building a Slab Model of Surfaces with Gdis

To build a slab model of $\gamma$-$Al_2O_3$ surface, the program *Gdis* [160] was employed. Starting from the bulk structure, the following operations were performed:

1. Cleave a plane 4.0 fractional units deep from the bulk structure using the utility *Tools→Building→Surfaces*.

2. Save the structure as a standard crystallographic CIF format [258].

3. Open the CIF file with a text editor and modify it: delete all the atom fractional coordinates and add to the c axis the required vacuum layer. Save the CIF file with a different name.

4. Open the original and the modified CIF files with *Gdis*. The modified CIF file appears as an empty box.

5. Click on the slab model of the surface (the original CIF file). Left-click and select the atoms in the model, then go to the menu *Edit→Copy*.

6. Click on the empty box (the modified CIF file). Go to the menu *Edit→Paste*.

7. The position of the slab inside the unit cell can be adjusted with the utility *Tools→Building→Editing*.

8. Water molecules and hydroxyl groups can be added following the same procedure. The position of a selected group of atoms can be changed graphically by pressing Ctrl + mouse central button, Ctrl + mouse right button or Ctrl + Shift + mouse right button.

## A.2 Gulp Input Files

**gamma-alumina14_100.08.gin**

```
# Original potential:
# Nora H. de Leeuw and Stephen C. Parker
# J. Am. Ceram. Soc. 82, 3209 (1999).
#
# Modified adding additionalpotential terms:
# * Buckingham interaction between H-H and H-O1
#   fitted on the experimental structure of diaspore.
# * three-body potential on surface Al2-O1-O1 Al2-O1-O2 Al2-O1-O3 groups.
#
# NOTE:
# The Buckingham potential acts on both Al and Al2 atoms.
#
# Keywords:
opti rfo conv

# Created by GDIS version 0.89.0
# Options:
maxcyc 2500
switch bfgs gnorm 0.2000
name gamma-alumina14_100.08
dump gamma-alumina14_100.08.res
output movie arc gamma-alumina14_100.08.arc
```

```
scell
8.056864 8.443484 90.000000
sfractional region 1
H    core     0.395664    0.968305    2.994247
H    core     0.998237    0.761688    2.725421
H    core     0.318827    0.722883    2.692477
H    core     0.954603    0.018702    2.442884
O2   core     0.355784    0.621931    2.419791
O2   core     0.356782    0.957424    2.118174
O2   core     0.920151    0.787319    2.104201
H    core     0.088443    0.141846    1.989189
O3   core     0.968797    0.117971    1.955344
H    core     0.127632    0.604360    1.450810
H    core     0.154953    0.921033    1.385929
H    core     0.697451    0.523079    1.137799
O2   core     0.644093    0.623502    1.096267
Al   core     0.420797    0.587050    0.854289
Al2  core     0.779918    0.791342    0.848360
O1   core     0.672648    0.969682    0.780758
O1   core     0.670624    0.305273    0.735703
Al2  core     0.455848    0.956236    0.613738
Al2  core     0.869406    0.229668    0.578453
O2   core     0.162588    0.595289    0.560043
O1   core     0.095639    0.257432    0.483014
O2   core     0.167359    0.935267    0.470836
O1   core     0.396018    0.764687   -0.345477
O1   core     0.376489    0.440014   -0.390406
O1   core     0.386407    0.112319   -0.497872
Al   core     0.128846    0.764691   -0.517851
Al   core     0.525048    0.279743   -0.550811
Al   core     0.146462    0.424009   -0.689957
O1   core     0.889060    0.762810   -0.695546
Al   core     0.160098    0.100925   -0.766643
O1   core     0.910102    0.419371   -0.870615
O1   core     0.910033    0.101104   -0.893167
O1   core     0.112646    0.611581   -1.858204
O1   core     0.110645    0.916250   -1.896027
Al   core     0.867401    0.589620   -1.959151
Al   core     0.864494    0.932426   -1.983553
Al   core     0.501483    0.752003   -2.034647
O1   core     0.640302    0.587165   -2.038634
O1   core     0.137150    0.263027   -2.074346
O1   core     0.638747    0.917889   -2.121468
O1   core     0.629916    0.262304   -2.150193
Al   core     0.885700    0.263357   -2.167316
O1   core     0.894019    0.760393   -3.266773
Al   core     0.603406    0.086092   -3.319314
Al   core     0.132976    0.763335   -3.327641
Al   core     0.610735    0.433563   -3.396194
O1   core     0.844053    0.102062   -3.402856
O1   core     0.361940    0.760334   -3.455955
O1   core     0.848812    0.417799   -3.460915
O1   core     0.378403    0.086039   -3.505886
O1   core     0.384142    0.427999   -3.559710
Al   core     0.254267    0.258889   -3.614521
Al   core     0.733095    0.764325   -4.618165
O1   core     0.604010    0.594690   -4.671498
O1   core     0.608651    0.937010   -4.723170
O1   core     0.139539    0.603518   -4.772887
O1   core     0.625972    0.261543   -4.774346
O1   core     0.142878    0.919439   -4.823151
Al   core     0.377617    0.588492   -4.843840
Al   core     0.383377    0.935888   -4.899359
Al   core     0.854888    0.257462   -4.902583
O1   core     0.093625    0.261369   -4.968052
Al   core     0.101500    0.758330   -6.059315
O1   core     0.357958    0.760561   -6.080088
O1   core     0.348533    0.103194   -6.105800
O1   core     0.850556    0.759305   -6.156154
O1   core     0.347407    0.433673   -6.191066
Al   core     0.485968    0.268652   -6.191637
Al   core     0.123104    0.088954   -6.251343
```

```
Al   core     0.120540    0.431782   -6.277510
O1   core     0.877321    0.105448   -6.334645
O1   core     0.875133    0.410113   -6.378897
O1   core     0.078381    0.919757   -7.342415
O1   core     0.077005    0.602265   -7.357847
Al   core     0.829048    0.920192   -7.476382
Al   core     0.840289    0.597259   -7.533565
O1   core     0.098343    0.258772   -7.543327
Al   core     0.463247    0.745083   -7.679431
Al   core     0.858651    0.257046   -7.714969
O1   core     0.603976    0.910122   -7.770806
O1   core     0.610246    0.582562   -7.797433
O1   core     0.590466    0.258118   -7.883706
O2   core     0.821926    0.086025   -8.694281
O1   core     0.892514    0.762370   -8.716750
Al2  core     0.118979    0.787974   -8.802764
O2   core     0.821025    0.425004   -8.803741
Al2  core     0.532426    0.067640   -8.861432
O1   core     0.317961    0.712380   -8.957651
O1   core     0.315339    0.049475   -8.988826
Al   core     0.563957    0.437746   -9.053345
Al2  core     0.207144    0.226901   -9.085373
O2   core     0.343030    0.393726   -9.366327
H    core     0.290342    0.493498   -9.493293
H    core     0.841457    0.093874   -9.605223
H    core     0.850824    0.414051   -9.706465
O3   core     0.021457    0.899080  -10.190490
H    core     0.902290    0.873819  -10.248180
O2   core     0.068299    0.228908  -10.351220
O2   core     0.623299    0.067408  -10.395710
O2   core     0.629472    0.417271  -10.636670
H    core     0.037260    0.996276  -10.704090
H    core     0.652642    0.154929  -10.931350
H    core     0.987321    0.254287  -10.949510
H    core     0.563274    0.392069  -11.376870
O2   shel     0.357588    0.626911    2.316514
O2   shel     0.366007    0.957569    2.086586
O2   shel     0.918015    0.785829    2.064186
O3   shel     0.969233    0.117611    1.948224
O2   shel     0.644419    0.623403    1.068942
O1   shel     0.665089    0.952839    0.767552
O1   shel     0.676798    0.297238    0.614747
O2   shel     0.161751    0.598422    0.539553
O2   shel     0.165571    0.931321    0.439702
O1   shel     0.087413    0.256713    0.366538
O1   shel     0.377554    0.438787   -0.324845
O1   shel     0.400208    0.764466   -0.343966
O1   shel     0.387001    0.112595   -0.444115
O1   shel     0.888707    0.764660   -0.676748
O1   shel     0.910919    0.106088   -0.940183
O1   shel     0.916228    0.418209   -0.978969
O1   shel     0.107155    0.618741   -1.803109
O1   shel     0.106100    0.909598   -1.845244
O1   shel     0.139648    0.261589   -2.068153
O1   shel     0.642562    0.592404   -2.102062
O1   shel     0.627080    0.262900   -2.152188
O1   shel     0.640880    0.914819   -2.170377
O1   shel     0.893474    0.760919   -3.244534
O1   shel     0.837584    0.110525   -3.338252
O1   shel     0.840943    0.407879   -3.398835
O1   shel     0.359063    0.758865   -3.429408
O1   shel     0.383506    0.092399   -3.575386
O1   shel     0.387640    0.423305   -3.625445
O1   shel     0.600447    0.599288   -4.606181
O1   shel     0.603601    0.930464   -4.653082
O1   shel     0.628772    0.263140   -4.801227
O1   shel     0.147308    0.613549   -4.834870
O1   shel     0.149468    0.910853   -4.887677
O1   shel     0.094113    0.260932   -4.989644
O1   shel     0.346368    0.106367   -6.056628
O1   shel     0.360907    0.759952   -6.077707
O1   shel     0.345076    0.428489   -6.128415
O1   shel     0.848154    0.760725   -6.162180
```

```
O1   shel     0.882018    0.112298   -6.383086
O1   shel     0.880532    0.403217   -6.437364
O1   shel     0.071126    0.603490   -7.251818
O1   shel     0.077128    0.914760   -7.292909
O1   shel     0.098625    0.256763   -7.561921
O1   shel     0.603032    0.909852   -7.816509
O1   shel     0.609517    0.583870   -7.869600
O1   shel     0.586171    0.258400   -7.885580
O1   shel     0.900782    0.763081   -8.599335
O2   shel     0.824309    0.089447   -8.662938
O2   shel     0.821479    0.421561   -8.784939
O1   shel     0.311861    0.720992   -8.838501
O1   shel     0.322687    0.066644   -8.980546
O2   shel     0.342473    0.394105   -9.340816
O3   shel     0.021016    0.899351  -10.184560
O2   shel     0.070119    0.230527  -10.308370
O2   shel     0.619925    0.074731  -10.328280
O2   shel     0.619336    0.416540  -10.573770

sbulkenergy -1270.459052

species
Al     core    3.00
O1     core    1.00
O1     shel   -3.00
O2     core    0.90
O2     shel   -2.30
O3     core    1.25
O3     shel   -2.05
H      core    0.40
end

buckingham
Al  core O1  shel   1474.40  0.3006   0.00 0.0 16.0
Al  core O2  shel   1032.08  0.3006   0.00 0.0 16.0
Al  core O3  shel    590.04  0.3006   0.00 0.0 16.0
O1  shel O1  shel  22764.00  0.1490  27.88 0.0 16.0
O1  shel O2  shel  22764.00  0.1490  13.94 0.0 16.0
O2  shel O2  shel  22764.00  0.1490   6.97 0.0 16.0
O1  shel O3  shel  22764.00  0.1490  28.92 0.0 16.0
O2  shel O3  shel  22764.00  0.1490   8.12 0.0 16.0
H   core O1  shel    353.73  0.2470   0.49 0.0 20.0
H   core O2  shel    311.97  0.2500   0.00 1.2 20.0
H   core O3  shel    396.27  0.2500  10.00 1.2 20.0
H   core H   core   1126.07  0.2520  32.86 1.7 20.0

lennard 12 6
O3 shel  O3 shel 39344.98 42.15 0.0 20.0

morse
H   core O2  shel   7.052500  3.17490  0.94285  0.0 1.2
H   core O3  shel   6.203713  2.22003  0.92376  0.0 1.2

coulomb
H   core O2  shel  0.5  0.0 1.2
H   core O3  shel  0.5  0.0 1.2
H   core H   core  0.5  0.0 1.7

three
O3  shel H   core H   core  4.19978 108.690 1.2 1.2 1.7
Al2 core O1  shel O1  shel  6.24339 119.658 2.1 2.1 4.5
Al2 core O1  shel O2  shel  6.24339 119.658 2.1 2.1 4.5
Al2 core O1  shel O3  shel  6.24339 119.658 2.1 2.1 4.5

spring
O1  60.78
O2  74.92
O3  209.449602

print 1
```

## A.3 Lanl2 ECP Basis Sets for Rhodium

| **Lanl2DZ+1d1f** (3,4,1/3,2,1/3,1,1/1) | | **Lanl2-[5s4p4d2f]** (11,12,3x1/9,3x1/10,1,1,1/1,1) | | **Lanl2-[10s8p7d3f2g]** (16,16,8x1/13,7x1/13,6x1/3x1/1,1) | |
|---|---|---|---|---|---|
| $\alpha$ | $c$ | $\alpha$ | $c$ | $\alpha$ | $c$ |
| **S** 3 1.00 | | **S** 11 1.00 | | **S** 16 1.00 | |
| 2.6460 | -1.3554084 | 327.68 | -0.00098 | 327.68 | -0.00098 |
| 1.7510 | 1.6112233 | 163.84 | 0.00555 | 163.84 | 0.00555 |
| 0.5713 | 0.5893814 | 81.92 | -0.01983 | 81.92 | -0.01983 |
| **S** 4 1.00 | | 40.96 | 0.05444 | 40.96 | 0.05444 |
| 2.6460 | 1.1472137 | 20.48 | -0.15623 | 20.48 | -0.15623 |
| 1.7510 | -1.4943525 | 10.24 | 0.35118 | 10.24 | 0.35118 |
| 0.5713 | -0.8589704 | 5.12 | -0.62654 | 5.12 | -0.62654 |
| 0.1438 | 1.0297241 | 2.56 | -0.12911 | 2.56 | -0.12911 |
| **S** 1 1.00 | | 1.28 | 0.84712 | 1.28 | 0.84712 |
| 0.0428 | 1.0000000 | 0.64 | 0.41475 | 0.64 | 0.41475 |
| **P** 3 1.00 | | 0.32 | 0.13264 | 0.32 | 0.13264 |
| 5.4400 | -0.0987699 | **S** 12 1.00 | | 0.16 | -0.04012 |
| 1.3290 | 0.7433595 | 327.68 | 0.00024 | 0.08 | 0.02865 |
| 0.4845 | 0.3668462 | 163.84 | -0.00133 | 0.04 | -0.01729 |
| **P** 2 1.00 | | 81.92 | 0.00490 | 0.02 | 0.00765 |
| 0.6595 | -0.0838056 | 40.96 | -0.01360 | 0.01 | -0.00197 |
| 0.0869 | 1.0244841 | 20.48 | 0.04123 | **S** 16 1.00 | |
| **P** 1 1.00 | | 10.24 | -0.09654 | 327.68 | 0.00024 |
| 0.0257 | 1.0000000 | 5.12 | 0.20073 | 163.84 | -0.00133 |
| **D** 3 1.00 | | 2.56 | 0.00361 | 81.92 | 0.00490 |
| 3.6690 | 0.0760059 | 1.28 | -0.30111 | 40.96 | -0.01360 |
| 1.4230 | 0.5158852 | 0.64 | -0.24362 | 20.48 | 0.04123 |
| 0.5091 | 0.5436585 | 0.32 | -0.09089 | 10.24 | -0.09654 |
| **D** 1 1.00 | | 0.16 | 0.21902 | 5.12 | 0.20073 |
| 0.1610 | 1.0000000 | **S** 1 1.0 | | 2.56 | 0.00361 |
| **D** 1 1.00 | | 0.07935 | 1.00000 | 1.28 | -0.30111 |
| 0.08 | 1.0000000 | **S** 1 1.0 | | 0.64 | -0.24362 |
| **F** 1 1.00 | | 0.03450 | 1.00000 | 0.32 | -0.09089 |
| 0.50 | 1.0000000 | **S** 1 1.0 | | 0.16 | 0.21902 |
| | | 0.015 | 1.00000 | 0.08 | 0.48529 |
| | | **P** 9 1.00 | | 0.04 | 0.42748 |
| | | 163.84 | 0.00047 | 0.02 | 0.07300 |
| | | 81.92 | -0.00324 | 0.01 | 0.00131 |
| | | 40.96 | 0.01012 | **S** 1 1.00 | |
| | | 20.48 | -0.04490 | 6.1035156 | 1.00000 |
| | | 10.24 | 0.09310 | **S** 1 1.00 | |
| | | 5.12 | -0.24125 | 2.4414063 | 1.00000 |
| | | 2.56 | 0.20575 | **S** 1 1.00 | |
| | | 1.28 | 0.54008 | 0.9765625 | 1.00000 |
| | | 0.64 | 0.35055 | **S** 1 1.00 | |
| | | **P** 1 1.0 | | 0.390625 | 1.00000 |
| | | 0.225 | 1.00000 | **S** 1 1.00 | |
| | | **P** 1 1.0 | | 0.15625 | 1.00000 |

```
     0.075          1.00000
P 1 1.0
     0.024          1.00000
D 10 1.00
37.481337          -0.00039
20.822965          -0.00320
11.568314           0.00202
6.4268410          -0.00457
3.5704672           0.04447
1.9835929           0.21699
1.1019961           0.27892
0.6122200           0.28645
0.3401222           0.21125
0.1889568           0.13850
D 1 1.0
     0.54           1.00000
D 1 1.0
     0.18           1.00000
D 1 1.0
     0.06           1.00000
F 1 1.0
      0.5           1.00000
F 1 1.0
     0.08           1.00000
```

```
S 1 1.00
     0.0625         1.00000
S 1 1.00
     0.025          1.00000
S 1 1.00
     0.01           1.00000
P 13 1.00
     163.84         0.00047
      81.92        -0.00324
      40.96         0.01012
      20.48        -0.04490
      10.24         0.09310
       5.12        -0.24125
       2.56         0.20575
       1.28         0.54008
       0.64         0.35055
       0.32         0.10109
       0.16         0.00394
       0.08         0.00354
       0.04        -0.00067
P 1 1.00
       5.0          1.00000
P 1 1.00
       2.0          1.00000
P 1 1.00
       0.8          1.00000
P 1 1.00
       0.32         1.00000
P 1 1.00
       0.128        1.00000
P 1 1.00
       0.0512       1.00000
P 1 1.00
     0.02045        1.00000
D 13 1.00
37.481337          -0.00039
20.822965          -0.00320
11.568314           0.00202
 6.426841          -0.00457
3.5704672           0.04447
1.9835929           0.21699
1.1019961           0.27892
 0.61222            0.28645
0.3401222           0.21125
0.1889568           0.13850
 0.104976           0.05512
 0.05832            0.01531
  0.0324            0.00037
D 1 1.0
     2.7648         1.0
D 1 1.0
```

| | | | |
|---|---|---|---|
| | | 1.152 | 1.0 |
| | | **D** 1 1.0 | |
| | | 0.48 | 1.0 |
| | | **D** 1 1.0 | |
| | | 0.2 | 1.0 |
| | | **D** 1 1.0 | |
| | | 0.0833333 | 1.0 |
| | | **D** 1 1.0 | |
| | | 0.0347222 | 1.0 |
| | | **F** 1 1.0 | |
| | | 1.215 | 1.0 |
| | | **F** 1 1.0 | |
| | | 0.27 | 1.0 |
| | | **F** 1 1.0 | |
| | | 0.06 | 1.0 |
| | | **G** 1 1.0 | |
| | | 0.5 | 1.0 |
| | | **G** 1 1.0 | |
| | | 0.08 | 1.0 |

**Table A.1:** Contracted gaussian basis set for the Rh atom constructed from the Lanl2DZ basis set. Orbital exponents are indicated as $\alpha$ and coefficients are indicated as $c$. Courtesy of Dr. Ed Lee (University of Southampton).

| | **Lanl2DZ+2s2p2d2f**[a] (3,4,3x1/3,2,3x1/3,3x1/1,1) | | **Lanl2-[6s4p4d2f]**[a] (11,12,4x1/9,3x1/10,3x1/1,1) | | | |
|---|---|---|---|---|---|---|
| **S** | 0.085 | 0.015 | 0.080 | 0.040 | 0.020 | 0.01 |
| **P** | 1.000 | 0.120 | 0.225 | 0.075 | 0.024 | |
| **D** | 1.000 | 0.080 | 0.540 | 0.180 | 0.060 | |
| **F** | 0.500 | 0.080 | 0.500 | 0.080 | | |

[a] Contracted gaussian functions are listed in Table A.1.

**Table A.2:** Exponents of uncontracted gaussian functions of two basis sets for the Rh atom. Contracted functions are the same as in Table A.1. Courtesy of Dr. Ed Lee (University of Southampton).

# A.4 Software

## Program `cell-dipole.pl`

```
#!/usr/bin/perl
# 1.0 -    2 Sept 2009
# 1.1 - 10 Nov    2009

# Static variables
$help="Usage: cell-dipole [OPTIONS] -f structure.cif\n
This program reads a crystal structure in CIF format
(ortorhombic cell, P1 space group only) and translates
atoms along a and b directions and computes the
coefficientsalpha_i and alpha_j that make the dipole
moment zero on the plane XY.\n
Option          Description
-----------------------------------------------------------
  -h, --help    Print this help.
  -d [int]      Output format (default is 6, e.g. %11.6f).
  \n";

$dig="11.6f";

for my $i(0 .. $#ARGV){
        if ($ARGV[$i] eq "-f"){
                $fileinput=$ARGV[$i+1];
        }
 elsif ($ARGV[$i] eq "-d" && $ARGV[$i+1] =~ /\d/){
                $dig=sprintf("%i"."."%i"."f",$ARGV[$i+1]+5,
                $ARGV[$i+1]);
        }
 elsif ($ARGV[$i] eq "-h" || $ARGV[$i] eq "--help"){die
$help;}
}
$char=length($fileinput)-4;
$fileout=substr($fileinput,0,$char);
$warning="Input file $fileinput not found.
Type 'cell-dipole -h' for more informations.\n";

# Read the input file.
$count=0;
open(INPUT,"<$fileinput") || die $warning;
while(my $line=<INPUT>){
 $cif_head=$cif_head.$line if $count == 0;
 my @data = field($line);

   # unit cell parameters.
 $cell[0]=$data[1] if $data[0] eq "_cell_length_a";
 $cell[1]=$data[1] if $data[0] eq "_cell_length_b";
 $cell[2]=$data[1] if $data[0] eq "_cell_length_c";

# check the fields in the fractional coordinate part.
 if ($data[0] =~ /^\_atom/){
  $cif_head=$cif_head.
  "_atom_site_fract_x\n_atom_site_fract_y\n_atom_site_fract_
  z\n";
  while($data[0] =~ /^\_atom/){
   $atom_label = $count if ($data[0] eq "_atom_site_label");
   $fract_x     = $count if ($data[0] eq
    "_atom_site_fract_x");
   $fract_y     = $count if ($data[0] eq
    "_atom_site_fract_y");
   $fract_z     = $count if ($data[0] eq
    "_atom_site_fract_z");
   my $line2=<INPUT>;
   @data = field($line2);
   $count++;
  }
  $count--;
 }

# reads the fractional coordinates
 if ($data[$atom_label] =~ /\w/ && $data[$fract_x] =~ /\d/
 && $data[$fract_y] =~ /\d/ && $data[$fract_z] =~ /\d/ &&
 $fract_x != $fract_y){
   push my @tmp, $data[$atom_label],$data[$fract_x],$data[
   $fract_y],$data[$fract_z];
   push @site, \@tmp;

   # check if $data[0] is present in @atom_type
   my $check=0;
   foreach my $tmp(@atom_type){
    $check++ if $tmp ne $data[$atom_label];
   }
   push(@atom_type,$data[$atom_label]) if $check >
   $#atom_type;
 }
}
close(INPUT);

# Atomic charges.
print "Enter the charge of each atomic species in the unit
cell.\n";
foreach my $i( 0 .. $#atom_type){
 print "$atom_type[$i]: ";
 $atom_charge[$i]=<STDIN>;
 chomp $atom_charge[$i];
}

# Compute the (fractional) dipole components a and b
for my $i(0 .. $#site){
 for my $j(0 .. 1){
  #print "$site[$i][$j+1] ";
  $dip[$j] += $site[$i][$j+1]*charge($site[$i][0]);
 }
 #print "\n";
}

# compute alpha coefficients along the directions a and b
printf "%5s %4s %19s %19s\n",'index','atom','alpha_x',
'alpha_y';
for my $i(0 .. $#site){
 #my $q=charge($site[$i][0]);
 printf "%-5i %4s ",$i,$site[$i][0];
 for my $j(0 .. 1){
  $alpha[$i][$j]= -$dip[$j]/charge($site[$i][0]);
  printf "%19.15f ",$alpha[$i][$j];
 }
 print "\n";
}
print "Select the index for the alpha coefficients\nalpha_x:";
for my $j(0 .. 1){
 print "alpha_y: " if $j == 1;
 $index[$j]=<STDIN>;
 chomp($index[$j]);
}
#print "0:$index[0] 1:$index[1]\n";

# Write a CIF file with the new fractional coordinates.
open(CIF,">$fileout"."_d.cif");
print CIF "$cif_head";
print CIF "_atom_site_occupancy\n";
# write a XYZ file.
open(XYZ,">$fileout".".xyzq");
printf XYZ "%i\n %12.6f %12.6f\n",$#site+3,$cell[0],$cell[1];

# Print a list of atoms
for my $i(0 .. $#site){
 if ($i != $index[0] && $i != $index[1]){
  printf CIF "%-3s %$dig %$dig %$dig %$dig\n",$site[$i][0],
  $site[$i][1],$site[$i][2],$site[$i][3],1.0;
  printf XYZ "%-3s %$dig %$dig %$dig %$dig\n",$site[$i][0],
  $site[$i][1]*$cell[0],$site[$i][2]*$cell[1],$site[$i][3]
  *$cell[2],charge($site[$i][0]);
 }
}
#print "$index[0] $index[1]\n";

# Print the components of the two border atoms
$i=$index[0];
printf CIF "%-3s %$dig %$dig %$dig %$dig\n",$site[$i][0],
$site[$i][1],$site[$i][2],$site[$i][3],1.-$alpha[$i][0];
printf CIF "%-3s %$dig %$dig %$dig %$dig\n",$site[$i][0],
$site[$i][1]+1.0,$site[$i][2],$site[$i][3],$alpha[$i][0];
printf XYZ "%-3s %$dig %$dig %$dig %$dig\n",$site[$i][0],
$site[$i][1]*$cell[0],$site[$i][2]*$cell[1],$site[$i][3]
*$cell[2],(1.-$alpha[$i][0])*charge($site[$i][0]);
printf XYZ "%-3s %$dig %$dig %$dig %$dig\n",$site[$i][0],(
$site[$i][1]+1.0)*$cell[0],$site[$i][2]*$cell[1],$site[$i][
3]*$cell[2],$alpha[$i][0]*charge($site[$i][0]);

$i=$index[1];
printf CIF "%-3s %$dig %$dig %$dig %$dig\n",$site[$i][0],
$site[$i][1],$site[$i][2],$site[$i][3],1.-$alpha[$i][1];
printf CIF "%-3s %$dig %$dig %$dig %$dig\n",$site[$i][0],
$site[$i][1],$site[$i][2]+1.0,$site[$i][3],$alpha[$i][1];
printf XYZ "%-3s %$dig %$dig %$dig %$dig\n",$site[$i][0],
$site[$i][1]*$cell[0],$site[$i][2]*$cell[1],$site[$i][3]
*$cell[2],(1.-$alpha[$i][1])*charge($site[$i][0]);
printf XYZ "%-3s %$dig %$dig %$dig %$dig\n",$site[$i][0],
$site[$i][1]*$cell[0],($site[$i][2]+1.0)*$cell[1],$site[$i][
3]*$cell[2],$alpha[$i][1]*charge($site[$i][0]);
close(CIF);
close(XYZ);

# Split a line into fields. Separators are one or more
# blankspaces (\s) and/of tabs (\t)
sub field{
 my $str=$_[0];
 chomp $str;
```

```
  my @out = split  /[\s\t]+/, $_[0];
  shift  @out if $out[0] eq "";
  return @out
}

# Retrieve the atomic charge from the atom label
sub charge{
  my $out=0;
  for my $tmp(0  .. $#atom_type){
  if ($atom_type[$tmp] eq $_[0]){
    $out=$atom_charge[$tmp];
  }}
  return $out;
}
```

## Program xyz_slab_NxM.f

```
      programs xyz_slab_nm
      implicit none
c
c    Peter V. Sushko   UCL   Oct 2008
c
c    Reads a slab supercell in expands it in X and Y
c    Generates coordinates for CRYSTAL slab calculations:
c    x_fra y_fra z_car
c
c    Format:
c
c    N_atm
c    lattice_vec_X  lattice_vec_Y
c    Smb1  X1  Y1  Z1
c    Smb1  X2  Y2  Z2
c    Smb1  X3  Y3  Z3


      integer max_atm
      parameter ( max_atm = 5000 )

      integer iof_inp
      integer iof_out
      integer n_atm_uc
      integer n_x,n_y
      integer i,j,ix,iy
      real*8 car_uc(3,max_atm)
      real*8 chg_uc(max_atm)
      real*8 vec_x,vec_y
      character*3 smb_uc(max_atm)
      character*30 file_inp
      character*80 line

      iof_inp = 51
      iof_out = 52

      call getarg(1,file_inp)


c ___ Read the input file

      open(iof_inp,file=file_inp,status='old')
      read(iof_inp,*) n_atm_uc
      if(n_atm_uc.gt.max_atm) stop 'Too many atoms '
      read(iof_inp,*) vec_x,vec_y
      do i = 1, n_atm_uc
          read(iof_inp,'(a)') line
          smb_uc(i) = line(1:3)
c       read(line(3:),*) (car_uc(j,i),j=1,3)
          read(line(4:),*) (car_uc(j,i),j=1,3),chg_uc(i)
      enddo
      close(iof_inp)


c ___ Read additional info

      write(*,'(a)')
      write(*,'(a)')'The unit cell will be expanded in X
     and Y'
      write(*,'(a)')'Expand in X by N lattice vectors.
     Enter N'
      write(*,'(a)')
      read(*,*) n_x
      write(*,'(a)')'Expand in Y by M lattice vectors.
     Enter M'
      write(*,'(a)')
      read(*,*) n_y

      write(*,'(a)')
      write(*,'(a,i5)')'Expand in X   (x times) = ',n_x
      write(*,'(a,i5)')'Expand in Y   (x times) = ',n_y

c ___ Delete atoms occupying the same position
c     do i = 1, n_atm_uc
c
c     enddo

c ___ Generate and print new coordinates

      open(iof_out,file='xyz_slab_nxm.xyz',status='unknown')
      write(iof_out,'(i6)') n_atm_uc*n_x*n_y
      write(iof_out,'(a,i3,a,i3)')
     +     'Slab extended by ',n_x,' x ',n_y
      do i = 1, n_atm_uc
          do iy = 1, n_y
              do ix = 1, n_x
                  write(iof_out,'(a,2x,3f12.6,3x,f12.6)')
     +                smb_uc(i),
     +                car_uc(1,i) + vec_x *(ix - 1),
     +                car_uc(2,i) + vec_y *(iy - 1),
     +                car_uc(3,i),
     +                chg_uc(i)
              enddo
          enddo
      enddo
      close(iof_out)


c ___ Input for CRYSTAL SLAB calculations

      open(iof_out,file='xyz_slab_nxm.slab_crd',
     status='unknown')
      write(iof_out,'(i6)') n_atm_uc*n_x*n_y
      write(iof_out,'(a,2f12.6)')'Input for CRYSTAL SLAB
     Vx Vy = ',
     +     vec_x * n_x,
     +     vec_y * n_y
      do i = 1, n_atm_uc
          do iy = 1, n_y
              do ix = 1, n_x
                  write(iof_out,'(a,2x,3f12.6)') smb_uc(i),
     +                (car_uc(1,i) + vec_x *(ix - 1)) / (
     vec_x * n_x),
     +                (car_uc(2,i) + vec_y *(iy - 1)) / (
     vec_y * n_y),
     +                car_uc(3,i)
              enddo
          enddo
      enddo
      close(iof_out)

      stop
      end
```

## Program nc_slab_to_guess.f

```
      program nc_slab_to_guess
      implicit none
c
c    Peter V. Sushko   UCL  Oct 2008
c
c    Generates a slab template for the GUESS calculations
c
c    Input file already contains coordinates of the
c    nanocluster, which were generated as N x M extension
c    of a "building block"
c
c    This program generates a semi-ready GUESS input ONLY.
c
c    Input format:
c
c    n_atm
c    emply line
c    Smb_1 x_1 y_1 z_1 q_1
c    Smb_2 x_2 y_2 z_2 q_2
c    Smb_3 x_3 y_3 z_3 q_3
c    ..... ... ... ... ...
c
c    It is assumed that the slab is oriented
c     perpendicular to Z-axis


      integer max_atm
      parameter ( max_atm = 100000 )

      real*8 tol_chg_typ
      parameter ( tol_chg_typ = 1.0d-5 )

      real*8 tol_dst_glue
      parameter ( tol_dst_glue = 0.01d0 )


      integer iof_inp
      integer iof_out
      integer iof_xyz
      integer n_atm,n_atm1,n_atm_r1
      integer n_chg_typ
      integer i,j,k,l,i_atm
      integer ityp_nc(max_atm)   !atom types
```

```
      real*8 car_cnt(3)
      real*8 car1(3,max_atm)
      real*8 car(3,max_atm)
      real*8 car_nc(3,max_atm)
      real*8 chg1(max_atm)
      real*8 chg(max_atm)
      real*8 chg_nc(max_atm)
      real*8 chg_typ(max_atm)
      real*8 dst(max_atm)
      real*8 rad_r1_cyl
      real*8 aux,z_max,dd

      character*3 smb1(max_atm)
      character*3 smb(max_atm)
      character*3 smb_nc(max_atm)
      character*3 smb_chg_typ(max_atm)
      character*3 ch2
      character*30 file_inp
      character*80 line
      logical l_found
      logical l_mark(max_atm)
      logical l_r1(max_atm)


c ------------------------------------------------------
c -----            Start here              -----
c ------------------------------------------------------

      iof_inp = 51
      iof_out = 52
      iof_xyz = 53

      call getarg(1,file_inp)


c ___ Read coordinates of the nanocluster with charges

      write(*,'(a)')
      write(*,'(a)')'Read coordinates of the nanocluster [A]'
      write(*,'(a)')

      open(iof_inp,file=file_inp,status='old')
      read(iof_inp,*) n_atm1
      if(n_atm1.gt.max_atm) stop 'Too many atoms '
      read(iof_inp,*)

      do i = 1,n_atm1
         read(iof_inp,'(a)') line
         smb1(i) = line(1:3)
         read(line(4:),*) (car1(j,i),j=1,3),chg1(i)
      enddo
      close(iof_inp)


c ------------------------------------------------------
c __ Scan all coordinates and "glue" atoms together IF
c   they occupy the same site
c ------------------------------------------------------
      l = 0

      do i = 1,n_atm1
         l_mark(i) = .false.
      enddo

      do i = 1,n_atm1 - 1
         if(.not.l_mark(i)) then
            do j = (i + 1),n_atm1
               if(.not.l_mark(j)) then

                  dd = 0.d0
                  do k = 1,3
                     dd = dd + (car1(k,i) - car1(k,j))**2
                  enddo
                  dd = sqrt(dd)
                  if(dd.lt.tol_dst_glue) then
c                    write(*,'(a,2i5,2x,2f12.6,2x,f12.6)')
c    +                'Found a pair to "glue":',
c    +                i,j,chg1(i),chg1(j),dd
                     l = l +1
                     chg1(i) = chg1(i) + chg1(j)
                     chg1(j) = 0.d0
                     l_mark(j) = .true.
                  endif
               endif
            enddo
         endif
      enddo

      write (*,'(i,a)') l,' pairs of atoms "glued".'
      write (*,*)


c ___ Update the list of coordinates:

      k = 0

      do i = 1,n_atm1
         if(.not.l_mark(i)) then
            k = k + 1
            do j = 1,3
               car(j,k) = car1(j,i)
            enddo
            chg(k) = chg1(i)
            smb(k) = smb1(i)
         endif
      enddo
      n_atm = k

c ------------------------------------------------------
c -----            Define regions              -----
c ------------------------------------------------------

c ___ Find the geometrical centre

      do i = 1,3
         car_cnt(i) = 0.d0
      enddo
      do i = 1,n_atm
         do j = 1,3
            car_cnt(j) = car_cnt(j) + car(j,i)
         enddo
      enddo
      do j = 1,3
         car_cnt(j) = car_cnt(j) / dfloat(n_atm)
      enddo


c ___ Shift the centre at the origin

      do i = 1,n_atm
         do j = 1,3
            car(j,i) = car(j,i) - car_cnt(j)
         enddo
      enddo


c ___ Define region I as a cylinder

      write(*,'(a)')
      write(*,'(a)')'Enter the radius of a cylinder region I [A]'
      write(*,'(a)')
      read(*,*) rad_r1_cyl

      do i = 1,n_atm
         l_r1(i) = .false.
         aux = car(1,i)**2 + car(2,i)**2
         if(sqrt(aux).lt.rad_r1_cyl) l_r1(i) = .true.
      enddo


c ___ Copy the coordinates into the NC list

      i_atm = 0

      ! Region I
      do i = 1,n_atm
         if(l_r1(i)) then
            i_atm = i_atm + 1
            do j = 1,3
               car_nc(j,i_atm) = car(j,i)
            enddo
            chg_nc(i_atm) = chg(i)
            smb_nc(i_atm) = smb(i)
         endif
      enddo
      n_atm_r1 = i_atm

      ! Region II
      do i = 1,n_atm
         if(.not.l_r1(i)) then
            i_atm = i_atm + 1
            do j = 1,3
               car_nc(j,i_atm) = car(j,i)
            enddo
            chg_nc(i_atm) = chg(i)
            smb_nc(i_atm) = smb(i)
         endif
      enddo


c ___ Order the atoms in Region I with respect to the
c    distance from the "top"

      ! Find the largest Z in Region I
      z_max = -1000000.d0
      do i = 1,n_atm_r1
         if(car_nc(3,i).gt.z_max) z_max = car_nc(3,i)
      enddo
```

```
      ! Calculate the distances from the point 0,0,z_max
      car_cnt(1) = 0.d0
      car_cnt(2) = 0.d0
      car_cnt(3) = z_max
      do i = 1, n_atm_r1
         aux = 0.d0
         do j = 1, 3
            aux = aux + (car_nc(j,i) - car_cnt(j))**2
         enddo
         dst(i) = dsqrt(aux)
      enddo

      ! Order
      do i = 1, (n_atm_r1 - 1)
         do j = (i + 1), n_atm_r1
            if(dst(j).lt.dst(i)) then
               aux      = dst(i)
               dst(i) = dst(j)
               dst(j) = aux
               aux          = chg_nc(i)
               chg_nc(i) = chg_nc(j)
               chg_nc(j) = aux
               do k = 1, 3
                  aux           = car_nc(k,i)
                  car_nc(k,i) = car_nc(k,j)
                  car_nc(k,j) = aux
               enddo
               ch2          = smb_nc(i)
               smb_nc(i) = smb_nc(j)
               smb_nc(j) = ch2
            endif
         enddo
      enddo


c ___ Print out Regions I and II

      open(iof_xyz,file='guess_region1.xyz',
      status='unknown')
      write(iof_xyz,'(i7)') n_atm_r1
      write(iof_xyz,'(a)') 'Region I'
      do i = 1, n_atm_r1
         write(iof_xyz,'(a,2x,3f12.6,2x,f12.6)')
     +          smb_nc(i),(car_nc(j,i),j=1,3),chg_nc(i)
      enddo
      close(iof_xyz)

      open(iof_xyz,file='guess_region2.xyz',
      status='unknown')
      write(iof_xyz,'(i7)') n_atm - n_atm_r1
      write(iof_xyz,'(a)') 'Region II'
      do i = (n_atm_r1 + 1), n_atm
         write(iof_xyz,'(a,2x,3f12.6,2x,f12.6)')
     +          smb_nc(i),(car_nc(j,i),j=1,3),chg_nc(i)
      enddo
      close(iof_xyz)



c ___ Calculate the number of atoms with different charges.
c    These are used to define the number of atom types
c    Assign the types to the atoms of the nanocluster

      n_chg_typ = 0

c     write(*,'(a)') '          smb   i   q'
      do i = 1, n_atm
         l_found = .false.
         do j = 1, n_chg_typ
            aux =   chg_nc(i) - chg_typ(j)
            if( dabs(aux) .lt. tol_chg_typ ) then
         if (smb_nc(i).eq.smb_chg_typ(j)) then
                        l_found = .true.
   endif
               endif
            enddo
            if(.not.l_found) then
               n_chg_typ = n_chg_typ + 1
               chg_typ(n_chg_typ) = chg_nc(i)
               smb_chg_typ(n_chg_typ) = smb_nc(i)
c       write(*,'(a,2x,a,i5,f12.6)') 'Found a new type',
c     +       smb_chg_typ(n_chg_typ),
c     +       n_chg_typ,chg_typ(n_chg_typ)
            endif
         enddo
c     write(*,'(a,i5)') 'Total number of different charges
= ',n_chg_typ

      write(*,'(a)')
      write(*,'(a)') 'Atom types found in the system:'
      write(*,'(a)')'    i   smb       q'

      do i = 1, n_chg_typ
         write(*,'(i4,2x,a,2x,f12.6)') i,
     +          smb_chg_typ(i),chg_typ(i)
      enddo


c ___ Assign atomic types

      do i = 1, n_atm
         do j = 1, n_chg_typ
            aux = dabs(chg_typ(j) - chg_nc(i))
            if(aux.lt.tol_chg_typ) then
        if (smb_nc(i).eq.smb_chg_typ(j)) then
           if(i.le.n_atm_r1) then
                        ityp_nc(i) = j
                  else
                     ityp_nc(i) = j + n_chg_typ
                  endif
   endif
         endif
      enddo
   enddo


c ---------------------------------------------------
c -----    Print the charges and the coordinates    -----
c ---------------------------------------------------

      open(iof_out,file='guess.template',status='unknown')

      write(iof_out,'(a)')'OPTIONS'
      write(iof_out,'(a)')'gauss'
      write(iof_out,'(a)')'single'
      write(iof_out,'(a)')'cluster'
      write(iof_out,'(a)')'bfgs'
      write(iof_out,'(a)')'#---------'
      write(iof_out,'(a)')'ROOTS'
      write(iof_out,'(a)')'gauss'
      write(iof_out,'(a)')'/PUT/IT/HERE/'
      write(iof_out,'(a)')'#---------'
      write(iof_out,'(a)')'THRES'
      write(iof_out,'(a)')'max_opt_count =  300'
      write(iof_out,'(a)')'max_eng_count =  600'
      write(iof_out,'(a)')'ee_tol        =  0.
      00000010000'
      write(iof_out,'(a)')'f_tol         =  0.
      00050000000'
      write(iof_out,'(a)')'x_tol         =  0.
      00050000000'
      write(iof_out,'(a)')'#---------'
      write(iof_out,'(a)')'INTER'
      write(iof_out,'(a)')'charges'
      write(iof_out,'(a)')'## '
      write(iof_out,'(a)')'## Classical relaxed '
      write(iof_out,'(a)')'## '
      do i = 1, n_chg_typ
         write(iof_out,'(a,a,3f10.6,2x,3f10.6,2x,f10.5,i5)')
     +          smb_chg_typ(i),
     +          '  1  ',
     +          chg_typ(i),0.d0,0.d0,
     +          chg_typ(i),0.d0,0.d0,
     +          0.d0,
     +          i
      enddo
      write(iof_out,'(a)')'## '
      write(iof_out,'(a)')'## Classical fixed '
      write(iof_out,'(a)')'## '
      do i = 1, n_chg_typ
         write(iof_out,'(a,a,3f10.6,2x,3f10.6,2x,f10.5,i5)')
     +          smb_chg_typ(i),
     +          '  1  ',
     +          chg_typ(i),0.d0,0.d0,
     +          chg_typ(i),0.d0,0.d0,
     +          0.d0,
     +          i+n_chg_typ
      enddo
      write(iof_out,'(a)')'## '
      write(iof_out,'(a)')'## QM and Interface: introduce
      them here'
      write(iof_out,'(a)')'## '
      write(iof_out,'(a)')'end_of_block'
      write(iof_out,'(a)')
      write(iof_out,'(a)')'potential'
      write(iof_out,'(a)')'end_of_block'
      write(iof_out,'(a)')
      write(iof_out,'(a)')'#---------'
      write(iof_out,'(a)')'GEOM'
      write(iof_out,'(a)')'## '
      write(iof_out,'(a)')'##  Region I'
      write(iof_out,'(a)')'## '
      do i = 1, n_atm_r1
         write(iof_out,'(a,i3,i3,3f12.6,3x,f12.6,2x,a)')
     +          smb_nc(i),ityp_nc(i),0,
     +          (car_nc(j,i),j=1,3),chg_nc(i),' 1 1 1 '
      enddo
      write(iof_out,'(a)')'## '
      write(iof_out,'(a)')'##  Region II'
      write(iof_out,'(a)')'## '
      do i = (n_atm_r1 + 1), n_atm
```

```
      write(iof_out,'(a,i3,i3,3f12.6,3x,f12.6,2x,a)')
     +          smb_nc(i),ityp_nc(i),2,
     +          (car_nc(j,i),j=1,3),chg_nc(i),' 0 0 0 '
      enddo
      write(iof_out,'(a)')'#---------'
      write(iof_out,'(a)')'GAUSS'
      write(iof_out,'(a)')'options'
      write(iof_out,'(a)')'%NprocShared=8'
      write(iof_out,'(a)')'%Mem=512Mb'
      write(iof_out,'(a)')'#P'
      write(iof_out,'(a)')'nosymm'
      write(iof_out,'(a)')'charge'
      write(iof_out,'(a)')'iop(5/13=1)'
      write(iof_out,'(a)')'iop(3/24=10)'
      write(iof_out,'(a)')'scf=(direct,conver=8)'
      write(iof_out,'(a)')'B3LYP'
      write(iof_out,'(a)')'gen'
      write(iof_out,'(a)')'gfinput'
      write(iof_out,'(a)')'guess=(huckel)'
      write(iof_out,'(a)')'pseudo=cards'
      write(iof_out,'(a)')'end_of_block'
      write(iof_out,'(a)')
      write(iof_out,'(a)')'comments'
      write(iof_out,'(a)')'end_of_block'
      write(iof_out,'(a)')
      write(iof_out,'(a)')'charge'
      write(iof_out,'(a)')'end_of_block'
      write(iof_out,'(a)')
      write(iof_out,'(a)')'basis'
      write(iof_out,'(a)')'end_of_block'
      write(iof_out,'(a)')
      write(iof_out,'(a)')'short_range'
      write(iof_out,'(a)')'end_of_block'
      write(iof_out,'(a)')'#---------'
      write(iof_out,'(a)')'#---------'
      write(iof_out,'(a)')

      close(iof_out)


      stop
      end
```

# Program epotential_2D.f

```
      programs epotential_2D
      implicit none
c
c     Otello M. Roscioni Univ. Southampton Aug 2009
c
c     Reads a slab model of surface (XYZQ format) and
c     computes the electrostatic potential for every atom
c     belonging to a given plane.
c
c     Input format:
c
c     N_atm
c     comment
c     Atom1  X1  Y1  Z1  Q1
c     Atom2  X2  Y2  Z2  Q2
c     Atom3  X3  Y3  Z3  Q3


      integer max_atm
      parameter ( max_atm = 30000 )
      real*8 ev
      parameter ( ev = 14.39964381 )

      integer iof_inp
      integer iof_out
      integer n_atm
      integer i,j,iz
      real*8 coord(3,max_atm)
      real*8 charge(max_atm)
      real*8 dist(max_atm)
      real*8 pot(max_atm)
      real*8 centre(3)
      real*8 z0,tol,z_min,z_max,rad
      character*3 atom(max_atm)
      character*3 atom_n(max_atm)
      character*3 str
      character*30 file_inp
      character*80 line
      iof_inp = 51
      iof_out = 52

      call getarg(1,file_inp)


c ___ Read the input file

      open(iof_inp,file=file_inp,status='old')
      read(iof_inp,*) n_atm
      if(n_atm.gt.max_atm) stop 'Too many atoms '
c     Discard the comment line.
      read(iof_inp,*)
      do i = 1,n_atm
         read(iof_inp,'(a)') line
         atom(i) = line(1:3)
         read(line(4:),*) (coord(j,i),j=1,3),charge(i)
      enddo
      close(iof_inp)

c ___ Find the geometrical centre

      write(*,'(a)')'Centre of the system'
      do i = 1,3
         centre(i) = 0.d0
      enddo
      do i = 1,n_atm
         do j = 1,3
            centre(j) = centre(j) + coord(j,i)
         enddo
      enddo
      do j = 1,3
         centre(j) = centre(j) / dfloat(n_atm)
      enddo
      write(*,'(a,f12.6)')'X = ',centre(1)
      write(*,'(a,f12.6)')'Y = ',centre(2)
      write(*,'(a,f12.6)')'Z = ',centre(3)

c ___ Read additional info

      write(*,'(a)')
      write(*,'(a)')'Enter the value of the plane
     Z=const'
      read(*,*) z0
      write(*,'(a)')'Enter the tolerance along Z (Angstrom)
     '
      read(*,*) tol
      z_min = z0 - tol
      z_max = z0 + tol


c ___ Compute the electrostatic potential for all the
c ___ atoms belonging to the plane z=z0

      iz = 1
      do i = 1,n_atm
         if ( (coord(3,i).le.z_max) .and. (coord(3,i).ge.
         z_min)) then
            rad = (coord(1,i) - centre(1))**2 + (coord(2,i) -
            centre(2))**2
            dist(iz) = sqrt(rad)
            pot(iz) = 0.d0
            atom_n(iz) = atom(i)
            do j = 1,n_atm
               if (j.ne.i) then
                  rad = (coord(1,i) - coord(1,j))**2 + (coord(2,i) -
                  coord(2,j))**2
     +            + (coord(3,i) - coord(3,j))**2
                  rad = sqrt(rad)
                  pot(iz) = pot(iz) + ( charge(j)*ev) / rad
               endif
            enddo
            iz = iz + 1
         endif
      enddo
      iz = iz - 1

c ___ Order the atoms with respect to the distance
c ___ from the central axis.

      do i = 1,(iz - 1)
         do j = (i + 1), iz
            if(dist(j).lt.dist(i)) then
               rad = dist(i)
               dist(i) = dist(j)
               dist(j) = rad
               str= atom_n(i)
               atom_n(i) = atom_n(j)
               atom_n(j) = str
               rad = pot(i)
               pot(i) = pot(j)
               pot(j) = rad
            endif
         enddo
      enddo

c __ Write the results to the the file epot.dat

      open(iof_out,file='epot.dat',status='unknown')
      write(iof_out,'(a)')    '# atom    r (Ang)    epot (eV)'
      do i = 1,iz
         write(iof_out,'(a4,f12.6,f12.6)') atom_n(i),dist(i)
         ,pot(i)
      enddo

      stop
      end
```

## Program glue_xyz.f

```
      programs xyz_glue
      implicit none

c
c   Check all the atoms in a XYZ file and glue together
c   the atoms occupying the same position
c   (tolerance = 0.01 Angstrom).
c
c   Format:
c
c   N_atm
c
c   Smb1  X1  Y1  Z1  Q1
c   Smb1  X2  Y2  Z2  Q2
c   Smb1  X3  Y3  Z3  Q3


      integer max_atm
      parameter ( max_atm = 100000 )

      integer iof_inp
      integer iof_xyz
      integer n_atm,n_atm_short,i_atm
      integer i,j,k
      real*8 car(3,max_atm)
      real*8 chg(max_atm)
      real*8 dist_tol,dd
      character*3 smb(max_atm)
      character*2 ch_key
      character*30 file_inp
      character*80 line,comment
      logical l_read_q
      logical l_use(max_atm)


      iof_inp = 51
      iof_xyz = 52

      call getarg(1,file_inp)
      call getarg(2,ch_key)


      if(ch_key.eq.'-q') then
         l_read_q =.true.
      else
         write(*,'(a)')
         write(*,'(a)')'Use key "-q" to read charges if ↵
         needed'
         write(*,'(a)')
         l_read_q =.false.
      endif

c ___ Read the input file

      open(iof_inp,file=file_inp,status='old')
      read(iof_inp,*) n_atm
      if(n_atm.gt.max_atm) stop 'Too many atoms '
      read(iof_inp,'(a)') comment

      if(l_read_q) then
         do i = 1,n_atm
            read(iof_inp,'(a)') line
            smb(i) = line(1:3)
            read(line(4:),*) (car(j,i),j=1,3),chg(i)
         enddo
      else
         do i = 1,n_atm
            read(iof_inp,'(a)') line
            smb(i) = line(1:3)
            read(line(4:),*) (car(j,i),j=1,3)
         enddo
      endif
      close(iof_inp)


c ___ Glue

      dist_tol = 0.01
      do i = 1,n_atm
         l_use(i) =.true.
      enddo

      do i = 1,(n_atm - 1)
         if(l_use(i)) then
            do j = (i+1),n_atm
               if(l_use(j)) then
                  dd = 0.d0
                  do k = 1,3
                     dd = dd + (car(k,i) - car(k,j))**2
                  enddo
                  dd = dsqrt(dd)
                  if(dd.lt.dist_tol) then
                     chg(i) = chg(i) + chg(j)
                     chg(j) = 0.d0
                     l_use(j) = .false.
                  endif
               endif
            enddo
         endif
      enddo


c ___ Calculate the number of atoms n the short list

      i_atm = 0
      do i = 1,n_atm
         if(l_use(i)) i_atm = i_atm + 1
      enddo
      n_atm_short = i_atm


c ___ Print the short list

      open(iof_xyz,file='fixed.xyz',status='unknown')
      write(iof_xyz,'(i7)') n_atm_short
      write(iof_xyz,'(a)') comment
      if(l_read_q) then
         do i = 1,n_atm
            if(l_use(i)) then
               write(iof_xyz,'(a,3x,4f12.6)')
     +              smb(i),(car(j,i),j=1,3),chg(i)
            endif
         enddo
      else
         do i = 1,n_atm
            if(l_use(i)) then
               write(iof_xyz,'(a,3x,3f12.6)') smb(i),(car(j,↵
               i),j=1,3)
            endif
         enddo
      endif
      close(iof_xyz)

      stop
      end
```

## Program make_input_guess.pl

```
#!/usr/bin/perl
# Note: the file "guess_charges" must contains the
# following comment lines:
#
# ## Classical relaxed
# ## Classical fixed
# ## QM and Interface
#
# The atom labels should be the same as in
# in the file "guess_charges" (e.g. O1, O2)

open(GUESS,"<guess_charges") || die "guess_charges not ↵
found\n";
open(GULP,"<gulp_potentials") || die "gulp_potentials not ↵
found\n";

# Read the atom species in "guess_charges"
while(my $line=<GUESS>){
  my @data = field($line);
  # check if $data[0] is present in @atom_type
  my $check=0;
  foreach my $tmp(@atom_type){
    $check++ if $tmp ne $data[0];
  }
  push(@atom_type,$data[0]) if $check > $#atom_type && $data[ ↵
  0] !~ /^#/;
}
close(GUESS);

# Initialise the array @index
for my $i(0 .. $#atom_type){
  $index[$i]=-1;
}

# Put guess atom indexes in the array-of-array @atom_index
# The array-of-array @region contains the information about
# the GUESS regions:
# 1="Classical relaxed"
# 2="Classical fixed"
# 3="QM and Interface"
open(GUESS,"<guess_charges");
$tmp=1;
while(my $line=<GUESS>){
  my @data = field($line);
  $tmp++ if $line =~ /Classical fixed/ || $line =~ /QM  and ↵
  Interface/;
```

```
  for my $i(0 .. $#atom_type){
    if ($atom_type[$i] eq $data[0]){
       $index[$i]++;
       $atom_index[$i][$index[$i]]=pop(@data);
       $region[$i][$index[$i]]=$tmp;
    }
  }
}
close(GUESS);

# Control routine
#for my $i(0 .. $#atom_type){
#       print "$index[$i]\n";
#       print "$atom_type[$i]:";
#       for my $j(0 .. $index[$i]){
#         print " $atom_index[$i][$j]";
#         print " $region[$i][$j]";
#       }
#       print "\n";
#}

while(my $line=<GULP>){
  my @data = field($line);
  $type=$data[0] if ($data[0] ne "" && $#data == 0);
# print "$type\n";

if ($type eq "buckingham" && $#data > 0){
    # atom 1
    push my @tmp, $data[0];
    # atom 2
    push @tmp, $data[2];
    # A [eV]
    push @tmp, $data[4];
    # r_0 [A]
    push @tmp, $data[5];
    # C [eV A^6]
    push @tmp, $data[6];
    # r_{min} [A]
    push @tmp, $data[7];
    # r_{max} [A]
    push @tmp, $data[8];
    # D [eV A^8]
    push @tmp, $data[9];
    push @buck, \@tmp;
  }
  elsif ($type eq "morse" && $#data > 0){
    # atom 1
    push my @tmp, $data[0];
    # atom 2
    push @tmp, $data[2];
    # A [eV]
    push @tmp, $data[4];
    # \alpha [A^{-1}]
    push @tmp, $data[5];
    # r_0 [A]
    push @tmp, $data[6];
    # r_{min} [A]
    push @tmp, $data[7];
    # r_{max} [A]
    push @tmp, $data[8];
    push @morse, \@tmp;
  }
  elsif ($type eq "three" && $#data > 0){
    # atom 1
    push my @tmp, $data[0];
    # atom 2
    push @tmp, $data[2];
    # atom 3
    push @tmp, $data[4];
    # k [eV rad^{-2}]
    push @tmp, $data[6];
    # \Teta_0 [deg]
    push @tmp, $data[7];
    # r_{12} [A]
    push @tmp, $data[8];
    # r_{13} [A]
    push @tmp, $data[9];
    # r_{23} [A]
    push @tmp, $data[10];
    push @three, \@tmp;
  }
  elsif ($type eq "spring" && $#data > 0){
    # atom 1
    push my @tmp, $data[0];
    # k_2 [eV A^{-2}]
    push @tmp, $data[1];
    # k_4 [eV A^{-4}]
    push @tmp, $data[2];
    push @spring, \@tmp;
  }
  elsif ($type eq "lenjen" && $#data > 0){
    # atom 1
    push my @tmp, $data[0];
    # atom 2
    push @tmp, $data[2];
    # A [eV A^m]
    push @tmp, $data[4];
    # m
    push @tmp, $data[5];
    # B [eV A^n]
    push @tmp, $data[6];
    # n
    push @tmp, $data[7];
    # r_{min} [A]
    push @tmp, $data[8];
    # r_{max} [A]
    push @tmp, $data[9];
    push @lenjen, \@tmp;
  }
}
close(GULP);

# Now write the potentials for GUESS.

# Buckingham potential
for my $i(0 .. $#buck){
  # Find the atom's index.
  for my $j(0 .. $#atom_type){
    $atom1=$j if $buck[$i][0] eq $atom_type[$j];
    $atom2=$j if $buck[$i][1] eq $atom_type[$j];
  }
  # remove numbers from atom names.
  my $atom1_s=$buck[$i][0];
  my $atom2_s=$buck[$i][1];
  $atom1_s=~ s/\d//g;
  $atom2_s=~ s/\d//g;
  # Print the allowed combinations of atom1 and atom2,
  # excluding interactions between region2-region2
  # and region3-region3.
  for my $j(0 .. $index[$atom1]){
    for my $k(0 .. $index[$atom2]){
      if ($region[$atom1][$j] == 2 && $region[$atom2][$k] == 2
      || $region[$atom1][$j] == 3 && $region[$atom2][$k]
      == 3) {
      } else {
          #print "$region[$atom1][$j]      $region[$atom2][$k]
          \n";
          # Do not count twice the interaction between
          # a couple of identical atoms.
          if ($buck[$i][0] eq $buck[$i][1]){
            if ($k >=$j){
              print "buck\n";
              printf "%-3s%3i%3s%3i%10.2f%10.5f%7.2f%5.1f%5.
              1f%5.1f\n",$atom1_s,$atom_index[$atom1][$j],
              $atom2_s,$atom_index[$atom2][$k],$buck[$i][2],
              $buck[$i][3],$buck[$i][4],$buck[$i][5],$buck[$i][
              6],$buck[$i][7];
            }
          } else {
            print "buck\n";
            printf "%-3s%3i%3s%3i%10.2f%10.5f%7.2f%5.1f%5.
            1f%5.1f\n",$atom1_s,$atom_index[$atom1][$j],
            $atom2_s,$atom_index[$atom2][$k],$buck[$i][2],
            $buck[$i][3],$buck[$i][4],$buck[$i][5],$buck[$i][
            6],$buck[$i][7];
          }
      }
    }
  }
}

# Morse potential
for my $i(0 .. $#morse){
  # Find the atom's index.
  for my $j(0 .. $#atom_type){
    $atom1=$j if $morse[$i][0] eq $atom_type[$j];
    $atom2=$j if $morse[$i][1] eq $atom_type[$j];
  }
  # remove numbers from atom names.
  my $atom1_s=$morse[$i][0];
  my $atom2_s=$morse[$i][1];
  $atom1_s=~ s/\d//g;
  $atom2_s=~ s/\d//g;
  # Print the allowed combinations of atom1 and atom2
  for my $j(0 .. $index[$atom1]){
    for my $k(0 .. $index[$atom2]){
      if ($region[$atom1][$j] == 2 && $region[$atom2][$k] == 2
      || $region[$atom1][$j] == 3 && $region[$atom2][$k] ==
      3) {
      } elsif ($region[$atom1][$j] == 2 && $region[$atom2][$k]
      == 3 || $region[$atom1][$j] == 3 && $region[$atom2][$k]
      == 2) {
      } else {
          #print "$region[$atom1][$j]      $region[$atom2][$k]
          \n";
          # Do not count twice the interaction between
          # a couple of identical atoms.
          if ($morse[$i][0] eq $morse[$i][1]){
            if ($k >=$j){
              print "morse\n";
              printf "%-3s%3i%3s%3i%10.6f%10.6f%10.6f%5.1f%5.
              1f\n",$atom1_s,$atom_index[$atom1][$j],$atom2_s,
```

```
            $atom_index[$atom2][$k],$morse[$i][2],$morse[$i][
            3],$morse[$i][4],$morse[$i][5],$morse[$i][6];
          }
        } else {
          print "morse\n";
          printf "%-3s%3i%3s%3i%10.6f%10.6f%10.6f%5.1f%5.
          1f\n",$atom1_s,$atom_index[$atom1][$j],$atom2_s,
          $atom_index[$atom2][$k],$morse[$i][2],$morse[$i][
          3],$morse[$i][4],$morse[$i][5],$morse[$i][6];
        }
      }
    }
  }
}

# Three body potential
for my $i(0 .. $#three){
  # Find the atom's index.
  for my $j(0 .. $#atom_type){
    $atom1=$j if $three[$i][0] eq $atom_type[$j];
    $atom2=$j if $three[$i][1] eq $atom_type[$j];
    $atom3=$j if $three[$i][2] eq $atom_type[$j];
  }
  # remove numbers from atom names.
  my $atom1_s=$three[$i][0];
  my $atom2_s=$three[$i][1];
  my $atom3_s=$three[$i][2];
  $atom1_s=~ s/\d//g;
  $atom2_s=~ s/\d//g;
  $atom3_s=~ s/\d//g;
  # Print the allowed combinations of atom1, atom2 and atom3
  for my $j(0 .. $index[$atom1]){
    for my $k(0 .. $index[$atom2]){
      for my $l(0 .. $index[$atom3]){
        if ($region[$atom1][$j] == 2 && $region[$atom2][$k] ==
        2 && $region[$atom3][$l] == 2 || $region[$atom1][$j]
        == 3 && $region[$atom2][$k] == 3 && $region[$atom3][$l]
        == 3) {
        } elsif ($region[$atom1][$j] == 2 && $region[$atom2][$k]
        == 3 || $region[$atom1][$j] == 3 && $region[$atom2][$k]
        == 2) {
        } elsif ($region[$atom2][$k] == 2 && $region[$atom3][$l]
        == 3 || $region[$atom2][$k] == 3 && $region[$atom3][$l]
        == 2) {
        } elsif ($region[$atom1][$j] == 2 && $region[$atom3][$l]
        == 3 || $region[$atom1][$j] == 3 && $region[$atom3][$l]
        == 2) {
        } else {
          # Do not count twice the interaction between
          # a couple of identical atoms.
          if ($three[$i][1] eq $three[$i][2]){
            if ($l >=$k){
              print "three\n";
              printf "%-3s%3i%3s%3i%3s%3i%10.6f%10.2f%5.1f%5.1f%5.
              1f\n",$atom1_s,$atom_index[$atom1][$j],$atom2_s,
              $atom_index[$atom2][$k],$atom3_s,$atom_index[$atom3][
              $l],$three[$i][3],$three[$i][4],$three[$i][5],$three[
              $i][6],$three[$i][7];
            }
          } else {
            print "three\n";
            printf "%-3s%3i%3s%3i%3s%3i%10.6f%10.2f%5.1f%5.1f%5.
            1f\n",$atom1_s,$atom_index[$atom1][$j],$atom2_s,
            $atom_index[$atom2][$k],$atom3_s,$atom_index[$atom3][
            $l],$three[$i][3],$three[$i][4],$three[$i][5],$three[
            $i][6],$three[$i][7];
          }
        }
      }
    }
  }
}

# Spring potential
for my $i(0 .. $#spring){
  # Find the atom's index.
  for my $j(0 .. $#atom_type){
    $atom1=$j if $spring[$i][0] eq $atom_type[$j];
  }
  # remove numbers from atom names.
  my $atom1_s=$spring[$i][0];
  $atom1_s=~ s/\d//g;
  # Print the spring potential (region1 only)
  for my $j(0 .. $index[$atom1]){
    if ($region[$atom1][$j] == 1) {
      print "spring\n";
      printf "%-3s%3i%12.6f%12.6f\n",$atom1_s,$atom_index[
      $atom1][$j],$spring[$i][1],$spring[$i][2];
    }
  }
}

# Lennard-Jones potential
for my $i(0 .. $#lenjen){
  # Find the atom's index.
  for my $j(0 .. $#atom_type){
    $atom1=$j if $lenjen[$i][0] eq $atom_type[$j];
    $atom2=$j if $lenjen[$i][1] eq $atom_type[$j];
  }
  # remove numbers from atom names.
  my $atom1_s=$lenjen[$i][0];
  my $atom2_s=$lenjen[$i][1];
  $atom1_s=~ s/\d//g;
  $atom2_s=~ s/\d//g;
  # Print the allowed combinations of atom1 and atom2
  for my $j(0 .. $index[$atom1]){
    for my $k(0 .. $index[$atom2]){
      if ($region[$atom1][$j] == 2 && $region[$atom2][$k] ==
      2 || $region[$atom1][$j] == 3 && $region[$atom2][$k]
      == 3) {
      } else {
        # Do not count twice the interaction between
        # a couple of identical atoms.
        if ($lenjen[$i][0] eq $lenjen[$i][1]){
          if ($k >=$j){
            print "lenjen\n";
            printf "%-3s%3i%3s%3i %10.4f%3i %10.4f%3i%5.1f%5.
            1f\n",$atom1_s,$atom_index[$atom1][$j],$atom2_s,
            $atom_index[$atom2][$k],$lenjen[$i][2],$lenjen[$i][3]
            ,$lenjen[$i][4],$lenjen[$i][5],$lenjen[$i][6],
            $lenjen[$i][7];
          }
        } else {
          print "lenjen\n";
          printf "%-3s%3i%3s%3i %10.4f%3i %10.4f%3i%5.1f%5.
          1f\n",$atom1_s,$atom_index[$atom1][$j],$atom2_s,
          $atom_index[$atom2][$k],$lenjen[$i][2],$lenjen[$i][3],
          $lenjen[$i][4],$lenjen[$i][5],$lenjen[$i][6],$lenjen[
          $i][7];
        }
      }
    }
  }
}

# Split a line into fields. Separators are one or more
# blank spaces (\s) and/of tabs (\t)
sub field{
        chomp $_[0];
        my @out = split /[\s\t]+/, $_[0];
        shift @out if $out[0] eq "";
        return @out
}
```

# Program `missing.sh`

```
#!/bin/bash
usage()
{
cat << EOF

Usage: missing [options] file1 file2

Write a XYZ file containing the atoms in file1 that
are not present in file2. file1 and file2 are XYZ
files.

Options:

   -l  Print the index of atoms in file1 that are not
       present in file2.

Example:

missing all.xyz left.xyz > missing.xyz

EOF
}

function error(){
      echo "Input file(s) missing."
      echo "Type missing -h for more information."
      exit 0;

}

# default input files
file1=$1
file2=$2

case "$1" in
 -h|--help)
   usage
          exit 0
          ;;
 -l)
   file1=$2
   file2=$3
   ;;
 "")
```

```
   error
esac

if [ "$file2" == "" ]; then
 error
fi

# Remove the header (i.e. the first two lines)
# from the input files
cat $file1 |(read; read; cat)>tmp1_$$
cat $file2 |(read; read; cat)>tmp2_$$

if [ "$1" == "-l" ]; then
  diff -e -B tmp1_$$ tmp2_$$ |sed -e "s/d//" -|tac -
else
  atoms=`diff -B tmp1_$$ tmp2_$$ |grep "<" -|wc -l`
diff -e -B tmp1_$$ tmp2_$$ |sed -e "s/d//" -e "s/,/ /" -)
  |tac -|awk '{if ($2 == "") print "head -n " $1 " dummy)
  |tail -n 1 -"}{if ($2 != "") printf "head -n %i dummy)
  |tail -n %i -\n",$2,1+$2-$1}' |sed -e "s/dummy/tmp1_$$/" -)
  >tmpscr_$$
echo $atoms
  echo "Atoms from $file1 that are not present in $file2"
bash tmpscr_$$
rm -f tmpscr_$$
fi

rm -f tmp1_$$ tmp2_$$
```

## Program `divide.sh`

```
#!/bin/bash
usage()
{
cat << EOF

Usage: divide file1 file2 file3

File1 and file2 corresponds to all.xyz and left.xyz
respectively. Cut the GEOM section from a GUESS input
file and paste it into file3 (without the GEOM keyword).
The number of atoms in file1 and file3 should be the
same and additionally they should be printed in the same
order.

The program 'divide' is used to divide the atom list in
file3 into two sections, corresponding to the QM region
and the classical relaxed region (i.e. region I).

Check your input files with:

  missing file1 file2 > qm.xyz

before you run this program.


Example:

divide all.xyz left.xyz geom.txt > temp

Then copy back the contents of 'temp' into the GEOM section
of your GUESS input file.

EOF
}

function error(){
        echo "Input file(s) missing."
        echo "Type divide -h for more information."
        exit 0;

}

# default input files
file1=$1
file2=$2
file3=$3

case "$1" in
  -h|--help)
    usage
              exit 0
              ;;
  "")
    error
esac

if [ "$file2" == "" ]; [ "$file3" == "" ]; then
 error
fi

# Remove the header (i.e. the first two lines)
# from the input files.
cat $file1 |(read; read; cat)>tmp1_$$
cat $file2 |(read; read; cat)>tmp2_$$

# print the QM region.
echo -n "sed -n 's/  0 / -1 /;" >tmp3_$$;\
for n in $(diff -e -B tmp1_$$ tmp2_$$ |sed -e "s/d/p/" -)
  |tac -);\
    do echo -n ${n}\;>> tmp3_$$;\
     done; echo -n \' $file3 >>tmp3_$$
echo """>>tmp3_$$

# print the classical relaxed region.
echo -n "sed '">>tmp3_$$;\
for n in $(diff -e -B tmp1_$$ tmp2_$$ |tac -);\
    do echo -n ${n}\;>> tmp3_$$;\
     done; echo -n \' $file3 >>tmp3_$$

# execute the script.
bash tmp3_$$

# remove the temporary files.
rm -f tmp1_$$ tmp2_$$ tmp3_$$
```

## Program `charge.sh`

```
#!/bin/bash
# determine the total charge of a cluster of atom, assuming
# that every atom is in its formal oxidation state.
#
# Usage: charge.sh input_file

# count the number of atoms for each element in the system.
al=`grep Al $1 |wc -l`
rh=`grep Rh $1 |wc -l`
h=`grep H $1 |wc -l`
c=`grep C $1 |wc -l`
o=`grep O $1 |wc -l`

# check if all the atoms have been included
lines=`grep '\w' $1 | wc -l`
total=$(echo "$al+$rh+$h+$c+$o" |bc -l)
if [ $lines != $total ]; then
   echo "There are unknown species in the system!!"
   exit 0;
fi

# compute the charge
charge=$(echo "$al*3+$rh+$h+$c*2 -$o*2" |bc -l)
echo "Total charge: $charge"
```

# A.5 Guess Tutorial

In this section a schematic flow-chart is presented, which can be followed in order to perform a hybrid QM/MM calculation using the program *Guess*.

**Step 1.** Prepare the finite-cluster model.

- Force field validation with the program *Gulp*. Obtain a minimum-energy structure to be used to create a finite-cluster model of the material investigated, and save the structure as a standard crystallographic CIF format.
- Create a structural unit with the program `cell-dipole`. The program takes the charges of each atomic species interactively. The atomic charges must be consistent with those of the force field used; for core–shell atoms, the sum of core and shell charges should be used.
- Create a $NxM$ supercell with the program `xyz_slab_NxM`.
- Determine the size of region I by studying the electrostatic potential inside the $NxM$ supercell. Fix the input structure with `xyz_glue` and then determine the electrostatic potential with the program `epotential_2D`.
- Create a template input file for a *Guess* calculation using the program `nc_slab_to_guess`.
- Create two files named `guess_charges` and `gulp_potentials`, containing the INTER section of the *Guess* template file and the force field as in a *Gulp* calculation.
- Run the program `make_input_guess.pl` and copy the output to the POTENTIAL section of the *Guess* template file. Examples are given at the end of this section.
- Replace any atom labels (*e.g.* O1) with the atomic symbol (*e.g.* O).
- Use *Guess* to optimise the region I at the MM level of theory. This will relax the position of all the shells.
- Use the restart file (`Guess.rst`) to perform a hybrid QM/MM calculation.

**Step 2.** Perform a hybrid QM/MM calculation.

- Open the file `Guess.xyz.region` with the program *Gdis*, go to the last frame from the menu *Tools→Visualization→Animation*. Save the last frame as a XYZ file (*e.g.* `all.xyz`).

- Select the QM cluster graphically: on the left-hand side panel of the program *Gdis* select *Model: Display* and then *Stick*. Left-click on each atom that will form the QM cluster and then on *Ball & Stick*. After the cluster is selected, the system should appear as in the following illustration:

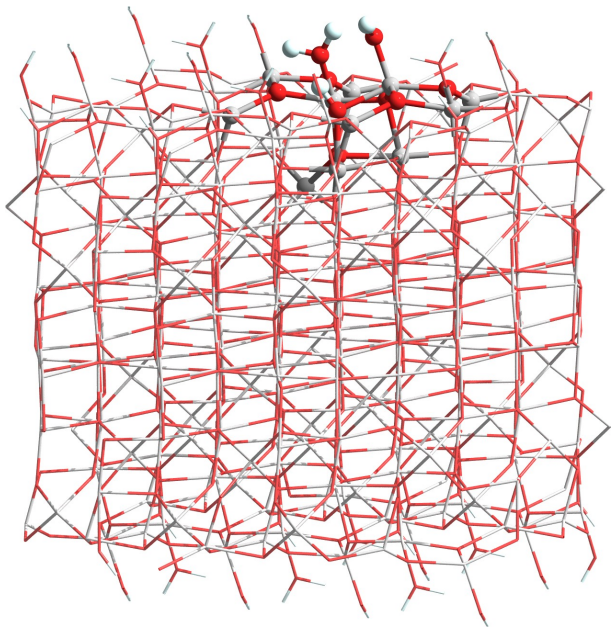

- Delete the atoms belonging to the QM cluster and save the remaining system as a XYZ file (*e.g.* `left.xyz`).

- Create a stand-alone file of the QM cluster with the program:

```
$ missing all.xyz left > qm.xyz
```

- Open the `Guess.rst` with a text editor, cut and paste the GEOM section into a new file (*e.g.* `geom.txt`).

- Divide the atoms of the GEOM section into the QM cluster region and the classical region (Region I) using the program:

```
$ divide all.xyz left.xyz geom.txt > temp
```

- Copy back the GEOM section from the file `temp` to the file `Guess.rst`. Change the labels in the QM cluster according to the INTER section. Finally, rename the file `Guess.rst` before to start a new calculation.

**File** `guess_charges`

*Notes:* The atom index is taken from the value on the last column. However, *Guess* takes the atom index from the line number.

```
##
## Classical relaxed
##
O2   2    0.900000 -2.300000  0.000000    0.900000 -2.300000  0.000000    15.99900    1
Al1  1    3.000000  0.000000  0.000000    3.000000  0.000000  0.000000    26.98200    2
H    1    0.400000  0.000000  0.000000    0.400000  0.000000  0.000000     1.00800    3
O1   2    1.000000 -3.000000  0.000000    1.000000 -3.000000  0.000000    15.99900    4
Al2  1    3.000000  0.000000  0.000000    3.000000  0.000000  0.000000    26.98200    5
O3   2    1.250000 -2.050000  0.000000    1.250000 -2.050000  0.000000    15.99900    6
##
## Classical fixed
##
O2   1   -1.400000  0.000000  0.000000   -1.400000  0.000000  0.000000    15.99900   11
Al1  1    3.000000  0.000000  0.000000    3.000000  0.000000  0.000000    26.98200   12
H    1    0.400000  0.000000  0.000000    0.400000  0.000000  0.000000     1.00800   13
O1   1   -2.000000  0.000000  0.000000   -2.000000  0.000000  0.000000    15.99900   14
Al2  1    3.000000  0.000000  0.000000    3.000000  0.000000  0.000000    26.98200   15
O3   1   -0.800000  0.000000  0.000000   -0.800000  0.000000  0.000000    15.99900   16
O1   1   -1.976307  0.000000  0.000000   -1.976307  0.000000  0.000000    15.99900   17
O1   1   -0.023693  0.000000  0.000000   -0.023693  0.000000  0.000000    15.99900   18
O1   1   -1.940792  0.000000  0.000000   -1.940792  0.000000  0.000000    15.99900   19
O1   1   -0.059208  0.000000  0.000000   -0.059208  0.000000  0.000000    15.99900   20
##
## QM and Interface: introduce them here
##
O2   1    0.000000  0.000000  0.000000    0.000000  0.000000  0.000000    15.99900   21
Al1  1    0.000000  0.000000  0.000000    0.000000  0.000000  0.000000    26.98200   22
H    1    0.000000  0.000000  0.000000    0.000000  0.000000  0.000000     1.00800   23
O1   1    0.000000  0.000000  0.000000    0.000000  0.000000  0.000000    15.99900   24
Al2  1    0.000000  0.000000  0.000000    0.000000  0.000000  0.000000    26.98200   25
O3   1    0.000000  0.000000  0.000000    0.000000  0.000000  0.000000    15.99900   26
Al1  1    3.000000  0.000000  3.000000    3.000000  0.000000  3.000000    26.98200   27
Al2  1    3.000000  0.000000  3.000000    3.000000  0.000000  3.000000    26.98200   28
```

**File** `gulp_potentials`

*Notes:* In *Guess* the coulomb subtraction potential is reproduced using the Lennard-Jones potential. The Coulomb potential (in eV) is defined as $14.4\frac{Z_1 Z_2}{r}$, where $Z_i$ is the atomic charge in $|e|$ and $r$ is the interatomic distance in Å.

```
buckingham
Al1 core O1  shel   1474.40  0.3006   0.00 0.0 16.0
Al1 core O2  shel   1032.08  0.3006   0.00 0.0 16.0
Al1 core O3  shel    590.04  0.3006   0.00 0.0 16.0
Al2 core O1  shel   1474.40  0.3006   0.00 0.0 16.0
Al2 core O2  shel   1032.08  0.3006   0.00 0.0 16.0
Al2 core O3  shel    590.04  0.3006   0.00 0.0 16.0
O1  shel O1  shel  22764.00  0.1490  27.88 0.0 16.0
O1  shel O2  shel  22764.00  0.1490  13.94 0.0 16.0
O2  shel O2  shel  22764.00  0.1490   6.97 0.0 16.0
O1  shel O3  shel  22764.00  0.1490  28.92 0.0 16.0
O2  shel O3  shel  22764.00  0.1490   8.12 0.0 16.0
H   core O1  shel    353.73  0.2470   0.49 1.2 20.0
H   core O2  shel    311.97  0.2500   0.00 1.2 20.0
H   core O3  shel    396.27  0.2500  10.00 1.2 20.0
H   core H   core   1126.07  0.2520  32.86 1.7 20.0

lenjen
O3  shel O3  shel 39344.98 12   42.15  6  0.0 20.0
H   core O2  shel     0.00  0  -6.624  1  0.0  1.2
H   core O3  shel     0.00  0  -5.904  1  0.0  1.2
H   core H   core     0.00  0   1.152  1  0.0  1.7

morse
H   core O2  shel   7.052500  3.17490  0.94285  0.0 1.2
H   core O3  shel   6.203713  2.22003  0.92376  0.0 1.2

three
O3  shel H   core H   core  4.19978 108.690 1.2 1.2 1.7
Al2 core O1  shel O1  shel  6.24339 119.658 2.1 2.1 4.5
Al2 core O1  shel O2  shel  6.24339 119.658 2.1 2.1 4.5
Al2 core O1  shel O3  shel  6.24339 119.658 2.1 2.1 4.5

spring
O1  60.78
O2  74.92
O3  209.449602
```

# BIBLIOGRAPHY


[1] S. M. George. *Chem. Rev.*, **95**, 475 (1995)

[2] M. A. Keane. *J. Mater. Sci.*, **38** (2003)

[3] B. M. Weckhuysen. *Nature*, **439**, 548 (2006)

[4] A. C. Yang and C. W. Garland. *J. Phys. Chem.*, **61**, 1504 (1957)

[5] H. F. J. van't Blik, J. B. A. D. van Zon, T. Huizinga, J. C. Vis, D. C. Koningsberger and R. Prim. *J. Am. Chem. Soc.*, **107**, 3139 (1985)

[6] P. Basu, D. Panayotov and J. T. J. Yates. *J. Am. Chem. Soc.*, **110**, 2074 (1988)

[7] M. A. Newton, D. G. Burnaby, A. J. Dent, S. Diaz-Moreno, J. Evans, S. G. Fiddy, T. Neisius, S. Pascarelli and S. Turin. *J. Phys. Chem. A*, **105**, 5965 (2001)

[8] B. C. Gates. *Top. Catal.*, **14**, 173 (2000)

[9] 'Platinum Today'. *Johnson Matthey* (2006)

[10] M. Raney. *Ind. Eng. Chem.*, **32**, 1199 (1940)

[11] G. B. Taylor. *Ind. Eng. Chem.*, **19**, 1250 (1927)

[12] J. M. Thomas. *Angew. Chem. Int. Ed.*, **38**, 3588 (1999)

[13] J. M. Thomas, R. Raja and D. W. Lewis. *Angew. Chem. Int. Ed.*, **44**, 6456 (2005)

[14] M. Bowker. *The Basis and Application of Heterogeneous Catalysis*. Oxford University Press (1998)

[15] 'AEROXIDE® Alu C'. *Evonik Degussa Corporation*

[16] X. Krokidis, P. Raybaud, A.-E. Gobichon, B. Rebours, P. Euzen and H. Toulhoat. *J. Phys. Chem. B*, **105**, 5121 (2001)

[17] M. Trueba and S. P. Trasatti. *Eur. J. Inorg. Chem.*, 3393 (2005)

[18] C. R. A. Catlow and W. C. Mackrodt. *Lect. Notes Phys.*, **166**, 1 (1982)

[19] F. H. Streitz and J. W. Mintmire. *Phys. Rev. B*, **50**, 11996 (1994)

[20] L. Minervini, M. O. Zacate and R. W. Grimes. *Solid State Ionics*, **116**, 339 (1999)

[21] S. P. Adiga, P. Zapol and L. A. Curtiss. *Phys. Rev. B*, **74**, 064204 (2006)

[22] F. Maglia, S. Gennari and V. Buscaglia. *J. Am. Ceram. Soc.*, **91**, 283 (2008)

[23] G. Gutiérrez, A. Taga and B. Johansson. *Phys. Rev. B*, **65**, 012101 (2001)

[24] M. Digne, P. Sautet, P. Raybaud, H. Toulhoat and E. Artacho. *J. Phys. Chem. B*, **106**, 5155 (2002)

[25] H. P. Pinto, R. M. Nieminen and S. D. Elliott. *Phys. Rev. B*, **70**, 125402 (2004)

[26] R.-S. Zhou and R. L. Snyder. *Acta Crystallogr.*, **B47**, 617 (1991)

[27] M. Digne, P. Sautet, P. Raybaud, P. Euzen and H. Toulhoat. *J. Catal.*, **226**, 54 (2004)

[28] G. Paglia, C. E. Buckley, A. L. Rohl, B. A. Hunter, R. D. Hart, J. V. Hanna and L. T. Byrne. *Phys. Rev. B*, **68**, 144110 (2003)

[29] M. Digne, P. Sautet, P. Raybaud, P. Euzen and H. Toulhoat. *J. Catal.*, **211**, 1 (2002)

[30] H. Knözinger and P. Ratnasamy. *Catal. Rev Sci. Eng.*, **17**, 31 (1978)

[31] T. H. Ballinger and J. T. J. Yates. *J. Am. Chem. Soc.*, **10074**, 114 (1992)

[32] J. C. S. Wong and J. T. J. Yates. *J. Phys. Chem.*, **99**, 12640 (1995)

[33] A. C. Cooper, K. Folting, J. C. Huffmann and K. G. Caulton. *Organometallics*, **16**, 505 (1997)

[34] E. A. Wovchko and J. T. J. Yates. *J. Am. Chem. Soc.*, **117**, 12557 (1995)

[35] U. Lassi, R. Polvinen, S. Suhonen, K. Kallinen, A. Savimäki, M. Härkönen, M. Valden and R. L. Keiski. *Appl. Cat. A-Gen.*, **263**, 241 (2004)

[36] M. I. Zaki, G. Kunzmann, B. C. Gates and H. Knozinger. *J. Phys. Chem.*, **91**, 1486 (1987)

[37] M. P. Keyes and K. L. Watters. *J. Catal.*, **110**, 96 (1988)

[38] F. Solymosi and H. Knozinger. *J. Chem. Soc. Faraday Trans.*, **86**, 389 (1990)

[39] D. K. Paul and J. T. Yates. *J. Phys. Chem.*, **95**, 1699 (1991)

[40] E. Novak, D. Sprinceana and F. Solymosi. *Appl. Cat. A-Gen.*, **149**, 89 (1997)

[41] D. A. Bulushev and G. F. Froment. *J. Mol. Catal. A-Chem.*, **139**, 63 (1999)

[42] M. A. Newton, D. G. Burnaby, A. J. Dent, S. Diaz-Moreno, J. Evans, S. G. Fiddy, T. Neisius and S. Turin. *J. Phys. Chem. B*, **106**, 4214 (2002)

[43] J. Evans and M. Tromp. *J. Phys.-Condens. Mat.*, **20**, 184020 (2008)

[44] A. Suzuki, Y. Inada, A. Yamaguchi, T. Chihara, M. Yuasa, M. Nomura and Y. Iwasawa. *Angew. Chem. Int. Ed.*, **42**, 4795 (2003)

[45] P. Johnston and R. W. Joyner. *J. Chem. Soc. Faraday Trans.*, **89**, 863 (1993)

[46] A. J. Dent, S. Diaz-Moreno, J. Evans, S. G. Fiddy, B. Jyoti and M. A. Newton. *Phys. Scripta*, **T115**, 72 (2005)

[47] M. A. Newton, B. Jyoti, A. J. Dent, S. G. Fiddy and J. Evans. *Chem. Commun.*, **2004**, 2382 (2004)

[48] H. Tolentino, E. Dartyge, A. Fontaine and G. Tourillon. *J. Appl. Cryst.*, **21**, 15 (1988)

[49] P. Kubelka. *J. Opt. Soc. Am.*, **38**, 448 (1948)

[50] P. Kubelka. *J. Opt. Soc. Am.*, **38**, 1067 (1948)

[51] P. Kubelka. *J. Opt. Soc. Am.*, **44**, 330 (1954)

[52] C. R. A. Catlow, S. A. French, A. A. Sokol and J. M. Thomas. *Phil. Trans. R. Soc. A*, **363**, 913 (2005)

[53] T. Mineva, N. Russo and H. J. Freund. *J. Phys. Chem. A*, **105**, 10723 (2001)

[54] F. Rondinelli, N. Russo and M. Toscano. *J. Chem. Theory Comput.*, **4**, 1886 (2008)

[55] M. Zhou and L. Andrews. *J. Phys. Chem. A*, **103**, 7773 (1999)

[56] M. Zhou and L. Andrews. *J. Am. Chem. Soc.*, **121**, 9171 (1999)

[57] F. Maseras and K. Morokuma. *J. Comp. Chem.*, **16**, 1170 (1995)

[58] P. V. Sushko, A. L. Shluger and C. R. A. Catlow. *Surf. Sci.*, **450**, 153 (2000)

[59] V. B. Sulimov, P. V. Sushko, A. H. Edwards, A. L. Shluger and A. M. Stoneham. *Phys. Rev. B*, **66**, 024108 (2002)

[60] T. Klüner, N. Govind, Y. A. Wang and E. A. Carter. *Phys. Rev. Lett.*, **86**, 5954 (2001)

[61] J. R. B. Gomes, F. Illas, N. C. Hernández, A. Márquez and J. F. Sanz. *Phys. Rev. B*, **65**, 125414 (2002)

[62] L. K ohler and G. Kresse. *Phys. Rev. B*, **70**, 165405 (2004)

[63] L. K ohler, G. Kresse, M. Schmid, E. Lundgren, J. Gustafson, A. Mikkelsen, M. Borg, J. Yuhara, J. N. Andersen, M. Marsman and P. Varga. *Phys. Rev. Lett.*, **93**, 266103 (2004)

[64] A. H. Zhang, J. Zhu and W. H. Duan. *J. Chem. Phys.*, **124**, 234703 (2006)

[65] A. M. Walker, J. D. Gale, B. Slatera and K. Wright. *Phys. Chem. Chem. Phys.*, **7**, 3227 (2005)

[66] M. Corral Valero, M. Digne, P. Sautet and P. Raybaud. *Oil Gas Sci. Technol.*, **61**, 535 (2006)

[67] S. C. Wang. *Phys. Rev.*, **31**, 579 (1928)

[68] E. Hückel. *Z. Phys. A-Hadron. Nucl.*, **72**, 310 (1931)

[69] D. R. Hartree. *Math. Proc. Cambridge*, **24**, 89 (1928)

[70] V. Fock. *Z. Phys. A-Hadron. Nucl.*, **61**, 126 (1930)

[71] D. R. Hartree, W. Hartree and B. Swirles. *Philos. T. Roy. Soc. A*, **238**, 229 (1939)

[72] M. Born and R. Oppenheimer. *Ann. Phys. ($4^{th}$ series)*, **84**, 457 (1927)

[73] J. C. Slater. *Phys. Rev.*, **34**, 1293 (1929)

[74] J. C. Slater. *Phys. Rev.*, **36**, 57 (1930)

[75] C. C. J. Roothaan. *Rev. Mod. Phys.*, **23**, 69 (1951)

[76] A. Szabó and N. S. Ostlund. *Modern quantum chemistry: introduction to advanced electronic structure theory*. Courier Dover Publications (1996)

[77] W. Pauli. *Z. Phys. A-Hadron. Nucl.*, **31**, 765 (1925)

[78] E. U. Condon. *Phys. Rev.*, **36**, 1121 (1930)

[79] P.-O. Widmark (editor). *European Summerschool in Quantum Chemistry*. Lund University (2007)

[80] L. Brillouin. *J. Phys. Radium*, **3**, 373 (1932)

[81] T. Koopmans. *Physica*, **1**, 104 (1934)

[82] J. A. Pople and R. K. Nesbet. *J. Chem. Phys.*, **22**, 571 (1954)

[83] C. C. J. Roothaan. *Rev. Mod. Phys.*, **32**, 179 (1960)

[84] W. Pauli. *Z. Phys. A-Hadron. Nucl.*, **36**, 336 (1926)

[85] S. F. Boys. *P. Roy. Soc. Lond. A Mat.*, **200**, 542 (1950)

[86] F. E. Harris. *Rev. Mod. Phys.*, **35**, 558 (1963)

[87] E. Clementi and D. R. Davis. *J. Comput. Phys.*, **1**, 223 (1966)

[88] J. S. Binkley, J. A. Pople and W. J. Hehre. *J. Am. Chem. Soc.*, **102**, 939 (1980)

[89] M. J. Frisch, J. A. Pople and J. S. Binkley. *J. Chem. Phys.*, **80**, 3265 (1984)

[90] P. J. Hay and W. R. Wadt. *J. Chem. Phys.*, **82**, 270 (1985)

[91] W. R. Wadt and P. J. Hay. *J. Chem. Phys.*, **82**, 284 (1985)

[92] P. J. Hay and W. R. Wadt. *J. Chem. Phys.*, **82**, 299 (1985)

[93] C. Herring. *Phys. Rev.*, **57**, 1169 (1940)

[94] M. C. Payne, M. P. Teter, D. C. Allan, T. A. Arias and J. D. Joannopoulos. *Rev. Mod. Phys.*, **64**, 1045 (1992)

[95] M. Born and P. Jordan. *Z. Phys. A-Hadron. Nucl.*, **34**, 858 (1925)

[96] P.-O. Löwdin. *Adv. Chem. Phys.*, **2**, 207 (1959)

[97] R. J. Boyd and C. A. Coulson. *J. Phys. B-At. Mol. Opt.*, **7**, 1805 (1974)

[98] O. Sinanoglu and D. F. tai Tuan. *J. Chem. Phys.*, **38**, 1740 (1963)

[99] R. H. A. Eade and M. A. Robb. *Chem. Phys. Lett.*, **83**, 362 (1981)

[100] M. Frisch, I. N. Ragazos, M. A. Robb and H. B. Schlegel. *Chem. Phys. Lett.*, **189**, 524 (1992)

[101] P. Knowles, M. Schutz and H.-J. Werner. In 'Modern Methods and Algorithms of Quantum Chemistry,', volume 3, 97 (2000)

[102] T. Kato. *Comm. Pure Appl. Math.*, **10**, 51 (1957)

[103] A. J. Thakkar and V. H. Smith. *Chem. Phys. Lett.*, **42**, 476 (1976)

[104] R. J. Bartlett and J. F. Stanton. *Rev. Comp. Chem.*, **5**, 65 (1995)

[105] E. Schrödinger. *Ann. Phys. (Berlin)*, **385**, 437 (1926)

[106] C. Møller and M. S. Plesset. *Phys. Rev.*, **46**, 618 (1934)

[107] R. J. Bartlett. *Ann. Rev. Phys. Chem.*, **32**, 359 (1981)

[108] R. J. Bartlett. *J. Phys. Chem.*, **93**, 1697 (1989)

[109] M. Head-Gordon. *J. Phys. Chem.*, **100**, 13213 (1996)

[110] P. Hohenberg and W. Kohn. *Phys. Rev.*, **136**, B864 (1964)

[111] M. Levy. *Proc. Natl. Acad. Sci. USA*, **76**, 6062 (1979)

[112] W. Kohn and L. J. Sham. *Phys. Rev.*, **140**, A1133 (1965)

[113] J. P. Perdew. *Phys. Rev. Lett.*, **55**, 1665 (1985)

[114] J. P. Perdew, K. Burke and M. Ernzerhof. *Phys. Rev. Lett.*, **77**, 3865 (1996)

[115] A. D. Becke. *J. Chem. Phys.*, **88**, 2547 (1988)

[116] C. Lee, W. Yang and R. G. Parr. *Phys. Rev. B*, **37**, 785 (1988)

[117] A. D. Becke. *J. Chem. Phys.*, **98**, 5648 (1993)

[118] N. W. Ashcroft and N. D. Mermin. *Solid State Physics*. Thomson Learning, Philadelphia (1976)

[119] F. Bloch. *Z. Phys. A-Hadron. Nucl.*, **52**, 555 (1928)

[120] J. C. Phillips. *Phys. Rev.*, **112**, 685 (1958)

[121] M. L. Cohen and V. Heine. *Solid State Phys.*, volume 24, 37 – 248. Academic Press (1970)

[122] M. T. Yin and M. L. Cohen. *Phys. Rev. B*, **25**, 7403 (1982)

[123] 'OPIUM pseudopotential package'. http://opium.sourceforge.net

[124] W. A. Al-Saidi, E. J. Walter and A. M. Rappe. *Phys. Rev. B*, **77**, 075112 (2008)

[125] D. R. Hamann. *Phys. Rev. B*, **40**, 2980 (1989)

[126] D. Vanderbilt. *Phys. Rev. B*, **41**, 7892 (1990)

[127] J. Gale and A. Rohl. *Mol. Simul.*, **29**, 291 (2003)

[128] J. E. Lennard-Jones. *P. Roy. Soc. Lond. A Mat.*, **106**, 463 (1924)

[129] R. A. Buckingham. *P. Roy. Soc. Lond. A Mat.*, **168**, 264 (1938)

[130] P. M. Morse. *Phys. Rev.*, **34**, 57 (1929)

[131] D. Bakowies and W. Thiel. *J. Phys. Chem.*, **100**, 10580 (1996)

[132] B. G. Dick and A. W. Overhauser. *Phys. Rev.*, **112**, 90 (1958)

[133] V. A. Nasluzov, E. A. Ivanova, A. M. Shor, G. N. Vayssilov, U. Birkenheuer and N. Rosch. *J. Phys. Chem. B*, **107**, 2228 (2003)

[134] A. A. Sokol, S. T. Bromley, S. A. French, C. R. A. Catlow and P. Sherwood. *Int. J. Quantum Chem.*, **99**, 695 (2004)

[135] S. Mukhopadhyay, P. V. Sushko, A. M. Stoneham and A. L. Shluger. *Phys. Rev. B*, **70**, 195203 (2004)

[136] A. A. Sokol, S. A. French, S. T. Bromley, C. R. A. Catlow, H. J. J. van Dame and P. Sherwoode. *Faraday Discuss.*, **134**, 267 (2007)

[137] D. M. Philipp and R. A. Friesner. *J. Comp. Chem.*, **20**, 1468 (1999)

[138] Y. Zhang, J. Kua and J. A. McCammon. *J. Am. Chem. Soc.*, **124**, 10572 (2002)

[139] S. O. Meroueh, J. F. Fisher, H. B. Schlegel and S. Mobashery. *J. Am. Chem. Soc.*, **127**, 15397 (2005)

[140] A. J. Mulholland. *Biochem. Soc. T.*, **036**, 22 (2008)

[141] T.-S. Lee, C. S. Lopez, G. M. Giambasu, M. Martick, W. G. Scott and D. M. York. *J. Am. Chem. Soc.*, **130**, 3053 (2008)

[142] T. K. Woo, P. E. Blochl and T. Ziegler. *J. Phys. Chem. A*, **104**, 121 (2000)

[143] J. Sauer and M. Sierka. *J. Comp. Chem.*, **21**, 1470 (2000)

[144] S. A. French, A. A. Sokol, S. T. Bromley, C. R. A. Catlow and P. Sherwood. *Top. Catal.*, **24**, 161 (2003)

[145] S. T. Bromley, C. R. A. Catlow and T. Maschmeyer. *Cattech*, **7**, 164 (2003)

[146] G. Drudis-Solé, G. Ujaque, F. Maseras and A. Lledós. *Chem. Eur. J.*, **11**, 1017 (2005)

[147] T. P. M. Goumans, C. R. A. Catlow and W. A. Brown. *J. Chem. Phys.*, **128**, 134709 (2008)

[148] C. Bo and F. Maseras. *Dalton Trans.*, 2911–2919 (2008)

[149] R. A. Friesner. *Drug Discovery Today: Technologies*, **1**, 253 (2004)

[150] I. Tuñón, M. T. C. Martins-Costa, C. Millot, M. F. Ruiz-López and J. L. Rivail. *J. Comp. Chem.*, **17**, 19 (1996)

[151] R. B. Murphy, D. M. Philipp and R. A. Friesner. *Chemical Physics Letters*, **321**, 113 (2000)

[152] T. Vreven, K. Morokuma, O. Farkas and H. B. Schlegel. *J. Comp. Chem.*, **24**, 760 (2002)

[153] H. Lin and D. G. Truhlar. *J. Phys. Chem. A*, **109**, 3991 (2005)

[154] H. Lin and D. G. Truhlar. *Theor. Chem. Acc.*, **117**, 185 (2007)

[155] M. J. Frisch, G. W. Trucks, H. B. Schlegel, G. E. Scuseria, M. A. Robb, J. R. Cheeseman, J. J. A. Montgomery, T. Vreven, K. N. Kudin, J. C. Burant, J. M. Millam, S. S. Iyengar, J. Tomasi, V. Barone, B. Mennucci, M. Cossi, G. Scalmani, N. Rega, G. A. Petersson, H. Nakatsuji, M. Hada, M. Ehara, K. Toyota, R. Fukuda, J. Hasegawa, M. Ishida, T. Nakajima, Y. Honda, O. Kitao, H. Nakai, M. Klene, X. Li, J. E. Knox, H. P. Hratchian, J. B. Cross, V. Bakken, C. Adamo, J. Jaramillo, R. Gomperts, R. E. Stratmann, O. Yazyev, A. J. Austin, R. Cammi, C. Pomelli, J. W. Ochterski, P. Y. Ayala, K. Morokuma, G. A. Voth, P. Salvador, J. J. Dannenberg, V. G. Zakrzewski, S. Dapprich, A. D. Daniels, M. C. Strain, O. Farkas, D. K. Malick, A. D. Rabuck, K. Raghavachari, J. B. Foresman, J. V. Ortiz, Q. Cui, A. G. Baboul, S. Clifford, J. Cioslowski, B. B. Stefanov, G. Liu, A. Liashenko, P. Piskorz, I. Komaromi, R. L. Martin, D. J. Fox, T. Keith, M. A. Al-Laham, C. Y. Peng, A. Nanayakkara, M. Challacombe, P. M. W. Gill, B. Johnson, W. Chen, M. W. Wong, C. Gonzalez and J. A. Pople. 'Gaussian 03, Revision C.02'. Gaussian, Inc., Wallingford, CT, 2004

[156] A. L. Shluger and J. D. Gale. *Phys. Rev. B*, **54**, 962 (1996)

[157] A. L. Shluger, P. V. Sushko and L. N. Kantorovich. *Phys. Rev. B*, **59**, 2417 (1999)

[158] S. J. Clark, M. D. Segall, C. J. Pickard, P. J. Hasnip, M. J. Probert, K. Refson and M. C. Payne. *Z. Kristallogr.*, **220**, 567 (2005)

[159] H.-J. Werner, P. J. Knowles, R. Lindh, F. R. Manby, M. Schütz *et al.* 'MOLPRO, version 2008.1, a package of ab initio programs' (2008)

[160] 'GDIS, a program for the display and manipulation of isolated molecules and periodic systems.' http://gdis.sourceforge.net

[161] S. W. H. Bragg. *J. Chem. Soc., Trans.*, **121**, 2766 (1922)

[162] L. Pauling and S. B. Hendricks. *J. Am. Chem. Soc.*, **47**, 781 (1925)

[163] J. Graham. *J. Phys. Chem. Solids*, **17**, 18 (1960)

[164] H. d'Amour, D. Schiferl, W. Denner, H. Schulz and W. B. Holzapfel. *J. Appl. Phys.*, **49**, 4411 (1978)

[165] N. Ishizawa, T. Miyata, I. Minato, F. Marumo and S. Iwai. *Acta Crystallogr.*, **B36**, 228 (1980)

[166] P. Thompson, D. E. Cox and J. B. Hastings. *J. Appl. Crystallogr.*, **20**, 79 (1987)

[167] N. Maslen, V. A. Streltsov, N. R. Streltsova, N. Ishizawa and Y. Satow. *Acta Crystallogr.*, **B49**, 973 (1993)

[168] S. Pillet, M. Souhassou, C. Lecomte, K. Schwarz, P. Blaha, M. Rérat, A. Lichanot and P. Roversi. *Acta Crystallogr.*, **A57**, 290 (2001)

[169] P. Ballirano and R. Caminiti. *J. Appl. Crystallogr.*, **34**, 757 (2001)

[170] S. Zhang, H. Li, H. Li, S. Zhou and X. Cao. *J. Phys. Chem. B*, **111**, 1304 (2007)

[171] F. D. Murnaghan. *Proc. Natl. Acad. Sci. USA*, **30**, 244 (1944)

[172] F. Birch. *Phys. Rev.*, **71**, 809 (1947)

[173] T. Williams and C. Kelley. 'Gnuplot 4.2.5' (1986-2007). An interactive plotting program.

[174] J. C. Boettger. *Phys. Rev. B*, **55**, 750 (1997)

[175] E. I. Proynov, E. Ruiz, A. Vela and D. R. Salahub. *Int. J. Quantum Chem.*, **56 (S29)**, 61 (1995)

[176] B. Hammer, L. B. Hansen and J. K. Nørskov. *Phys. Rev. B*, **59**, 7413 (1999)

[177] J. Sun, T. Stirner, W. E. Hagston, A. Leyland and A. Matthews. *J. Cryst. Growth*, **290**, 235 (2006)

[178] L. Ouyang and W.-Y. Ching. *J. Am. Ceram. Soc.*, **84**, 801 (2001)

[179] R. Ahuja, J. M. Osorio-Guillen, J. Souza de Almeida, B. Holm, W. Y. Ching and B. Johansson. *J. Phys.-Condens. Mat.*, **16**, 2891 (2004)

[180] W. Y. Ching, L. Ouyang, P. Rulis and H. Yao. *Phys. Rev. B*, **78**, 014106 (2008)

[181] D. Liu, Y. Jin and J. Deng. *Comp. Mater. Sci.*, **45**, 310 (2009)

[182] A. Banerjea and J. R. Smith. *Phys. Rev. B*, **37**, 6632 (1988)

[183] J. C. Boettger and S. B. Trickey. *Phys. Rev. B*, **53**, 3007 (1996)

[184] H. J. F. Jansen and A. J. Freeman. *Phys. Rev. B*, **35**, 8207 (1987)

[185] M. L. Cohen. *Phys. Rev. B*, **32**, 7988 (1985)

[186] R. H. French. *J. Am. Ceram. Soc.*, **73**, 477 (1990)

[187] T. V. Perevalov, A. V. Shaposhnikov, V. A. Gritsenko, H. Wong, J. H. Han and C. W. Kim. *JETP Letters*, **85**, 165 (2002)

[188] C.-K. Lee, E. Cho, H.-S. Lee, K. S. Seol and S. Han. *Phys. Rev. B*, **76**, 245110 (2007)

[189] I. P. Batra. *J. Phys. C Solid State Phys.*, **15**, 5399 (1982)

[190] S. J. Wilson. *J. Solid State Chem.*, **30**, 247 (1979)

[191] B. Ealet, M. H. Elyakhloufi, E. Gillet and M. Ricci. *Thin Solid Films*, **250**, 92 (1994)

[192] M. R. Gallas and G. J. Piermarini. *J. Am. Ceram. Soc.*, **77**, 2917 (1994)

[193] S. Yip (editor). *Handbook of Materials Modeling*. Springer (2005)

[194] N. H. de Leeuw and S. C. Parker. *J. Am. Ceram. Soc.*, **82**, 3209 (1999)

[195] N. H. de Leeuw and S. C. Parker. *J. Chem. Soc. Faraday Trans.*, **93**, 467 (1997)

[196] N. H. de Leeuw and S. C. Parker. *Phys. Rev. B*, **58**, 13901 (1998)

[197] S. C. Parker. *Private communication.* University of Bath (2008)

[198] W. R. Busing and H. A. Levy. *Acta Crystallogr.*, **11**, 798 (1958)

[199] M. L. McKee and S. D. Worley. *J. Phys. Chem.*, **92**, 3699 (1988)

[200] L. A. Barnes, M. Rosi and C. W. Bauschlicher, Jr. *J. Chem. Phys.*, **93**, 609 (1990)

[201] D. Dai and K. Balasubramanian. *J. Chem. Phys.*, **101**, 2148 (1994)

[202] M. Couty, C. A. Bayse, R. Jimenez-Catano and M. B. Hall. *J. Phys. Chem.*, **100**, 13976 (1996)

[203] M. L. McKee and S. D. Worley. *J. Phys. Chem. A*, **101**, 5600 (1997)

[204] C. Ribbing, B. Gilliams, A. Ceulemans, K. Pierloot, D. Vandenbroucke and B. O. Roos. *J. Chem. Phys.*, **110**, 6849 (1999)

[205] D. Steele and P. F. M. Verhoeven. *Vib. Spectrosc.*, **25**, 29 (2001)

[206] P. Seuret, F. Cicoira, T. Ohta, P. Doppelt, P. Hoffmann, J. Weber and T. A. Wesolowski. *Phys. Chem. Chem. Phys.*, **5**, 268 (2003)

[207] O. Sizova, Y. Varshavskii and A. Nikol'skii. *Russian J. of Coord. Chem.*, **31**, 875 (2005)

[208] A. D. Allian, Y. Wang, M. Saeys, G. M. Kuramshina and M. Garland. *Vib. Spectrosc.*, **41**, 101 (2006)

[209] F. Stevens, V. V. Speybroeck, I. Carmichael, F. Callens and M. Waroquier. *Chem. Phys. Lett.*, **421**, 281 (2006)

[210] Y. Zhao, N. González-García and D. G. Truhlar. *J. Phys. Chem. A*, **109**, 2012 (2005)

[211] Y. Zhao and D. G. Truhlar. *J. Chem. Phys.*, **124**, 224105 (2006)

[212] P. J. Hay and W. R. Wadt. *J. Chem. Phys.*, **82**, 270 (1985)

[213] W. R. Wadt and P. J. Hay. *J. Chem. Phys.*, **82**, 284 (1985)

[214] P. J. Hay and W. R. Wadt. *J. Chem. Phys.*, **82**, 299 (1985)

[215] C. L. Callender, P. A. Hackett and D. M. Rayner. *J. Opt. Soc. Am. B*, **5**, 614 (1988)

[216] H. Hotop and W. C. Lineberger. *J. Phys. Chem. Ref. Data*, **14**, 731 (1985)

[217] M. Scheer, C. A. Brodie, R. C. Bilodeau and H. K. Haugen. *Phys. Rev. A*, **58**, 2051 (1998)

[218] G. A. Ozin and A. J. L. Hanlan. *Inorg. Chem.*, **18**, 2091 (1979)

[219] 'Molekel 5.3.0'. http://molekel.cscs.ch

[220] F. P. Billingsley II and M. Krauss. *J. Chem. Phys.*, **60**, 4130 (1974)

[221] J. S. Muenter. *J. Mol. Spectrosc.*, **55**, 490 (1975)

[222] Z. Hu and R. J. Boyd. *J. Chem. Phys.*, **113**, 9393 (2000)

[223] Z. Hu, R. J. Boyd and H. Nakatsuji. *J. Am. Chem. Soc.*, **124**, 2664 (2002)

[224] F. Furche and J. P. Perdew. *J. Chem. Phys.*, **124**, 044103 (2006)

[225] N. C. Handy and A. J. Cohen. *Mol. Phys.*, **99**, 403 (2001)

[226] W.-M. Hoe, A. J. Cohen and N. C. Handy. *Chem. Phys. Lett.*, **341**, 319 (2001)

[227] M. Swart, A. R. Groenhof, A. W. Ehlers and K. Lammertsma. *J. Phys. Chem. A*, **108**, 5479 (2004)

[228] M. Swart, A. W. Ehlers and K. Lammertsma. *Mol. Phys.*, **102**, 2467 (2004)

[229] L. Walz and P. Scheer. *Acta Crystallogr.*, **C47**, 640 (1991)

[230] C. W. Garland and J. R. Wilt. *J. Chem. Phys.*, **36**, 1094 (1962)

[231] B. T. Heaton, C. Jacob and J. T. Sampanthar. *J. Chem. Soc. Dalton Trans.*, 1403–1410 (1998)

[232] A. J. Pribula and R. S. Drago. *J. Am. Chem. Soc.*, **98**, 2784 (1976)

[233] P. W. Atkins and J. de Paula. *Physical Chemistry*. Oxford University Press (2006)

[234] H.-J. Werner, P. J. Knowles, R. Lindh, F. R. Manby, M. Schütz, P. Celani, T. Korona, A. Mitrushenkov, G. Rauhut, T. B. Adler, R. D. Amos, A. Bernhardsson, A. Berning, D. L. Cooper, M. J. O. Deegan, A. J. Dobbyn, F. Eckert, E. Goll, C. Hampel, G. Hetzer, T. Hrenar, G. Knizia, C. Köppl, Y. Liu, A. W. Lloyd, R. A. Mata, A. J. May, S. J. McNicholas, W. Meyer, M. E. Mura, A. Nicklass, P. Palmieri, K. Pflüger, R. Pitzer, M. Reiher, U. Schumann, H. Stoll, A. J. Stone, R. Tarroni, T. Thorsteinsson, M. Wang and A. Wolf. 'MOLPRO, version 2008.1, a package of ab initio programs' (2008)

[235] E. P. F. Lee, J. M. Dyke, W.-K. Chow, F.-T. Chau and D. K. W. Mok. *Chem. Phys. Lett.*, **417**, 256 (2006)

[236] J. M. L. Martin. *Chem. Phys. Lett.*, **259**, 669 (1996)

[237] P. L. Fast, M. L. Sánchez and D. G. Truhlar. *J. Chem. Phys.*, **111**, 2921 (1999)

[238] T. van Mourik, A. K. Wilson, K. A. Peterson, D. E. Woon and T. H. Dunning, Jr. *Adv. Quantum Chem.*, **31**, 105 (1998)

[239] P. V. Sushko, A. L. Shluger, R. C. Baetzold and C. R. A. Catlow. *J. Phys.-Condens. Matter*, **12**, 8257 (2000)

[240] D. M. Ramo, P. V. Sushko, J. L. Gavartin and A. L. Shluger. *Phys. Rev. B*, **78**, 235432 (2008)

[241] L. Giordano, P. V. Sushko, G. Pacchioni and A. L. Shluger. *Phys. Rev. B*, **75**, 024109 (2007)

[242] L. Giordano, P. V. Sushko, G. Pacchioni and A. L. Shluger. *Phys. Rev. Lett.*, **99**, 136801 (2007)

[243] M. V. Ganduglia-Pirovano, K. Reuter and M. Scheffler. *Phys. Rev. B*, **65**, 245426 (2002)

[244] K. Sohlberg, S. Zhuo, P. Nellist, Y. Peng and S. Pennycook. *J. Phys. Chem. C*, **112**, 11831 (2008)

[245] L. G. V. Briquet, C. R. A. Catlow and S. A. French. *J. Phys. Chem. C*, **113**, 16747 (2009)

[246] P. W. Atkins, T. Overton, J. Rourke, M. Weller and F. Armstrong. *Inorganic Chemistry, 4 ed.* Oxford University Press (2006)

[247] N. Binsted, J. Evans, G. N. Greaves and R. J. Price. *Organometallics*, **8**, 613 (1989)

[248] M. A. Newton, A. J. Dent, S. Diaz-Moreno, S. G. Fiddy and J. Evans. *Angew. Chem. Int. Edit.*, **41**, 2587 (2002)

[249] M. A. Newton, B. Jyoti, A. J. Dent, S. G. Fiddy and J. Evans. *Chem. Commun.*, 2382–2383 (2004)

[250] A. J. Dent, J. Evans, S. G. Fiddy, B. Jyoti, M. A. Newton and M. Tromp. *Angew. Chem. Int. Edit.*, **46**, 5356 (2007)

[251] G. N. Vayssilov and N. Rosch. *J. Am. Chem. Soc.*, **124**, 3783 (2002)

[252] J. F. Goellner, B. C. Gates, G. N. Vayssilov and N. Rosch. *J. Am. Chem. Soc.*, **122**, 8056 (2000)

[253] A. Filipponi, M. Borowski, D. T. Bowron, S. Ansell, A. D. Cicco, S. D. Panfilis and J.-P. Itiè. *Rev. Sci. Instrum.*, **71**, 2422 (2000)

[254] P. Kizler, P. Lamparter and S. Steeb. *Phys. B (Amsterdam, Neth.)*, **158**, 392 (1989)

[255] A. L. Ankudinov, B. Ravel, J. J. Rehr and S. D. Conradson. *Phys. Rev. B*, **58**, 7565 (1998)

[256] M. Fernandez-Garcia, A. Martinez-Arias, I. Rodriguez-Ramos, P. Ferreira-Aparicio and A. Guerrero-Ruiz. *Langmuir*, **15**, 5295 (1999)

[257] T. H. Dunning. *J. Chem. Phys.*, **90**, 1007 (1989)

[258] I. D. Brown. *J. Res. Natl. Inst. Stand. Technol.*, **101**, 341 (1996)

[259] H. Nakai and Y. Kikuchi. *J. Comput. Chem.*, **27**, 917 (2006)

[260] C. R. A. Catlow, S. T. Bromley, S. Hamad, M. Mora-Fonz, A. A. Sokol and S. M. Woodley. *Phys. Chem. Chem. Phys.*, **12**, 786 (2010)